Alma Mater Studiorum – Università di Bologna

DOTTORATO DI RICERCA IN

Scienze della Terra, della Vita e dell'Ambiente

Ciclo XXXII

Settore Concorsuale: 04/A1

Settore Scientifico Disciplinare: GEO/09

THE ROLE OF FLUIDS ON STRAIN LOCALIZATION AT THE BASE OF THE SEISMOGENIC CRUST: A CASE STUDY FROM THE OLKILUOTO DEEP NUCLEAR WASTE REPOSITORY, SOUTHWESTERN FINLAND

Presentata da: **Barbara Marchesini**

Coordinatore Dottorato	**Supervisore**
Prof. Giulio Viola	Dott. Paolo S. Garofalo
	Co-Supervisore
	Prof. Giulio Viola

Esame finale anno 2020

Abstract

This study focuses on the detailed investigation of the role played by fluids in triggering and controlling transient and repeated fluctuations between the frictional and viscous deformation end-members at structural levels corresponding with the brittle-ductile transition zone (BDTZ) of the continental crust. The Paleoproterozoic basement of southwestern Finland was the chosen study area. There, a deep repository for the storage of high-grade nuclear waste is being built on the Olkiluoto Island offering unprecedented 3D access to the rock volume. The migmatitic Olkiluoto basement is deformed by numerous sets of brittle-ductile deformation zones that nucleated and were later repeatedly reactivated at the BDTZ. A representative set of subvertical, conjugate brittle-ductile to fully brittle strike-slip faults was thus studied at a variety of scales of observations by applying several analytical techniques in order to derive quantitative constraints on the physical and chemical boundary conditions during faulting. The studied fault system is formed by a "wet" dextral brittle fault zone (BFZ300), which forms the main focus of this study, and by its conjugate sinistral counterpart (BFZ045), which, however, is only partially discussed herein as it is the core of a second Ph.D. study.

A multiscalar structural study was carried together with fluid inclusion and mineral chemistry analysis on synkinematic and authigenic minerals to reconstruct the temporal variations in fluid pressure (P_f), temperature (T), composition (X) and salinity (%wt NaCleq) of the synkinematic fluids that triggered and later mediated deformation steering strain localization along the BFZ300.

The BFZ300 fault core contains two laterally continuous quartz veins formed by two distinct types of quartz – Qtz I and Qtz II, respectively, with Qtz I older than Qtz II. The damage zone is formed by a fault-fracture mesh filled exclusively by Qtz I. Recurrent cycles of mutually overprinting brittle and ductile deformation were documented. The trigger to these fluctuations is identified in the role played by repeating oscillations of fluid pressure peaking at a maximum value of 210 MPa. The two quartz types precipitated from distinct aqueous fluid batches. Bulk salinities are in the 1-5 wt% NaCleq range for Qtz I and in the 6-11 wt% NaCleq range for Qtz II. The temperature of the fluids causing initial strain localization and later fault reactivation evolved through time from > 350° C during Qtz I precipitation to < 300° C at the time of Qtz II crystallization. Initial, fluid-mediated embrittlement occurred at the expense of a rock system that was under overall ductile conditions. It generated a diffuse network of joints and hybrid/shear fractures in the damage

zone. Subsequent deformation led to continued localization within the fault core, thus forming a narrowing deformation zone.

Laser ablation mapping of trace element distribution and Electron Back-Scattered Diffraction (EBSD) were combined to study the micromechanics of sulphide (particularly pyrite) deformation and, additionally, to gain insights into the potential role played by authigenic sulphides in strain accommodation and deformation-induced mass transport during the last brittle stages of the BFZ300 activity. Sulphides occur within the Qtz II vein as polycrystalline aggregates. Their EBSD analysis reveals that intracrystalline deformation at a temperature of c. 300° C in the Qtz II-sulphide bi-phase system was accommodated by the interplay of several, coexisting brittle and low-temperature crystal-plastic processes. Strain created high diffusivity pathways within the pyrite crystal lattices contributing to and enhancing the net transport of a significant range of heavy elements (e.g. Co, Ni, Cu, Sn, Ag, As, Sb, Pb) within the wet BFZ300 during its late stages of deformation.

This study shows that fluid overpressure at the BDTZ plays a key role in the initial embrittlement of the deforming rock and steers subsequent strain localization. Under overall brittle conditions (T < 300° C), temperature combined with fluid-rock interactions induced by repeating ingress of multiple fluid batches are the key factors steering strain localization and inducing elemental mobility in wet fault systems.

Table of contents

Chapter 1. Introduction and organization of the Ph.D. thesis

This thesis presents the results of a comprehensive and multidisciplinary study of the architecture and structural evolution of a fluid-rich fault system deforming the migmatitic Proterozoic crystalline basement of southwest Finland on the Island of Olkiluoto. The main goal of the study was to constrain as quantitatively as possible the physical and chemical parameters that steered the fault (seismic) evolution in space and through time. In particular, given the abundance of syntectonic veins in the fault architecture, the study focussed specifically upon the role played by fluids in triggering and controlling deformation at seismogenic depth. The basement of the Olkiluoto Island has been selected as the host for the Finnish deep repository of high-grade nuclear waste. It will be the first repository in the world to contain high-level nuclear waste to become operational in just a few years.

A set of conjugate subvertical structures, exhumed from the brittle-ductile transition zone (BDTZ), were used as a proxy to study fault initiation and reactivation in a crystalline basement in response to fluid pressure oscillations. The study was mainly aimed at understanding the complex history of fault reactivation at the BDTZ and seismogenic depth in general and the implications thereof on the long-term stability of the Olkiluoto repository. The study has shown that the studied faults underwent multiple episodes of reactivation. To constrain the details and the triggers of these reactivation phases as well as the environmental conditions prevailing during faulting, it was important to reconstruct the time-space evolution of the fault system. This information is crucial to make inferences of the deformation at the regional scale and make qualified guesses as to the hydro-thermo-mechanical behaviour of faults on long (geological) terms.

The bedrock of Olkiluoto has already been studied extensively and in great detail in order to characterise and better understand its mechanical discontinuities so as to generate sound inputs to the evaluation of the long-term stability of the site and the related risk assessment. However, aiming at further refining the knowledge of faulting and mechanical reactivation in general and in the basement block being excavated in Olkiluoto, Posiva Oy, the Finnish organisation responsible for the management of the nuclear waste and the construction of the national repository (http://www.posiva.fi/en), decided to support the research activities of this Ph.D. project. This study, moreover, was conducted in collaboration with the University of Plymouth, UK, where a second Ph.D. project is still

ongoing focussing mostly on the early ductile precursors to the many brittle-ductile deformation zones of the Proterozoic basement.

The structure of this research was designed to allow the study of these topics in a gradual, progressive fashion such that, after the necessary field and microstructural analysis, more advanced analytical techniques were used to generate (semi)quantitative constraints upon the activated faulting processes. The thesis layout follows this approach and is explained herein.

Chapter 2 introduces the basic concepts of rock mechanics and fault rheology in the lithosphere that form the necessary conceptual basis to the following chapters. Particular focus is reserved to the specific role of fluids on fault rheology at the BDTZ. Some relevant concepts of the high-level nuclear waste storage and deep geological repository field of study are also treated in Chapter 2 in order to provide the necessary background information to the research done herewith.

Chapter 3 provides an overview of the regional geology of southwestern Finland, with a particular focus on the local geology of the Olkiluoto Island. A concise description of the long-term evolution of its basement and of the deformation stages registered is presented.

Chapter 4 introduces the used toolbox, that is, the set of analytical techniques employed in the study of the Olkiluoto fault rocks to constrain fluid pressure (P_f), temperature (T), salinity (wt% NaCleq) and composition (X) of the synkinematic fluids that were involved during the multi-stage deformation of the area.

In Chapter 5, the fault BFZ300, the brittle dextral fault zone (BFZ) that forms the main focus of the Ph.D., is described and characterised. Many mesoscopic details of its internal architecture and of its mesoscopic characteristics are given and explained. A brief summary of the main structural features of the sinistral fault system, named BFZ045, that is interpreted as the conjugate structure to BFZ300, is also presented in that Chapter.

The microstructural analysis of the BZ300 fault is presented in Chapter 6. It was carried out on both the host rock as well as the fault rocks and synkinematic veins that form BFZ300 and its results are used as the base for the interpretation of fluid inclusion trails presented in Chapter 7. Chapter 7 is dedicated to the study of fluid inclusions within BFZ300 fault rocks and includes petrographic descriptions, microthermometric and micro-Raman analysis.

With the aim to reconstruct the variability of chemical composition and temperature of the synkinematic fluids that repeatedly ingressed the fault, Chapter 8 presents the detailed investigation of the composition of synkinematic fault minerals and uses them to derive

thermometric estimates on the conditions of faulting. Chemical compositions were derived by combining electron microprobe microanalysis and a state-of-the-art laser ablation mapping technique, whereas formation temperatures were obtained by using mineral pair geothermometers. The temperature of the last event of mobilization and subsequent recrystallization of carbonaceous material during the metamorphic retrograde path of the Olkiluoto basement was also constrained.

Chapter 9 presents a discussion of the fluid inclusion dataset and the determination of salinities of the paleofluids. Salinities are then combined with independent geothermometric constraints on formation-temperatures to reconstruct the overall fluid evolution and its pressure oscillations as registered in the fault zone rock record.

Field evidence, microstructural observations, fluctuations of fluid pressure and paleotemperatures are then combined to elaborate an integrated mechanical evolutionary model of the BFZ300, which is presented and discussed in detail in Chapter 10. This chapter also includes a discussion about the potential seismic behaviour of the fault.

Chapter 11 lays out a detailed micromechanical and microchemical study of the sulphides that are found within the quartz veins emplaced along BFZ300 during its latest reactivation stages. Microstructural analysis, laser ablation mapping of trace elements and Electron Back-Scattered Diffraction on sulphides were used to understand how BFZ300 sulphides accommodated strain at T < c. 300° C. Results are used to explore the feedbacks between deformation and elemental mobility within the sulphide crystal lattice. A micromechanical model that accounts for the different elemental spatial distribution patterns is discussed within the background knowledge of the deformation properties of sulphides.
The last chapter, Chapter 12, is dedicated to final remarks and potential future development of this research.

Resulting from the original work of this Ph.D., one scientific paper was already published by Marchesini and coauthors in 2019. The published final version of the paper is reported in Appendix C. A second paper with Marchesini as one of the coauthors is currently under review for Solid Earth (Prando et al., under review; the discussion forum format of the paper is reported in Appendix D). The latter represents part II of the Marchesini et al. (2019) paper. A third manuscript, which is based on the Chapter 11, is currently in preparation and will be soon ready for submission.

Chapter 2. Concepts overview

2.1 Brief introduction to the mechanics of rocks and adopted nomenclature

In the last century, the combination of material and Earth sciences, encompassing both experimental data and direct geologic observations, has led to the in-depth knowledge of the mechanisms that steer deformation of solid matter at different scales. In particular, this combined approach has had significant impact upon our understanding of the Earth's rheology and of the mechanisms that make strain accommodation possible, from the micrometric- to the plate-tectonics scale (e.g. Ranalli, 1987; Turcotte and Schubert, 2002).

The rheology of materials whose behaviour can be analysed and described through the theoretical approach of continuum mechanics can be coarsely classified as elastic, plastic or viscous (Jaeger and Cook, 1976). Stressed materials can also respond to the applied stress field by deforming in a brittle manner, i.e. a response to stress in which the spatial continuity of the material is interrupted by fractures. Brittle deformation is beyond the field of continuum mechanics and it will be treated in detail separately.

The deformation of a continuous medium is commonly explained by constitutive equations, which describe the relationship between stress and strain or stress and strain rate. Deformation is usually represented in a xy Cartesian plane where strain or strain rate are commonly plotted on the horizontal- and stress on the vertical axis (Fig. 1.1a).

When a stress is applied to a material, we define the material "elastic" if it exhibits an instantaneous linear strain in response to the applied stress. Ideally, when the applied force or stress is removed, the material returns to its original shape without any permanent strain. As an example, rubber can be considered as a typical elastic material of everyday life. During a perfectly elastic deformation, the strain increases with stress in a linear manner, following the Hooke's constitutive law:

$$\sigma = Ee$$

where σ is the stress, e the extension (i.e. one-dimensional strain), and E is the Young's elastic modulus (or a different appropriate elastic modulus such as G, the shear modulus in the case of shear deformation).

Each material has a specific elastic limit, called the yield point corresponding to a yield stress (Fig. 2.1a), beyond which permanent strain is achieved and accommodated by the deforming material. Permanent deformation is commonly referred to as "plastic" deformation (Fig. 2.1a). In this scenario, playdough can be considered as an analogue of

plastic material because of its very low yield stress. Plastic deformation after the yield point can generically proceed in three ways: 1) perfectly plastic behaviour or steady-state conditions, wherein the stress at which deformation continues is constant; 2) strain hardening behaviour, in which stress increases as deformation proceeds and 3) strain weakening behaviour, where stress decreases with increasing strain. Plastic deformation can be followed by brittle failure that may indeed occur as the result of continuous and repeated strain hardening and/or weakening (e.g. Fig. 2.1).
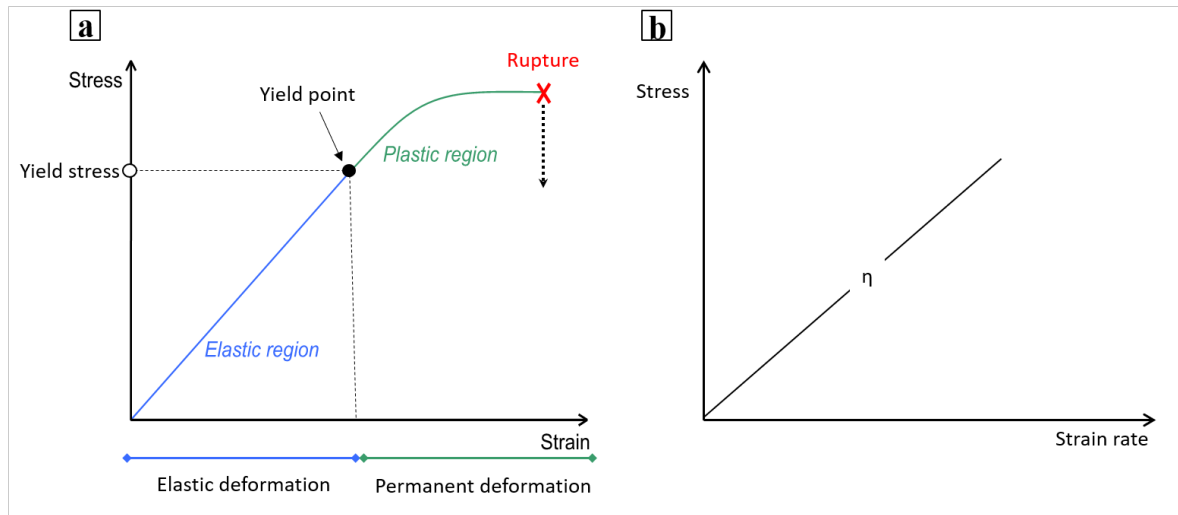
Figure 2.1. (a) Stress-strain curve for elastic-plastic deformation. Permanent plastic deformation is obtained when the applied stress oversteps the stress limit (yield stress) of a material. (b) Stress-strain rate linear curve for Newtonian fluids.

Fluids exhibit the typical "viscous" behaviour, characterized by a distributed flow that involves a stress that correlates to the applied strain rate. The derivative of the stress vs. strain rate relationship is known as the viscosity of the material. In its simplest case, i.e. considering Newtonian fluids in which stress follows a linear relationship with the strain rate and the slope of the curve defines the viscosity of a material (Fig. 2.1b):

$$\sigma = \eta \, \dot{e}$$

where η is the viscosity and $\dot{e}$ the strain rate. This linear relationship is, however, not always valid as demonstrated by the case of, for example, shear thinning fluids, which follow a non-Newtonian behaviour (stress decreasing with strain rate) or shear thickening fluids (stress increasing with strain rate).

All materials, including rocks, can be considered at a first approximation as viscous, at an appropriate time scale of deformation. As a general rule, a material behaves in a viscous manner if a given strain increment occurs over a timescale that is longer than at the time

defined by the ratio between the viscosity and the shear modulus (Maxwell time). Intuitively, this ratio can be understood as the typical time in which the processes that accommodate viscous deformation are more energy efficient than brittle processes, which are, instead, virtually strain-rate independent. This is the reason why high-temperature rocks in the lower crust and mantle can mechanically behave as fluids over geologic time.

In slight contrast with the commonly adopted physical terminology, in structural geology and rock mechanics the rheological behaviour of rocks is commonly classified as brittle and ductile.

The mechanical behaviour of a volume of rock is defined "brittle" when deformation beyond the yield point occurs by fracturing, creating visible discontinuities (i.e. fractures and fault) at both the macroscopic and microscopic scale. On the contrary, geologists define "ductile" as the overall mechanical behaviour whereby strain is accumulated in rocks by a "flow" without discrete, strongly localized deformation. Typical examples of ductile behaviour are folds and mylonitic shear zones. This terminology is therefore used to describe geometrically discontinuous or continuous deformation of rocks, respectively. However, these definitions are simple geometrical descriptions that strongly depend on the spatial and temporal scale of observation: for example, major shear zones are discontinuities between different rock units but are continuous zones of deformation at the scale of the outcrops. Another example is the common observation that brittle deformation overprints ductile deformation over the long history of deformation and exhumation in several shear zones.
Brittle and/or ductile deformation at a given scale depend on the overall mechanical properties of the studied rock, on their history of deformation and, lastly, on the specific deformation processes that cause the rock to fail mechanically in either a ductile or brittle fashion.

In nature there exist numerous meso-scale geological structures that document the effects of ductile continuous deformation, but, when studied at the microscopic scale, exhibit evidence of also discontinuous brittle localization. For instance, rocks that deform by cataclastic flow (ductile mode) at the macroscopic scale, deform by brittle processes at the grain scale. This is a typical example of how the macroscopic mode of deformation is fundamentally different from the actual physical processes of deformation.

Often, in geology it is preferable to use the term "plastic" instead of ductile. In the geological literature, "plastic" is thus used to describe all those intracrystalline deformation mechanisms that occur at the sub-solidus state and are generally associated with a change in

shape or size of a rock without inducing brittle fracturing. In particular, "plastic" is often referred to rock deformation dominated by intracrystalline deformation occurring by movement of dislocations and other crystal defects.

In general, the lithosphere of the Earth behaves in a brittle manner in its uppermost part, whereas behaves in a more ductile way at greater depth, where crystalloplastic processes are highly efficient because of the elevated ambient temperature (see below).

Breaking of atomic bonds and fracture growth and propagation are the characteristics of brittle deformation. In geology brittle deformation is typically associated with fracturing and slip processes that involve dilation. Therefore, the brittle mechanical strength of rocks depends on the confining pressure, because the confinement works against the dilation. Brittle deformation obeys to empirical laws such as the Mohr-Coulomb principle (see below) and Amontons' laws of friction and thus is at times also termed "frictional" (the two will be used interchangeably hereinafter). On the other hand, in geology, ductile deformation is commonly associated with dominant crystal plastic processes such as diffusion creep, dislocation creep, twinning etc., which obey specific "viscous" flow laws. In detail, plastic processes involve the migration of crystalline defects (e.g. dislocations and vacancies) or migration of components (vacancies, interstitials, ions in solution) to change the shape of crystals without causing the actual breakage of chemical bonds. As mentioned above, such processes are strongly enhanced and facilitated by high temperatures.

From direct field observations and on rock deformation laboratory experiments performed over a broad temperature range we know that a lower temperature threshold value has to be overstepped in order for plastic deformation to be activated. Beyond this limit, rocks gradually accumulate strain without the formation of physical discontinuities.

Looking at the rheology of Earth's lithosphere (Fig. 2.2a), the cooler upper crust (<300 °C) is dominated by faulting and other mechanisms typical of the frictional regime (e.g., Kohlstedt et al., 1995; Ben-Zion and Sammis, 2003; Smith et al. 2011). Deformation therein occurs mostly by cataclasis (the combination of fracturing, grain rotation and frictional sliding; e.g. Sibson 1977), leading to intense intra- and intercrystalline fracturing steering to the progressive mechanical comminution of the deforming rock. Representative fault rocks of this structural regime are breccias and the complete series of cataclasites (e.g. cataclasite example in Fig. 2.2b). As mentioned above, the upper crustal strength is thus pressure-sensitive, because it is fundamentally controlled by the amount of stress necessary to create new or reactivate existing fractures, i.e. to dilate the rock by overcoming the confinement. The deformation of the upper crust follows the Coulomb failure criterion:

$$\sigma_s = \sigma_n \tan \phi + C$$

where σ_s is the critical shear stress, σ_n is the normal stress acting on a fracture plane at the moment of failure and $\tan \phi$ is the coefficient of friction (commonly indicated as μ), with ϕ being the angle of internal friction. μ it is a variable that depends on the physical properties of the deforming material. A value of 0.6 is commonly chosen for general calculations. Byerlee's empirical frictional law predicts an increase in critical shear stress (i.e. the amount of stress required for fracturing, commonly indicated as σ_s or τ) through the frictional upper crust. At low confining pressure, the shear stress is given by:

$$\sigma_s = 0.85\sigma_n$$

whereas at higher confining pressure the equation becomes:

$$\sigma_s = 0.5 + 0.6\sigma_n$$

where σ_n is the stress normal to the actual or incipient fracture plane. This relation implies that faults in the lithosphere are stronger at greater depth in the brittle layer. Instead, at even greater depth the high temperature and confinement cause the Earth's crust to become progressively weaker (Kohlstedt et al., 1995; T > 450° C). This is because the increasing temperature activates dislocation movements and intracrystalline plasticity within minerals. Although the lithosphere is not monomineralic, at a first approximation we can estimate its strength by relying on strength determinations of its most abundant constituent minerals. In the typical quartzo-feldspathic crust, the transition between the frictional and ductile regime occurs between c. 350° and 450° C, which mark the inception of crystal plasticity in quartz and feldspar, respectively (e.g. Passchier and Trouw, 2005; Fig. 2.3). Conversely, in the olivine and pyroxene-rich rocks of the oceanic crust and mantle or in the amphibole-rich lower crust, this transition occurs at temperatures higher than about 700-800° C (e.g. Hirth and Kohlstedt, 1995; Passchier and Trouw, 2005). Temperature-sensitive power law creep equations are therefore used to estimate the lower crustal strength. Different flow laws exist, and they depend on the active crystal-plastic mechanisms (e.g. Carter and Tsenn, 1987; Schmid, 1982; Hirth et al., 2001).

This compositional mineralogical heterogeneity between different parts of the lithosphere results in a complex rheological layering of the lithosphere, which end up being characterized by alternating brittle and viscous layers (Brace and Kohlstedt, 1980; Ranalli and Murphy, 1987; Ranalli, 2000; Burgmann and Dresen, 2008).

In the context of this Ph.D. thesis, particular emphasis is placed on the bittle-ductile transition zone (BDTZ hereinafter), wherein with greater depth brittle frictional processes pass to crystal plasticity over a crustal volume where they coexist, act transiently and

compete (e.g. Sibson, 1977, 1980, 1983; Rutter et al., 1986; Kohlstedt et al., 1995; Stipp and Kunze, 2008; Behr and Platt, 2014).
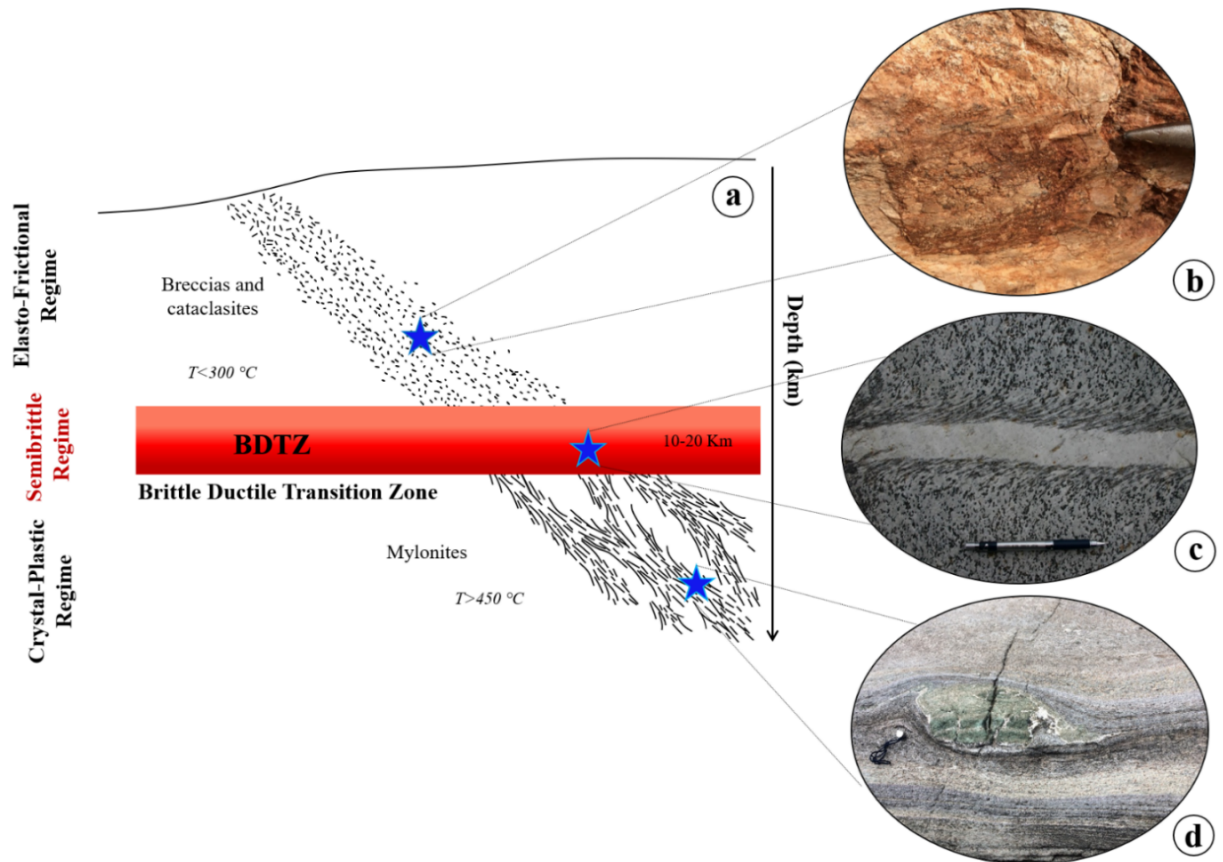
Figure 2.2. Schematic representation of a crustal continuous shear zone. Modified after Sibson (1977). (a) From the surface to an increasingly greater depth, the shear zone is characterized by texturally distinctive fault rocks produced by varying deformation mechanisms activated under different environmental conditions (e.g. brittle vs crystal-plastic regimes). The cool upper crust (T<300° C) is commonly characterized by a brittle behaviour and deformation therein occurs predominantly by frictional processes producing gouge, breccia and cataclasite. (b) Fault plane view of a dextral strike slip fault hosted in carbonates of the Paleogene Scaglia Rossa Formation from the Umbria-Marche sequence of the Italian Northern Apennines (locality: Postignano). The cataclastic fault plane picture is used as a representative field example of brittle deformation in the upper crust. The middle crust is otherwise characterized by a competition between brittle and crystal-plastic deformation mechanisms that create a complex structural domain usually referred to as the "brittle—ductile transition zone" (BDTZ). (c) Example of ductile deformation overprinting a brittle precursor at the BDTZ. Paired shear zones developed along the edges of an aplitic dyke (locality: Östlicher Nöfesferner glacier, South Tyrol) as representative example of competing and coexisting processes at mid crustal depth. High temperature lower crustal rocks commonly accommodate deformation by intracrystalline plasticity. At even lower crustal depths, deformation is accommodated within a diffuse rock volume and mylonites are the most characteristic fault rocks. (d) Delta porphyroclast formed by an eclogite lens within a blueschist facies matrix (locality: Lago di Cignana, Western Alps) used as field example of spatially distributed deformation. The related depth-temperature ranges are given assuming a "normal" geothermal gradient of 26° C/km.

This zone has a key rheological significance and importance because it is the region of highest resistance in the lithosphere, where the largest earthquakes occur, and where remarkable fluid rock interaction also occurs (e.g. see Paragraph 2.2). In this region, both brittle and viscous deformation may be intermittently activated in a cyclic fashion (e. g. Fig. 2.2c). The BDTZ does not occur at a constant and well-defined depth in the crust. Instead, the BDTZ is an extremely complex and dynamic volume of rock that is affected by numerous parameters and

whose depth can vary between 10 and 20 km. Its depth, thickness, lateral variability and persistence in time are affected by the simultaneous activity of numerous factors, which can be intrinsic to the rock (e.g. composition, mineralogy and crystallography) and/or express the external environment (e.g. stress, temperature, fluid content, strain rate, chemical activity).

Because rocks are polymineralic and different minerals have different brittle-plastic transition windows, the brittle-ductile transition zone of the entire lithosphere may be up to several kilometre-thick (Fig. 2.3). The most representative example of these competing processes is represented by the deformation of a quartz-feldspatic crust at 400° C, where quartz flows plastically while feldspar accommodates deformation by fracturing (Fig. 2.3).
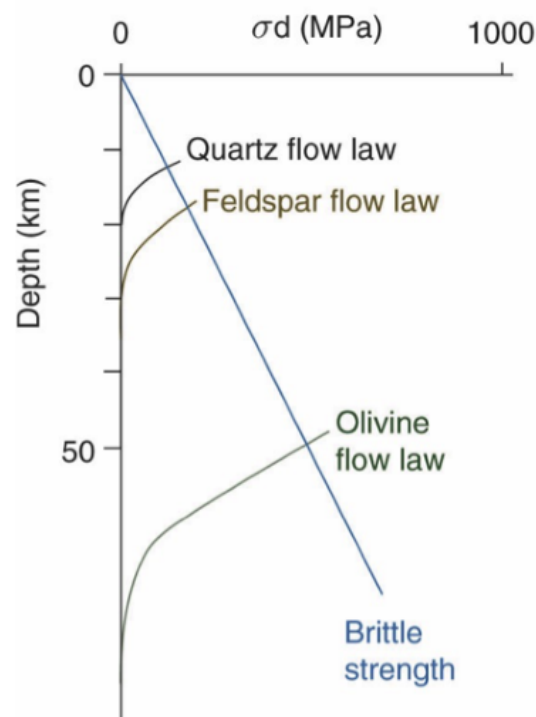
Figure 2.3. Rheologic stratification of the continental lithosphere based on a combination of the brittle friction law and the plastic flow laws derived experimentally for quartz (quartzite), feldspar (diabase) and olivine (dunite). The brittle-ductile transition occurs where the brittle (frictional) and plastic flow laws intersect. Modified from Fossen 2006.

Temperature, however, is not the only parameter affecting the brittle-ductile transition depth. Mineral-filled extension fractures observed in exhumed low-grade metamorphic rocks as well as the nucleation of earthquakes at lower crustal depth indicate that also middle-lower-crustal rocks can accommodate deformation by frictional mechanisms. The presence of fluids, as free phase or even overpressured fluid pockets in addition to the presence of hydrate minerals (e.g. phyllosilicates), commonly lowers the strength of the rocks, i.e. rocks can sustain lower differential stress than in a dry environment (Fig. 2.4). In a "wet" rock environment the presence of water lowers the activation energy of plastic processes.
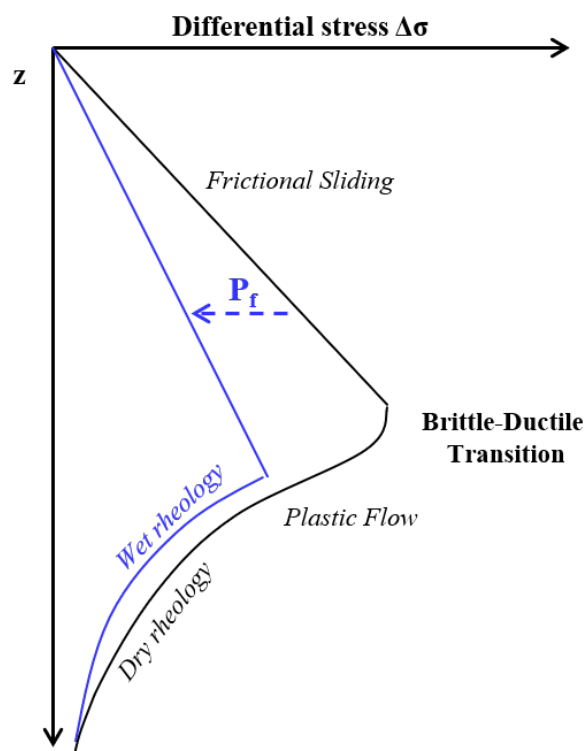
Figure 2.4. The upper crust obeys the Byerlee frictional sliding law whereas the lower crust rheology is steered by plastic flow laws. The brittle-ductile transition zone is gradual and occurs at the zone of interaction between frictional and plastic flow. The effect of fluids on the strength of the lithosphere: Black curves/envelops are related to "dry" rocks, whereas the blue curves represent "wet" conditions.

In addition, the fluid pressure (P_f) plays a direct physical role in rock mechanics and greatly affects fault stability (Fig. 2.5). This is because the fluid pressure counteracts the tectonic stress, decreasing the effective stress (σ' i.e. the difference between the applied stress and the fluid pressure). As a consequence of high fluid pressure, faulting may occur at lower stress conditions and faults that normally are in stable conditions maybe be reactivated under the effect of the fluid pressure (Fig. 2.5).
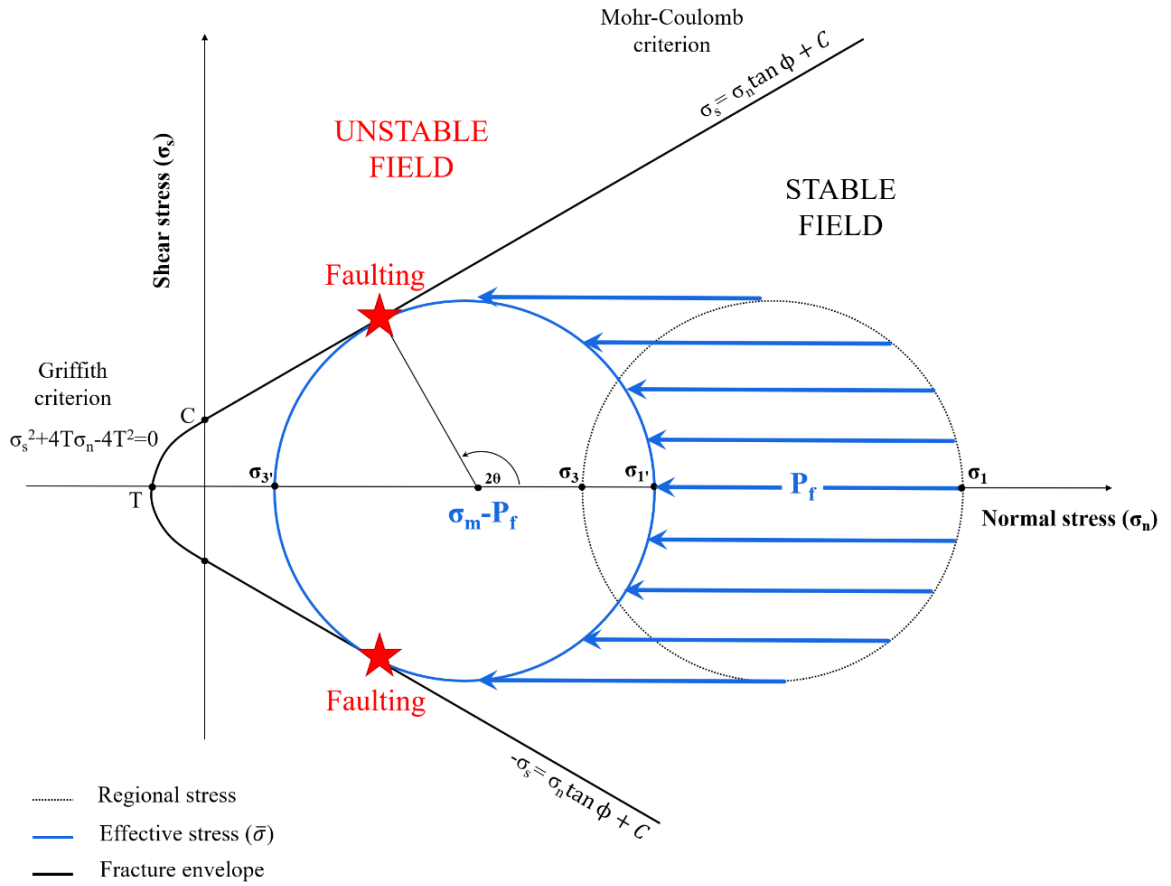
Figure 2.5. The effect of increasing fluid pressure (P_f) in an intact rock or generally in rock. An increase in the fluid pressure causes a reduction in the mean stress (σ_m) of the system, while the differential stress remains the same. This can be schematically represented in Mohr-Coulomb space as a Mohr circle translated to the left toward the origin of the axes. At these new conditions, a shear fracture will form if the fracture envelope is touched while σ_3 still positive.

In a Mohr diagram, the stress circle representing the stress state of the rock mass is shifted toward lower effective pressures as the fluid pressure increases. If the fluid pressure is high enough, this shifting causes the circle to eventually touch the Mohr-Coulomb failure envelope, thus leading to mechanical brittle failure. The failure can be either seismic or aseismic. Under particular conditions, extremely high fluid pressures ($P_f > \sigma_3+T$) cause the formation of pure tensional or hybrid shear-tensional fractures (i.e. hydrofractures, e.g. Secor 1965). Such high fluid pressures at the BDTZ may be due to prograde metamorphic reactions typical of lower-greenschist facies conditions releasing water and carbon dioxide.

The mineral-filled extensional fractures documented in many exhumed low-grade metamorphic rocks are widely explained as field evidence of these processes. In the following paragraph a detailed overview of the role of fluids at the brittle-ductile transition is given.

2.2 The role of fluids in steering brittle-ductile cyclicity at the brittle-ductile transition zone: a closer look

Fault systems and their physical chemical properties play a fundamental role in controlling the rheological behaviour of the Earth's crust and in steering channelled fluid flow (e.g. Caine et al., 1996). Deformation and fluid flow are closely related and mutually dependent via a number of feedbacks, such as the control that fluids exert upon the effectiveness of deformation processes and the development of fault systems at all scales, and the control by rock heterogeneities and/or fracture system topology on the net fault transmissivity (e.g. Crider and Peacock, 2004). The nucleation and development of permeable fault systems and the mechanisms whereby individual faults may weaken and eventually fail are, therefore, complex functions of a number of processes. In this perspective, the interaction between fluid and mineral phases within fault rocks needs to be studied with a system approach in order to single-out the role and importance of all processes involved (Kaduri et al., 2017).

An obvious effect of fluid involvement, particularly in crustal volumes that have experienced large deformation-controlled fluid fluxes, is the precipitation of authigenic and hydrothermal minerals within faults (Oliver and Bons, 2001; Viola et al., 2016) and their immediately adjacent host rock (Mancktelow and Pennacchioni, 2004). In the seismogenic region of the crust, where fluids may even be the primary driver of the seismic cycle (e.g Miller, 2013), faults have been shown to have the potential to function like a "fluid-activated valve", whereby they experience transient and cyclic fluid pressure build-up before sudden fluid venting, pore pressure- and mechanical strength drop concomitant with seismic failure (e.g. Sibson, 1989, 1992b, 1993; Cox, 1995;Viola et al., 2006; De Paola et al., 2007; Wehrens et al., 2016). Hydrothermal ore deposits, where fault networks focus relatively large volumes of ore fluids and precipitate economic minerals (Cox et al. 2001; Boiron et al., 2003; Moritz et al., 2006; Scheffer et al., 2017a) are also pertinent examples of significant deformation-controlled fluid ingress.

The seismogenic depth down to 10-20 km (e.g. Kohlstedt et al., 1995) is thus a key region of the crust where to study the whole range of fluid-rock interaction processes occurring within fault zones. Deformation at that depth might be accommodated under overall brittle-ductile conditions along fault systems crossing or rooting into the BDTZ. In detail, the deformation style in the BDTZ is generally characterized by the cyclicity, also at the short time scale, between brittle and ductile behaviour (Famin et al., 2004; Famin et al., 2005;

Siebenaller et al., 2013). This is induced and regulated by the complex and transient interplay of numerous parameters, among which the lithological composition and transient variation of temperature, pore pressure and strain rate within the deforming system. Field studies have documented unequivocally that ductile and brittle deformation may even be simultaneously active during deformation as a function of the transient and spatially heterogeneous evolution of the chemical and physical parameters steering deformation, leading to the broad coexistence of geological features expressing frictional deformation and viscous creep, and to mutual crosscutting relationships thereof (e.g., Guermani and Pennacchioni, 1998; Kjøll et al., 2015; Pennacchioni et al., 2006; Wehrens et al., 2016; Scheffer et al., 2017b).
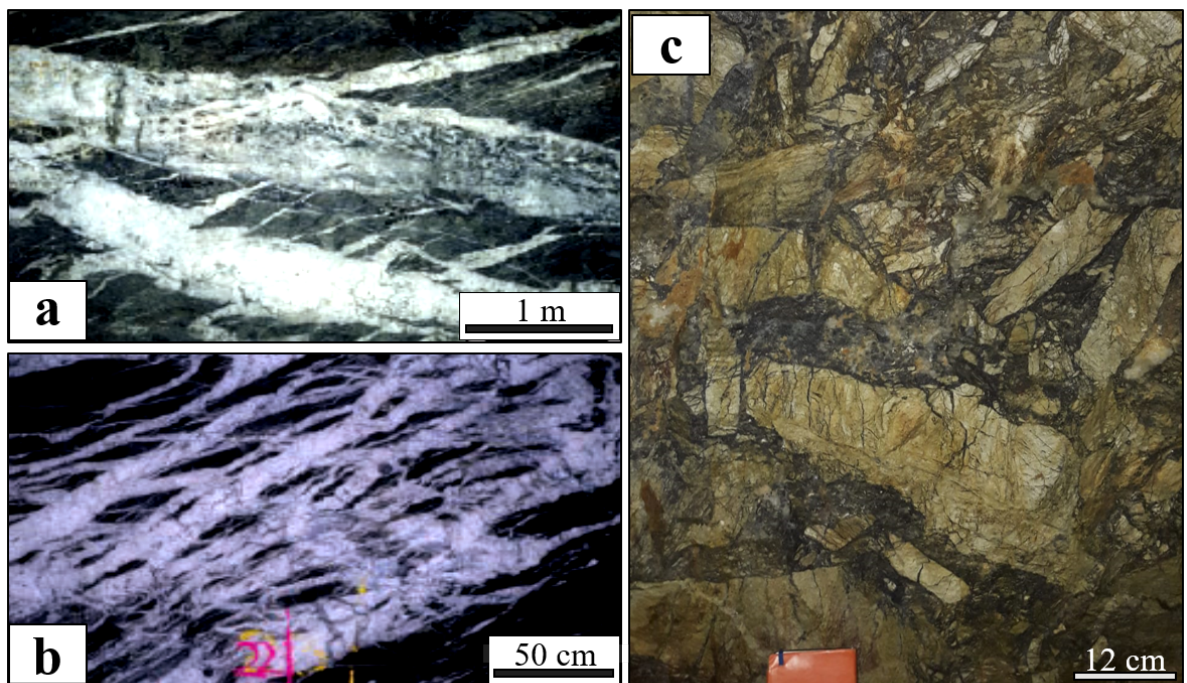
Figure 2.6. (a) Quartz-rich extensional fault veins in two adjacent reverse fault zones (Defiance lode, St. Ives goldfield, Western Australia; from Cox, 2016). (b) Zone of intense development of extension veins (Conqueror lode system, St Ives goldfield, Western Australia; from Cox, 2011). (c) Hydraulic breccias within the European Variscan basement, as evidence of local fluid overpressure activity (Teufelsgrund mine, Münstertal, SW Germany; we refer the reader to the study of Staude et al., 2009 for the description of the Teufelsgrund mine structures).

Veins are particularly important in this context because they attest to the relative abundance of aqueous fluids in the deformation history (e.g. Cox et al., 2001). Portions of the seismogenic crust that experience large fluid fluxes (e.g. wet condition or even fluid-rich environment) host pervasive and vertically extensive vein networks (Sibson et al., 1988,

Figs. 2.6a-b), within which up to several millions of m^3 of hydrothermal minerals may deposit from the flowing fluid (e.g. Heinrich et al., 2000; Cox, 2005; Bons, 2001). Also, hydraulic breccias are commonly interpreted as evidence of local tensile overpressure conditions (Sibson 1986; Fig. 2.6c). In contrast, portions of the crust deforming in the absence of significant fluid flow (e.g. dry condition or even fluid-poor environment) would show less abundant and spatially continuous veins (Fig. 2.7a). Also, pseudotachylytes (i.e. solidified friction-induced melts; Fig. 2.7b) is commonly interpreted as evidence of environmental dry conditions.
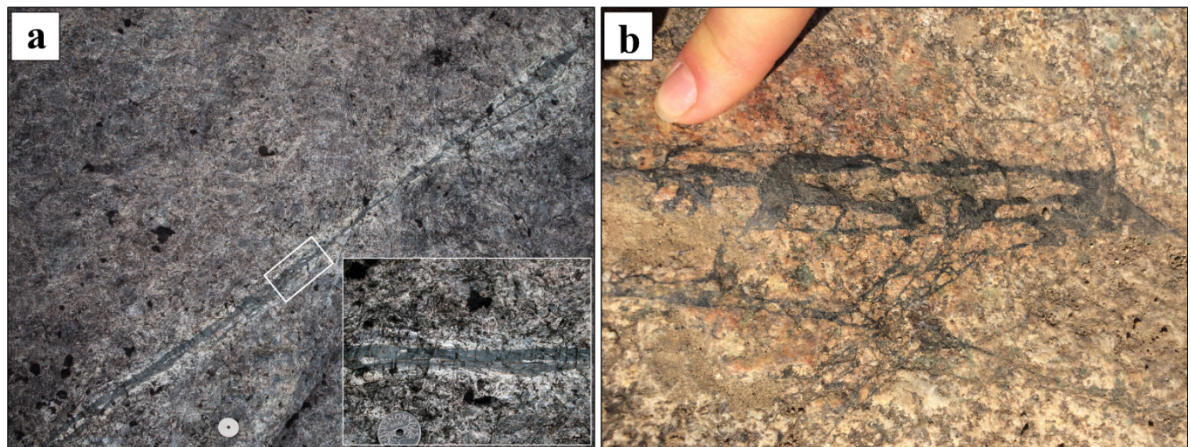
Figure 2.7. Example ductile shear zones in the dry and strong lower crust. (a) Thin (<2 cm) ductile shear zone bordered by a bleached halo within the darker coarse host anorthosite. The inset shows the fine grained, dark green, sharply terminated mylonitic core enveloped by an only mildly sheared bleached halo (Flakstadøy, Lofoten; modified from Menegon et al., 2017). (b) Pseudotachylyte injection vein, Corte, North Corsica.

The physical-chemical conditions of fluid-rock interaction in the BDTZ have been studied within exhumed faults by applying a set of geochemical tools that include fluid inclusion analysis (e.g. Morrison, 1994; Morrison and Anderson, 1998; Mulch et al., 2004; Ault and Selverstone, 2008; Siebenaller et al., 2016; Compton et al., 2017), determination of the isotopic compositions of fault fluids, and mass transfer calculations between host rock and fault rocks (e.g. Goddard and Evans, 1995; Mittempergher et al., 2014; Spruzeniece and Piazolo, 2015). This approach yields important constraints on the PT conditions of fluid-rock interaction within the BDTZ, on the source region of the fluids reaching and flowing within the deformation zones, and on element mobility during syn-tectonic fluid flow. These studies, however, do not specifically address the role of fluids on the mechanisms that trigger and permit the aforementioned cycles of brittle-ductile deformation. Open questions thus remain, such as, for example, which pressure, temperature, composition (P, T, X)

conditions are best for a fluid to trigger brittle-ductile deformation cycles in a fault system within the BDTZ and which fluid property is specifically most effective in controlling the cycles.

2.3 Geological storage of high-level nuclear waste (HLW)

Nuclear waste, like many other industrial wastes, has to be managed with caution and disposed of in a proper way in order to avoid the risk of it posing a danger to humans and the environment at large.

Nuclear waste is commonly divided into three main classes, in accordance to the half-life time (i.e. the time required for a quantity of waste to reduce to half of its initial value of radioactivity) and activity of radioactive isotopes (i.e. radionuclides). This classification accounts for the time that the waste takes to decay down to a harmless level of radioactivity. Following this principle, radioactive waste is divided in low (LLW)-, intermediate (ILW)- and high-level waste (HLW).

Waste classified as LLW includes materials that contain only traces of radioactivity and that were contaminated through exposure to radiations. Equipment used in radiation medical therapies and laboratory animal carcasses and tissues are an example of this kind of waste.

ILW materials contain a higher level of radiations than the LLW. Operational waste such as resins, chemical sludge and contaminated materials as well as waste from reactor decommissioning procedures are examples of intermediate-level wastes.

Materials classified as HLW include spent fuel rods, which are discarded periodically from operating nuclear reactors when production of energy is no longer efficient, and reprocessed spent fuel. HLW is therefore the most dangerous waste because of the long-lived and highly active radionuclides and it has to be managed with caution and properly disposed.

Much of the LLW waste is usually placed within canisters and disposed by burial in shallow trenches only a few meters deep (c. 10 m; Fig. 2.8).

Subsurface burial of HLW is also considered as the most appropriate disposal solution, in terms of technical practicality, safety, cost and environmental impact (Bodansky,1996; European Commission, 2004b), even though no waste of this sort has yet been placed permanently underground. In Finland the first deep nuclear waste repository is under construction and excavation began in 2004. Finland will therefore soon be the first country in the world to have an operational deep underground spent fuel repository.

The final disposal of HLW in carefully engineered facilities located in stable rock formations at depths of several hundreds of metres (>300 m) is at the moment the favoured strategy in many countries (e.g. Europe, USA, Canada, Japan; Kim et al., 2011) to guarantee the long-term isolation and safety or the highly active and long-lived material.

However, such deep repositories, also known as "geological storage" or "deep geological waste repositories" have to fulfil a number of requirements.

Figure 2.8. Trench for shallow disposal of low- and intermediate-level nuclear waste. Locality: Vaalputs radioactive waste disposal facility, South Africa. Photograph courtesy of Giulio Viola (University of Bologna).

As a geological barrier, the rock excavated for the construction of deep repositories needs to be well protected from surface disturbances, either natural or man-made for a time commensurate to the decay time of HLW (see below). Moreover, the geological host has to be sufficiently thick and little permeable as possible to minimize and even slow down the diffusion of contaminated fluids and radiations from the depth of the repository to the subsurface over geological timescales.

The half-life time of some of the most important radionuclides in long-lived waste is of tens of thousands of years or even longer (e.g. Chapman 2006). Deep geological repositories need therefore to guarantee isolation and immobilization of radionuclides for a range of containment time (i.e. estimated minimum time of immobilization of radionuclides, e.g. Chapman 2006) between a few thousand to a few hundred thousand of years. After the containment period, immobilization of radionuclides in waste cannot be guaranteed because

of the natural corrosion processes that can involve the canisters containing the nuclear waste and the consequent dissolution of some radionuclides in circulating waters. To compensate for this inevitable destiny, a multibarrier approach has been developed for the construction of deep geological repositories and for the management of nuclear wastes by the Swedish Nuclear Fuel and Waste Management Company (SKB). The disposal method actually in use is the KBS-3 method (more details are publicly available at https://www.skb.com/). Following this conceptual approach, the individual engineered barriers around the solid waste act together to provide a variety of safety functions, which control and minimize the natural release of radioactive isotopes from the repository and their movement through the overall volume of rocks. The potential design concept of the final repository for spent nuclear fuel and multi-barrier systems is shown in Fig. 2.9. The concept of multi-barrier system is descripted in the next paragraph.

2.3.1 Site selection processes for a HLW deep repository: a general overview

A carefully chosen geological environment has the potential to act as a cocoon for the repository engineered barrier system, protecting it from gross fluctuations in stress, water flow and aggressive hydrochemistry. The selection of the site is thus a crucial aspect to consider in the planning of nuclear waste repositories so as to ensure durable safety. Some key features have to always be taken in consideration during the stages of in-depth evaluation of any potential disposal sites. Areas characterized by tectonic stability over long periods of time (i.e. cratons) are good candidates. The chosen disposal environment has to have geotechnical properties that allow for underground excavation, low fracture-secondary permeability and very low fracture interconnectivity and transmissivity to ingress and infiltration of large amounts of water in and out of the repository (e.g. Mattila and Tammisto 2012). The thermal stability of the rock–water system is also essential because the thermal field immediately around the repository is to invariably become altered by the presence of the canisters containing the heat-emitting nuclear waste.

In addition, it is important for the host rock to easily diffuse any gas produced through time. Some studies have shown that some clay lithologies chosen as potential host for the construction of HLW repository, as in the case of the Boom clay layers in Belgium, naturally generate gas (i.e. hydrogen and methane) by anaerobic corrosion of the metallic waste canisters and by the metabolic reaction of sulphate-reducing bacteria (e.g. Ortiz et al., 2002). A gas phase can therefore be generated in the repository galleries hosting the deposition canisters and if the gas generation rate becomes higher than the rate of gas

diffusion, the pressure of the gas increases. Potential mechanical instability of the host formation and consequent formation of preferential pathways for the migration of gas and also possibly contaminated waters can therefore be produced (e.g. Ortiz et al., 2002).

A broad range of host geological formations has been considered worldwide for the construction of deep repositories, including:

i) Hard crystalline rocks, such as granite and gneiss (Olkiluoto basement constituted by migmatite and layers of gneiss and pegmatitic granite, SW Finland; e.g. Hudson and Cosgrove 2006; Kärki and Paulamäki, 2006; Viola et al., 2011; Aaltonen et al. 2010, 2016).

ii) Volcanic tuff, as for example ignimbrite in the Yucca Mountain, Nevada, USA (e.g. Bodvarsson et al. 1999; Witherspoon and Bodvarsson 2001; Long and Ewing 2004).

iii) Argillaceous rocks (i.e. clays, mudrocks, shales). The Boom Clay formation in Belgium (e.g. Mallants et al. 2001, Wileveau and Bernier 2008) and the Opalinus Clay Unit, OPA, Jura Mountains, NE Switzerland (e.g. Nussbaum et al. 2011; Laurich et al. 2014; Orellana et al. 2018) are examples of argillaceous formations investigated for the construction of HLW deep geological waste repositories.

iv) Evaporitic formations as domes and bedded salt, as for example the Gorleben salt dome in Lower Saxony, Germany (e.g. Grambow et al., 1998).

Each of these lithologies offers both favourable and unfavourable characteristics for the construction of deep HLW repositories. Numerous studies carried out over the last twenty years show that some lithologies are more suitable than others (for example, the claystones and crystalline rocks are more suitable than the salt because of documented leakage of ^{137}Cs from a repository in salt in the USA; Hansen and Leigh 2011) but no single rock type can be suggested as the best in all circumstances and for every type of geological environment. Too many are the variables connected with site evaluations for generalizations of global validity to be made and while a solution may be adequate in one area it is questionable or completely inadequate elsewhere. The choice of a specific lithology as a suitable medium to exploit for the construction of a deep nuclear waste repository depends on so many factors that continuous studies and investigations are essential to lead to an increasingly detailed knowledge of the disposal environment to guarantee long-term safety.

The selection of a site has to also consider other aspects that obviously do not pertain to the geological world such as the overall logistics, the impact on the society and economy of the area where the repository is built as well as the impact on land-use and the consequent environmental stress.

An example about the importance of these aspects can be reported from the case of the Yucca Mountain site, Nevada, USA. This site is located c. 160 km from Las Vegas and detailed investigations for the construction of a deep nuclear waste repository in ignimbrites were carried out over a long period of time (e.g. Witherspoon and Bodvarsson, 2001). Despite numerous studies having shown that the Yucca Mountain site offers multiple natural characteristics that are indeed favourable to its long-term performance (e.g. Witherspoon and Bodvarsson, 2001), the site is no longer considered as an option for the disposal of nuclear waste because of the high health hazard induced by the heavily populated cities close to the area and because of the social and economic high impacts that the construction of the site can produce to Las Vegas.
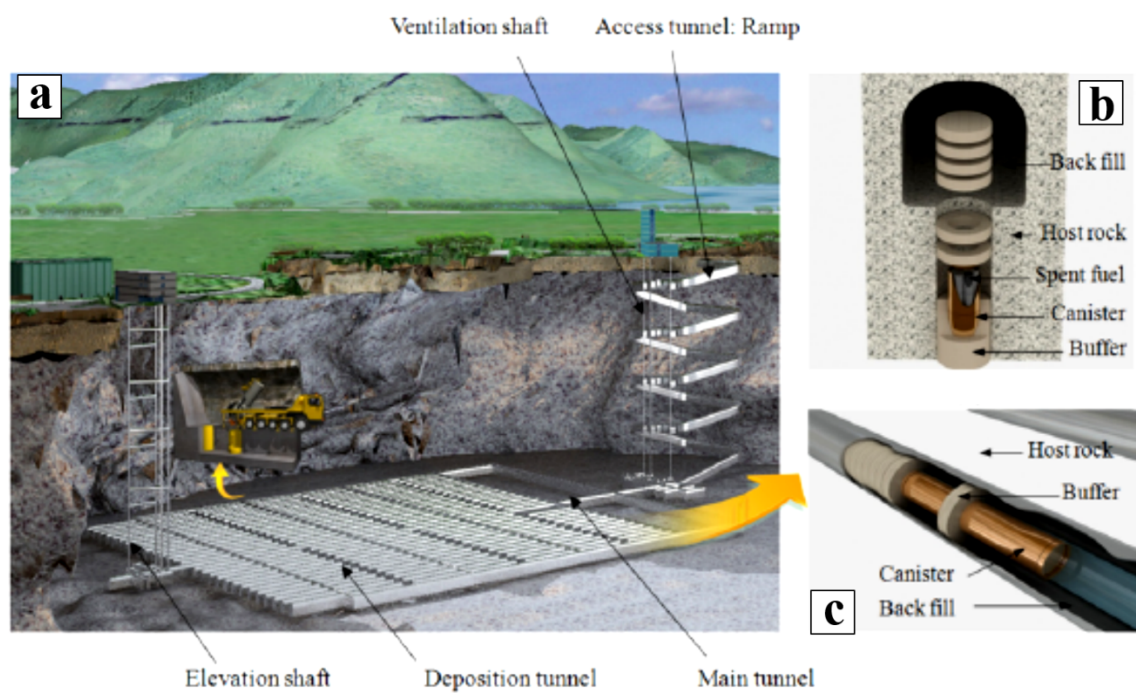
Figure 2.9. (a) Conceptual design of a deep nuclear waste repository excavated at down to depths >300 m within a given geological host rock. The layout includes an access ramp, a ventilation shaft, an elevator built with the aim to take the radioactive material at depth during the final disposal phase, a main transport tunnel and numerous depositional tunnels. Additional vertical and/or horizontal deep deposition holes to contain the canisters for their long-term storage are also part of the project. (b)Multi-barrier system for the isolation of metallic canisters containing the spent fuel in a vertical KBS-3V- and (c) horizontal KBS-3H-configuration. Modified from Kim et al. (2011).

In the case of the Olkiluoto site in SW Finland, the final decision to build there the national Finnish HLW repository took in consideration the hazard and the socio-economic impact that the construction of the site could have produced, and great effort was devoted to have as much interaction as possible with the local community and to listen to and take account of all opinions (e.g. Witherspoon and Bodvarsson, 2001).

The choice of a site for the construction of a deep nuclear waste repository therefore requires a great amount of work, on several fronts, and it is anyway always necessary to identify the best compromise between structural feasibility of the geological environment and hazard.

2.3.2 Deep geological disposal in crystalline rock: the case study of Olkiluoto site

The first deep nuclear waste repository for high-level waste in crystalline rocks is under construction in the Olkiluoto Island in SW of Finland, in the proximity of the Olkiluoto nuclear power plants.

Olkiluoto already hosts a repository for low- and intermediate-level wastes. This repository is built at a depth of 60-100 m b.s.l. and consists of two vertical silos.

The area planned for the high-lever repository is a few kilometres towards the east from the existing LLW- and ILW facility and it is hosted within the Paleoproterozoic crystalline basement of southern Finland at c. 450 m b.s.l (Fig. 2.11a). Waste disposal and plant inauguration are currently scheduled to begin in 2020 even if final approval from the competent authorities is still missing.

Detailed scientific investigations and numerous projects to evaluate the feasibility and the long-term safety of the site have been systematically carried out over the last twenty years, and research is still ongoing. All the scientific reports produced during these years of research are open access and are stored on the Posiva website (http://www.posiva.fi/en).
One of the main scientific aspects that were investigated by both direct observations and a combined statistical and numerical approach is the assessment of the potential seismic rick of the bedrock during the repository projected lifetime (i.e. 100.000 yrs). In particular, it was studied in detail how the pre-existing fractures of the crystalline basement that interest the Olkiluto bedrock may affect and steer earthquake nucleation and consequent shear displacement potentially dangerous for the integrity of the deposition canisters. The brittle structures that affect the Olkiluoto region and the repository rock volume were mapped and

studied in detail by Viola et al. 2011 and Mattila and Viola 2014. They identified 7 stages of brittle deformation starting from c. 1.7 Ga and continuing until 0.8 Ga ago. Brittle faults in many cases were found to exploit and reactivate ductile precursors (e.g. Aaltonen et al. 2016). More details on the geological setting of the Olkiluoto region are described in Chapter 3.

Because of the very long-time framework that is involved in the successful life of a repository, a change in the environmental conditions and regional stress field has to be taken in consideration for the safety assessment of a site. In the case of Olkiluoto, two main scenarios have been considered when modelling the potential seismic risk of the site. These scenarios are:

1) The reactivation of deformation zones within the repository area and in its vicinity induced by a stress alteration induced by future glacial cycles, which increases the risk of earthquake triggering (e.g. Hökmark and Fälth 2014; Lund et al. 2009).

2) Thermal anomalies produced by the release of heat by nuclear waste induces an increase in temperature in the volume of rocks close to the repository. This thermal stress anomaly affects the stability of the pre-existing fault zones and fractures in the repository and in its vicinity, with important implications on the risk assessment (e.g. Hökmark et al. 2010).
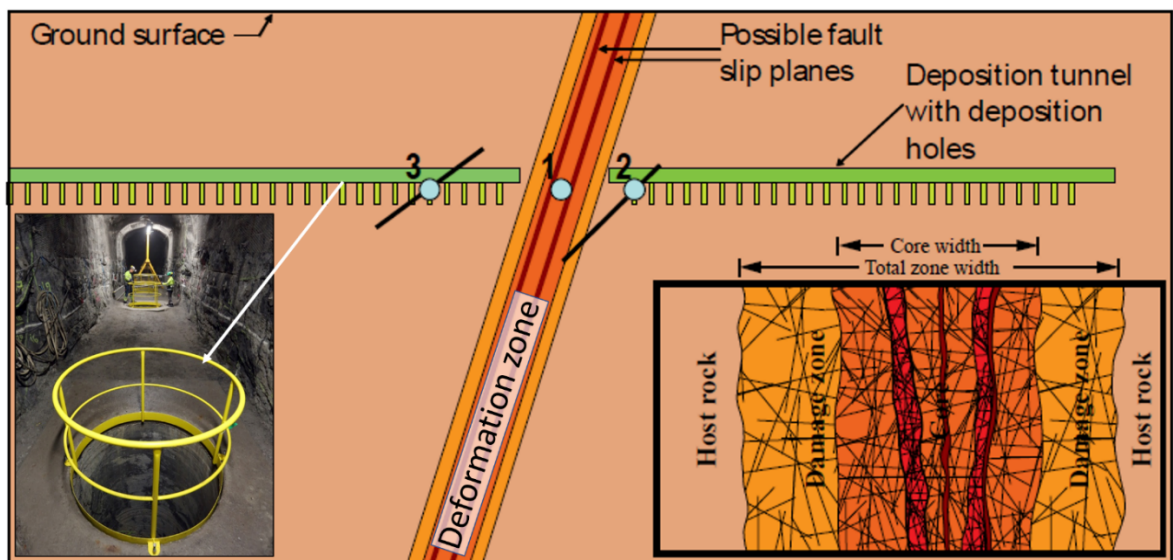
Figure 2.10. Schematic representation of the position of the deposition holes with respect to a major through going deformation zone (1) and smaller fractures located at different distance from the main deformation zone (2 and 3). Deposition holes are not built within deformation zones that are large enough to host major earthquakes (1). Stress redistribution after an earthquake might induce sufficient displacement along secondary shear fractures that can damage the canisters. Inset on the left shows one of the deposition holes. Inset on the right shows the architecture of a representative damage zone. Modified from Fälth et al. (2019).

Both scenarios can induce a seismic reactivation of the existing main slip surfaces (1, Fig. 2.10) and consequent displacement along secondary shear fractures (2 and 3, Fig. 2.10) caused by a stress redistribution. Shear displacement along fractures that are intersecting the deep deposition holes in the repository can thus damage the canisters and cause a leakage of radionuclides. Following this consideration, an engineering method was adopted on the planning of the deposition holes in relation to structural discontinuities location. A safety distance to maintain between fractures and location of depositional tunnels (Fig. 2.10) was estimated from numerical models. For major details about this topic the Reader is referred to Munier et al., 2006 and Munier and Kärnbränslehantering 2004.
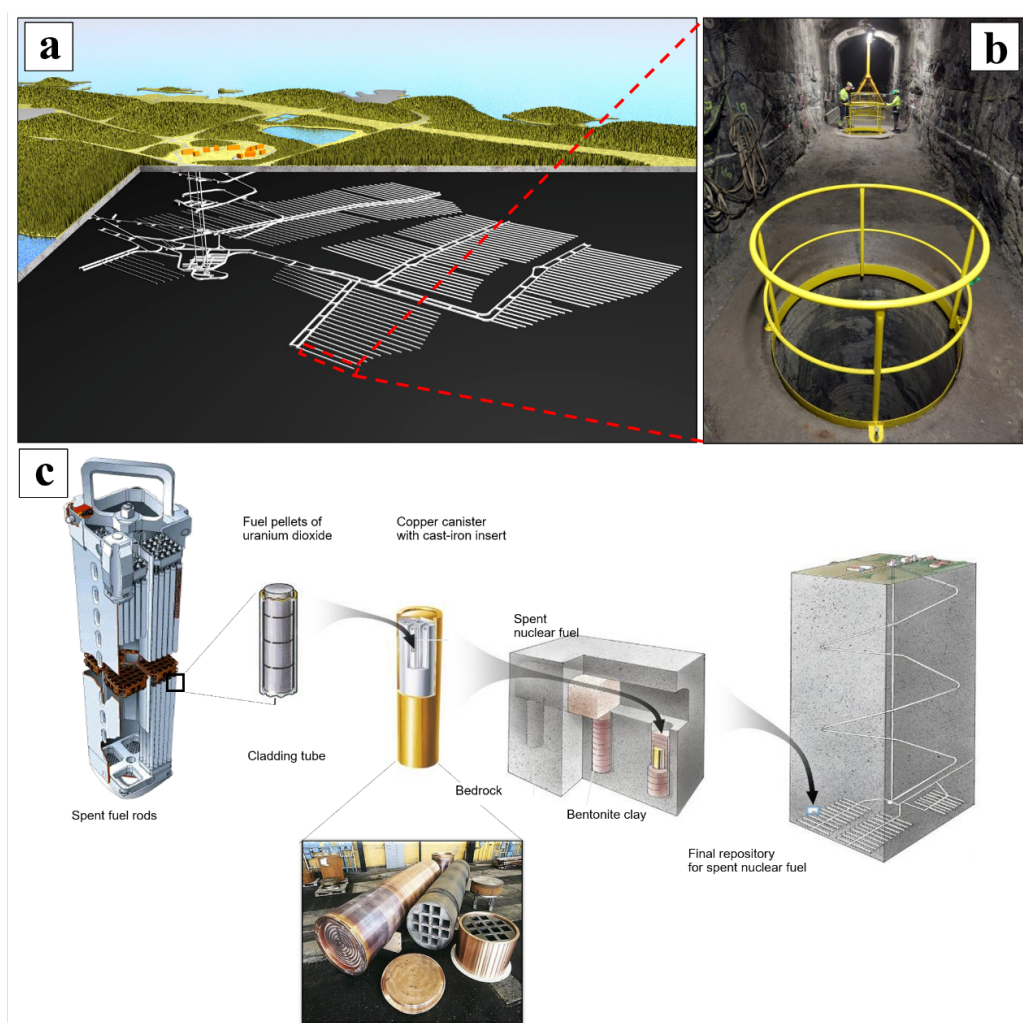
Figure 2.11. Posiva's plans for the final disposal of HLW in Olkiluoto. (a) Subsurface representation of the repository. (b) The excavated vertical deep deposition hole on the floor of one of the horizontal galleries of Olkiluoto where the canister containing the nuclear fuel will be placed. (c) The KBS-3V multi-barrier system is the method of disposal chosen for the final disposal of HLW in Finland. The fuel rods are encapsulated within durable copper-iron canisters, disposed within vertical holes and then sealed by a buffer of bentonite. Photos courtesy of Posiva Oy, Finland.

Combined to this engineering approach, a multi-barrier system was implemented to further isolate the canisters and the waste contained therein (Fig. 2.11).

Plans for final disposal of HLW in Finland are based on the KBS-3V technology (Fig. 2.11b), developed by the Swedish Nuclear Fuel and Waste Management Company (SKB). The spent fuel rods will be encapsulated in canisters consisting of a cast iron insert that is surrounded by an oxygen-free copper shell-corrosion resistant and with a high ductility (Fig. 2.11c). Canisters will be disposed in vertical deep deposition holes (Figs. 2.11b, c), excavated in the bedrock at depth >450 m b.s.l (Fig. 2.11c). Between host rock and canisters, a buffer of bentonite clay will be installed to permit the final isolation of the nuclear waste (Fig. 2.11c). When the capacity of the repository will be saturated, all access routes from the surface to the disposal galleries will be closed and the repository sealed, such that it will not require routine maintenance or controls.

Chapter 3. Geological setting

3.1 Regional geological setting of southwestern Finland

The study area is located in southwestern Finland on the island of Olkiluoto (Fig. 3.1) within the Paleoproterozoic Svecofennian orogenic province, which is formed by supracrustal high-grade metamorphic sequences and plutonic rocks. The most abundant lithologies in the study area are amphibolite facies, variably migmatitic metasedimentary rocks interleaved with metavolcanic rocks up to several metres thick in addition to calc-alkaline synorogenic tonalite-trondhjemite-granodiorite-type (TTG) granitoids, as well as late orogenic leucogranites (Figs. 3.1). For a detailed lithological characterization of the area, the reader is referred to Hudson and Cosgrove (2006) and Aaltonen et al. (2016).

Numerous studies carried out on Olkiluoto have highlighted the long geological evolution of the region, which is commonly summarised by tectonic models proposing either an evolution during a single and semi-continuous Svecofennian orogenic event (Gorbatschev and Bogdanova, 1993) or, alternatively, a sequence of up to five distinct accretion events leading to the amalgamation of several microcontinents and island arcs at the margin of the Archean craton between 1.92 and 1.79 Ga (e.g. Lahtinen et al., 2005). In this scenario, several subduction systems developed, and the collision of the involved microcontinents and island arc complexes resulted in conspicuous continental growth, forming the major part of the Paleoproterozoic domain of the Fennoscandian Shield (1.89-1.87 Ga). According to Lahtinen et al. (2005), this "Fennian accretionary event" ended with a phase of orogenic collapse associated with regional extension and remarkable crustal thinning between c. 1.86 and 1.84 Ga. Renewed compression ensued during collision of the "Sarmatian Plate" with the previously consolidated Svecofennian Shield, causing major crustal shortening, high temperature regional metamorphism (Kukkonen and Lauri, 2009) and the emplacement of S-type granites (e.g. Ehlers et al., 1993). Migmatisation occurred during this collisional stage between 1.84 and 1.82 Ga (Aaltonen et al. 2016). Stable mineral assemblages constrain the formation of the migmatites at 3.7-4.2 kbar and 660-700° C (Tuisku, P. and Kärki, 2010). Tectonic activity ascribable to this orogenic phase ceased with a distinct orogenic collapse phase at 1.79-1.77 Ga (Lahtinen et al., 2005).

Pervasive reworking of the Svecofennian domain took place in the Mesoproterozoic when the crust underwent significant stretching and was intruded by voluminous Rapakivi granites and diabase dykes resulting from the widespread melting of the lower crust at c. 1.65-1.50 Ga. This tectonic phase was probably due to the development of a rift along the

present Baltic Sea (Korja et al., 2001). Crustal thinning caused also the formation of the "Satakunta Graben", a NW-SE trending graben located c. 50 km to the north of Olkiluoto, which was later filled by Mesoproterozoic sandstone (Jotnian sandstones, Fig. 3.1). The latest stage of crustal evolution in southern Finland is expressed by the intrusion of 1.27-1.25 Ga, N-S striking olivine diabase dikes (Fig. 3.1; e.g., Suominen, 1991).
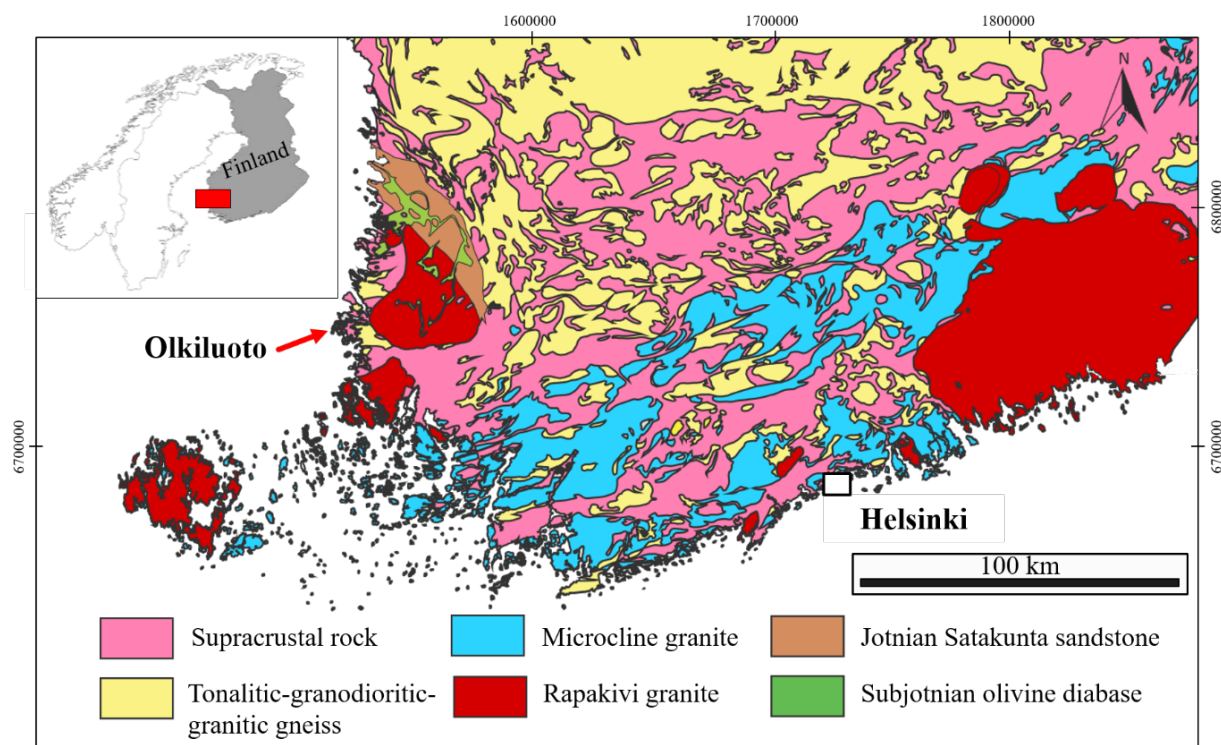
Figure 3.1. (a) Simplified geological map of southwestern Finland modified after Mattila and Viola (2014). Olkiluoto island is also highlighted. Coordinates are given in the local KKJ1 coordinate system.

3.2 Geological setting of the Olkiluoto region

As to the structural evolution of the study area, the Olkiluoto bedrock was affected by complex history of structural overprinting and reactivation in response to the many tectonic episodes listed above.

According to the evolutionary deformation scheme proposed by Aaltonen et al. (2010), the Paleoproterozoic supracrustal rocks in SW Finland have undergone polyphasic ductile deformation (up to five different phases, referred to as D_1-D_5) between 1.86 and 1.79 Ga. These distinct ductile phases are partially preserved in the local structural record of the Olkiluoto region, with each phase being characterised by structures with distinctive mineral composition, metamorphic grade, geometry, and kinematics. In the following section, a

summary of the deformation stages and related structures is presented. For more details, the reader is referred to Aaltonen et al. (2010) and (2016).
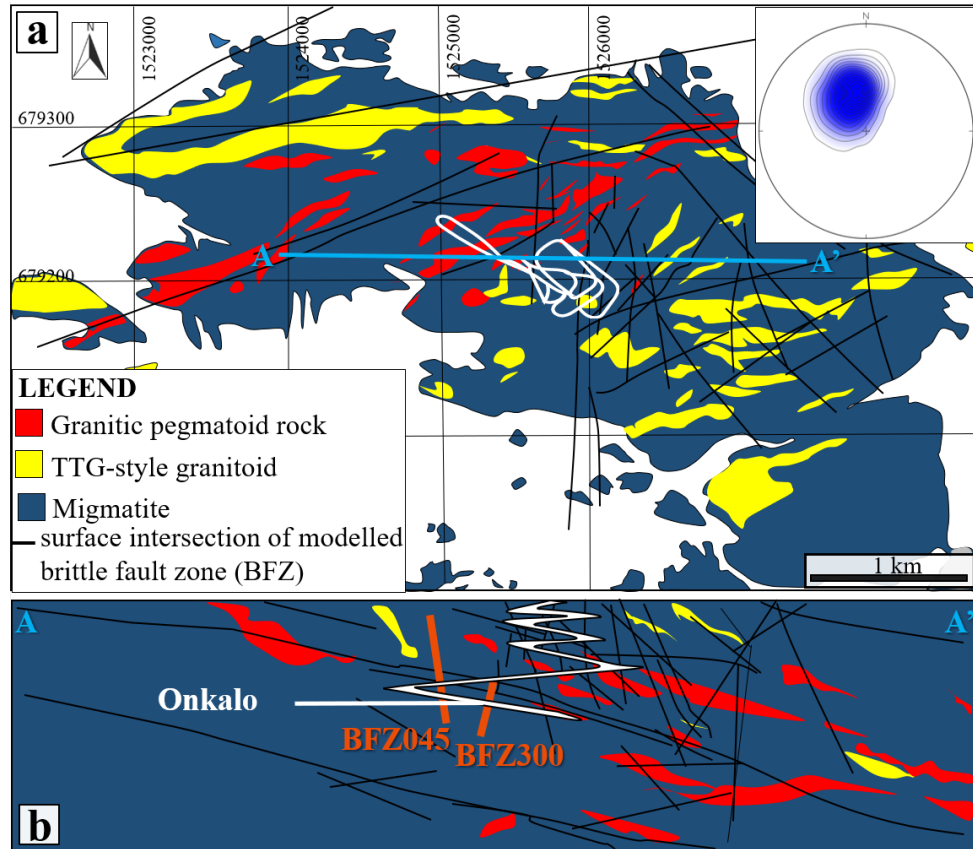
Figure 3.2. (a) Geological sketch of the Olkiluoto Island and structural map, showing the surface intersection of modelled brittle fault zone (BFZ; modified from Aaltonen et al., 2016). The white line indicates the surface projection of the underground investigation facility Onkalo. A-A' is the trace of the cross section shown in (b). The upper right inset plots the poles to foliation planes measured from all available Olkiluoto drill cores (N = 4479, equal area, lower hemisphere projection; Mattila and Viola, 2014). Coordinates are given in the local KKJ1 coordinate system. (b) E-W cross section across the Olkiluoto basement, passing though the Onkalo underground infrastructure, shown as white line. The studied set of sub-vertical conjugates fractures (BFZ045 and BFZ300) are shown as orange lines.

The earliest observed tectonic structures are biotite-rich foliation planes parallel to subparallel to the now transposed bedding, which formed during the first deformation stage, named D_1. This represents a pre-migmatite deformation stage. Stage D_1 was followed at 1.86-1.83 Ga by a major deformation event, named D_2, when a penetrative regional NE-SW trending foliation dipping moderately towards SE, as well as NE–SW striking mesoscopic shear zones, formed, accompanied by widespread anatexis of the metasedimentary rocks and emplacement of leucocratic granites. D_1 and D_2 related structures are in turn deformed by a later deformation event, named D_3, which took place between 1.83 and 1.81 Ga. It

resulted in a NNE-SSW striking foliation and E-W to NE-SW trending, S to SE dipping shear zones.

The last documented deformation stage, named D_4, occurred under greenschist facies conditions during a retrograde path between 1.81 and 1.79 Ga, according to zircon and monazite U/Pb dating of syn-kinematic pegmatites (Mänttäri et al., 2010). The related structures are NNE-SSW and N-S striking, subvertical ductile shear zones, varying in width from c. 0.5 m to 200 m.

The Olkiluoto bedrock was later affected by a long brittle deformation history starting at 1.75 Ga (Mattila and Viola, 2014, Aaltonen et al., 2016) during progressive regional exhumation and cooling. Mattila and Viola (2014) have identified seven distinct brittle stages that developed in the time span from 1.75 to 0.8 Ga. These brittle deformation stages are characterized by both the reactivation of optimally oriented pre-existing ductile structures and faults/fractures, and by the formation of new, Andersonian-type faults and joints, which deeply affect the Olkiluoto basement (Fig. 3.2a).

Brittle faults at Olkiluoto can be grouped into two main sets: (1) an E-W to NE-SW trending set of low-angle faults exploiting the regional migmatitic foliation, and (2) a set of subvertical faults striking N-S to NW-SE (Fig. 3.2a; Aaltonen et al., 2016). Low-angle faults cut across the subvertical faults and they indeed represent a later stage of deformation (Aaltonen et al., 2016).

The subvertical faults have orientation compatible with the first two stages of brittle deformation identified by Mattila and Viola (2014; Stage 1 and Stage 2 of Fig. 3.3), and they typically form conjugate systems of NNW–SSE sinistral and NW–SE dextral strike-slip faults (Mattila and Viola, 2014). This set of conjugate systems has been interpreted as the result of the NW–SE to NNW–SSE compression proposed by numerous authors for the late- to post- Svecofennian orogenic evolution (e.g., Viola et al., 2009; Torvela and Ehlers, 2010; Saintot at al., 2011, Fig. 3.3).

Previous studies have highlighted that N-S faults typically exploited mica-rich precursor ductile shear zones (Pere, 2009, Aaltonent et al., 2016, Skyttä and Torvela, 2018). In this study, a conjugate set of strike-slip faults has been chosen as representative example of the regional faults striking N-S to NW-SE (Fig. 3.3) to investigate in more detail the first stages of embrittlement of the Olkiluoto basement. One fault exploits and reactivates the ductile fabric of the Proterozoic migmatitic basement (brittle fault zone BFZ045, Fig. 3.2b) whereas a second, BFZ300 in Fig. 3.2b, cuts discordantly the ductile structural grain and is not affected by the pre-existing anisotropy. BFZ300 is the main topic of this thesis while

BFZ045 was investigated in collaboration with the University of Plymouth as it is the topic of another Ph.D. thesis.
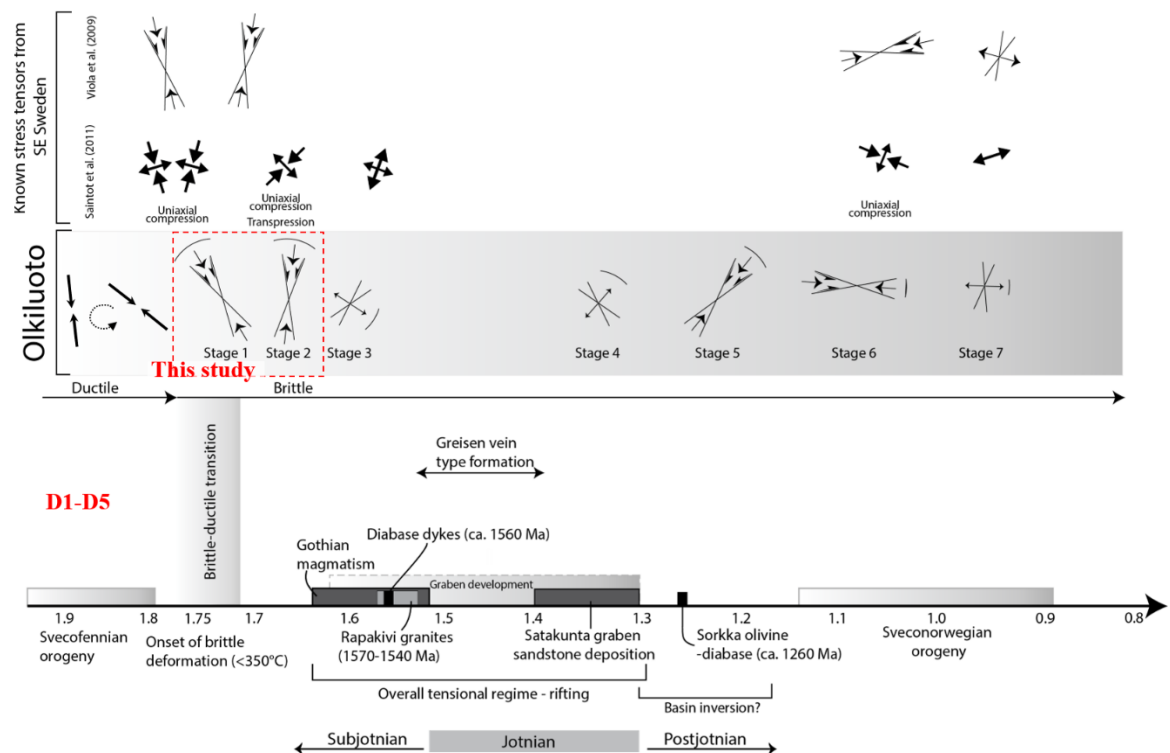
Figure 3.3. Conceptual model of the main tectonic events that have occurred in Olkiluoto. Major crustal events that have affected southwestern Finland are here combined with the paleostress tensors of the ductile evolution pre-dating the brittle deformation and of the brittle evolution, modified after Lahtinen et al., 2005, Mattila and Viola (2014) and Skytta and Torvela (2018). The set of sub-vertical conjugate faults object of this study are NW-SE to N-S striking structures, which are compatible with the first two stages identified by Mattila and Viola (2014). The paleostress tensor reconstructions directly relevant to this study are highlighted with a red dashed line.

Chapter 4. Methods

In order to reconstruct the structural brittle evolution of the studied brittle fault zone and to constrain the environmental conditions that induced and steered embrittlement of the basement at the BDTZ, meso- and microscale observations have been systematically combined with a plethora of analytical techniques.

The analytical methods applied to this study and their chosen experimental conditions are briefly presented in the following paragraphs.

4.1 Field documentation and sampling

Field documentation and sampling were carried out at the underground Onkalo exposures of BFZ300 (Fig. 5.2), which were necessarily limited in areal extent to the actual excavated volume of rock at the time of our study but that, together with the logged diamond drill cores from the underground exploration, allow for a well-constrained 3D reconstruction of the local geology.

4.2 Fluid inclusion analysis

Petrographic analysis, fluid inclusions microthermometry and micro-Raman analysis have been conducted on "fluid inclusion assemblages" – FIAs, i.e., on petrographically discriminated cogenetic groups of fluid inclusions located along trails or (less commonly) within clusters (Bodnar, 2003a; Goldstein, 2003). By definition, FIAs are groups of inclusions that have been trapped together (i.e., they are cogenetic) at a specific stage of mineral formation (and/or deformation) and, as such, give the highest level of confidence when characterizing the properties of trapped fluids and discriminating possible stages of post-entrapment re-equilibration (Bodnar, 2003b, and references therein). We applied Roedder's identification criteria of FIAs according to the timing of entrapment (i.e., primary, secondary, pseudosecondary, Fig. 4.1a) in order to link stages of fluid entrapment with stages of brittle and ductile deformation of quartz.

Keeping in mind the nomenclature commonly used for fluid inclusions characterization, we note that the term "primary" is used when referring to fluid inclusions that were trapped during and as a direct result of crystal growth. "Secondary" FI are those trapped after crystal growth is completed and they normally are arranged in trails which cut across the growth zones of the mineral phase. "Pseudosecondary" FI are those that were trapped before crystal growth is complete and they are similar in origin to secondary fluid

inclusions because in general they are trapped along microfractures and are also arranged in trails.
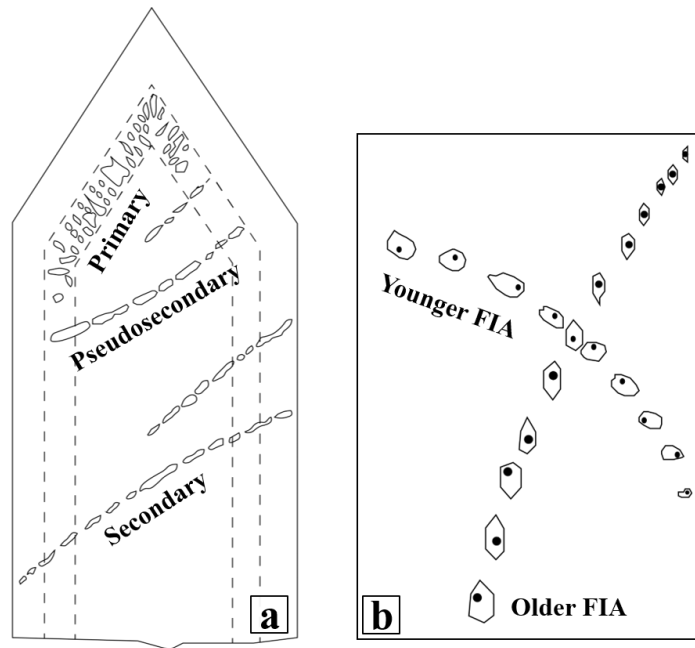
Figure 4.1. (a) Schematic representation of composite primary, secondary and pseudosecondary generations of fluid inclusion assemblages (FIAs) within a hypothetical single quartz crystal, as viewed under microscope. Concentric growth zones are outlined by black dashed lines. Modified from Lambrecht and Diamond (2014). (b) Cross-cutting relationships between two petrographically distinct trails of secondary FIAs, where the older trail is crosscut by a younger one. Older FIA trail is composed of angular-shaped FIs with a volume fraction of 20% while the younger has round-shaped FIs. Modified from Goldstein (2003).

In a multiply reactivated faults system, deformed under fluid-rich and fluid overpressure conditions, multiple planar arrays of secondary FIAs can be generally identified. Identifying the petrographic relationships between distinct FI trails, and between FIAs and the host mineral, is therefore crucial to determine their relative timing of entrapment. In this regard, cross-cutting relationships between petrographically distinct trails of FIs (Fig. 4.1b) have been used.

Determining the relative timing of entrapment between distinct sets of FI trails is a fundamental step in the study of fluid inclusions. As important is also to report the estimated fluid properties (i.e. fluid pressure, P_f, temperature, T, composition, X, and salinities wt% NaCleq)) obtained from the study of sets of FI trails to a specific stage of fault activity (nucleation or reactivation) and fluid entrapment registered by the system. In this regard, we considered as cogenetic, and therefore representative of one specific stage of brittle deformation and fluid circulation, only those FIAs that exhibited both similar orientation

and petrographic characteristics (FIs size, shape and volume fraction), at the scale of the thin section.

Microthermometric properties of fluid inclusions were determined at the Department of Biological, Geological and Environmental Sciences of the University of Bologna using a Linkam THMSG 600 heating/freezing stage coupled with an Olympus BX51 polarizing microscope. The microthermometry stage was calibrated by using synthetic fluid inclusion samples at –56.6, 0.0, and 374° C, which correspond to the melting of CO_2, ice melting, and final homogenization of H_2O inclusions, respectively. Obtained accuracies were ±0.3° C for final ice melting temperature (Tm_{ice}) and ±3° C for final homogenization temperature (Th_{tot}). In order to produce an internally consistent dataset, all phase transitions were exclusively collected for individual FIAs and measured with the same standard procedure. Low-temperature phase changes were measured first, to avoid decrepitation or stretch of the host mineral to avoid volume changes during the heating experiments. Samples were thus first rapidly cooled to c. -180° C and then slowly heated to detect the potential formation of a solid carbonic phase, eutectic phases, salt hydrates, ice, and clathrates. The Th_{tot} were later determined in the FIAs by heating the samples from room temperature and recording the mode of homogenization (i.e., by bubble or liquid disappearance). All phase transitions were measured by using the cycling method described by Goldstein and Reynolds (1994), and care was taken also to record the minimum and maximum values for each assemblage. Volume fractions of individual fluid inclusions determined as % of the ratio $\varphi=V_v/V_{tot}$ (cf. Diamond, 2003), were estimated optically at room temperature using calibrated charts. Salinity, bulk densities and isochores were computed from the measured Tm_{ice} values using the HokieFlincs Excel spreadsheet (Steele-MacInnis et al., 2012 and references therein).

4.3 Electron Micro Probe Analyzer (EMPA)

Electron probe microanalysis of fault minerals was carried out with a JEOL-8200 wavelength-dispersive electron microprobe housed at the Department of Earth Sciences of the University of Milan, Italy. The instrument fits 5 WDS spectrometers utilizing lithium fluoride (LiFH), pentaerythritol (PETJ and PETH), and thallium acid pthalate (TAP) analysing crystals and an optical microscope. Samples were probed with a beam size of ~1 μm at 15 keV and 5 nA beam current. Synthetic and natural materials were used as calibration standards at the beginning of each session. Analytical 1-σ errors are typically < 4% for major elements and for the minor elements.

To avoid contaminated analyses, we used only chlorite EPMA analyses that yielded $K_2O + Na_2O + CaO < 1$ wt%.

Panchromatic cathodoluminescence (CL) imaging was also performed by using the CL CCD detector adjacent to the optical microscope of the JEOL-8200 on the sections used for microstructural work. The electron beam was focused on the sections with an accelerating voltage of 15 kV and 30 nA beam current. Black/white digital images were collected with a 40x magnification by beam mapping with the CCD detector at a spatial resolution of 1 μm (beam resolution), which resulted in imaged areas of 27.8 x 22.2 mm. The exposure time for image acquisition was 120 s.

4.4 Mineral-pair geothermometry

The EMPA compositions of fault minerals were used to estimate their formation-temperatures, which were reconstructed by means of empirical and semi-empirical geothermometers. Formation temperatures were estimated using two distinct mineral-pair geothermometers that are: i) quartz-chlorite, and ii) sphalerite-stannite geothermometers. Both the geothermometers are based on the equilibrium between two coexisting phases.

The estimated formation-temperatures were used as independent constrain to reconstruct the temperature of the synkinematic fluids. They were also combined with the calculate fluid inclusion isochores to constrain the pressure of the fluids, which repeatedly were injected within the studied system.

A brief introduction to their functioning and their applicability are reported in the paragraphs below.

4.4.1 Quartz-chlorite geothermometer

Because the chemical composition of chlorite is extremely sensitive to the variation of the environmental conditions (pressure, temperature, redox state and fluid composition), chlorite can track down very reliably the evolution of those parameters. Many geothermometers based on the chemical composition of chlorite and on the chlorite + quartz equilibrium have thus been recently proposed, especially for low-T chlorites (T < 350° C; e.g. Inoue et al., 2009; Inoue et al., 2010; Bourdelle et al., 2013).

In this study, chlorite-quartz equilibrium temperatures were estimated by using the T-compositional diagram proposed by Bourdelle and Cathelineau (2015). In that diagram, the relationship between chlorite composition and temperature of formation is represented in the

R^{2+}-Si diagram (R^{2+} refers to the sum of divalent cations Fe^{2+} and Mg^{2+}; Wiewóra and Weiss, 1990). All compositions in equilibrium at a given temperature plot on the same graphic isotherm in the diagram. The Bourdelle and Cathelineau (2015) method, moreover, is quite straightforward in that it leads to the estimation of chlorite formation temperatures by simply plotting the Si and R^{2+} contents without the need to calculate thermodynamic parameters.

4.4.2 Sphalerite-Stannite geothermometer

To estimate the formation temperature of cogenetic sulphides associated with a second generation of quartz vein (Qtz II, see below) we used the stannite-sphalerite formation temperature following the method proposed by Shimizu and Shikazono (1985). This geothermometer uses the temperature dependency of iron and zinc partitioning between stannite and sphalerite as a temperature indicator of the association quartz-stannite and sphalerite (Nekrasov et al., 1979) and follows the logaritmic correlation:

$$logK_d=1.274x10^3T^{-1}-1.74$$

where K_d is the partition coefficient and is given by:

$$K_d = (\frac{XCu_2FeSnS_4}{XCu_2ZnSnS_4})/(\frac{XFeS}{XZnS})$$

and X is mole fraction. The temperature is much lower as the exchange between Fe and Zn is low (i.e. little Zn quantity in favour of Fe).

<u>4.5 Raman spectroscopy</u>

Raman spectrometry has been used to analyse the composition of the fluid inclusion vapour bubbles and for carbonaceous material (CM) characterization. This latter has been performed with the aim to apply the CM geothermometer to graphite grains arranged along the metamorphic foliation of the host rock and estimate the temperature of the latest ductile stage recorded by the host rock before its embrittlement. During the metamorphic retrograde path the new temperature conditions generally cause the mobilization and subsequent recrystallization of the potentially present CM and may constrain the temperature of last remobilization of CM within the host rock during the last deformation stages (see Paragraph 8.4)

Analyses were carried out at the Department of Mathematical, Physical and Computer Sciences of the University of Parma (Italy) using a Jobin-Yvon Horiba LabRam spectrometer equipped with He–Ne laser (emission line 473.1 nm) and motorized XY stage.

The spectral resolution of the measurements was determined as nearly 2 cm^{-1}. The confocal hole was adjusted to obtain a spatial (lateral and vertical) resolution of 1–2 μm. Most spectra from fluid inclusions were obtained with a 50× objective (N.A. 0.75), although to analyse shallow inclusions we also used a 100× objective (N.A. 0.90).

For fluid inclusion analysis, a wide spectral range (100–3600 cm^{-1}) was scanned for each inclusion to test for the presence of CO_2, N_2, CH_4, and H_2S. The final acquisitions were made mainly between 1100 and 1800 cm^{-1} for the study of CO_2 spectra, and between 2500 and 3300 cm^{-1} for CH_4 and H_2S.

Raman spectra for CM were acquired between 1000-1900 cm^{-1} and 2400-3200 cm^{-1} for the study of the first and second order regions, respectively. The acquisition time for each spectral window was 120–240 s, with two accumulations.

4.5.1 Raman spectrum of carbonaceous material and geothermometry

The Raman spectrum of CM is composed of first order (1100–1800 cm^{-1}) and second order (2500–3100 cm^{-1}) regions (Tuinstra & Koenig, 1970; Nemanich & Solin, 1979). For the purposes of this work, we focus on the former (Fig. 4.2).
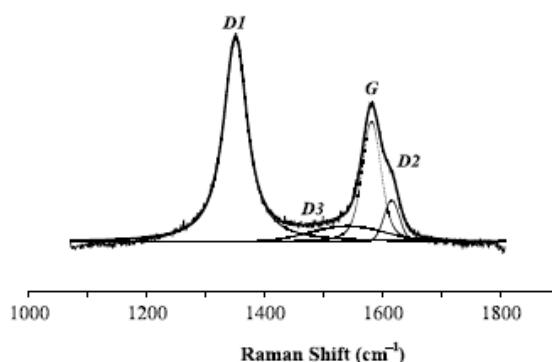
Figure 4.2. Decomposition of the first order region of the Raman spectrum of carbonaceous material (CM), and peak positions. The spectrum is composed of a G band, which includes the graphite G s.s. band and the D1 and D2 defect bands. D3 is a deformation band between D1 and D2 that can be found in particular situations. Modified after Beyssac et al. (2002).

The first order region of the Raman spectrum is composed of a main high frequency band that occurs at c. 1580 cm^{-1} and it is generally known as "G band". Other first order bands are at around 1350 cm^{-1}, known as "D1 band", around 1620 cm^{-1} ("D2 band") and around 1500 cm^{-1} ("D3 band"). D1, D2 and D3 bands correspond to physicochemical defects in the

graphitic structure (Bèny-Bassez & Rouzand, 1985) and they are commonly known as "defect" bands.

In pristine graphite only the G band is observed, whereas in polycrystalline graphite and/or disordered graphitic carbon, the G band is observed with other defect bands. After decomposition of the Raman spectrum into G, D1 and D2, each decomposed band peak can be characterized by parameters such as the band position, the band intensity, band area (integrated area) and band width.

Many correlations between the band parameters and the temperature-controlled degree of crystallinity of graphitic carbon are documented in literature (e.g., Beyssac et al. 2002; Aoya et al., 2010; Lahfid et al., 2010; Kouketsu et al., 2014). Among these, one of the most reliable is the area ratio, R2, which is the ratio between the areas of the defect bands characteristic of the first order region of graphitic carbon Raman spectrum ($R2=A_{D1}/(A_G + A_{D1} + A_{D2})$), where A_i= area of the ith peak; Beyssac et al. 2002. The linear relationship between temperature and R2 forms the basis of the CM geothermometer (Beyssac et al., 2002), where the temperature can be estimated to uncertainties of $\pm 50°$ C in the 330–650° C range by using the following linear correlation

$$T =(-445R2) + 641.$$

To assure a good statistical analysis of the CM structural heterogeneity within the host rock, we recorded more than 10 CM in the studied sample. The "Omnic software (Thermo Fisher Scientific) was used for Raman spectrum decomposition by running the Lorentian/Gaussian function, following the procedure described in Koeketsu et al., (2014).

Measurements were made on polished thin section cut as close as possible to perpendicular to the main metamorphic fabric. Deformation can affect the internal disorder and lead to underestimations of the temperature obtained from the spectra analysis (Kirilova et al., 2017). Care was therefore taken to avoid CM within cracks, and to prevent altered measurement from CM damaged during the thin section polishing Raman spectra measurements were collected by focusing the laser beam on CM beneath the surface of a transparent adjacent grain of quartz as suggested in Beyssac et al. (2002). Thermometer calibration were done for a laser wavelength of 514 nm.

4.6 Laser Ablation Inductively Coupled Plasma Time-of-Flight Mass Spectrometry (LA-ICP-TOFMS) analysis

The combination of inductively coupled plasma mass spectrometry (ICPMS) with direct solid sample introduction systems such as laser ablation (LA) has become a widely

used technique for the analysis of the distribution and/or concentration of major, minor and trace elements on geological samples. Moreover, because this analytical technique requires little-to-no sample preparation its use is becoming increasingly widespread.

Laser-ablation inductively coupled plasma time-of-flight mass spectrometry (LA-ICP-TOFMS) was applied to study in more detail the chemical composition of synkinematic and authigenic fault minerals. In particular, chlorite and pyrite were the phase of major interest and I dedicated mostly of the time of my abroad period studying these phases.

Multi-elemental 2D maps were acquired by means of laser-ablation inductively coupled plasma time-of-flight mass spectrometry (LA-ICP-TOFMS) at the Laboratory of Inorganic Chemistry of the ETH Zurich in Switzerland. TOFMS imaging was performed with an ArF excimer laser ablation system (193 nm, GeoLas C, Lambda Physik, Goettingen, Germany) coupled to an ICP-TOFMS instrument (icpTOF, TOFWERK AG, Thun, Switzerland) and an in-house built low dispersion single cell (Graham and Günther, 2016). A low-dispersion LA cell enhanced sensitivity compared to conventional LA cells because the analyse ion signal becomes less diluted during aerosol transport. When connected to simultaneous ICPMS instruments, these low-dispersion LA cells offer a platform for high speed and high lateral resolution shot-resolved LA-ICPMS imaging. Therefore a LA-ICP-TOFMS combined with a low-dispersion LA cell has the potential to generate large format chemical images (in the orders of mm), high-resolution (5 µm) and multi-elemental two-dimensional compositional maps in a relative small amount of time (in the order of few hours). Currently, low dispersion LA-ICP-TOFMS offers a best detection limit of around 100 ppm for a 1-µm LA spot diameter, whereas LA-ICP-QMS offers a detection limit of ~8 ppm for the measurement of only a single isotope. The plasma was sustained with argon gas (99.996%, PanGas AG, Dagmersellen, Switzerland) and laser ablation was done in He atmosphere (99.999%, PanGas AG, Dagmersellen, Switzerland).

Laser ablation (LA) analysis followed a hole-drilling approach (e.g. Burger et al., 2017) with a 5 µm laser spot-size and a repetition rate of 2 Hz so that positions of successive LA craters were edge-to-edge without overlapping areas. LA-ICP-TOFMS experiments started with 20-30 s of background data acquisition, or gas blank, which was followed by pre-cleaning each individual spot with several laser bursts to minimize surface contamination.

Compositional data were acquired in 2 or 4 consecutive subsections according to the size of the analysed area with a motorized stage. Semi-quantitative elemental maps were assembled using an in-house Matlab script.

Chapter 5. Mesoscopic structural analysis

The studied system is a set of conjugate strike-slip faults that belongs to a regional set of subvertical faults striking N-S to NW-SE (Fig. 3.3). The system is formed by a N-S-trending sinistral fault named BFZ045 (Fig. 5.1a) and a NW-SE dextral fault named BFZ300 (Fig. 5.1a). BFZ045 is a steeply dipping fault zone with a modelled orientation of 095°/87° (dip direction/dip angle, Fig. 5.1a) and modelled dimensions of 1048 x 518 m (length and height; Fig. 5.1b). BFZ300 has a modelled orientation of 250°/80° (Fig. 5.1a) and modelled dimensions of 1030 x 245 m (Fig. 5.1b). The fault surfaces as modelled in the Posiva database are shown in Fig. 5.1b.
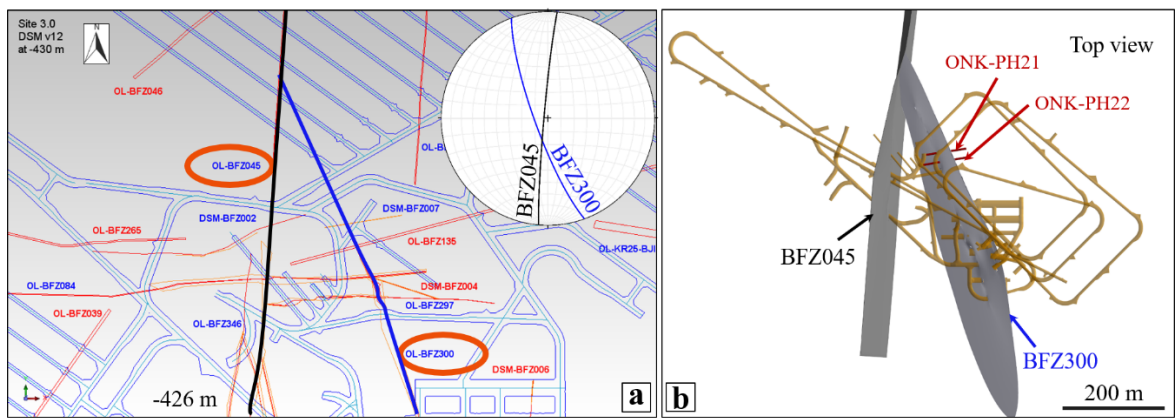
Figure 5.1. Site-scale view of the studied system of faults. (a) Deposit layout, plan view and intersection of the studied fault segments at 426 m b.s.l. The stereonet is a lower-hemisphere projection of the modelled orientation of the two conjugate faults. (b) View to the northwest of the studied set of conjugate faults and site-scale modelled fault surfaces. The BFZ300 is the dextral fault while its conjugate, the BFZ045, is characterised by a general sinistral sense of shear. The underground infrastructures and galleries are marked in yellow. BFZ300 is intercepted at several locations in the tunnels at a depth of c. 430-440 m (ONK-TPH-120), as well as in several drill cores (ONK-PH21 and ONK-PH22). Drill cores intercepting the BFZ300 fault surface used for this study are also highlighted in panel b. Photo courtesy of Posiva Oy, Finland.

Previous studies have shown that the BFZ045 overprints and reactivates mylonitic precursor likely related to earlier, localized ductile deformation (Altonen et al., 2016). The precursor contains evidence of both local dextral (Figs. 5.2a-d) and sinistral shearing (Altonen et al., 2016, Prando et al. in review). This precursor was reactivated by sinistral fractures (Figs. 5.2e-f) that was overprinted and reworked by cataclasites and pseudotachylyte injection veins (see details below). Conversely, the BFZ300 cuts across discordantly the metamorphic foliation and does not show any correlation with older ductile fabrics (e.g. Aaltonen et al., 2016, see details below).
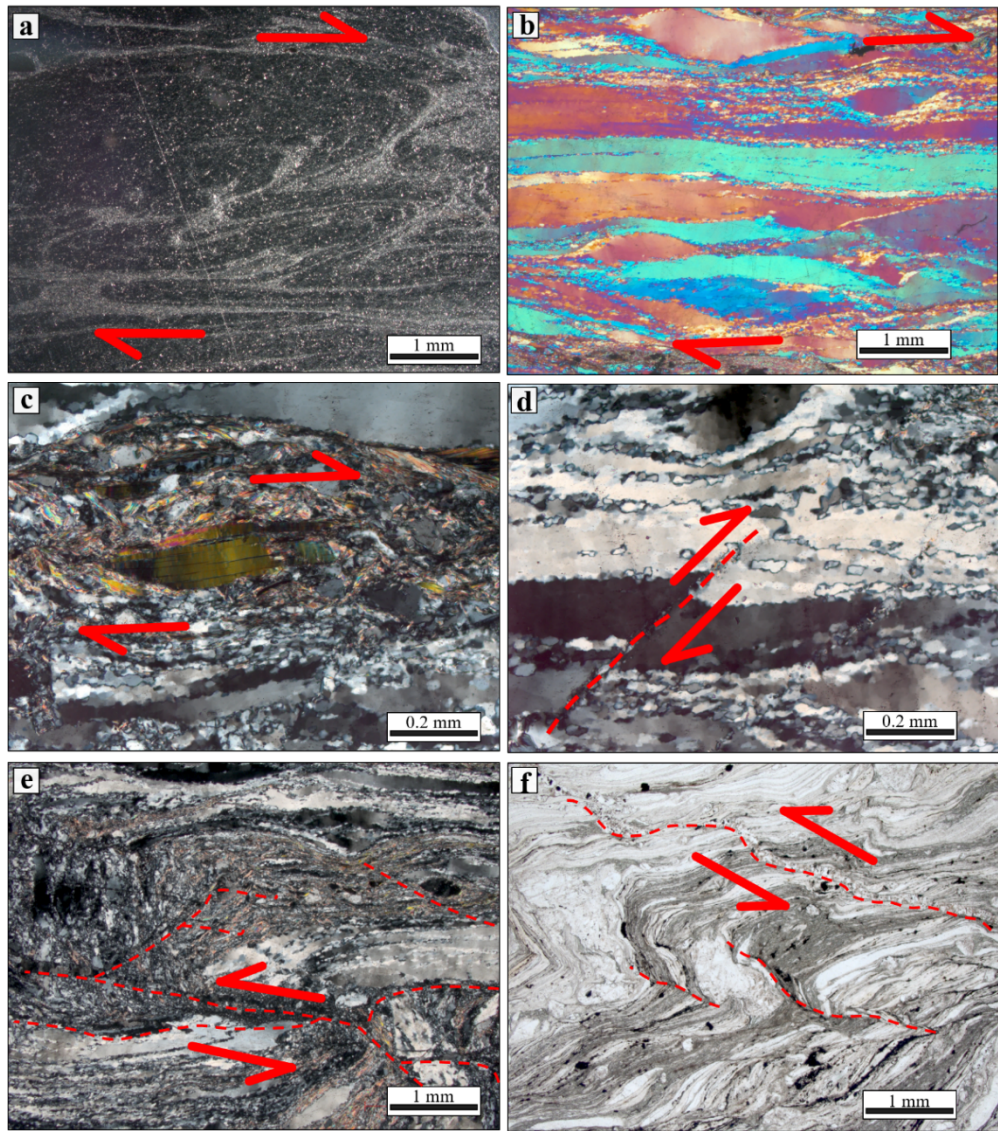
Figure 5.2. Selected examples of the mylonitic precursor to BFZ045 related to early, localized ductile deformation. (a) Reflected light image of BFZ045 ultramylonitic precursor not affected by later brittle overprint. (b) Dynamically recrystallized, stretched quartz ribbons of BFZ045 mylonites. Overall dextral kinematics is inferred. (c) Mica fish within quartz mylonite indicating dextral kinematics. (d) Microfault within a quartz ribbons with a general dextral kinematics. The ductile precursor also exhibits local dextral kinematics. (e) Example of sinistral brittle-ductile reactivation of the ductile mylonite with dextral S-C fabrics. (f) Sinistral brittle-ductile reactivation along the axial trace of a box fold deforming the mylonitic foliation. Photographs by Giulio Viola (University of Bologna).

The text below is mainly focused on the presentation and interpretation of data derived from the study of the BFZ300 fault zone, which represents the main topic of this Ph.D. study. BFZ045 was instead studied by a second Ph.D. project at the University of Plymouth (UK). This integrated approach has led to a very comprehensive understanding of the structural evolution of this set of conjugate structures. Results are presented in a set of two companion papers, Part I and Part II, which are: 1) "Fluid-mediated, brittle–ductile

deformation at seismogenic depth − Part 1: Fluid record and deformation history of fault veins in a nuclear waste repository (Olkiluoto Island, Finland)", by Marchesini, B., Garofalo, P. S., Menegon, L., Mattila, J., & Viola, G. (2019), Solid Earth (10(3), 809-838)"; 2) "Fluid-mediated, brittle-ductile deformation at seismogenic depth-Part 2 − Stress history and fluid pressure variations in a shear zone in a nuclear waste repository (Olkiluoto Island, Finland)", by Prando, F., Menegon, L., Anderson, M.W., Marchesini, B., Mattila, J. and Viola, G., which is currently in review.

5.1 BFZ045 general overview

Field observations made at underground exposures suggest that BFZ045 is a strike-slip fault, with an average orientation of 095°/87° (dip direction/dip angle, Fig. 5.3b, c.f. Aaltonen et al., 2016). Slickensides formed by the alignment of chlorite are common all along the exposed BFZ045 fault plane and indicate a dominant sinistral sense of shear. Slickenlines associated with dextral kinematics have also been locally observed on the fault plane. Chlorite-defined slicken-lines plunge generally to the south (mean orientation 169°/07°, trend/plunge, Fig. 5.3b).

The full BFZ045 architecture has been reconstructed from the structural interpretation of drill core PH28, which intercepts the fault zone at 420 m below the sea level. A schematic representation of the fault architecture is presented in Fig. 5.3a.

BFZ045 is characterized by a mixed ductile-brittle deformation style that manifests itself as a 10-100 cm wide mylonite with a sinistral sense of shear, overprinted by cataclasites, cemented fault breccias, and by a network of veins typically filled with chlorite, quartz, and calcite.

The structural interpretation of drill core PH28 suggests that the damage zone of BFZ045 is 2 m thick and envelops a c. 60 cm thick fault core characterised by a sub-vertical network of cohesive cataclasite strands and veins that overprint a mylonitic core oriented 075°/61° (Figs. 5.3a).

Damage zone boundaries were defined by the farthest occurrence of chlorite filled fractures, identified microscopically as deformation bands, as they are associated with visible slip. The fault core is characterized by multiple slip surfaces marked by 0.5 − 10 cm thick cataclastic domains that overprint the mylonite (Fig. 5.3a, III). Along one specific slip surface, two pseudotachylytes injection veins were found injecting discordantly the mylonite, which demonstrates the transient seismogenic behaviour of BFZ045 (Fig. 5.3a, III). The pseudotachylyte main generation surface is less than 1 mm thick and is parallel to

the mylonitic foliation (Fig. 5.3d). For the complete description of the BFZ045 fault architecture and microstructures we refer the reader to the Appendix D.
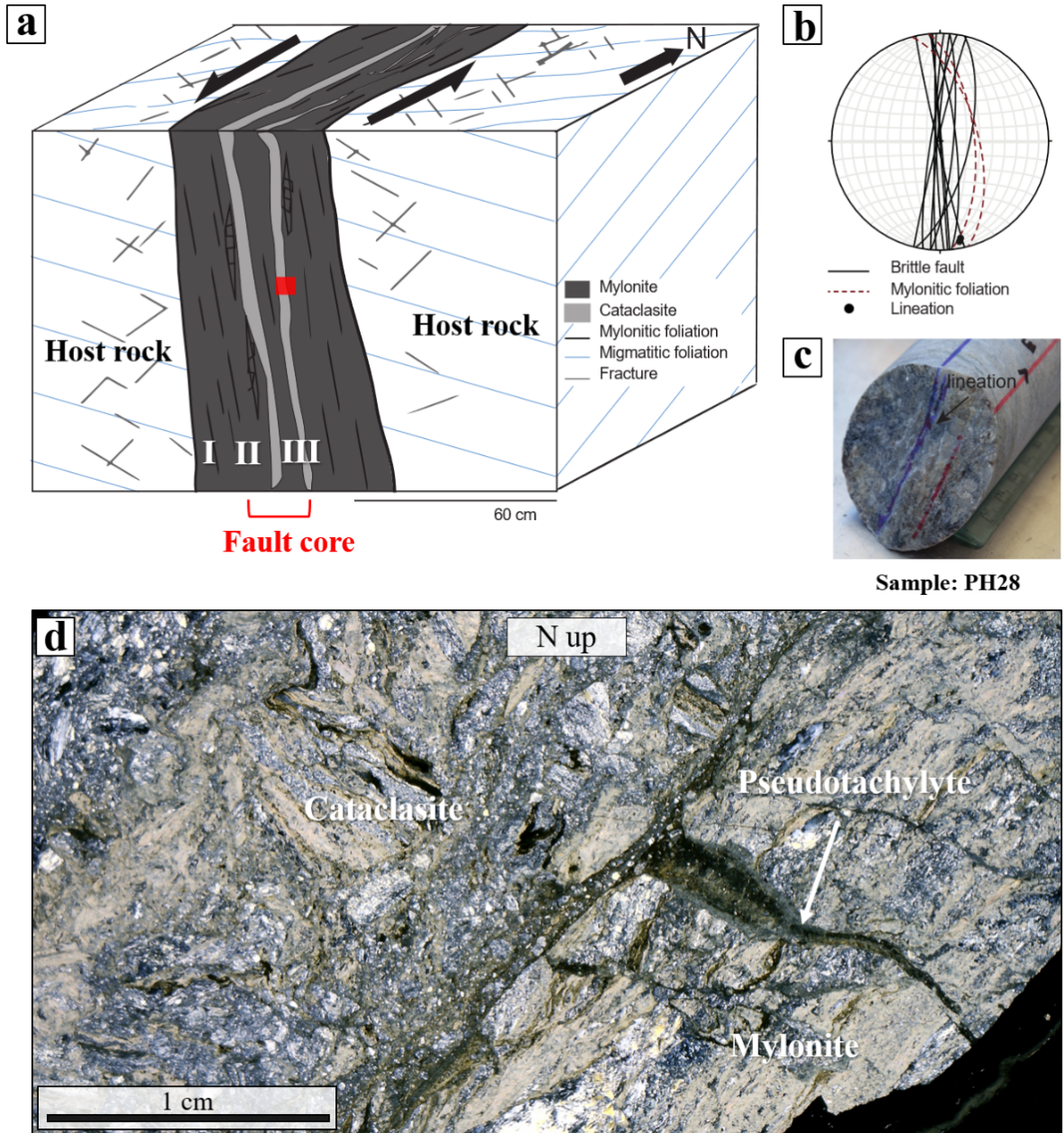
Figure 5.3. (a) Block diagram of the BFZ045 fault architecture reconstructed from the structural interpretation of drill core PH28. Fault architecture consists of: (I) damaged coarse-grained host rock, and (II) fault core with mylonites, chlorite-rich cataclasites and (III) pseudotachylyte injection vein. (b) Lower-hemisphere, equiangular projection of sinistral fault structures (black great circles), mylonitic foliation (red dashed line) and lineation on fault plane (black dots). (c) Core sample along PH28 drill core within the fault core unit. The core sample is mylonitic, and the blue line indicates the stretching lineation, which is parallel to chlorite striae. (d) Stitched photomicrographs of BFZ045 fault core composed by cataclasite with characteristic pseudotachylyte injection veins intruding the mylonite at a high angle. The cataclasite matrix is enriched in chlorite. Location of thin section within the fault core is indicated with a red square on panel (a). Modified from Prando et al. (in review, Solid Earth).

5.2 BFZ300 architecture

The BFZ300 was intercepted at several locations in the tunnels at a depth of c. 430-440 m, by, for example, drill core ONK-TPH-120, which was extensively used in this study, as well as by several other drill cores such as ONK-PH21 and ONK-PH22. Drill cores ONK-PH21 and ONK-PH22 are shown in Fig. 5.1b.
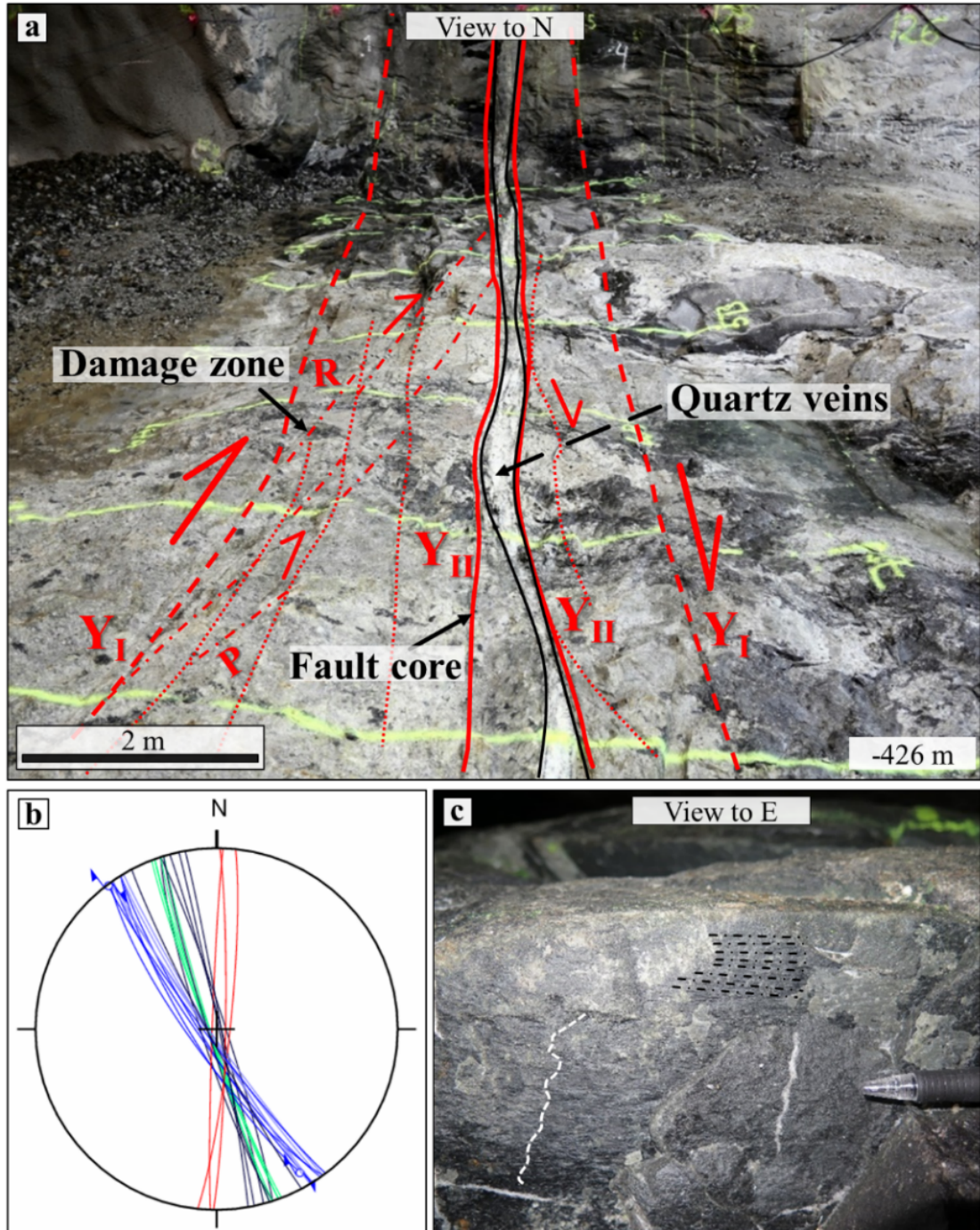
Figure 5.4. (a) View to the north and interpretation of the structural elements of BFZ300. (b) Lower-hemisphere, equiangular projection of conjugate fault segments (blue great circles: dextral faults; red great circles: sinistral faults), cleavage (green great circles) and Qtz I-chlorite veins infilling joints (black great

circles). (c) Slickensides (white dashed line) and slickenlines (black dashed lines) on a chlorite-decorated, NW-SE striking fracture plane at the vein-host interface indicating dextral strike-slip kinematics.

The studied BFZ300 section is located at a depth of 426 m b.s.l. and is about 8 m long (Figs. 5.1a, 5.4a). It strikes NNW-SSE and dips very steeply to subvertically to the southwest (Fig. 5.4b). It cuts through the high-grade veined migmatite, interlayered with gneiss and pegmatitic granite. The fault is a strike-slip fault system formed by two main subparallel fault segments connected by a mesoscopic sinistral step-over zone. Subhorizontal striae defined by elongated trails of chlorite grains and kinematic indicators such as chlorite slickensides (Fig. 5.4c) and R and R' planes invariably indicate dextral strike-slip kinematics. The most striking mesoscopic characteristic of BFZ300 is the presence in the fault core of a composite set of almost continuos quartz veins (between 1 and 20 cm in thickness) along the entire exposed strike length. A schematic representation of the fault zone is shown in Fig. 5.5.

The fault contains a 0.5-2 m thick damage zone separated from the undeformed host rock by two discrete bounding surfaces (Y_I planes according to Tchalenko, 1970 Fig. 5.4a). The damage zone can be defined in the field on the basis of the presence of a fractured volume containing sets of conjugate dextral and sinistral hybrid fractures (Fig. 5.5a) intersecting to form a tight acute angle of c. 38° (Figs. 5.4b, 5.5a). Laterally continuos, NNW-SSE striking Mode I fractures (joints) invariably bisect this angle (Figs. 5.4b), helping to constrain the stress field orientation at the time of fracture formation, with the greatest compressive stress axis σ_1 parallel to the Mode I fracture strike and oriented c. NNW-SSE. Joints are sharp and have a regular spacing of c. 10 cm. The joints and the hybrid fractures of the damage zone contain quartz, referred to as Qtz I hereinafter, forming veins up to 1-1.5 cm thick (Fig. 5.5a). Fractures and faults decorated by Qtz I have a translucid look that reflect the generally fine grain size of Qtz I (< 1 cm, Fig. 5.5b). Locally they are formed by en-echelon tensional segments connected by shear planes not decorated by any quartz infill (Fig. 5.5b). Joints occur also as barren fractures defining a penetrative sympathetic fracture cleavage (sensu Basson and Viola, 2004; green lines in Fig. 5.4b). Field evidence also suggests that the fracture density within the damage zone tends to increase towards the fault core.

The fault core is bounded by two main discrete slip surfaces (Y_{II}, Figs. 5.4a, 5.5d, f, h). It contains, and is defined by, two distinct generations of quartz veins (Fig. 5.5c) that are interrupted and offset laterally by a metric sinistral step-over zone (Fig. 5.5d-f). The main quartz vein of the core is infilled by quartz exhibiting the same mesoscopic appearance of
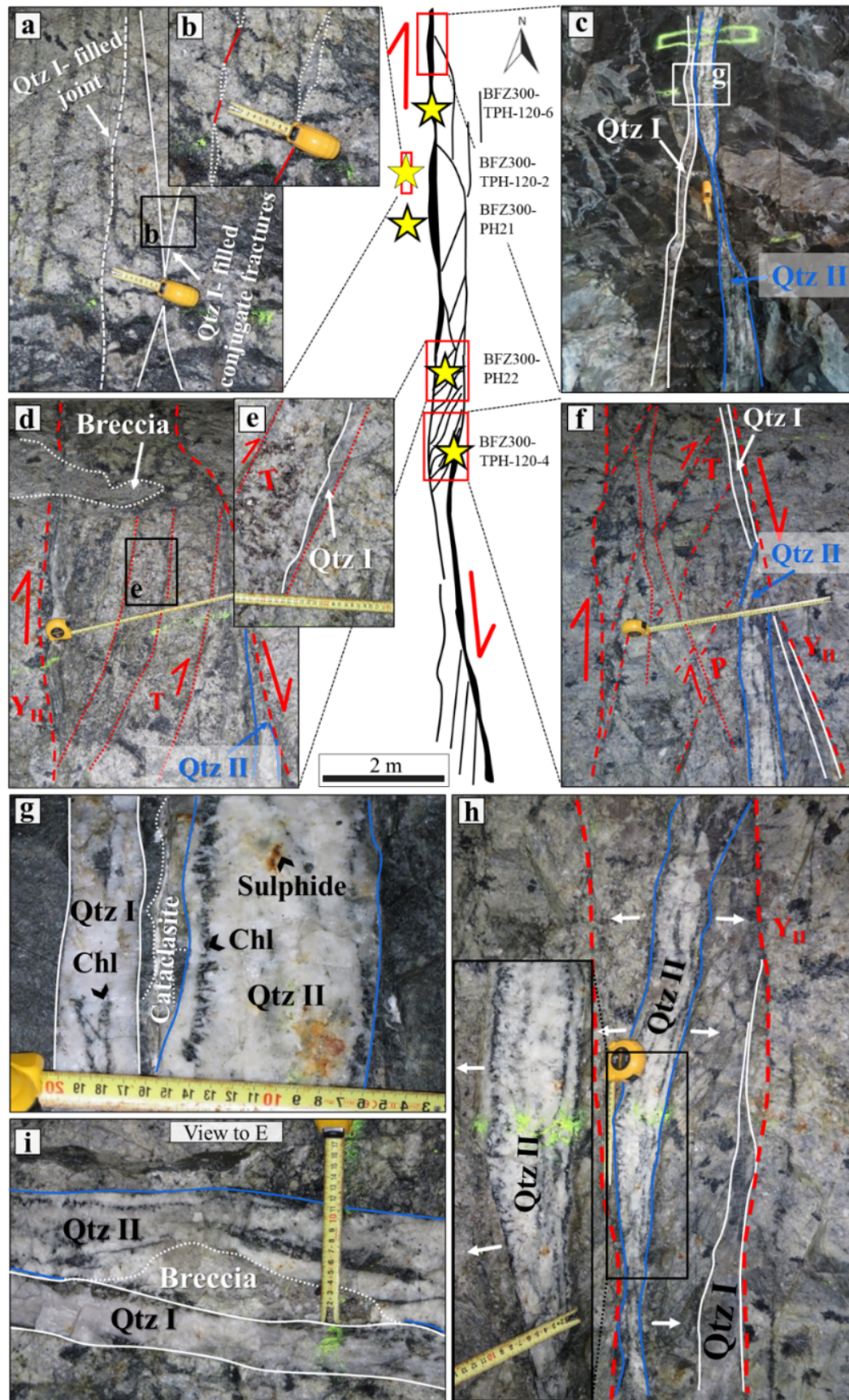
Figure 5.5. BFZ300 architecture with examples of representative structural features. The red rectangles locate the areas where detailed outcrop photos were taken. Stars locate hand and drill core samples. Stars with a

black outline identify samples used for the microthermometric study. Note that the fault is made of two main segments offset laterally at a sinistral compressive step-over zone. Fault core quartz veins are shown by thicker black lines in the schematic model (centre of figure), while blue and white lines highlight the positions of the two types of quartz veins in the outcrop pictures. (a) Damage zone made of mm-thick, en-echelon veins connected by conjugate shear segments. (b) Detail of (a) showing fractures filled by the first quartz generation (Qtz I). (c) Two distinct generations of quartz-chlorite veins recognised in the fault core (Qtz I and Qtz II). (d) Detail of the sinistral compressional step-over zone characterized by multiple and parallel T fractures, filled by Qtz I. A brecciated body is crosscut by the Y planes. (e) Tensional fracture infilled by Qtz I. (f) Compressional structures (P shears) from the step-over zone and relationships between Qtz I and Qtz II. The Riedel geometry suggests that the Qtz II vein formed due to the reactivation of the internal principal slip zones (Y_{II}). Note the Qtz II vein cutting the Qtz I vein. (g) Juxtaposed Qtz I and Qtz II veins. Qtz I veins are thinner and made of a translucid, small grained quartz. In contrast, Qtz II veins, which contain pockets of sulphide aggregates, are thicker and made of larger and euhedral quartz. Chlorite occurs as minor phase in both veins. Notice the presence of a cataclastic band between the two veins. (h) Spatial continuity of the chlorite aggregates within the Qtz II veins, which grow always orthogonal to the vein boundaries. This open space filling texture suggests hybrid conditions of reactivation of the older Qtz I veins. (i) Small quartz breccia formed between the two generations of quartz veins.

Qtz I in the damage zone; we therefore refer to it as a Qtz I vein. It is accompanied by a younger, subparallel vein formed by a milky-white type of quartz with a significantly larger grain size than Qtz I (>1 cm) that we refer to as Qtz II (Fig. 5.5c). Locally, pockets of cataclasite and breccia formed at the expense of the host migmatitic gneiss are also observed along and in between the two veins (Figs. 5.5g, i). The Qtz II vein exhibits a quite irregular, curved geometry (Figs. 5.5c, h) and a variable thickness up to a maximum of c. 20 cm. The minimum Qtz II vein thickness coincides spatially with an apparent lateral displacement of the vein.

The BFZ300 core varies in thickness between 20 and 30 cm along most of the exposed fault length, but becomes thicker (up to 50 cm) in the compressional step-over zone that connects the two fault segments that are offset laterally by c. 1 m. The sinistral step-over zone is defined by synthetic T fractures (Figs. 5.5d, e) and contains a decimetric brecciated lens (Fig. 5.5d). T fractures are filled by Qtz I veins (Fig. 5.5e).

Chlorite is present as a secondary phase, with a modal abundance between 5 and 10 vol% in both Qtz I and Qtz II veins. In Qtz I veins it occurs as euhedral/subhedral crystals up to 1-2 mm in size (Fig. 5.5g). Chlorite is present mostly as a disseminated, interstitial phase, concentrated mainly in the internal part of the Qtz I veins (Fig. 5.5g). In the Qtz II vein, however, it occurs as elongated crystals (5-8 mm in length) arranged perpendicularly to the walls of the vein, which suggests orthogonal dilation at the time of opening (Fig.

5.5h). The Qtz II vein contains also small (1-2 cm) aggregates of sulphides (sphalerite, pyrite, galena, and chalcopyrite) mainly concentrated in the central part of the vein (Fig. 5.5g).

As observed in the field, the presence of Qtz I veins along the joints in the damage zone and the continuity of the fault core Qtz I vein suggest Mode I fracturing during Qtz I emplacement (Figs. 5.4a, 5.5a, c). The semi-continuous parallelism of Qtz I and Qtz II veins in the fault core, combined with the location of the Qtz II vein along the walls of the Qtz I vein, suggest the partial reactivation of the Qtz I vein during Qtz II emplacement. Dilation leading to Qtz II emplacement exploited and further reworked the Qtz I-host rock contact, that seemingly had a lower tensile strength than the pristine migmatite. The reconstructed time relationship between the two vein generations is also consistent with local evidence of the Qtz II vein partly crosscutting the Qtz I vein (Fig. 5.5f).

Chapter 6. BFZ300 microtectonics

To constrain the spatial and temporal association of fault rocks and the type of fluid involved in the deformation, several outcrop samples, each representative of a specific structural domain, were collected (TPH-120-2, TPH-120-3, TPH-120-4, TPH-120-5 and TPH-120-6), in addition to samples PH21 and PH22 from diamond drill cores that intersect BFZ300 at the same depth in an area that is currently not excavated. From these samples we prepared 10 petrographic thin sections (samples TPH-120-2, TPH-120-4, TPH-120-6, PH21 and PH22) and 9 doubly-polished sections for fluid inclusion analysis (thickness ~150 μm, samples TPH-120-2, TPH-120-4, TPH-120-6, PH21 and PH22). Due to the extensive reactivation of the fault zone and the consequent obliteration of the FI record, the FI study was carried out only in samples TPH-120-4, TPH-120-6 and PH21. Hand samples and drill cores localities are shown in Fig. 5.5.

The microstructural work was carried out on oriented petrographic thin sections cut orthogonally to the migmatitic foliation and parallel to the slickenlines.

In the following we provide a description of the microstructural characteristics of BFZ300 by detailing our findings and observations separately for the main structural domains of the fault zone.

6.1. Microstructural analysis

6.1.1 Damage zone

Qtz I veins within the damage zone invariably cut across the migmatitic host rock (Fig. 6.1a). The migmatite is characterized by the typical alternation of leucosome and melanosome layers (Fig. 6.1a). The host rock is affected by a pervasive metamorphic foliation defined by chloritized muscovite and graphite grains. These occur as elongated grains aligned along the metamorphic foliation (Fig. 6.1b) and have an average grain size between 100 and 300 μm (Fig. 6.1c).

Qtz I veins form the infill of conjugate sets of hybrid fractures, which, when studied at the microscale, appear as formed by dilatant segments joined by cataclastic shear fractures (Fig. 6.2a). Shearing on the latter is well documented by the asymptotic bending into the shear surfaces of foliation planes formed by the alignment of chlorite and muscovite, both partly altered to sericite and chlorite, respectively (Fig. 6.2a). Qtz I infilling the tensional segments has an average grain size between 200 μm and 3 mm and exhibits a rather heterogeneous texture, from purely blocky to mixed elongated-blocky (Figs. 6.2b, c). The
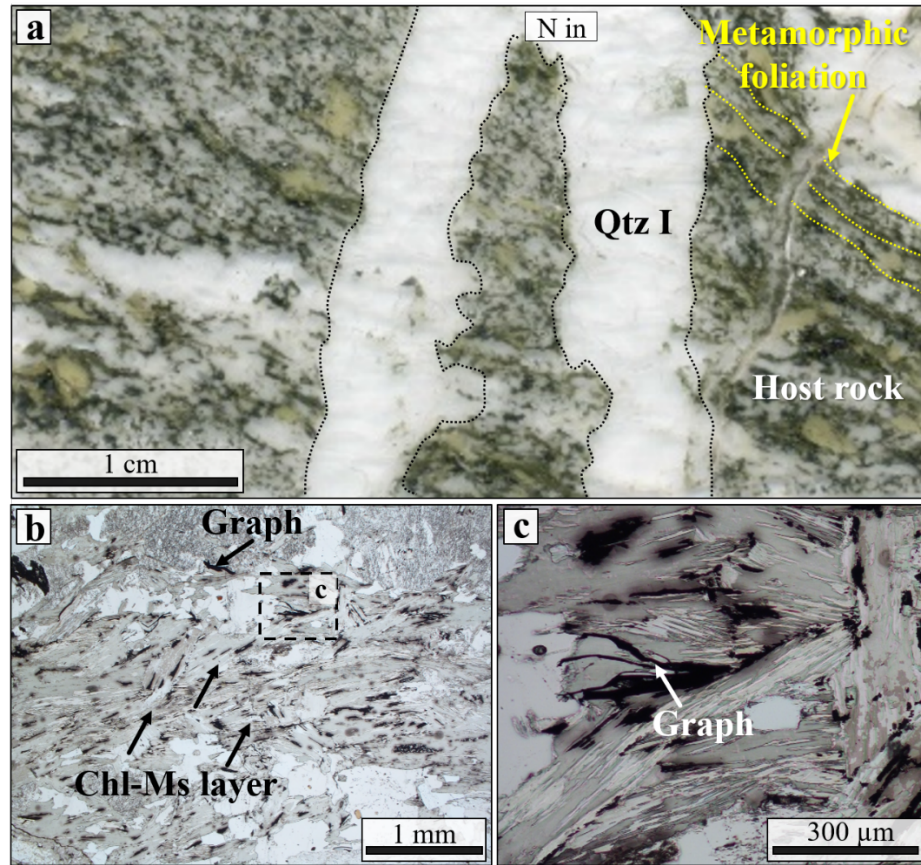
Figure 6.1. Microtextural characteristics of the migmatitic basement hosting BFZ300. (a) Scanned double-polished thin section with cross-cutting relationships between Qtz I from the damage zone and the migmatite. After metamorphic peak conditions (3.7-4.2 kbar and 660-700° C; Tuisku and Lauri, 2009), the migmatite was deformed by polyphase ductile deformation (i.e. D2-D4) under lower metamorphic conditions, which generated a pervasive metamorphic foliation. (b) The metamorphic foliation is marked by the alignment of chloritized muscovite and (c) graphite grains.

largest crystals (800 µm to 1 mm) are elongated and stretched from the vein walls towards the inner part of the vein (Figs. 6.2c, 6.3a). At least two episodes of vein growth/renewed dilation, as indicated by the presence of median lines (ML), are visible within one of the studied veins and confirm a syntaxial growth mechanism for the vein (Fig. 6.3; e.g. Bons et al., 2012). Medial lines are defined by the alignment of chlorite, sericite, and carbonate aggregates (Figs. 6.3a, b, d). Blocky euhedral quartz crystals are also found varying in grain size between 300 and 600 µm. These crystals are juxtaposed against very fine grained quartz (<200 µm) within sericite-rich cataclastic bands (Fig. 6.2b). These cataclasites contain also hydrothermally altered host-rock fragments including pervasively altered K-feldspar-bearing lithic fragments and phyllosilicates.
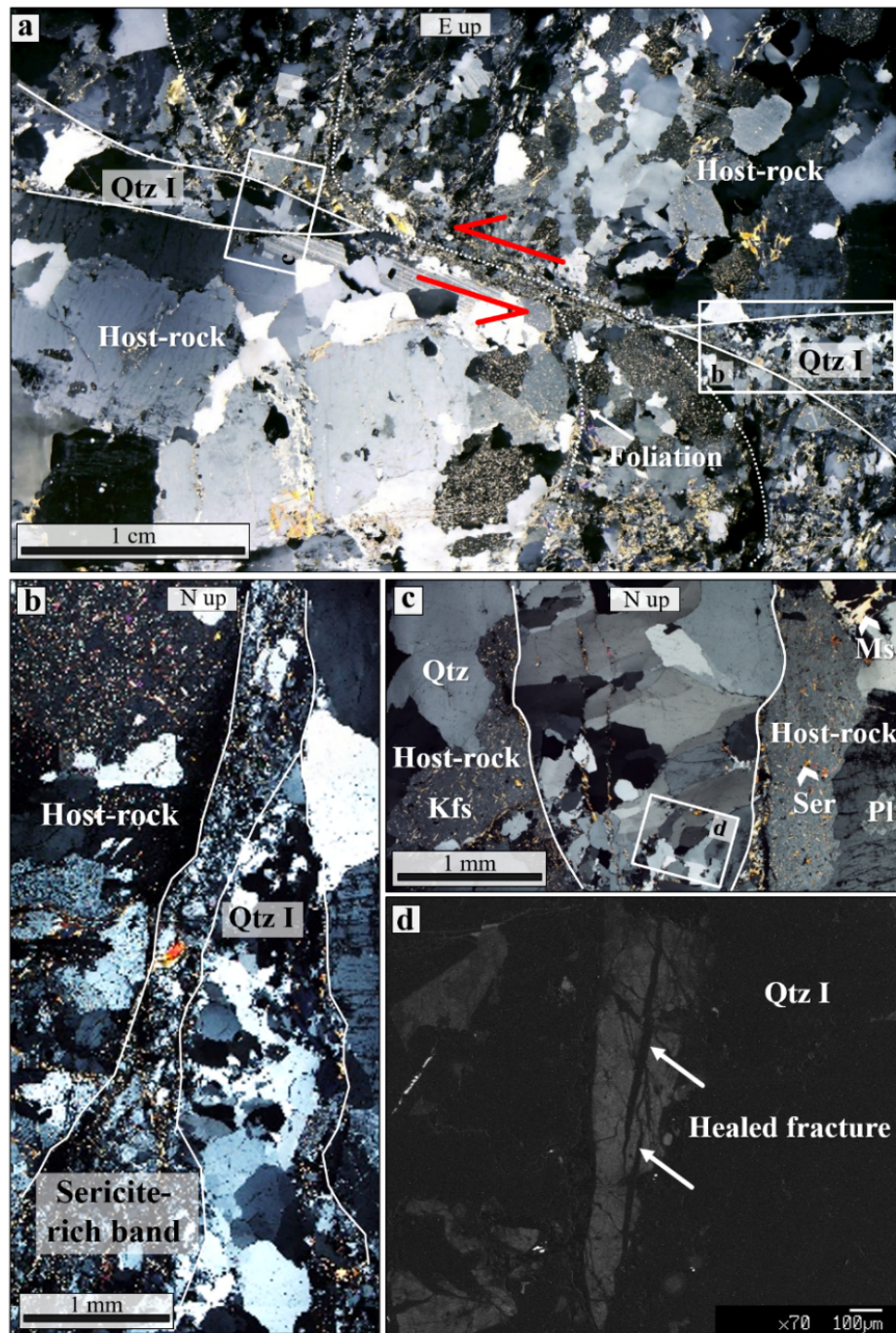
Figure 6.2. Microtextural characteristics of Qtz I from the damage zone of BFZ300 (sample: TPH-120-2). (a) Stitched photomicrographs of a Qtz I vein interconnecting with a sinistral shear band (crossed nicols). Faulting kinematics is suggested by drag folds in the host rock. (b) Tip of Qtz I vein hosted by a sericite-rich cataclastic band of the host rock. (c) Detail of panel a showing open-space filling texture in the Qtz I vein. Notice the sericite microfractures crosscutting Qtz I. (d) Panchromatic cathodoluminescence image of Qtz I showing healed microfractures crosscutting the crystal.

With the exception of the blocky variety, Qtz I crystals exhibit various degrees of crystal-plastic deformation and recovery. They contain widespread evidence of undulose

extinction and extinction bands (Fig. 6.3b), and incipient bulging along grain boundaries is also evident (Fig. 6.3c). Millimetric intracrystalline barren fractures are also recognized (e.g. Fig. 6.3c). Cathodoluminescence imaging of Qtz I from the damage zone also shows the presence of a dense network of healed quartz microfractures (Fig. 6.2d), which demonstrates healing subsequent to brittle deformation and fracturing.

Chlorite occurs along the ML of the veins, secondary cracks, along grain boundaries and as inclusions within quartz crystals. It has a vermicular texture (Fig. 6.3d) and crystal dimensions up to 50 µm.
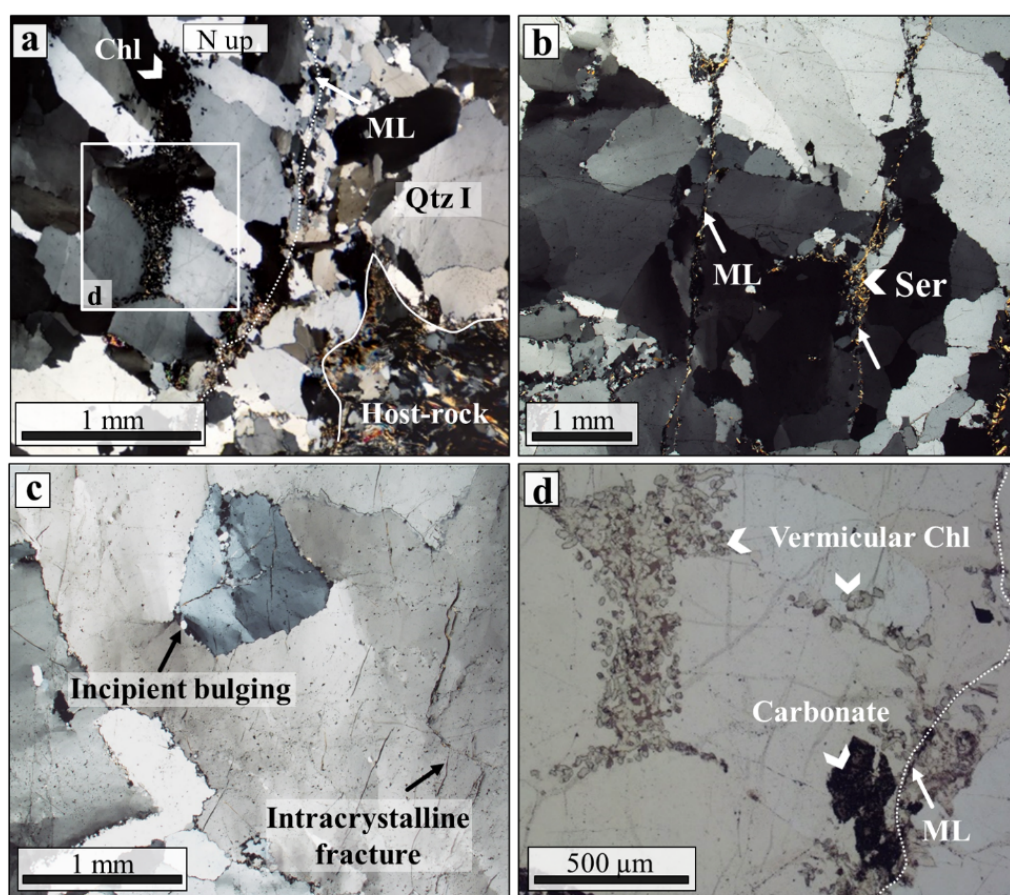
Figure 6.3. Microtextural characteristics of Qtz I from the damage zone of BFZ300 (samples PH21 and TPH-120 2). (a) Stitched microphotographs of a Qtz I vein showing elongate-blocky texture with crystals growing obliquely with respect to the vein boundaries, which suggests growth under oblique dilatation. A series of median lines (ML) are marked by (b) sericite crystals suggesting repeated crack-and-seal. Quartz crystals show low temperature crystal-plastic deformation by undulose extinction and extinction bands. (c) Detail of plastic deformation in damage zone quartz veins: distorted crystals showing incipient bulging and intracrystalline fracturing. (d) Detail (plane polarized light) of a ML and secondary fractures both decorated by vermicular chlorite and aggregates of REE-bearing carbonate.

6.1.2 Fault core

In the fault core, Qtz I grain size reaches the smallest observed value (range: 30-800 µm, Fig. 6.4a), although it is strongly variable within the vein, suggesting the presence of heterogeneous and complex structural sub-domains. The earliest post-vein emplacement deformation stage is reflected by the low-temperature, intracrystalline deformation of the largest crystals (400-800 µm in size). Undulose extinction, wide extinction bands (WEBs, Derez et al., 2015), and bulging along grain boundaries are the most common microstructures ascribable to this deformation stage (Figs. 6.4a, b). A first brittle deformation event is documented by narrow, intracrystalline fractures that crosscut the largest quartz crystals (Fig. 6.4c) and which locally contain new grains of quartz ranging in size between 20-100 µm (Fig. 6.4d). More in detail, these new grains form parallel bands that are oriented at low angle (<30°) to the vein walls and that can be up to 2 mm in length and 200 µm in thickness. Plastically deformed Qtz I crystals hosting these intracrystalline bands of new grains are cut across by another later set of subparallel intercrystalline fractures, which are interpreted as the expression of yet another deformation event that occurred under overall brittle conditions. These fractures are parallel to the strike of BFZ300 and are in turn sealed by partly recrystallized new quartz grains (grain size: 50-150 µm; Fig. 6.4e). The cathodoluminescence imaging of these fractures shows that they are sealed, yielding a homogeneous dark signal (Fig. 6.4f). They are locally decorated by trails of fluid inclusions (Figs. 6.4g) and can be up to 2.5 cm in length and up to 500 µm in width (Fig. 6.4a). EBSD maps were acquired along some of these intercrystalline bands, and results suggest that the new grains sealing the fractures reflect the combined effect of initial cracking, grain nucleation and subsequent partial dynamic recrystallization. EBSD working conditions and results were reported in Appendix A.

Qtz II within the fault core is typically coarse grained (individual crystals: 300 µm-1 cm in size) and exhibits a regular blocky texture devoid of any shape or crystal preferred orientation (Fig. 6.5a). Locally, these large crystals display primary growth textures, such as primary FIAs oriented parallel to specific crystallographic planes. With the exception of undulose extinction, Qtz II does not show clear evidence of plastic deformation, although cathodoluminescence imaging of optically continuous Qtz II has also shown that a dense network of healed quartz microfractures locally crosscuts Qtz II crystals (Fig. 6.5c). These are relatively thin (hundreds of micrometres thick) networks that are poorly visible to invisible by standard petrographic analysis. The only petrographic evidence for these healed

microfractures within quartz are well defined trails of fluid inclusions crosscutting primary growth bands (Fig. 6.5d).
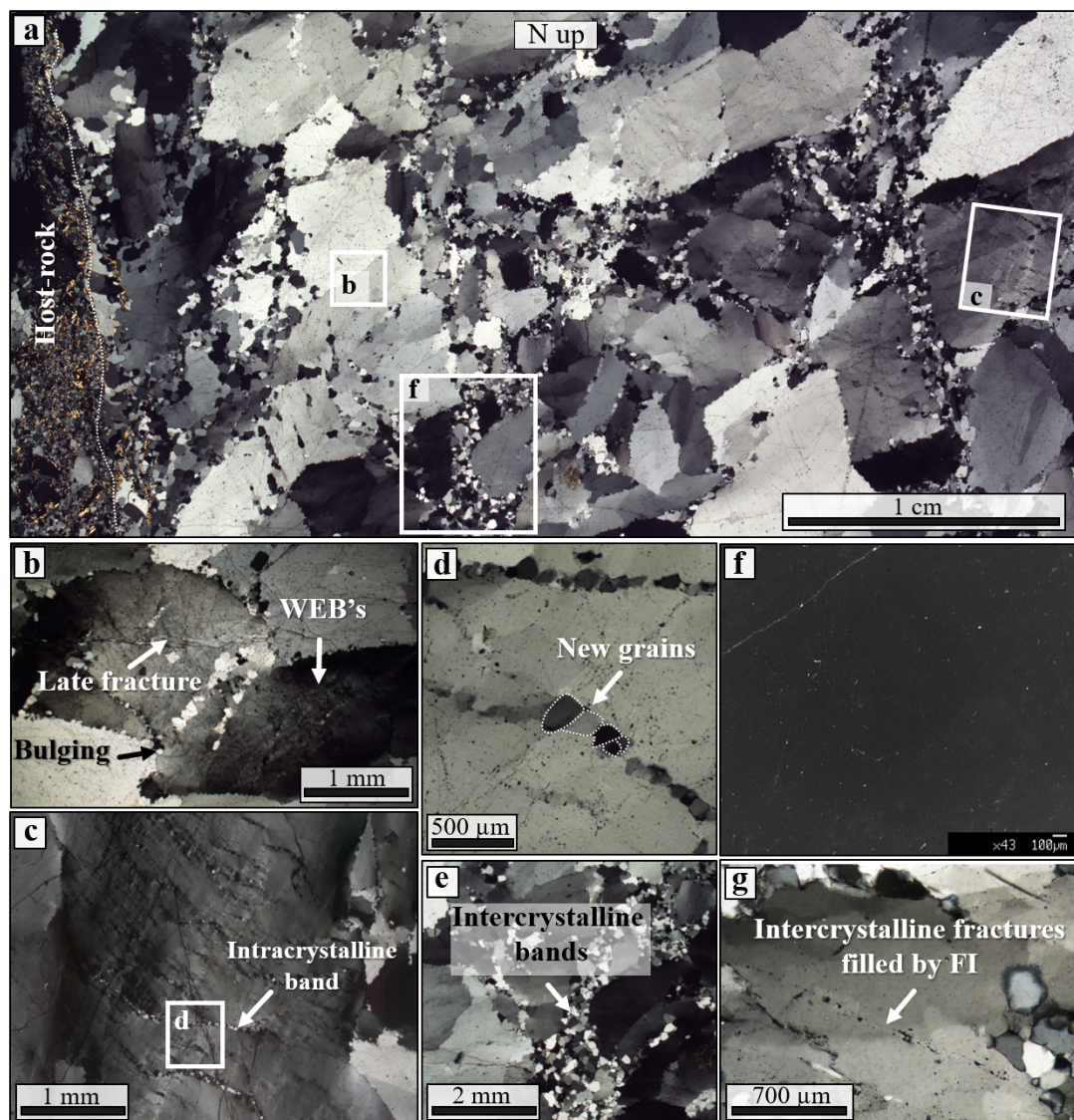
Figure 6.4. Microtextural characteristics of Qtz I from the BFZ300 core (sample TPH-120-4). (a) Stitched photomicrographs showing the typical heterogeneous grain size of Qtz I (30-800 μm). (b) Evidence of plastic deformation of Qtz I from the fault core given by bulging of the largest crystals, wide extinction bands and undulose extinction. Note the late brittle fractures crosscutting all the previously formed plastic features. (c) Intracrystalline deformation bands within a large crystal. (d) Detail of (c) showing the typical grain size of the band (50-250 μm). Intracrystalline deformation bands are oriented at <30° with respect to the BFZ300 vein walls and can be up to 2 mm in length. (e) Intercrystalline deformation band showing a thickening at the triple junction of larger grains. These intercrystalline bands are parallel to the strike of BFZ300. (f) Panchromatic cathodoluminescence image of intercrystalline fracture occurring within Qtz I from the fault core, showing homogeneous-dark signal. (g) Intercrystalline bands are also marked by trails of fluid inclusions.
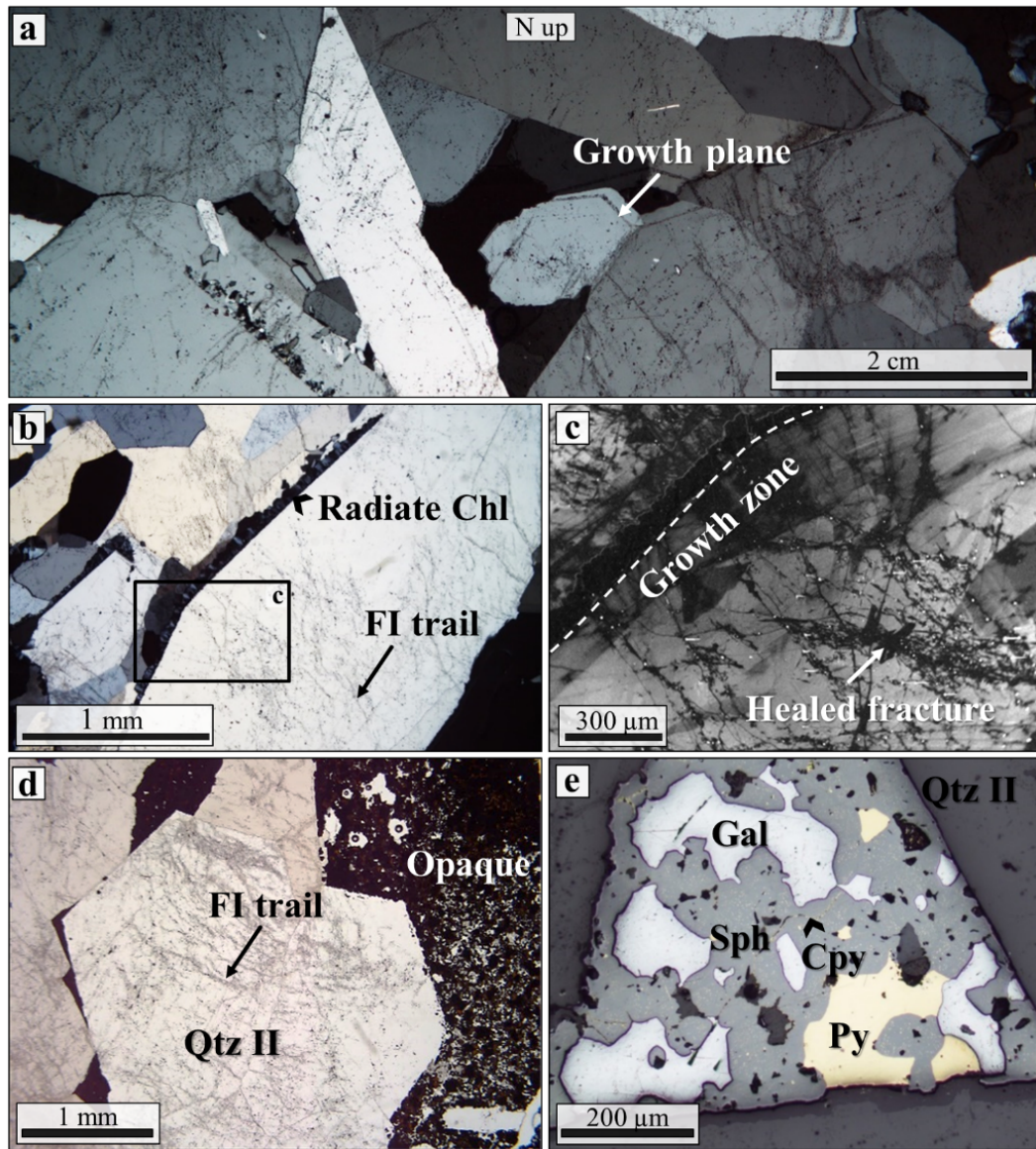
Figure 6.5. Microstructural characteristics of Qtz II from BFZ300 (samples TPH-120-6, PH21, PH22). (a) Stitched photomicrographs of Qtz II vein from the fault core. Notice the coarse quartz crystals and their elongated-blocky texture. Primary growth textures are sometimes visible and are marked by solid inclusions and decrepitated FIAs. (b) Radiate chlorite crystals along a prismatic Qtz II crystal boundary. Note that Qtz II is crosscut by numerous trails of FIs. (c) Panchromatic cathodoluminescence image of the same large Qtz II crystal from panel b, showing radiate chlorite along the crystal boundary and a primary growth zone cut by a set of healed fractures. (d) Euhedral quartz crystals set within opaque phases and crosscut by a network of thin microfractures. (e) Reflected light photomicrograph showing the opaque mineral assemblage typically associated with Qtz II, i.e. subhedral to anhedral sphalerite, pyrite, and galena. Chalcopyrite is a minor phase and occurs as small round inclusions within sphalerite (chalcopyrite "disease") or as large subhedral/anhedral masses together with galena.

Chlorite is the second most abundant phase within Qtz I-fault core and Qtz II veins and occurs with a variety of textures. Aggregates of vermicular chlorite similar to that occurring
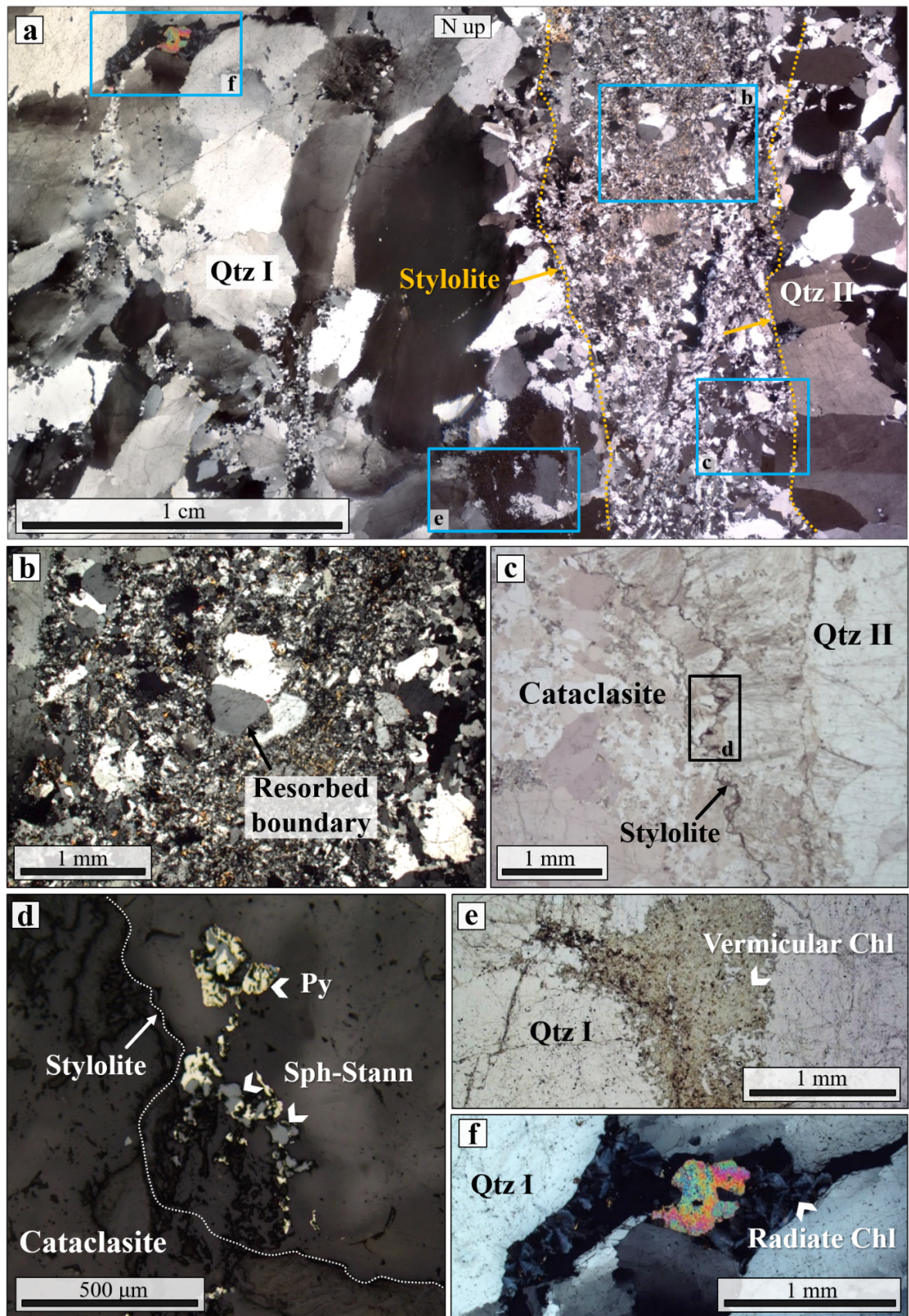
Figure 6.6. Microstructures of the cataclasite juxtaposing Qtz I and Qtz II veins (sample TPH-120-4). (a) Stitched photomicrographs covering the contact between the two quartz veins and the intervening 5 mm-thick cataclastic band. (b) Cataclastic band containing large Qtz I fragments (8-12 mm) embedded within a finer matrix (20-200 µm in size) of sericite and recrystallized quartz. The largest crystals show lobate boundaries, suggesting dissolution and local resorption along the clast-matrix interface. (c) Stylolite seams at the boundary of the cataclasite that strike parallel to the BFZ300. (d) Reflected-light photomicrograph showing

anhedral to subhedral pyrite, chalcopyrite, stannite, and sphalerite arranged along the stylolite as residual products of pressure solution. (e) Vermicular and radiate (f) chlorite aggregates associated with Qtz I close to the cataclastic band.

in the damage zone are also present in Qtz I from the core (Fig. 6.6e), although chlorite with flaky and radiate textures (Fig. 6.6f) is also present. The latter is generally 100-300 μm in size and is in textural equilibrium with quartz and rare calcite. Radiate chlorite overgrowing fractured Qtz II (Fig. 6.5b) suggests late Qtz II precipitation.

Associated with Qtz II, a sulphide assemblage made of pyrite, sphalerite, galena and chalcopyrite (Figs. 6.5d, e, see also Fig. 5.3g) forms aggregates that are commonly located along quartz grain boundaries. These aggregates have dimensions between 10 and 600 μm. Chalcopyrite occurs as μm sized irregular inclusions within sphalerite forming the typical "chalcopyrite disease" texture (e.g., Barton and Bethke, 1987, Fig. 6.5e).

Multiply reworked breccias and cataclasites occur within and crosscut BFZ300. In the studied sections, a cataclastic band between 5 and 8 mm thick crosscuts both Qtz I and Qtz II veins (Fig. 6.6a), but is in turn crosscut by a different quartz-radiate chlorite vein displaying evidence of syntaxial growth. This cataclasite contains poorly sorted and angular quartz clasts between 8 and 12 mm in size set in a finer (20-200 μm in size) white mica-quartz matrix. The largest quartz fragments show irregular, lobate grain boundaries and are affected by undulose extinction. We interpret these textures as the product of dissolution and cataclastic reworking of Qtz I.

Parallel sets of stylolitic seams trend c. N-S, parallel to the strike of BFZ300, and mark the two sides of the cataclastic band (Figs. 6.6a, c). They host anhedral sphalerite, stannite, galena, pyrite, and chalcopyrite (Fig. 6.6d), which are coeval with the formation of the Qtz II vein. We interpret the presence of these anhedral sulphide minerals along the stylolite as the product of passive concentration by pression-solution.

Chapter 7. Fluid inclusion data

Fluid inclusions were studied to constrain the physical-chemical conditions (P_f, T, X) of synkinematic fluids, trapped within the system as multiple planar trails of FIs (cf. Chapter 4).

In the following, petrographic analysis, microthermometric results and micro-Raman analysis of fluid inclusions are presented. The fluid inclusion dataset is presented for each structural domain, in accordance with mesoscale observations and microstructural analysis.

7.1 Fluid inclusion petrography

The studied FIAs contain invariably a two-phase fluid (liquid-vapour) and are mainly arranged in secondary trails within Qtz I crystals in the damage zone and also within Qtz I fault core, where they form dismembered trails and also appear as individual clusters inside the crystals affected by crystal-plastic deformation. Within Qtz II, FIAs are arranged as pseudosecondary and secondary trails.

Petrographic analysis shows that the studied FIAs can be grouped into 5 main subgroups, where each subgroup is characterized by FIAs with specific dimensions, shape, volume fraction and crosscutting relationship with the host crystal (i.e. quartz). The 5 main subgroups were named Type S1, Type S2, Type 3, Type PS and Type S4. A detailed petrographic description is given in the following text.

7.1.1 Damage zone

Within Qtz I grains (Fig. 7.1), secondary FIAs are found as trails (Figs. 7.1a-c) that parallel what we interpret as healed, old microfractures. In these assemblages, FIs have a maximum size between 2 and 20 μm (Figs. 7.1d-f), a regular equidimensional shape (i.e. negative crystal morphology), and a volume fraction, φ (φ= V_v/V_{tot}; c.f. Chapter 4), ranging between 5 and 15% (Figs. 7.1d-f). FIAs corresponding to these petrographic features were grouped as Type S1.

7.1.2 Fault core

Qtz I grains host secondary FIAs, which are transgranular trails (Fig. 7.2a) along healed joints and hybrid fractures. These trails are locally interrupted and dismembered by aggregates of new, fine-grained quartz grains (Fig. 7.2a), and generate a texture that is indeed typical of Qtz I from the fault core (Fig. 6.4a). Fluid inclusions vary in size between

1 and 10 μm, have a φ of 10-20%, and show a negative crystal morphology (Fig. 7.2b). FIAs corresponding to these petrographic features were grouped as Type S2.
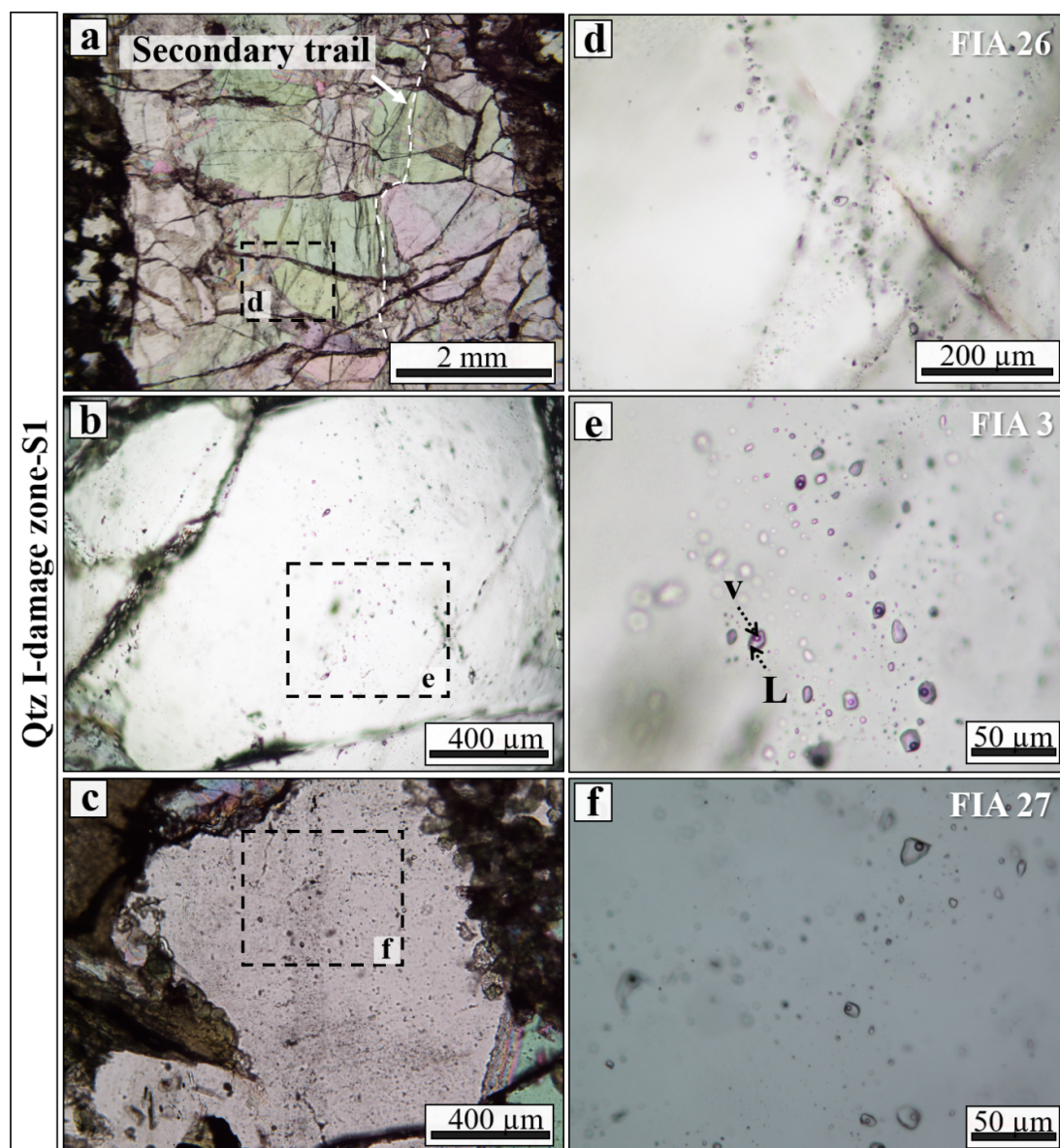
Figure 7.1. Representative textures of FIAs hosted within Qtz I from the damage zone (sample PH21) and most representative examples of Type S1 FIA. (a-c) Secondary trails crosscutting large Qtz I crystals of the damage zone. (d-f) Enlargements show the phase ratio details (FIA26, FIA3 and FIA27). North points up in all photographs.

Fluid inclusions are also found as isolated clusters inside intensely recrystallised quartz domains (Fig. 7.2a). FIAs inside these recrystallized quartz domains were pervasively obliterated during later episodes of ductile deformation. The development of WEBs, intercrystalline bands and bulging resulted in the remobilization (i.e., "transposition" sensu Anderson et al., 1990; Figs. 7.2a, c, d) of these assemblages. This is regularly observed and

is documented, for instance, by the presence of short, secondary trails of regularly shaped inclusion oriented at a high angle with respect to a longer, parent trail (Figs. 7.2a, c, d). Morphologically, these trails resemble the transposed trails documented in high-grade metamorphic rocks (Andersen et al., 1990; Van den Kerkhof et al., 2014).
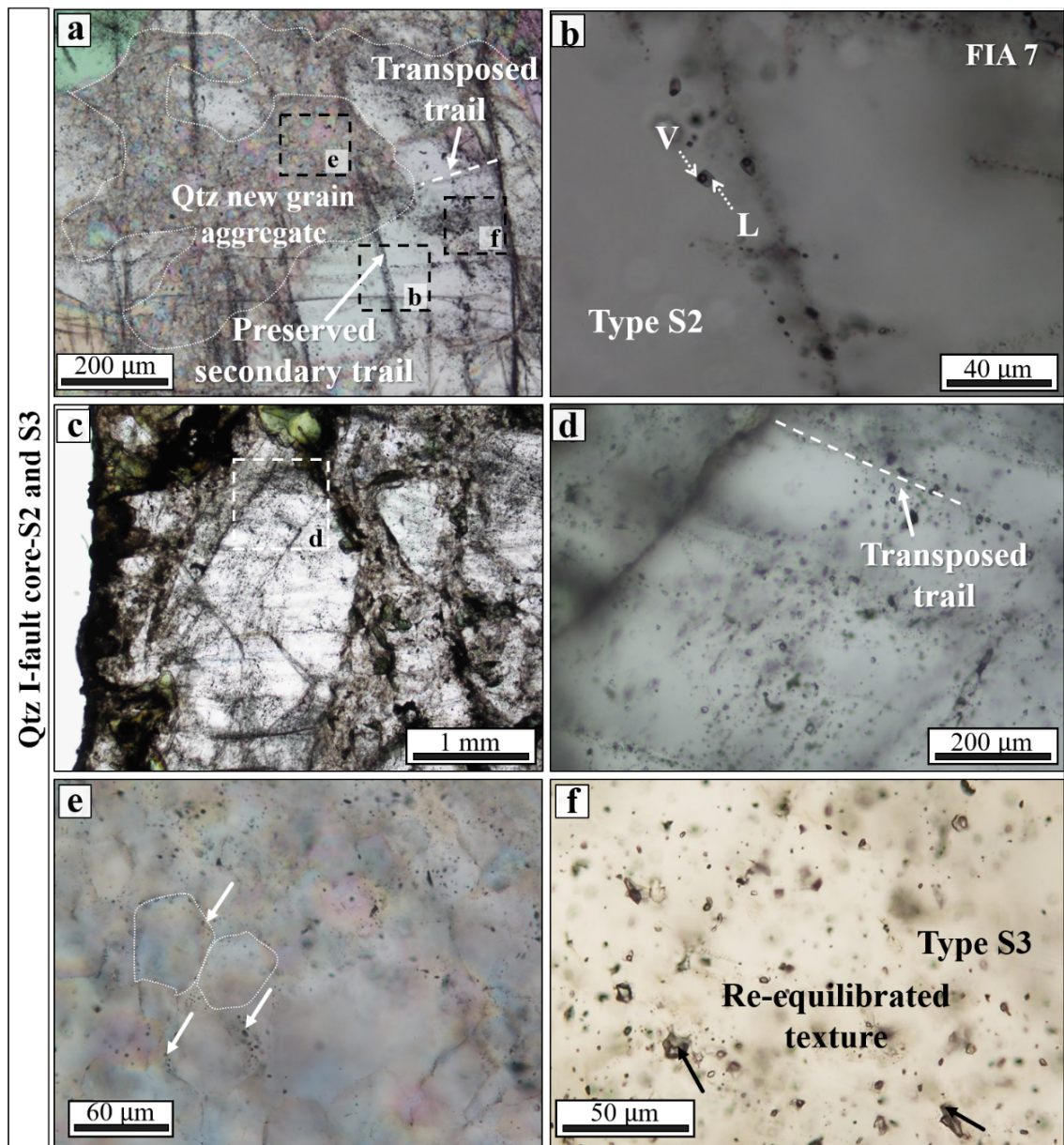
Figure 7.2. Representative textures of FIAs hosted within Qtz I from the fault core (sample TPH-120-4). (a) Long secondary transgranular trails dismembered by intercrystalline fractures, infilled by quartz new grains. (b) Detail of Type S2 FIA entrapped along a preserved secondary fracture. (c) Qtz I grains from the fault core locally host sets of short sub-trails developed at (d) high angle to the long trails (i.e. transposed trails). (e) Small fluid inclusions (<1µm) along the boundaries of new polygonal quartz crystals. (f) Example of Type S3 FIA as isolated clusters within the ductile fault core Qtz I. These trails formed during a brittle deformation stage that pre-dates ductile re-crystallization. North points up in all photographs.
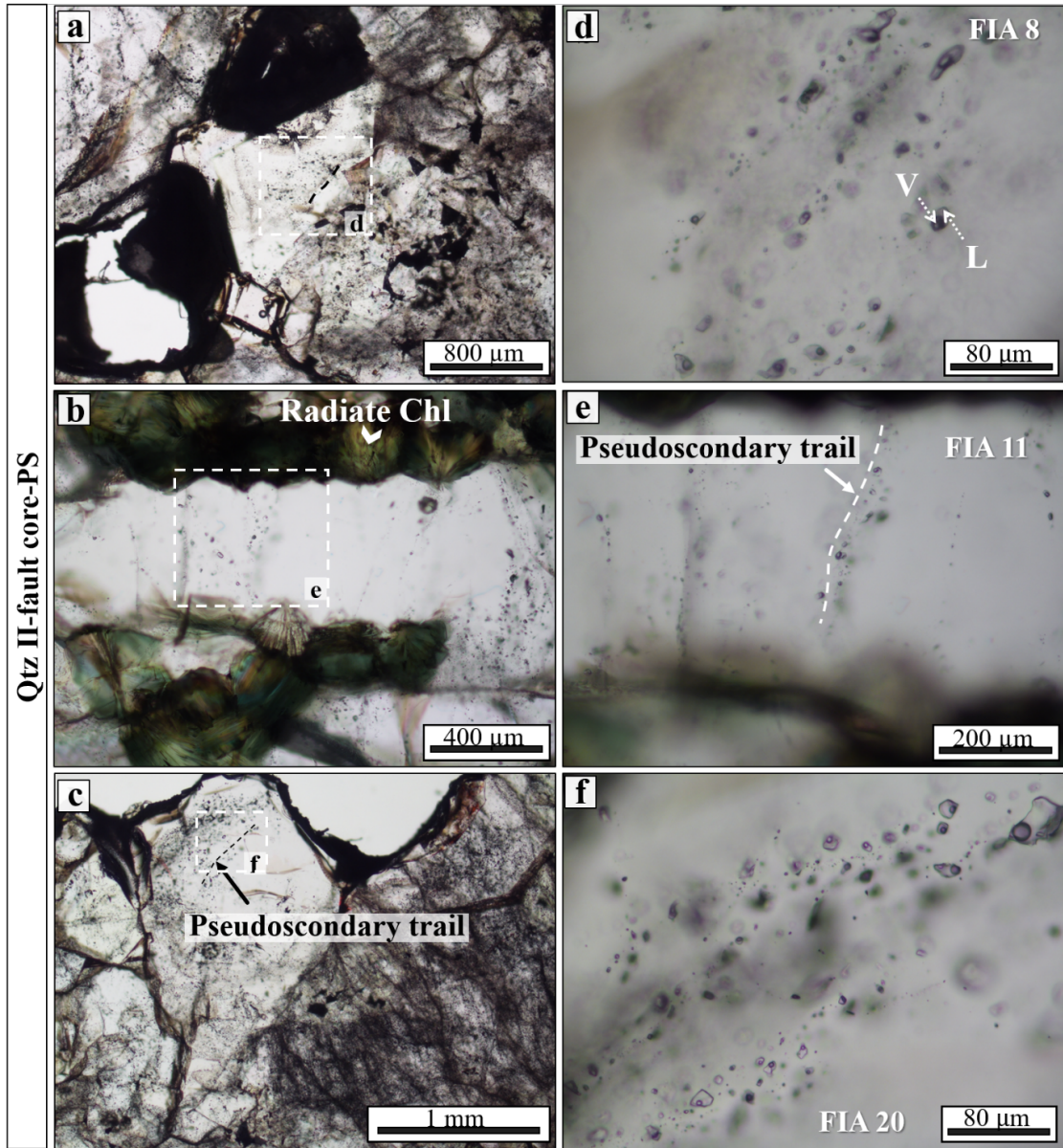
Figure 7.3. Representative textures of pseudosecondary FIAs hosted within Qtz II (samples TPH-120-4, TPH-120-6). (a-c) Pseudosecondary FIAs associated with Qtz II-chlorite (FIA8, FIA 11, FIA 20). (d-f) The enlargement shows the phase ratio details. North points up in all photographs.

Different types of fluid inclusion morphologies are found within the intensely recrystallized quartz domains. Negative crystal morphology is observed in some areas of the selected samples, but it is uncommon. More typical is instead the "dismembered" morphology (cf: Vityk and Bodnar, 1995; Tarantola et al., 2010), which is observed in the relatively large inclusions (> 20 μm). This morphology is made of a central (often empty) inclusion, showing several tails and re-entrants, surrounded by three-dimensional clusters of small "satellite" inclusions. These clusters might be arranged with a quasi-planar geometry inside the host (i.e. in a trail-like fashion). Another typical texture found in most assemblages is the "scalloped" morphology of small- to medium-sized inclusions (<10-15

μm), which is defined by the presence of indentations, embayments, irregularities, and sharp tips of the inclusion walls (Fig. 7.2f). FIAs corresponding to these petrographic features were grouped as Type S3.

Small inclusions (<1 μm) are also found at the edge of the straight, regular boundaries of new quartz grains; they are mostly dark, i.e. they are vapour-rich or empty, and are equant in shape (Fig. 7.2e). Although small inclusions do not allow a microtermometric study of the fluid-phase behaviour in this structural domain, they confirm the complex reactivation history of BFZ300.

Qtz II contains both pseudosecondary (Fig. 7.3) and secondary (Fig. 7.4) assemblages. The first type is arranged in trails that cut at low angle the hosting quartz (Figs. 7.3a-b) but not the neighbouring phases (e.g. chlorite; Figs. 7.3b, e). In these assemblages, FIs are relatively large (2-45 μm; Figs. 7.3d-f) and exhibit elongated shape and φ values between 15 and 30 % (Figs. 7.3d-f). FIAs corresponding to these petrographic features were grouped as Type PS.
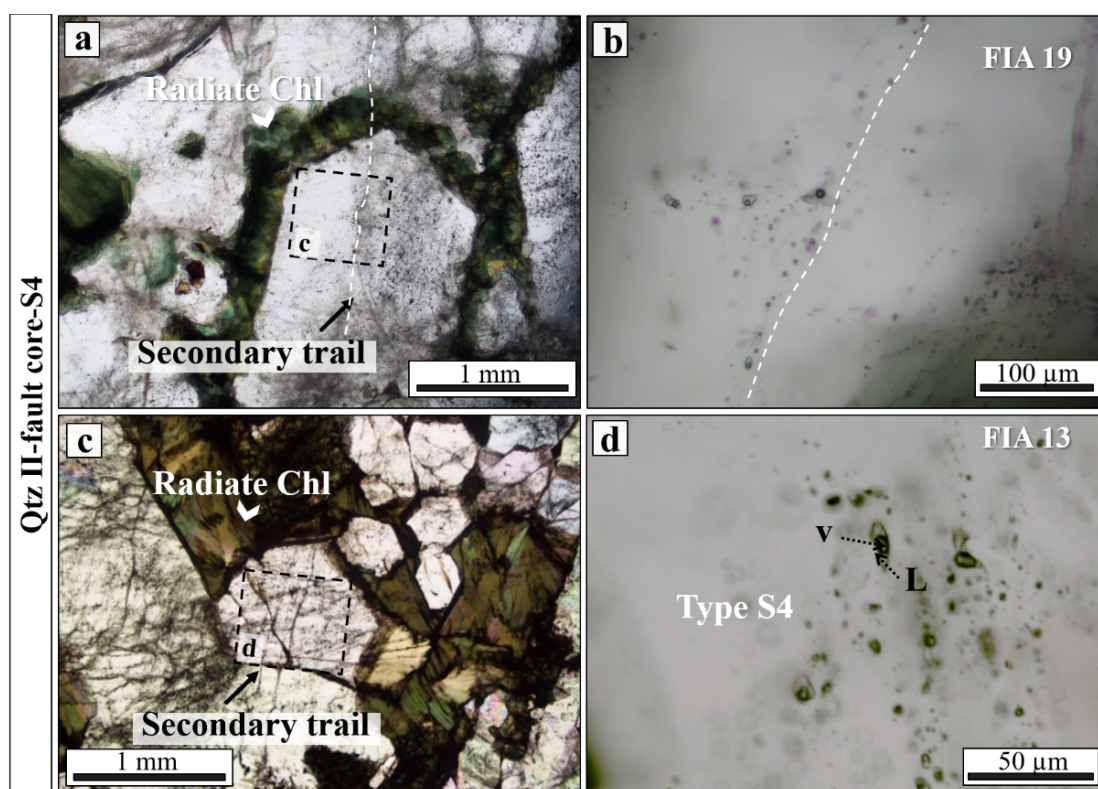
Figure 7.4. Representative textures of secondary FIAs hosted within Qtz II (sample TPH-120-4, TPH-120-6). (a) Transgranular secondary trails crosscutting the host quartz and the neighbouring radiate chlorite crystals. (b) Detail of secondary trail crosscutting euhedral Qtz II (FIA 19). (c) Small scale view of secondary FIAs crosscutting Qtz II. (d) Detail of secondary trails crosscutting euhedral Qtz II (FIA 13). North points up in all photographs.

FIAs within Qtz II are also arranged as transgranular trails cutting through largest crystals of Qtz II (Figs. 7.4a, c) and the neighbouring chlorite (Fig. 7.4a). They host two-phase inclusions whose size (5-35 µm; Figs. 7.4b, d) is similar to that of PS trails, but show a φ between 30 and 40 % (Figs. 7.4b, d). FIAs corresponding to these petrographic features were grouped as Type S4.

Primary FIAs are also present along growth planes of Qtz II, where they have a relatively large size (20-50 µm; Fig. 7.5). They present irregular and dismembered textures, which suggest intense post-entrapment re-equilibration.
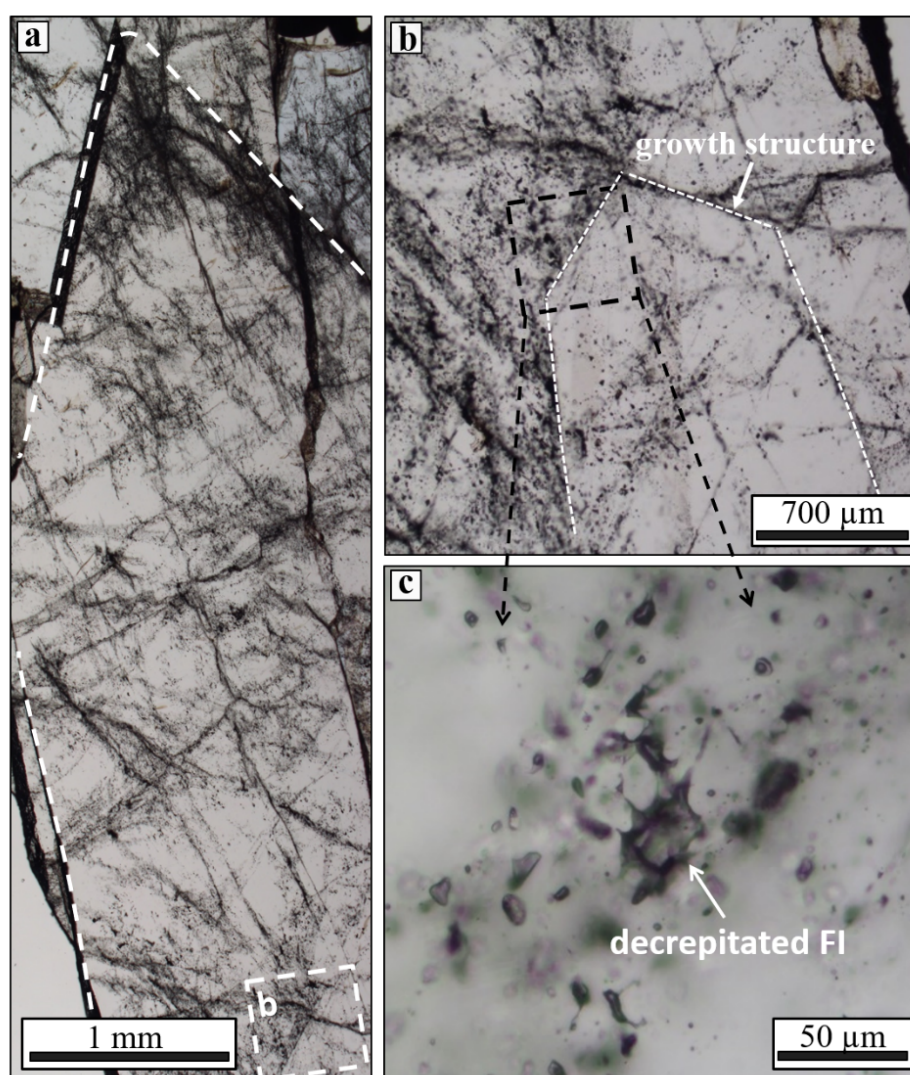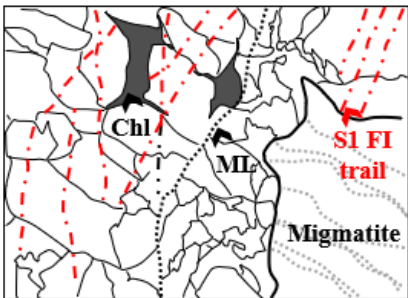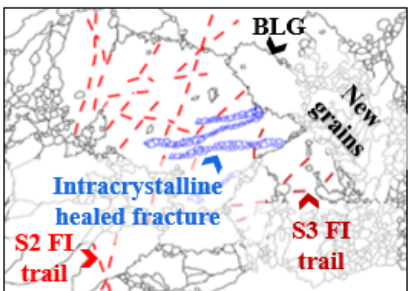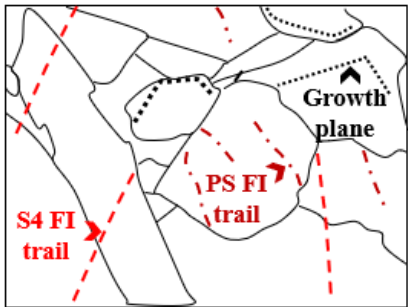
Figure 7.5. Petrographic relationships between fluid inclusions and Qtz II (sample TPH-120-6). a) Optically continuous, single crystal (highlighted). The white dashed square at the bottom right corner marks a possibly primary FIA entrapped during crystal growth. b) Enlargement of the growth structure. c) Enlargement of a portion of the primary growth zone, showing a re-equilibrated cluster of fluid inclusions along the primary growth zone. Note that the largest fluid inclusion is decrepitated and is surrounded by planes of tiny and irregular FIs (satellite inclusions). In the light of this structures, microthermometric estimations from this type of assemblages are excluded.

In summary, our microtextural study shows that the FIAs to be selected for the microthermometric study are only those hosted within Qtz I and Qtz II crystals with little to no recrystallization and whose inclusions have textures corresponding to the least intense post-entrapment re-equilibration (Bodnar, 2003b and references therein; Tarantola et al., 2010). These are the pseudosecondary and secondary FIAs in which dendritic or transposed inclusions are absent, and in which the host quartz exhibits only undulose extinction (S1, S2, S4 and PS). Table 1 provides a schematic representation of the location of the FI types, in addition to their location within the fault architecture.

Table 1. Schematic summary of main microstructures of quartz veins associated with BFZ300 and the fluid inclusion assemblages (FIAs) selected for microthermometric estimations.

Structural zone and sample	Qtz type	Deformation type	Microstructures	Studied FIAs
Damage zone (PH21)	Qtz I	Brittle/Ductile		FIA 3- TypeS1 FIA 4-Type S1 FIA 26-Type S1 FIA 27 Type S1
Fault core (TPH120-4A)	Qtz I	Cyclic Brittle/Ductile		FIA 1-Type S2 FIA 2-Type S2 FIA 5-Type S2 FIA 6-Type S2 FIA 7-Type S2 FIA 22-Type S2 FIA 23-Type S2 FIA 24-Type S2 FIA 25-Type S2
Fault core (TPH120-6) (TPH120-4)	Qtz II	Brittle		FIA 8-Type PS FIA 9-Type PS FIA 10-Type PS FIA 11-Type PS FIA 12-Type PS FIA 19-Type PS FIA 20-Type PS FIA 21-Type PS FIA 13- Type S4 FIA 14-Type S4 FIA 15-Type S4 FIA 16-Type S4 FIA 18-Type S4 FIA 19-Type S4

7.2 Microthermometry of fluid inclusions

In the selected samples, we studied 28 FIAs entrapped within the two distinct generations of quartz (Qtz I and Qtz II). We studied those FIAs that exhibits the least petrographic evidence of post-entrapment overprinting by later ductile and/or brittle deformation, which provided c. 800 microthermometric properties. Due to the well-documented tendency of fluid inclusions to modify their shape, volume, and composition after their initial entrapment even at low deviatoric stress conditions (e.g. Diamond et al., 2010; Kerrich, 1976; Tarantola et al., 2010; Wilkins and Barkas, 1978), working on FIAs that show the least possible degree of textural re-equilibration is essential when aiming at constraining the physical and chemical properties of the fluid(s) involved in the fault activity.

7.2.1 Damage zone

Secondary FIAs hosted within Qtz I from the damage zone (Type S1) show a range of Tm_{ice} between -5.9 and -0.1° C, which corresponds to a salinity of 0-9 wt% NaCleq (Fig. 7.6a). In these FIAs, final homogenization (Th_{tot}) occurs into the liquid phase (i.e. by disappearance of the vapour bubble) and mainly between 150-400° C (Fig. 7.6e).

7.2.2 Fault core

The secondary FIAs hosted within Qtz I in the fault core (Type S2) show a range of Tm_{ice} between -8.2 and -0.4° C, which corresponds to salinities between 0 and 14 wt% NaCleq (Fig. 10b), and final homogenization occurs into the liquid phase between 130 and 410° C (Fig. 10f).

Pseudosecondary FIAs entrapped within Qtz II (Type PS) show a range of Tm_{ice} between -13.6 and -0.1° C, which corresponds to a salinity range between 0 and 18 wt% NaCleq (Fig. 7.6c); final homogenization occurs into the liquid phase and is comprised between 150 and 440° C (Fig. 7.6g). Secondary FIAs in Qtz II (Type S4) show a range of Tm_{ice} between -11 and 0° C, which corresponds to a 0-15 wt% NaCleq range of salinity (Fig. 7.6d), while final homogenization into the liquid phase is comprised between 130 and 430° C (Fig. 10h).

FI microthermometric properties are also presented as Homogenization temperature vs. Salinity plots (e.g. Yang et al., 2005) to identify possible correlations between temperature and salinity. In accordance with the overall structure of the study, data are presented for each structural domain (Fig. 7.7). Data are scattered, also within cogenetic fluid inclusions belonging to the same FIA. No clear relationships between salinities and homogenization

temperatures are obvious. These plots are of difficult interpretation and reflect the post-entrapment modifications as clearly highlighted by the frequency diagrams in Fig. 7.6.
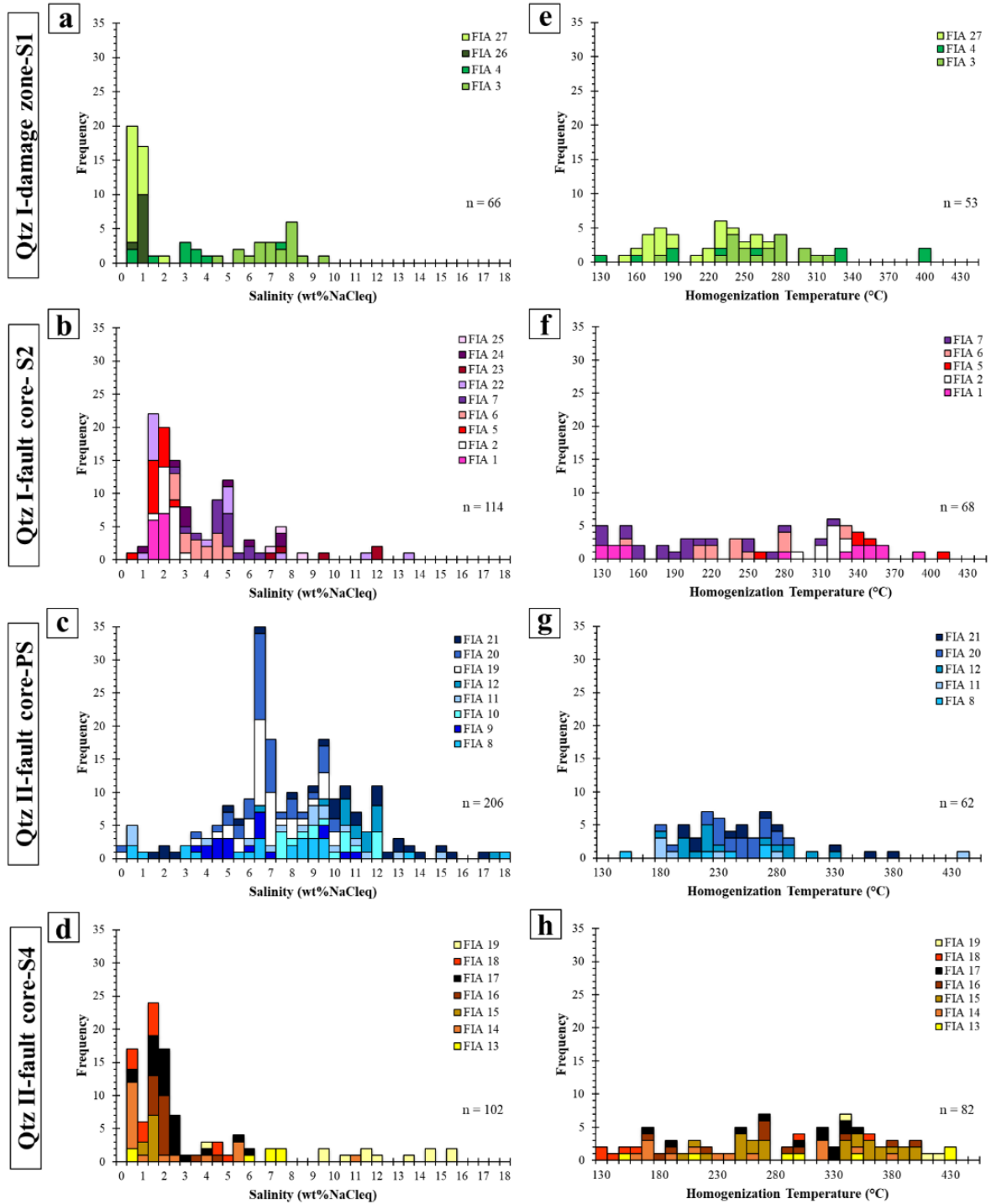
Figure 7.6. Microthermometric data of the studied FIAs. Panels a-d show the bulk salinities of individual FIAs calculated from the Tm_{ice} data, while panels e-h refer to the temperatures of final homogenization of the same assemblages. Notice that the data report the properties of individual FIAs according to their occurrence within Qtz I of the damage zone, Qtz I from the fault core, and Qtz II from the fault core. Notice that pseudosecondary (PS) and secondary (S) FIAs identify progressive later stages of fluid entrapment, and can be used to constrain the fluid properties in the fault zone. Notice also that the measured ranges of Th_{tot} spread

70

across T intervals that are too large to represent entrapment at equilibrium (e.g., FIA7 of Qtz I from fault core: 130-320° C), which suggests post-entrapment re-equilibration of the inclusions. Fluid bulk composition is expressed as salinity, which is conventionally reported as weight percent of NaCl equivalents (wt% NaCleq, Roedder,1984).

Figure 7.7. Homogenization Temperature vs. Salinity plots for fluid inclusions types identified in each structural domain: a) Qtz I-damage 29 zone; b) Qtz I-fault core; c) Pseudosecondary FI in Qtz II-fault core; d) secondary FI entrapped within Qtz II vein. These plots are used to estimate the most probable composition of the fluids.

7.3 Micro-Raman analysis

As no gases were determined during the microthermometric analysis (i.e. melting of carbonic phase and/or clathrate hydrates were not detected during the freezing experiments), additional micro Raman analysis was performed on a set of representative FIAs (samples: TPH-120-4; TPH-120-6; PH21; PH22), in order to detect other possible molecular species dissolved in low concentration in the fluids. Raman analysis indicates that few fluid inclusions hosted both by the Qtz I and Qtz II from the fault core show a very weak CH_4 signal in addition to the expected and dominant H_2O signal. Additionally, very few analysed FI of only one sample of the fault core (TPH-120-4, Fig. 7.8) showed a very weak CO_2 signal. An example of the data collected from FIAs hosted within sample TPH-120-4, FIA7 is schematically reported in Fig. 7.8.

In spite of their spectroscopic detection, CO$_2$- and CH$_4$-bearing inclusions are not systematically associated with specific quartz vein generations or microstructures (i.e. intracrystalline healed cracks, WEB's planes, intercrystalline fractures). We could not, therefore, associate the presence of CO$_2$ and/or CH$_4$ with any specific deformation stage of the fault. In a more probable scenario, the limited presence of CO$_2$ and CH$_4$ in only few inclusions is likely due to their presence in low concentration in the system during the fluid trapping.

The obtained spectroscopic determinations are consistent with the documented lack of microthermometric evidence of a carbonic phase or clathrate hydrates during the freezing experiments (cf. Rosso and Bodnar, 1995; Dubessy et al., 2001). The impossibility to detect CO$_2$- and CH$_4$-bearing fluids during the freezing experiments indicate a gas pressure that is systematically lower than that required to observe clathrate dissociation (e.g., 1.4 MPa in CO$_2$-H$_2$O fluids, Rosso and Bodnar, 1995), i.e. it shows low gas concentrations. As a consequence, we have modelled the fluid phases as simple H$_2$O-NaCl systems.
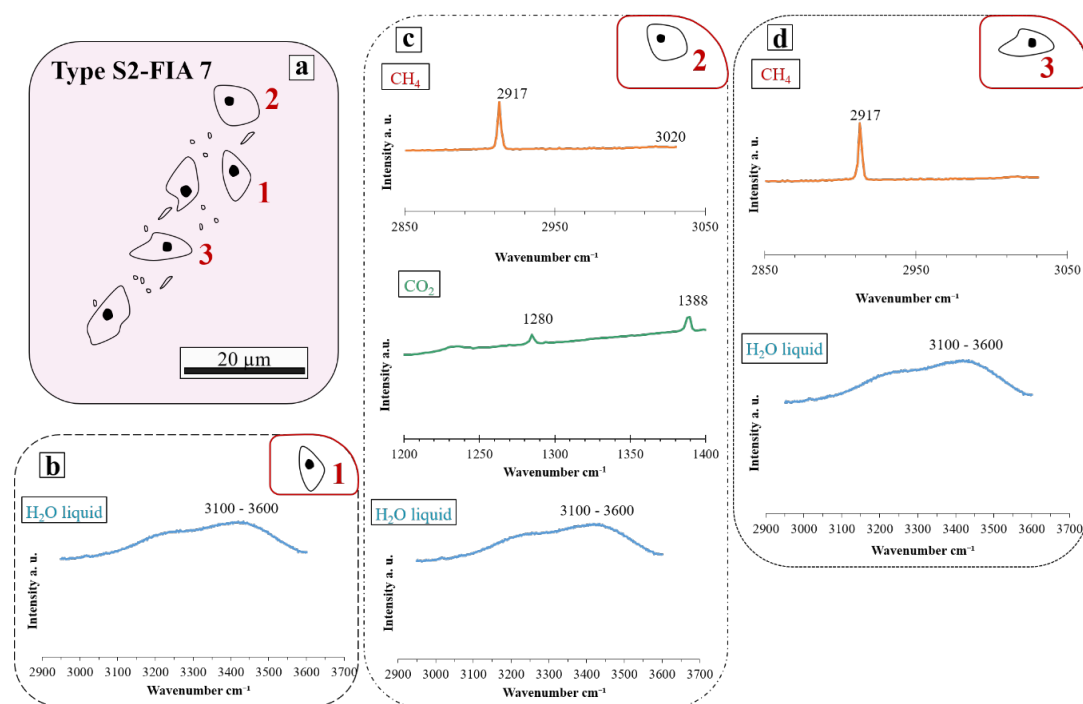
Figure 7.8. Micro-Raman spectra collected from a representative FIA hosted in Qtz I from the fault core (FIA 7). (a) Based on its petrographic analysis, FIA 7 is interpreted as a secondary trail of fluid inclusions and despite their cogenetic nature, micro-Raman spectra collected from three distinct fluid inclusions do not show coherent signals of vapour bubble compositions. (b) Raman signal acquired from a first FI showing a peak at the characteristic wavenumber range of H$_2$O (3100-3600 cm^{-1}) within the vapour bubble. (c) FI 2 exhibits instead three distinct peaks at the characteristic wavenumber of CH$_4$ (2917 cm^{-1}), CO$_2$ (1280-1388 cm^{-1}) and H$_2$O (3100-3600 cm^{-1}). (c) FI 3 exhibits signals of the characteristic wavenumber of CH$_4$ (2917 cm^{-1}) and liquid H$_2$O (3100-3600 cm^{-1}).

Chapter 8. Mineral chemistry and geothermometric constraints on synkinematic and authigenic BFZ300 minerals

8.1 Chlorite chemical composition and quartz-chlorite geothermometer

Chlorite composition has been determined using EMPA (Table 2) for several generations of chlorites found in association with Qtz I and II (Fig. 8.1a). Microstructural and petrographic analysis permitted the identification of the following chlorite textural types, each of which was microprobed: (1) vermicular chlorite associated with Qtz I from the damage zone (Fig. 8.1b); (2) vermicular and radiate chlorite associated with Qtz I from the fault core (Figs. 8.1c-d), and (3) radiate chlorite associated with Qtz II from the fault core (Fig. 8.1e). For the detailed petrographic description of these chlorite textures as documented within the distinct structural domains of BFZ300 the reader is referred to Chapter 6. The structural formula of chlorite was calculated based on 14 oxygens, and representative compositions are shown in Table 2. The complete chlorite dataset is reported in Appendix B.

Chlorite compositions are also shown in Figure 8.2a and are expressed as function of the Fe/(Fe+Mg) ratio (XFe) and Si content. Chlorite compositional data are presented in the figure according to the structural domain of the fault they are associated with and to the corresponding texture. Vermicular chlorite associated with Qtz I in the damage zone has a XFe ranging between 0.50 and 0.55, while vermicular chlorite associated with Qtz I from the fault core has a XFe of 0.53. Radiate chlorite associated with Qtz I from the fault core has a XFe ranging between 0.71 and 0.81 while that of radiate chlorite associated with Qtz II from the fault core varies between 0.65 and 0.80, thus constraining compositions within the ripidolite and aphrosiderite end-members (Fig. 8.2a).

Temperature-composition relationships for the quartz-chlorite pair portrayed in the T-R^{2+}–Si diagram of Bourdelle and Cathelineau (2015) show that, in the hypothesis of quartz-chlorite equilibrium, the precipitation of vermicular chlorite together with Qtz I took place in the damage zone in the 175-240° C range (green diamonds of Fig. 8.2b). This range is distinct from the temperature estimated from vermicular and radiate chlorite from Qtz I in the fault core, which is about 350° C. A better resolution is not possible because the measured R^{2+}–Si compositional parameters (R^{2+} = Mg+Fe) plot at the edge of, or even slightly outside, the calibrated region of the Bourdelle and Cathelineau plot (red diamonds of Fig. 8.2b). We

Table 2: Chlorite EMPA data from different BFZ300 structural domains.

Sample	4A	4A	4A	4A	4A	4A	PH21	PH21	PH21	2	2	2	6	6	6	6
Structural zone	FC	FC	FC	FC	FC	FC	DZ	DZ	DZ	DZ	DZ	DZ	FC	FC	FC	FC
Quartz type	Qtz I	Qtz I	Qtz I	Qtz I	Qtz I	Qtz I	Qtz I	Qtz I	Qtz I	Qtz I	Qtz I	Qtz I	Qtz II	Qtz II	Qtz II	Qtz II
Textural type	Verm	Verm	Verm	Rad	Rad	Rad	Verm	Verm	Verm	Verm	Verm	Verm	Rad	Rad	Rad	Rad
Na_2O	0.04	0.07	0.00	0.08	0.08	0.03	0.05	0.02	0.04	0.03	0.01	0.05	0.04	0.06	0.01	0.01
TiO_2	0.02	0.01	0.00	0.00	0.03	0.01	0.09	0.04	0.01	0.01	0.01	0.03	0.03	0.03	0.04	0.13
MnO	0.59	0.65	0.62	0.53	0.56	0.48	0.24	0.24	0.30	0.48	0.37	0.43	0.64	0.57	0.71	0.60
K_2O	0.06	0.02	0.04	0.07	0.06	0.04	0.01	0.01	0.03	0.10	0.05	0.07	0.03	0.02	0.05	0.01
MgO	13.66	13.79	13.74	6.61	5.13	6.75	13.95	14.06	13.29	12.85	12.57	12.59	4.85	4.87	8.73	8.05
SiO_2	25.49	26.00	25.83	23.62	22.89	23.91	27.24	27.02	27.49	27.43	27.88	27.79	25.63	25.64	26.5	26.13
Cr_2O_3	0.00	0.01	0.04	0.00	0.00	0.06	0.04	0.03	0.06	0	0.06	0.01	0	0.02	0.01	0
FeO	27.86	27.74	27.87	36.61	38.49	36.75	24.68	25.21	26.07	25.97	26.06	25.77	34.26	33.84	30.08	30.47
CaO	0.03	0.04	0.05	0.00	0.06	0.03	0.01	0.02	0	0.05	0.05	0.03	0.01	0.04	0.04	0.02
Al_2O_3	22.04	22.13	22.00	22.89	23.35	22.98	24.13	24.75	24.91	24.02	23.48	23.21	24.23	24.64	24.49	25.02
Cl	0.00	0.00	0.01	0.03	0.02	0.04	0.01	0	0	0.01	0	0	0.03	0.02	0.02	0.01
Total	89.78	90.45	90.20	90.44	90.67	91.09	90.69	91.42	92.23	91.12	90.81	90.08	89.82	89.94	90.78	90.48
No. ions in formula based on 28 (O,OH)																
Na	0.02	0.03	0	0.03	0.03	0.01	0.02	0.01	0.01	0.01	0.01	0.02	0.02	0.03	0	0.01
Ti	0	0	0	0	0	0	0.01	0.01	0	0	0.01	0	0.01	0.0	0.01	0.02
Mn	0.10	0.11	0.11	0.10	0.10	0.09	0.04	0.04	0.05	0.08	0.06	0.07	0.12	0.10	0.12	0.11
K	0.01	0	0.01	0.02	0.02	0.01	0	0	0.01	0.02	0.01	0.02	0.01	0	0.01	0
Mg	4.25	4.25	4.25	2.14	1.68	2.17	4.18	4.19	3.93	3.86	3.79	3.82	1.55	1.55	2.69	2.49
Si	5.32	5.37	5.36	5.14	5.02	5.15	5.48	5.40	5.46	5.53	5.64	5.66	5.49	5.47	5.48	5.43
Cr	0	0	0.01	0	0	0.01	0.01	0	0.01	0	0.01	0	0	0	0	0
Fe^{2+}	4.86	4.79	4.83	6.66	7.06	6.62	4.15	4.21	4.33	4.38	4.40	4.39	6.14	6.04	5.20	5.29
Ca	0.01	0.01	0.01	0	0.01	0.01	0	0	0	0.01	0.01	0.01	0	0.01	0.01	0
Al	5.42	5.39	5.38	5.86	6.04	5.84	5.72	5.83	5.83	5.71	5.59	5.57	6.12	6.20	5.97	6.13
Cl	0	0	0	0.01	0.01	0.01	0	0	0	0	0	0	0.01	0.01	0.01	0
Fe	4.86	4.79	4.83	6.66	7.06	6.62	4.15	4.21	4.33	4.38	4.40	4.39	6.14	6.04	5.20	5.29
Al Tetr	2.68	2.63	2.64	2.86	2.98	2.85	2.52	2.60	2.54	2.47	2.37	2.34	2.51	2.53	2.52	2.57
Al Oct	2.73	2.76	2.73	3.00	3.06	2.99	3.20	3.22	3.29	3.24	3.23	3.23	3.61	3.67	3.45	3.56
Fe/(Fe+Mg)	0.53	0.53	0.53	0.76	0.81	0.75	0.50	0.50	0.52	0.53	0.54	0.53	0.80	0.79	0.66	0.68
Based on 28 (O,OH)																
R^{2+}	9.11	9.04	9.08	8.80	8.74	8.79	8.33	8.40	8.26	8.24	8.19	8.21	7.69	7.59	7.90	7.79
Si	5.32	5.37	5.36	5.14	5.02	5.15	5.48	5.40	5.46	5.53	5.64	5.66	5.49	5.47	5.48	5.43
Based on 14 (O,OH)																
R^{2+}	4.55	4.52	4.54	4.40	4.37	4.40	4.17	4.20	4.13	4.12	4.10	4.10	3.84	3.79	3.95	3.89
Si	2.66	2.68	2.68	2.57	2.51	2.58	2.74	2.70	2.73	2.77	2.82	2.83	2.75	2.74	2.74	2.71

note, however, that the high-T chlorite data plot parallel to the 350° C isotherm, suggesting that it precipitated most probably at that temperature or not too far from it. Radiate chlorite associated with Qtz II from the fault core is instead compatible with an equilibrium precipitation at 160-220° C (light-blue diamonds in Fig. 8.2b).
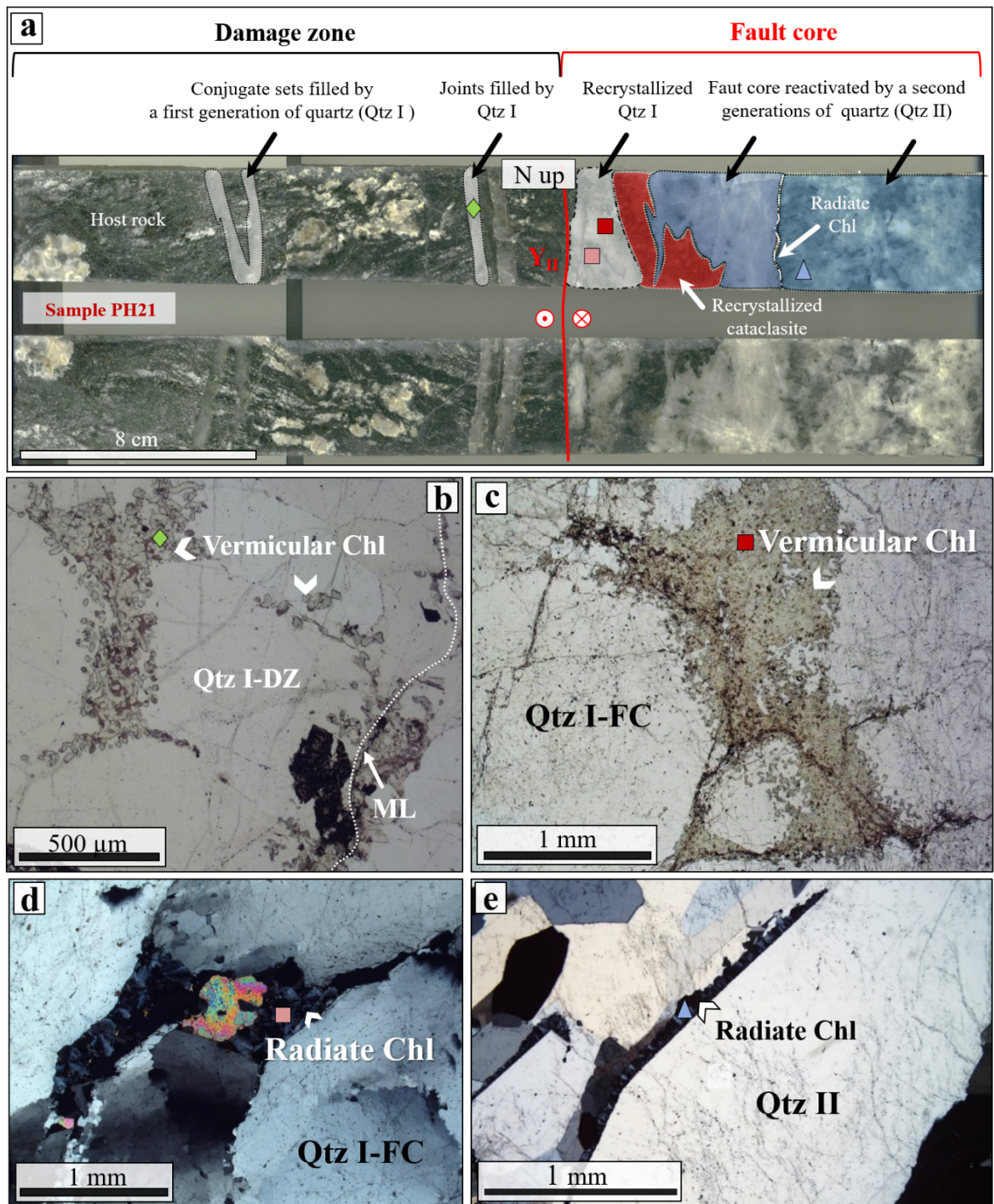
Figure 8.1 Overview of the generations of chlorite identified in the studied samples and their relationships to the structural domains of BFZ300 with which they are associated. (a) Logging of drill core PH21 reveals that BFZ300 is composed of three distinct structural domains and supports field observations: 1) the damage zone, which is characterized by Qtz I-filled conjugate sets of fractures and joints crosscutting the migmatitic host rock; 2) the fault core, which is characterized by the recrystallized Qtz I vein and also contains 3) the Qtz II vein. Chlorite exhibits (b) a vermicular texture in association with Qtz I from the damage zone, (c) vermicular and radiate (d) textures in association with Qtz I from the fault core. (e) Radiate chlorite is instead invariably found within Qtz II. Green diamond, pink and red squares and light-blue triangle indicate the location of the different generations of chlorite with the fault architecture.

75
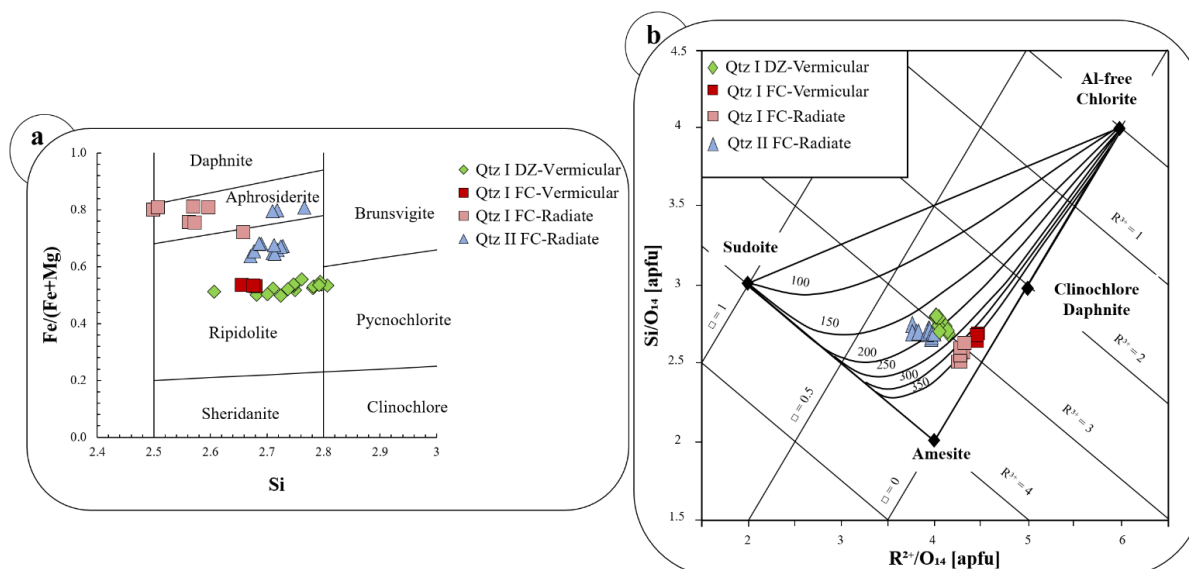
Figure 8.2. Chlorite chemical composition diagram and mineral-pair geothermometry applied to assemblages of Qtz I- and Qtz II veins. (a) Green, red, pink and light blue symbols indicate distinct chlorite textures in association with Qtz I and Qtz II veins and their related compositions. The chlorite compositional diagram is based on Hey (1954). (b) Chlorite-quartz crystallization temperatures estimated using the method of Bourdelle and Cathelineau (2015). The maximum temperature is from the Qtz I-chlorite pair from the fault core.

8.2 Chlorite elemental imaging

Further analyses on synkinematic chlorites were carried out to investigate in detail the chemical composition of the fluids that repeatedly ingressed the BFZ300 fault zone. An area of 200 x 200 μm containing a ripidolite-type vermicular chlorite associated with Qtz I from the fault core (Fig. 8.1c and 8.2a) and a second area of 500 x 500 μm with radiate chlorite with composition between the ripidolite and aphrosiderite end-members associated with Qtz II (Fig. 8.1e and 8.2a) were selected to study the chemical composition of fluids leading to crystallization of these synkinematic chlorite types. The selected areas were analysed with LA-ICP-TOFMS and the semi-quantitative elemental images are presented herein.

LA-ICP-TOFMS analyses were performed on aggregates of chlorite crystals instead of individual crystals to produce a reliable statistical dataset and to evaluate if there are chemical heterogeneities within the analysed samples. Figures 8.4 and 8.5 report a selection of element distribution maps acquired from the analysis of vermicular and radiate chlorite, respectively. The selection of the maps was carried out taking in consideration only those chemical elements that show depletion and/or enrichment between the two distinct generation of chlorites (i.e. Mg, Al, Sc, Ti, V, Mn, Fe, Ni, Co, Ga and Sr) to create a semi-quantitative chemical comparison between the two chlorites.
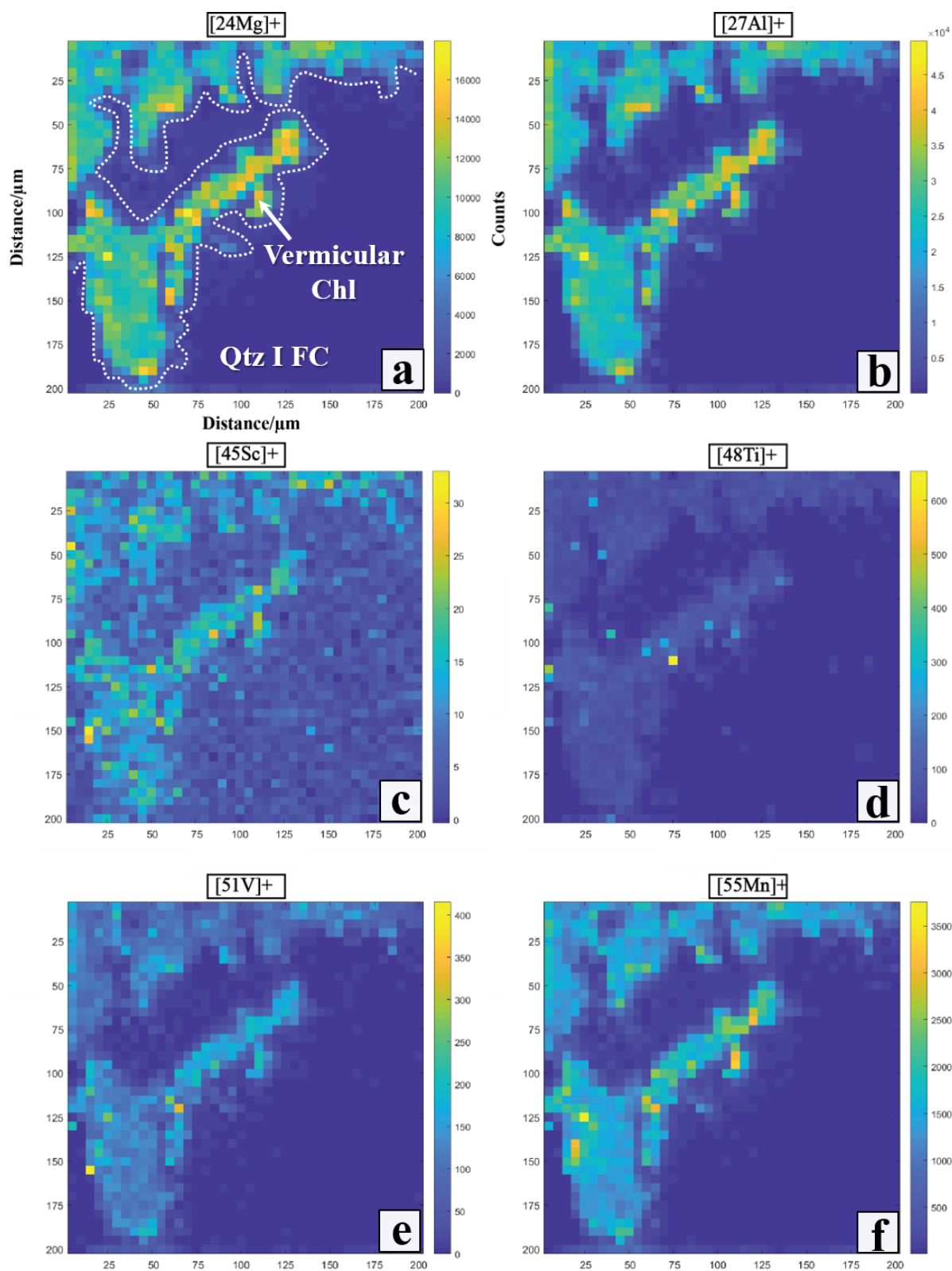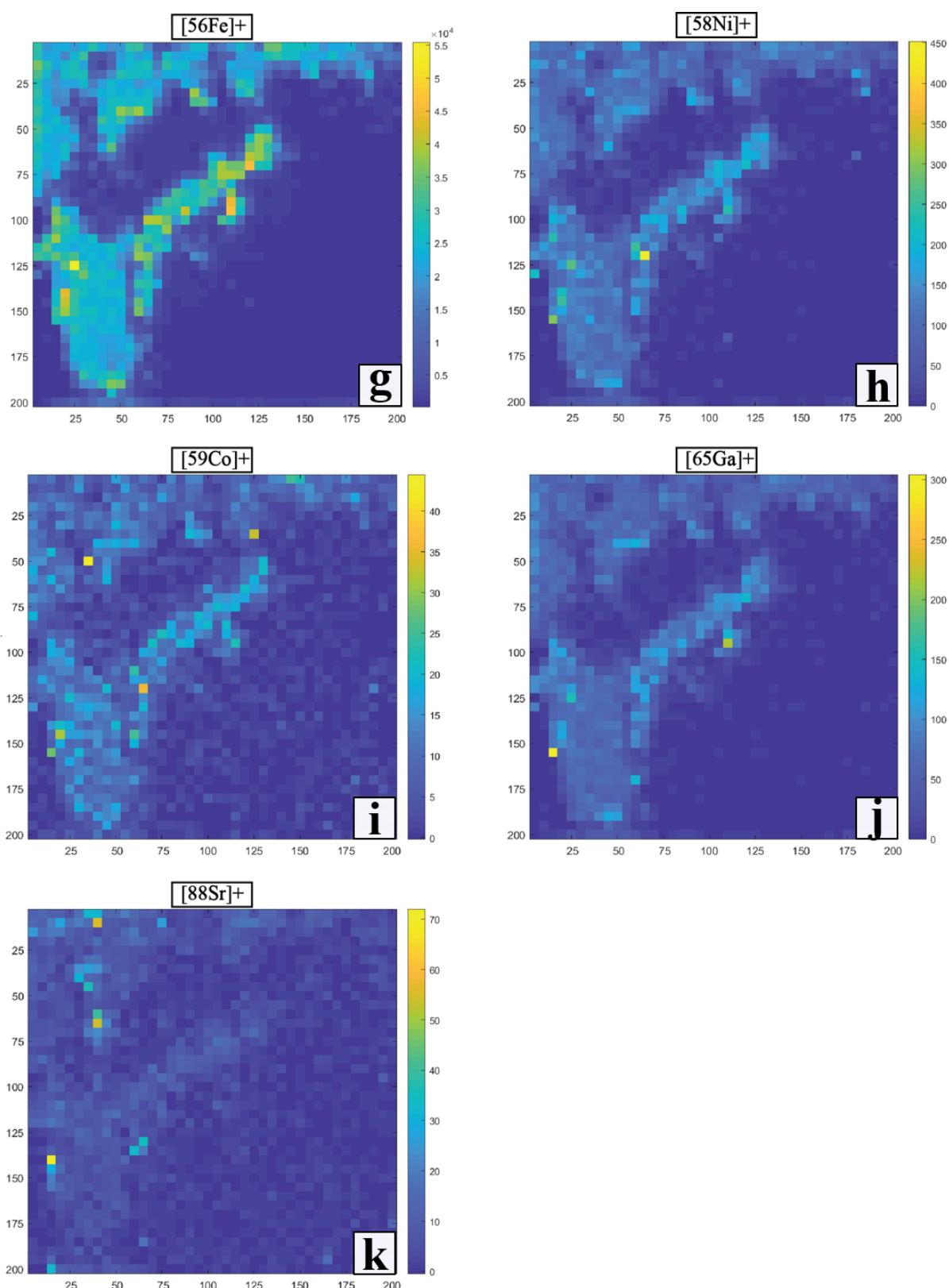
Figure 8.3. LA-ICP-TOFMS element imaging obtained from spot analysis of vermicular chlorite crystals associated with Qtz I from the fault core. (a-k) Chemical maps show qualitative elemental distribution of major and trace elements within the analysed area. The colour-coded scale is related to the intensity of the signal for each element. The signal intensity is given in counts per second while the analysed area is given in μm.
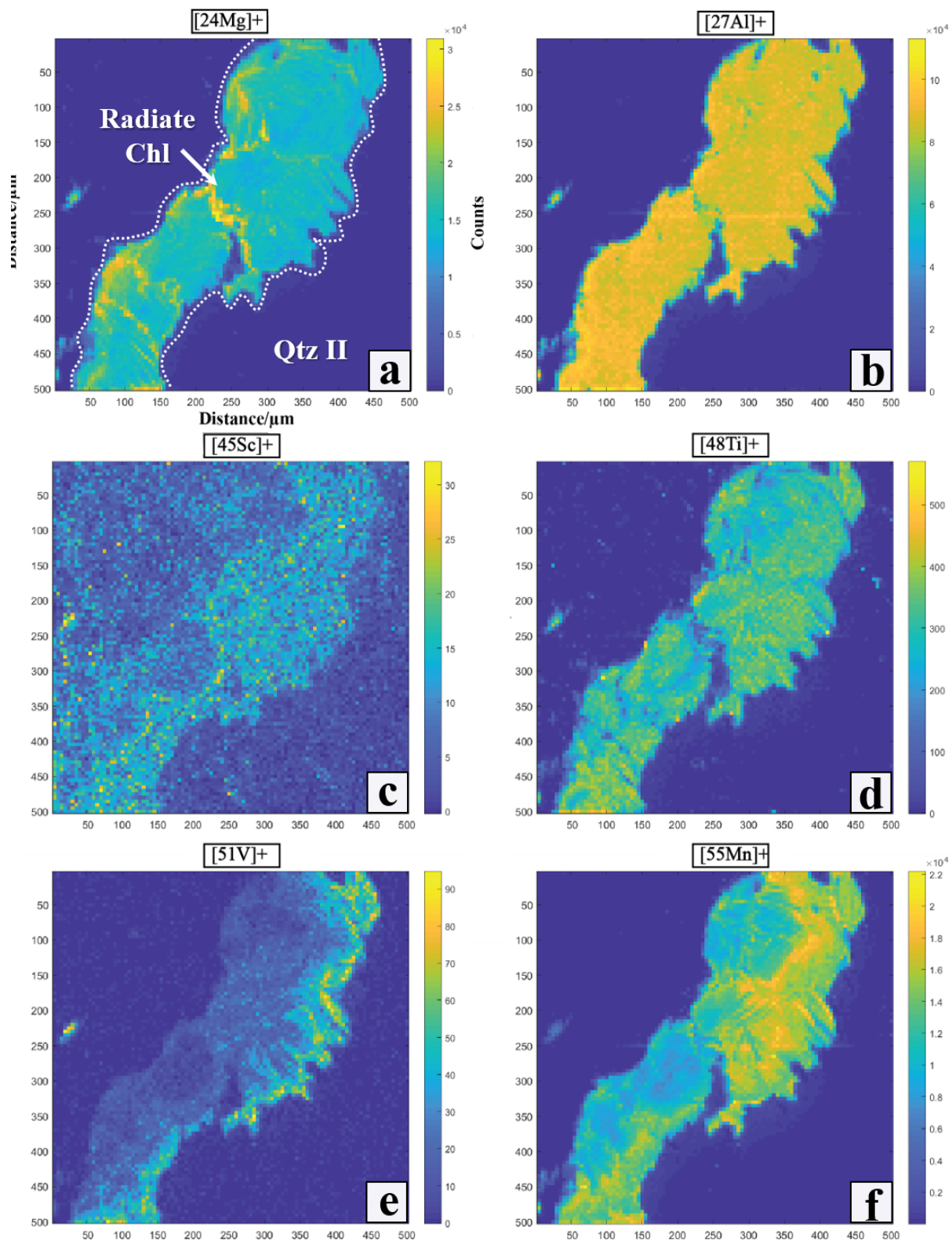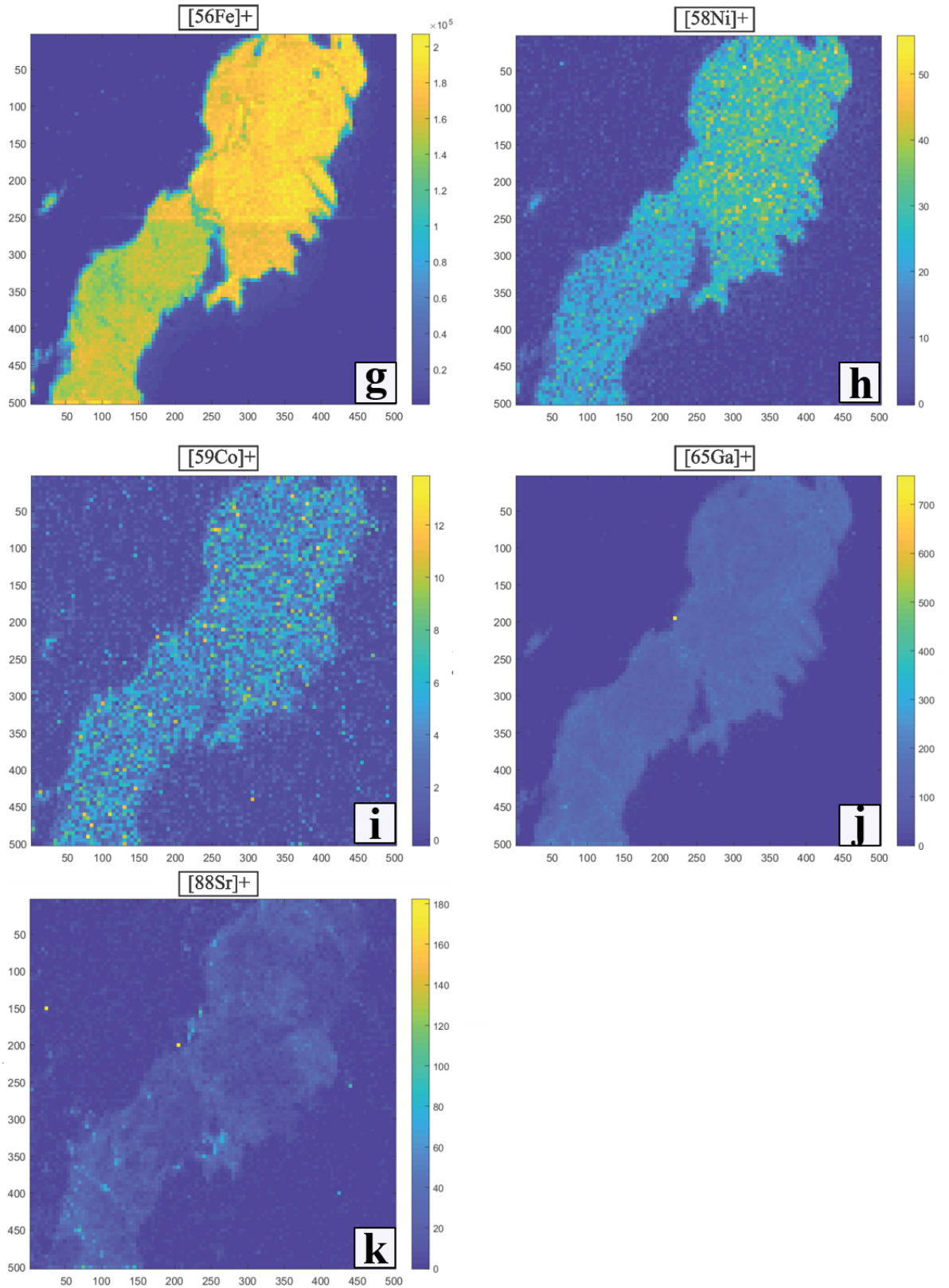
Figure 8.4. LA-ICP-TOFMS element imaging obtained from spot analysis of radiate chlorite associated with Qtz II. (a-k) Chemical maps show qualitative elemental distribution of major and trace elements within the analysed area. The colour-coded scale is related to the intensity of the signal for each element. The signal intensity is given in counts per second while the analysed area is given in μm.

Element concentrations are shown in the chemical maps as counts per second, whereby the higher counts are related to a higher signal and presumably a higher concentration of the measured specific element. High counts in the elemental maps are identified from shades of colour between dark green and yellow, following the colour key bar reported in Figs. 8.3 and 8.4. Low counts are instead given by shades of colour between dark blue and light blue (Figs. 8.3 and 8.4).

Map analysis reveals that major Mg, Al, Mn and Fe are major elements within the studied BFZ300 chlorites, and that Sc, Ti, V, Ni, Co, Ga and Sr are instead present as trace elements (Figs. 8.3 and 8.4). Moreover, vermicular and radiate chlorite aggregates are characterized by specific elemental spatial distributions that defined clear chemical spatial patterns. Indeed, the chemical distribution of Mg, Al, Mn and Fe within the studied aggregates of vermicular chlorite (shown as [24Mg]+, [27Al]+, [55Mn]+ and [56Fe]+) shows that elements are not homogenously or randomly distributed within the aggregates but are instead concentrated along the outermost boundary of the aggregate, forming a chemically distinct volume (Fig. 8.3 panels a, b, f, g). LA-ICP-TOFMS analysis indicates that the distribution of Sc, V, Ni, Ni, Co and Ga ([45Sc]+, [51V]+, [58Ni]+, [59Co]+ and [65Ga]+) within vermicular chlorite is also characterized by an enrichment along the same external boundary, mirroring the chemical distribution of the major elements (Fig. 8.3 panels c, e, h, i, j). The signal of Ti and Sr ([48Ti]+ and [88Sr]+) shows, instead, an homogeneous distribution and no visible chemical spatial patterns are obvious (Fig. 8.3 panels d, k).

LA-ICP-TOFMS analysis of the aggregates of radiate chlorite (Fig. 8.4) reveals a completely different elemental distribution pattern for the same selection of elements (i.e. Mg, Al, Sc, Ti, V, Mn, Fe, Ni, Co, Ga, Sr). In particular, the spatial distribution of Al and Fe (Fig. 8.4 panels b, g) shows that Al and Fe are overall homogenously distributed within the mapped chlorite aggregate with a constant high cps signal. On the contrary, the imaging of Mg distribution (Fig. 8.4 panel a) reveals an heterogeneous spatial distribution of this element.

The most intense signal was acquired from the left, outermost part of the ablated chlorite aggregate, from along some internal structural discontinuities (here interpreted as healed fractures or lattice kinks). Else, the elemental distribution maps of V and Mn (Fig. 8.4, panels e, f) show similar chemical spatial distribution patterns. V and Mg are both concentrated within the right, outermost domain of the aggregate, mimicking a chemical zonation similar to that characteristic of primary growth structures. The distribution of the Sc, Ni and Co signals (Fig. 8.4, panels c, h, i) are quite heterogenous and does not define

clear chemical spatial patterns. The elemental distribution of Ti (Fig. 8.4, panel d) indicates a generally high Ti content within the analysed aggregate. The Ga and Sr elemental maps (Fig. 8.4, panels j, k) exhibit a very low signal across the entire analysed area, even though some internal patterns associated with tiny intracrystalline fractures are defined by relatively higher concentrations.

In summary, the two comprehensive datasets show that Mg, Al, Sc, Ti, V, Mn, Fe, Ni, Co, Ga, Sr have a different concentration and distribution pattern within the aggregates of ripidolitic vermicular chlorite associated with Qtz I from the fault core and aggregates of radiate chlorite of ripidolotic to aphrosideritic composition associated with Qtz II.

8.3 Sphalerite-stannite geothermometer

Sulphides are present as minor phases within the Qtz II vein (Figs. 6.5 and 8.4a). The collected EMPA data show that the sulphides associated with Qtz II have compositions that approach those of pure phases (Table 3). Pyrite has trace element concentrations (Cu, As, Pb, Ni, Zn) that are in general below the EMPA detection limit, while galena, sphalerite, and chalcopyrite show only some significant contents of Fe and Zn (e.g., Fe: 0.22-1.00 wt% in galena; Zn: 0.11-3.95 wt% in chalcopyrite). Pyrite and sphalerite from the Qtz II veins (Fig. 6.5e) have trace element concentrations that are, again, mostly below detection limits.

Figure 8.4. (a) Reflected-light photomicrograph showing anhedral to subhedral pyrite, chalcopyrite, stannite, and sphalerite arranged along the stylolite as residual products of pressure solution. (b) Reflected-light

Table 3: Representative EMPA of sulphides associated with Qtz II

Analysis	Structural zone	Qtz type	Mineral	S	Fe	Cu	As	Pb	Ni	Zn	Ti	Sn	Total
TPH120-6-14	Core	II	pyrite	55.02	47.50	0.01	0.00	0.00	0.02	0.00	0.00		102.55
TPH120-6-17	Core	II	pyrite	54.08	47.19	0.00	0.01	0.00	0.00	0.00	0.00		101.28
TPH120-6-18	Core	II	sphalerite	34.46	6.46	0.09	0.01	0.00	0.03	59.62	0.02		100.69
TPH120-6-19	Core	II	sphalerite	34.48	6.24	0.08	0.06	0.00	0.04	59.61	0.02		100.53
TPH120-4A-34	Core	II	pyrite	54.49	47.40	0.05	0.00	0.00	0.00	0.00	0.00		101.94
TPH120-4A-35	Core	II	pyrite	54.13	47.26	0.02	0.04	0.00	0.00	0.01	0.55		102.01
TPH120-4A-38	Core	II	galena	13.40	0.00	0.00	0.00	86.63	0.00	0.32	0.01		100.36
TPH120-4A-59	Core	II	galena	13.50	0.06	0.00	0.01	87.04	0.00	0.10	0.01		100.72
TPH120-4A-40	Core*	II	sphalerite	35.06	9.46	0.05	0.00	0.00	0.00	56.74	0.01		101.32
TPH120-4A-43	Core*	II	sphalerite	34.69	9.04	0.01	0.03	0.00	0.00	57.51	0.01		101.28
TPH120-4A-41	Core	II	chalcopyrite	35.40	30.53	33.51	0.00	0.00	0.00	1.32	0.00		100.76
TPH120-4A-42	Core	II	chalcopyrite	35.78	30.78	33.59	0.03	0.00	0.01	1.22	0.01		101.42
TPH120-4A-19	Core **	II	stannite	29.79	12.53	28.41	0.07	0.08	0.00	0.92	0.000	27.86	99.66
TPH120-4A-22	Core **	II	sphalerite	33.82	8.15	0.06	0.00	0.03	0.02	57.27	0.006	0.00	99.36

Note: * - located within cataclastic band and close to stylolite. ** - located along stylolite
Sphalerite and stannite compositions from locations indicated by ** have been used to calculate the temperatures of sphalerite-stannite equilibrium following the geothermometer of Shimizu and Shikazono (1985). See text for more explanations.

The stylolites bordering the cataclasite bands (Fig. 6.6) and formed at the contact between the Qtz I and Qtz II vein contain pyrite, galena, and sphalerite-stannite pairs (Figs. 8.4a-b), with the latter exhibiting the largest compositional variation. This pair represents a well-calibrated mineral geothermometer because partitioning of Zn and Fe between sphalerite and stannite is known to be temperature dependent but pressure independent (Nekrasov et al., 1979; Shimizu and Shikazono, 1985). In the fourteen analysed pairs, stannite shows a range of Zn concentrations varying between 0.48 wt% and 3.25 wt%, whereas those of Fe, Cu and Sn vary within narrow ranges (Fe: 12.74±0.56 wt%; Cu: 28.30 ±0.33 wt%; Sn: 27.65 ±0.71 wt%). Sphalerite in the pair has concentrations of Fe and Zn of 7.63±0.87 wt% and 56.68 ±1.17 wt%, respectively. These ranges allow the calculation of the partition coefficient (K_d) of the reaction: Cu_2FeSnS_4 (in stannite) + ZnS (in sphalerite) = Cu_2ZnSnS_4 (in stannite) + FeS (in sphalerite). We have used the $\log K_d$–T relationship of Shimizu and

Shikazono (1985) to calculate the formation temperature of the pair, which is shown in the $(X_{Cu_2FeSnS_4}/X_{Cu_2ZnSnS_4})$-$(X_{FeS}/X_{ZnS})$ plot of Shimizu and Shikazono (Fig. 8.4c). The resulting 220-305° C interval lies at the low end of, or slightly outside as far as the lowest temperature estimate is concerned, the 250-350° C interval of the geothermometer.

We, therefore, consider the 250-305° C interval as the best estimation of the formation T of sphalerite-stannite along the stylolite.

8.4 Raman spectroscopy and carbonaceous material (CM) geothermometry

Raman spectroscopy was applied to determine the degree of organization of graphitic carbon within the host rock fabric. After the regional peak of metamorphic and migmatite formation (i.e. 660-700° C, 3.7-4.2 kbar; Tuisku and Lauri, 2009), the Olkiluoto basement was affected by different stages of ductile deformation (D2-D4, see also Paragraph 3.2) under greenschist facies conditions, during a metamorphic retrograde path capable to cause mobilization and subsequent recrystallization of carbonaceous material.

In the studied samples, graphitic carbon was observed as elongated grains of graphite arranged along the metamorphic foliation of the host rock (Fig. 8.6a). Graphite grains appear along the foliation planes with an average grain size between 100 and 300 µm (Figs. 8.6b-c). For detailed petrographic descriptions of the host rock, the reader is referred to Section 6.1.

Raman measurements were collected from several graphite grains within three different analytical areas (Fig. 8.6a). Decomposition of Raman spectra shows that G, D1 and D2 band position (centre) are respectively at c. 1580, c. 1350 and c. 1620 cm^{-1} (Table 4). Peak area ratios, R2 (Raman parameter derived from the area of the defect bands relative to the ordered graphite band; cf. Chapter 4), were therefore calculated to estimate the graphite temperature.

The calculated R2 value shows a substantial scatter, ranging from 0.1 to 0.38 (Table 4), suggesting a great heterogeneity within the studied sample. To obtain a reliable metamorphic temperature that adequately reflects the range of sample heterogeneity, the average value of R2 (Table 4) was determined following the method proposed by Aoya et al. (2010) and we defined the metamorphic temperature on the average R2 (Fig. 8.6d). We estimated a metamorphic temperature of 530° C with a maximum error of ± 50° C for the carbonaceous material within the host rock (by using the thermometer calibration for a laser 370 wavelength of 514 nm, Beyssac et al. 2002). We interpret this value as the temperature

of last remobilization of carbonaceous material within the host rock took place during the D3 and D4 deformation stages (see Chapter 3).
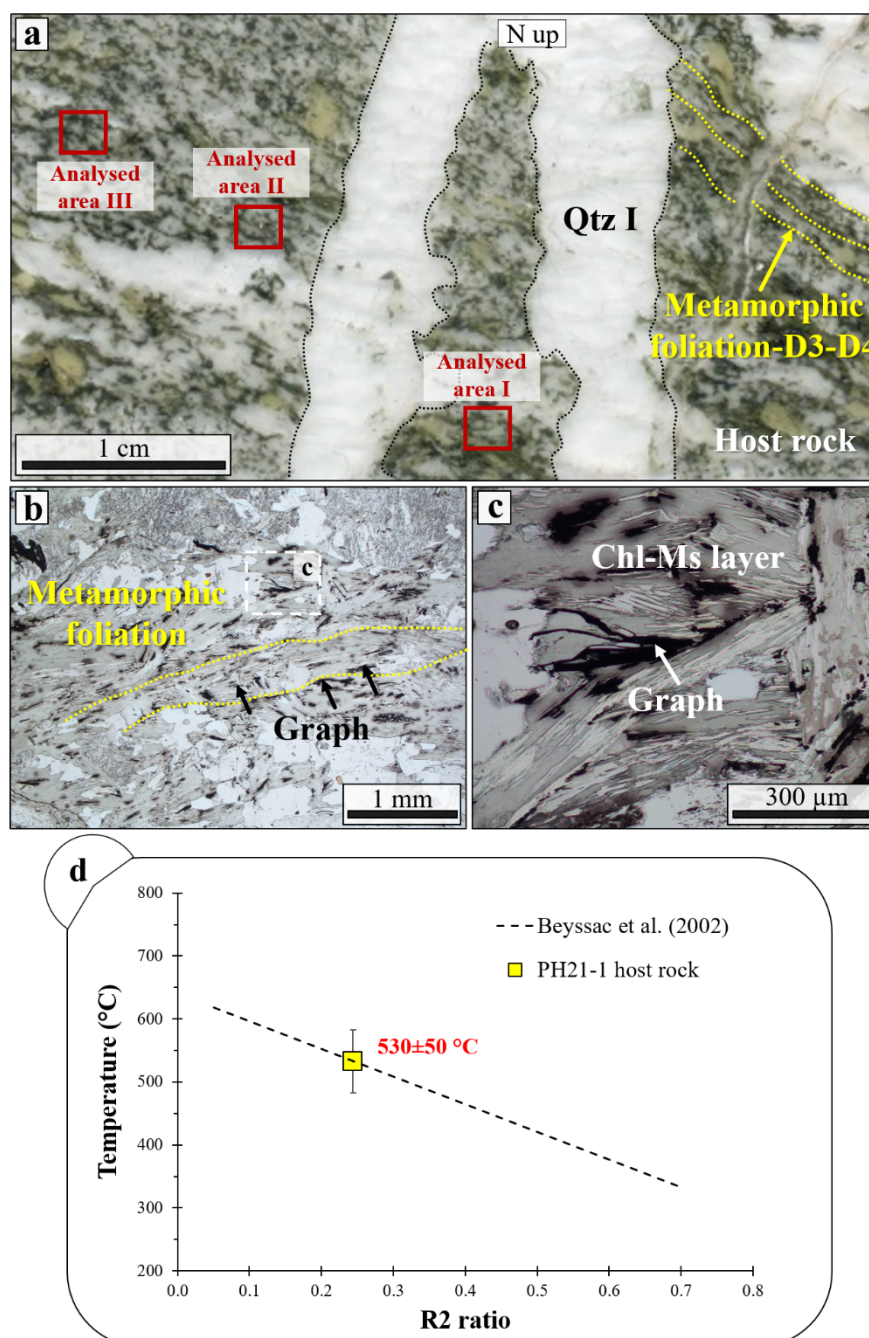
Figure 8.6. (a) Scanned double-polished thin section showing metamorphic foliation in the host rock (sample PH21_1). Red squares in figure (a) identify the three areas where Raman spectra of graphite grains were acquired. (b-c) Elongated grains of graphite are aligned along the metamorphic foliation, marked by the chloritized muscovite. (d) R2 ratio vs. metamorphic temperature estimated from the graphite thermometry in the host rock fabric. The error bar is the standard deviation obtained for 15 spectra and is a measure of CM heterogeneity within sample. Decomposition of graphite Raman spectra and the calculated R2 ratio and temperature are shown on Table 4.

Table 4: Parameters obtained from the decomposition of 15 Raman spectra of graphitic carbon

Sample	D1 position (centre)	G position (centre)	D2 position (centre)	R2 ratio	T (° C)
PH21- analysed area I_1	1365.00	1583.00	1620.00	0.32	497
PH21- analysed area I_2	1366.00	1583.00	1623.00	0.31	503
PH21- analysed area I_3	13688.00	1584.40	1619.96	0.12	587
PH21- analysed area I_4	1370.34	1584.37	1587.81	0.14	577
PH21- analysed area I_5	1366.93	1584.24	1626.62	0.27	519
PH21- analysed area II_1	1375.55	1585.93	1620.86	0.10	596
PH21- analysed area II_2	1365.29	1583.36	*	0.21	549
PH21- analysed area II_3	1365.90	1584.11	1623.00	0.26	525
PH21- analysed area II_4	1382.74	1585.14	*	0.21	548
PH21- analysed area II_5	1366.43	1584.70	1625.00	0.38	471
PH21- analysed area II_6	1367.55	1584.81	1623.80	0.35	485
PH21- analysed area III_1	1375.57	1585.93	1619.31	0.10	595
PH21- analysed area III_2	1366.61	1584.41	1622.29	0.30	595
PH21- analysed area III_3	1366.32	1584.09	1625.01	0.26	524
PH21- analysed area III_4	1366.42	1584.47	1622.10	0.31	503
average R2 (based on N=15 measurements)	0.24				
Estimated T using average R2, based on Aoya et al. 2010 (°C)	532				

* not identified peak

These results are part of the following manuscript: "Fluid-mediated, brittle-ductile deformation at seismogenic depth: Part 2 –Stress history and fluid pressure variations in a shear zone in a nuclear waste repository (Olkiluoto Island, Finland) by Prando, F., Menegon, L., Anderson, M. W., Marchesini, B., Mattila J. and Viola, G. The manuscript is the Part 2 companion paper of "Fluid-mediated, brittle–ductile deformation at seismogenic depth–Part 1: Fluid record and deformation history of fault veins in a nuclear waste repository (Olkiluoto Island, Finland)", Marchesini, B., Garofalo, P. S., Menegon, L., Mattila, J., & Viola, G. (2019), Solid Earth (10(3), 809-838)" and is at the moment in review for Solid Earth.

Chapter 9. Composition, salinity and fluid pressure estimates of fluids involved in the BFZ300

Field evidence combined with microstructural observations, fluid inclusion analysis and the documented distinct generations of synkinematic chlorites confirm that Qtz I and Qtz II veins precipitated from distinct batches of aqueous fluid (i.e. H_2O-NaCl), that flowed within the fault zone during different stages of its evolution.

We documented a wide range of bulk salinity for each FIAs entrapped within the quartz veins in each structural domain (Figs. 7.6a-d). This suggests post-entrapment re-equilibration of fluid inclusions (cf. Bakker and Jansen, 1990; Diamond et al., 2010). The Th_{tot} varies between c. 130 and 440° C without a clear mode or a skew (Figs. 7.6e-h) indicating that no common range of entrapment temperature can be identified in the dataset. Therefore, we conclude that even the properties of petrographically intact FIAs do not correspond to chemically well-preserved assemblages. Indeed, the ranges of Th_{tot} in individual FIAs are typically of the order of 150-200° C (Figs. 7.6e-h), i.e. a value that is much higher than the ~10° C range expected for homogeneous FIAs entrapped isochorically and isoplethically (Fall et al., 2009; Vityk and Bodnar, 1998) and that demonstrates post-entrapment re-equilibration (cf. Vitik and Bodnar, 1998; Bodnar, 2003b; Sterner and Bodnar, 1989; Invernizzi et al., 1998). A major implication of fluid inclusion re-equilibration in our study is that the calculated fluid properties do not rigorously reflect those of the pristine fluid originally entrapped within BFZ300, but rather that of a fluid that modified its properties during the fault activity.

Then, a possible approach to interpret our FI dataset is the comparison with the experimental work on synthetic fluid inclusions subjected to a range of post-entrapment re-equilibration conditions (Bakker, 2017; Bakker and Jansen, 1990, 1991, 1994; Vityk and Bodnar, 1995, 1998; Vityk et al., 1994; Invernizzi et al., 1998). A straight comparison to the experiments is in our case difficult because most experimental work was carried out at high TP conditions (500-900° C; 90-300 MPa) and also only few experiments were carried out under deviatoric stress conditions that approach those of natural rocks (Diamond et al., 2010; Tarantola et al., 2010). Despite these limitations, however, some key experimental results provide fundamental constraints on our dataset. First, both hydrostatic and uniaxial compression experiments showed that in each re-equilibrated FIA a number of inclusions survive virtually intact the modified post-entrapment PT conditions, showing that only severe deformation brings to total re-equilibration and complete obliteration of pristine

inclusions (i.e., $\Delta\sigma$ >100 MPa in uniaxial compression experiments; > 400 MPa change of confining P in hydrostatic experiments). Second, under conditions leading to only low to moderate re-equilibration, the bulk chemical composition of the fluid inclusions does not change significantly from that of the pristine inclusions.

All of this implies that natural quartz samples with microstructures typical of moderate T deformation, such as deformation lamellae, deformation bands, undulose extinction and bulging, and hosting FIAs with moderately re-equilibrated textures, should still contain a number of inclusions whose properties resemble those of the pristine fluid. In this scenario, our microthermometric dataset can be used to constrain the more probable salinity ranges of the fluid batches which trigger BZ300 reactivation stages. Two possible interpretations of the microthermometric dataset can be follow and we can give accordingly different salinity ranges for the fluids.

One possibility is that the different quartz veins and the fluids trapped within fluid inclusions originated from multiple pulses of a single, low salinity fluid, with a salinity between 0 and 7 wt% NaCleq, as shown by the distribution of >70% of the bulk salinities skewed towards values of 7 wt% NaCleq or less (Fig. 7.6a-d). Thus, it is possible that aliquots of the 0-7 wt% NaCleq FIAs from Qtz I and II crystals from both the damage zone and fault core is still representative of the pristine sampled fluid. These inclusions would be those that survived or were relatively less affected by deformation events postdating their entrapment. Inclusions falling outside the most typical 0-7wt% NaCleq salinity range would instead correspond to those which progressively modified their properties as a consequence of fluid-rock interaction during faulting and that experienced significant H_2O loss and consequent salinity increase during the successive stages of fault deformation (cf. Bakker and Jansen, 1990; Diamond et al., 2010). The large documented range of Th_{tot} lacking a specific mode observed in individual FIAs is the product of fluid density changes caused by fluid inclusion re-equilibration during post-entrapment deformation. This would have happened repeatedly and cyclically within the host quartz during all ductile and brittle stages of deformation of the multi-stage deformation history of BFZ300.

Alternatively, multiple batches of fluids with different salinities (from low to intermediate salinity) may have ingressed and evolved within BFZ300 during its activity. In fact, considering the salinity dataset presented for each structural domain, fluid salinity can be seen clustering in restricted ranges typical for each domain: 1) the salinity of 60% of secondary fluid inclusions in Qtz I from the damage zone is between 0 and 1 wt% NaCleq; 2) > 80% of the secondary inclusions in Qtz I from the fault core preserve a salinity in the 1

to 5 range wt% NaCleq; 3) 75% of pseudosecondary inclusions in Qtz II show salinity values between 6 and 11 wt% NaCleq and 4) ~70% of the secondary inclusions trapped within Qtz II show salinity values between 0 and 3 wt% NaCleq. These clusters may best represent the original compositional ranges of different batches of fluids, each involved during a different faulting stage. Salinities outside these clusters may instead be explained again as resulting from the post-entrapment re-equlibration of those fluids with different salinities. This hypothetical scenario, in which chemically distinct fluids ingressing the fault and interacting with the rock at different times (e.g. Selverstone et al., 1992; Boiron et al., 2003; Famin et al., 2005) is also reinforced by several lines of observation such as: the variation of chlorite composition, the slight change in paragenesis/redox state with Qtz II and Qtz I (i.e. the absence of massive sulphides in Qtz I) and by the prolonged history of faulting (see below).

Fully aware of the interpretative uncertainties of our dataset, we have combined the microthermometric data of the studied FIAs with the independent quartz-chlorite and sphalerite-stannite geothermometers to constrain the most probable fluid pressure during the faulting events. With this approach, we use the formation temperatures of the mineral pairs as independent geothermometers and consider the intersection between these values and the FIA isochores to derive the ranges of trapping pressure (cf. Roedder and Bodnar, 1980). In Figure 12, we present the ranges of the possible pressure (P_f) of the fluids involved during faulting as calculated by combining the fluid inclusion data with the constraints provided by the pair-mineral geothermometry and the hydro- and lithostatic pressure gradients and a possible geothermal gradient (e.g. Van Noten et al., 2011; Selverstone et al., 1995; Jaques and Pascal, 2017). The reconstructed regional gradients at the time of vein emplacement are derived from peak metamorphic conditions (4-5 kbar; 650-700° C leading to c. 40° C/km; from Kärki and Paulamäki, 2006). Hydrostatic and lithostatic pressures are then calculated by using pure water density and assuming a rock density of 2700 kg m^{-3}, respectively. These gradients are used to constrain the upper and lower bounds to physically possible fluid pressures. We computed the maximum and minimum isochores by using the entire salinity and Th$_{tot}$ ranges obtained from the FIAs in each structural domain (Fig. 7.6). We also computed the isochores of the inclusions with the most representative salinity estimates for each structural domain obtained by comparing the frequency diagrams (Fig. 7.6) with the Th$_{tot}$ vs. salinity plots (Fig. 7.7). Considering the peak temperature of each structural zone from the geothermometric estimations in combination with the computed isochores, the estimated peak conditions of the fluid pressure are: 1) 80 MPa for Qtz I from the damage

zone, 2) 210 MPa for Qtz I from the fault core; 3) 140 MPa from pseudosecondary inclusions in Qtz II from the core and 4) 180 MPa from secondary inclusions in Qtz II, still from the core (Fig. 9.2, Table 5).
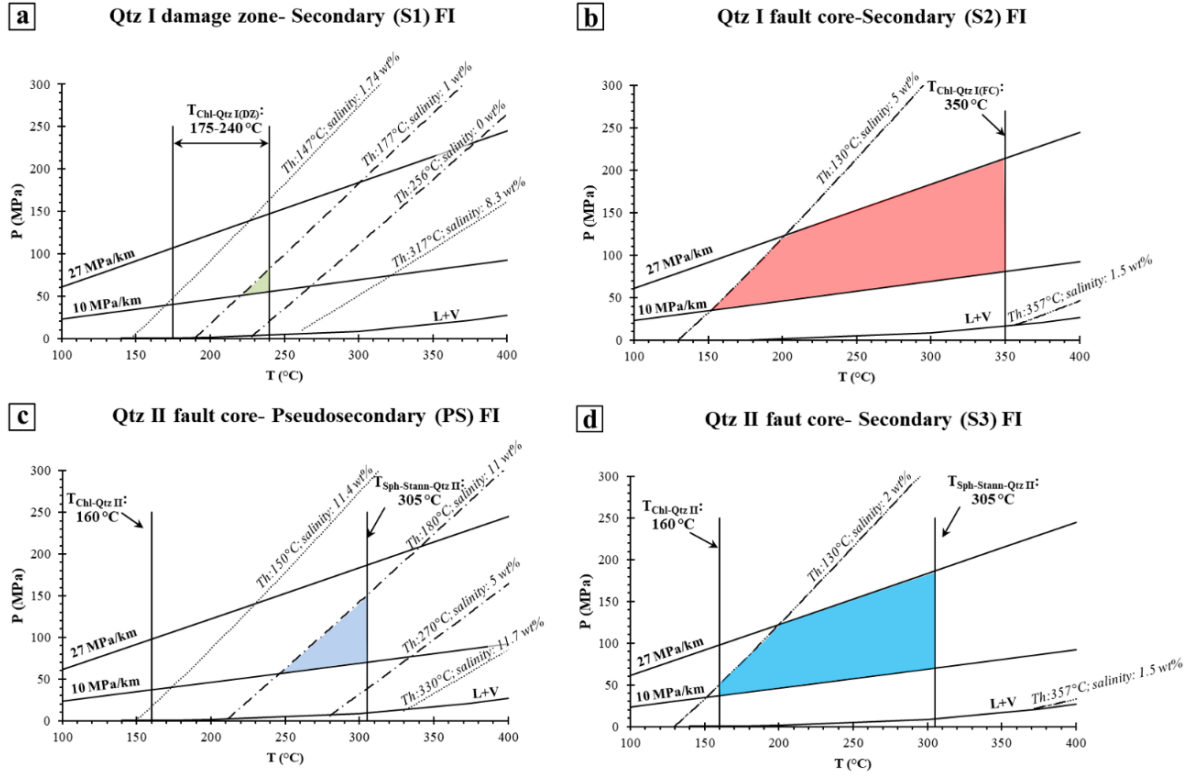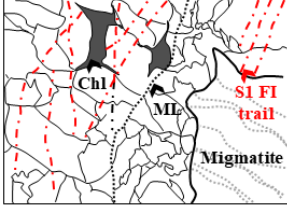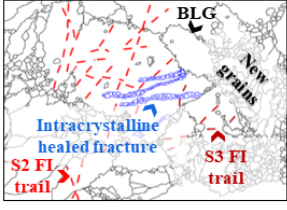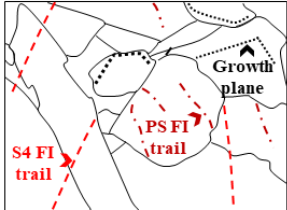
Figure 9.2. P-T diagrams showing the ranges of PT trapping conditions of the analysed fluid inclusions: (a) secondary inclusions in Qtz I from the fault damage zone; (b) secondary inclusions from Qtz I in the fault core; (c) pseudosecondary inclusions trapped in Qtz II in the fault core and (d) secondary inclusions in the Qtz II. Thin dashed lines indicate maximum and minimum isochores of FIAs in each structural domain. The coloured areas identify the probable PT trapping ranges defined by: i) the slope and position of the fluid inclusion isochores as determined by the most representative salinity and homogenization temperature range (Supplementary Material for details); ii) mineral pairs geothermometry and iii) hydrostatic and lithostatic fluid pressures computed assuming a regional geothermal gradient of c. 40° C/km (assuming retrograde conditions of 4 kbar and 650° C, from c). The liquid-vapour equilibrium curve for the H_2O-NaCl modeled fluid is also indicated.

In addition to the P_f peak conditions, we can also constrain the physically possible fluid pressure ranges for each stage of fluid ingress, which are derived by considering the temperature range estimated for each structural domain. Thus, for the damage zone, a P_f interval of 50-80 MPa (Fig. 9.2a) can be derived by intersecting the range of T obtained from the chlorite-quartz pair in the Qtz I from the damage zone with the range of isochores from the same quartz. As to the fault core, we combine the 350° C constraint from the chlorite-quartz pair from Qtz I in the fault core with the isochores from the same quartz,

which yields P_f between c. 30 and 210 MPa (Fig. 9.2b). Similarly, the intersection between the equilibrium T of the sphalerite-stannite pair in the Qtz II from the fault core and the range of isochores of the pseudosecondary FIAs of Qtz II defines P_f values between 50 and 140 MPa (Fig. 9.2c). Estimations from secondary FIAs in Qtz II constrain a range between 40 and 180 MPa (Fig. 9.2d).

Table 5: Schematic summary of main microstructures, fluid properties, and P_f-T deformation conditions in the quartz veins of the BFZ300 fault.

Structural zone and sample	Qtz type	Deformation type	Microstructures	Studied FIAs	Microthermometric properties	Fluid pressure (Pf) and mineral pair thermometry
Damage zone (PH21)	Qtz I	Brittle/Ductile		FIA 3- TypeS1 FIA 4-Type S1 FIA 26-Type S1 FIA 27 Type S1	Tm_{ice} S1: -5.9 to -0.1° C Th_{tot} S1: 150-400° C	$T_{Chl-QtzI (DZ)}$: 175-240° C P_f(S1): 50-80 MPa
Fault core (TPH120-4A)	Qtz I	Cyclic Brittle/Ductile		FIA 1-Type S2 FIA 2-Type S2 FIA 5-Type S2 FIA 6-Type S2 FIA 7-Type S2 FIA 22-Type S2 FIA 23-Type S2 FIA 24-Type S2 FIA 25-Type S2	Tm_{ice} S2: -8.2 to -0.4° C Th_{tot} S2: 130-410° C	$T_{Chl-QtzI (FC)}$: 350° C P_f(S2) 30-210 MPa
Fault core (TPH120-6) (TPH120-4)	Qtz II	Brittle		FIA 8-Type PS FIA 9-Type PS FIA 10-Type PS FIA 11-Type PS FIA 12-Type PS FIA 19-Type PS FIA 20-Type PS FIA 21-Type PS FIA 13- Type S4 FIA 14-Type S4 FIA 15-Type S4 FIA 16-Type S4 FIA 18-Type S4 FIA 19-Type S4	Tm_{ice} PS: -13.6 to -0.1° C Th_{tot} PS: 150-440° C Tm_{ice} S4: -11 to 0° C Th_{tot} S4: 130-430° C	$T_{Chl-QtzII}$: 160-220° C $T_{Sph-Stann-QtzII}$: 250-305°C P_f(PS): 50-140 MPa P_f(S4): 40-180 MPa

As also supported by the microstructures described above, we propose that these values are sufficiently accurate to constrain at least four stages of fault reactivation, each triggered by a fluid with distinct physical and compositional properties.

As shown by the T vs. P plots of Figure 9.2, the secondary FIAs entrapped in Qtz I from the damage zone constrain the lowest value of P_f (i.e. 50-80 MPa) of the entire dataset. We interpret this not as representative of the early BFZ300 localization, but rather as possibly resulting from fluid entrapment during a later stage of fault reactivation at T ~200° C. This is also consistent with the calculated temperature of crystallization of the vermicular chlorite associated with Qtz I from the damage zone (175-240° C, Fig. 8.1b) and with the

secondary nature of the entrapped FIAs. Also, the most abundant salinities observed in the Qtz I from the damage zone (0-1 wt% NaCleq) coincide with the lowest Th_{tot} measured in the same structural domain. Later fracturing of Qtz I in the damage zone may thus have been coeval with the formation of vermicular chlorite preserved therein, which is found along secondary cracks and median lines (Fig. 6.3d).

In light of these considerations, we propose that initial BFZ300 localization occurred in the presence of a fluid with T and P of at least 350° C and 210 MPa, respectively. Later faulting continued by cyclic brittle-ductile switches induced and assisted by fluid batches at progressively lower temperature and pressure.

Chapter 10. Structural evolution and seismicity of BFZ300

10.1 Structural evolution and fluid flow of BFZ300: a conceptual model

Based on the integration of field, microstructural, thermometric and fluid inclusions constraints (Table 5), we propose a conceptual model for the structural evolution of BFZ300 (Fig. 10.1). The fault's finite strain results from several slip episodes mediated by multiple events of fluid ingress and fluid-rock interaction. A first constraint provided by our study is that the analysis of the chemical composition of the fluids that ciclycally ingressed the fault suggests the likely presence of several batches of fluids of varying salinity and composition.

Geothermometry of the carbonaceous material has clearly shown that its last remobilization within the host rock took place during the D3 and D4 deformation stages (see Chapter 3) at ~530° ± 50° C (see Chapter 8). We interpreted this thermometric estimate a reliable constraint of the last ductile event registered by the Olkiluoto basement.

The embrittlement of the Olkiluoto metamorphic basement (time t_1 of Figs. 10.1a, b) represents the initial stage of the deformational history of BFZ300, when conditions for brittle dilation and fracturing of the Paleoproterozoic basement were first met in a transient fashion. We propose that brittle failure under still ductile environmental conditions was caused by transiently elevated P_f (> 210 MPa), as also demonstrated by field evidence of hydrofracturing (pure tensional en enchelon veins at the BDTZ depth). Hydrofracturing of the host basement is also indicated by the emplacement of Qtz I veins within the diffuse network of joints and conjugate hybrid/shear fractures of the damage zone (Figs. 10.1a, 5.5). These brittle features are quite broadly distributed suggesting an initial volumetrically diffuse strain distribution. Their formation caused the overall mechanical weakening of the host rock volume, which in turn facilitated later strain localization. Brittle structures formed during this stage are discordant to the ENE-WSW striking metamorphic foliation (Fig. 3.2a), which they cut at high angle (Fig. 10.1a). Conditions for tensional and hybrid failure require low differential stress, i.e. σ_1- σ_3 ~ 4T, where T is the tensional strength of the rock. Opening of fractures caused a stress drop, sudden increase of permeability, fluid venting and inhibited further build-up of P_f. Dilatant fractures were partially infilled by Qtz I, which precipitated from a first fluid, with inferred low salinity (in the range between 1 and 5 wt% NaCleq). Precipitation of Qtz I and formation of veins within these fractures caused

hardening of the system. The progressive recovery of shear stresses altered the overall background stress conditions such that failure, after causing initial pure dilation, was later accommodated by hybrid extensional - and, eventually, by shear fracturing (Fig. 10.1b), thus forming laterally continuous and interconnected shear fractures associated with breccia pockets and cataclasites (Figs. 5.5d, g, i). Conjugate shear fractures connected the previously formed extensional fractures through fracture coalescence (e.g. Griffith, 1921; Sibson, 1996; Fig. 10.1a). At the micro-scale this is demonstrated by the elongated blocky texture of Qtz I crystals from the damage zone (Figs. 6.2c and 6.3a), where crystals grew at high angle to the vein boundaries (thus suggesting initial near-orthogonal dilation) and are physically connected by cataclastic shear bands to form a fault-fracture mesh (e.g. Sibson, 1996). Cataclastic bands formed at the expense of the migmatitic host rock are enriched in authigenic, synkinematic sericite, likely due to the interaction between K-feldspar and fluids circulating in the dilatant fault zone (Fig. 6.2b). Shear fractures thus deformed the migmatitic host rock to connect dilatant and mostly Qtz I-filled tension gashes during a continuum of deformation. The conjugate shear fractures ascribable to this stage invariably define tight acute angles (Figs. 5.4b, 5.5a), which we take as further evidence of overall low differential stress conditions at the time of failure (Fig. 10.1b).

In synthesis, Qtz I veins from the damage zone are interpreted as the expression of the earliest stage of fault nucleation, before strain localization affected a progressively narrower rock volume to eventually form the main fault core. Indeed, the meso- and microscale features observed in Qtz I-damage zone, lacking of pervasive crystal-plastic deformation as otherwise occurred in Qtz I-fault core, are used to document the initial stage of embrittlement. Based on geometric, kinematic and deformation style characteristics, we tentatively assign this deformation episode to Stage 1 by Mattila and Viola (2014, their Fig. 18), i.e. to a discrete brittle episode considered the expression of the earliest onset of brittle conditions in southwestern Finland c. 1.75 Ga ago, under overall NW-SE to NNW-SSE transpressive conditions.

Further deformation of the BFZ300 (time t_2 of Fig. 10.1c) occurred by progressive inward strain localization and narrowing of the actively deforming volume of the deformation zone (from a wide damage zone to a narrow fault core). The early BFZ300 core, consisting of the main Qtz I vein is interpreted as having formed at this stage, within an overall dextral strike-slip kinematic framework. Emplacement of the Qtz I vein in the core represents the last pulse of this brittle deformational episode (Fig. 10.1b). Major fluid
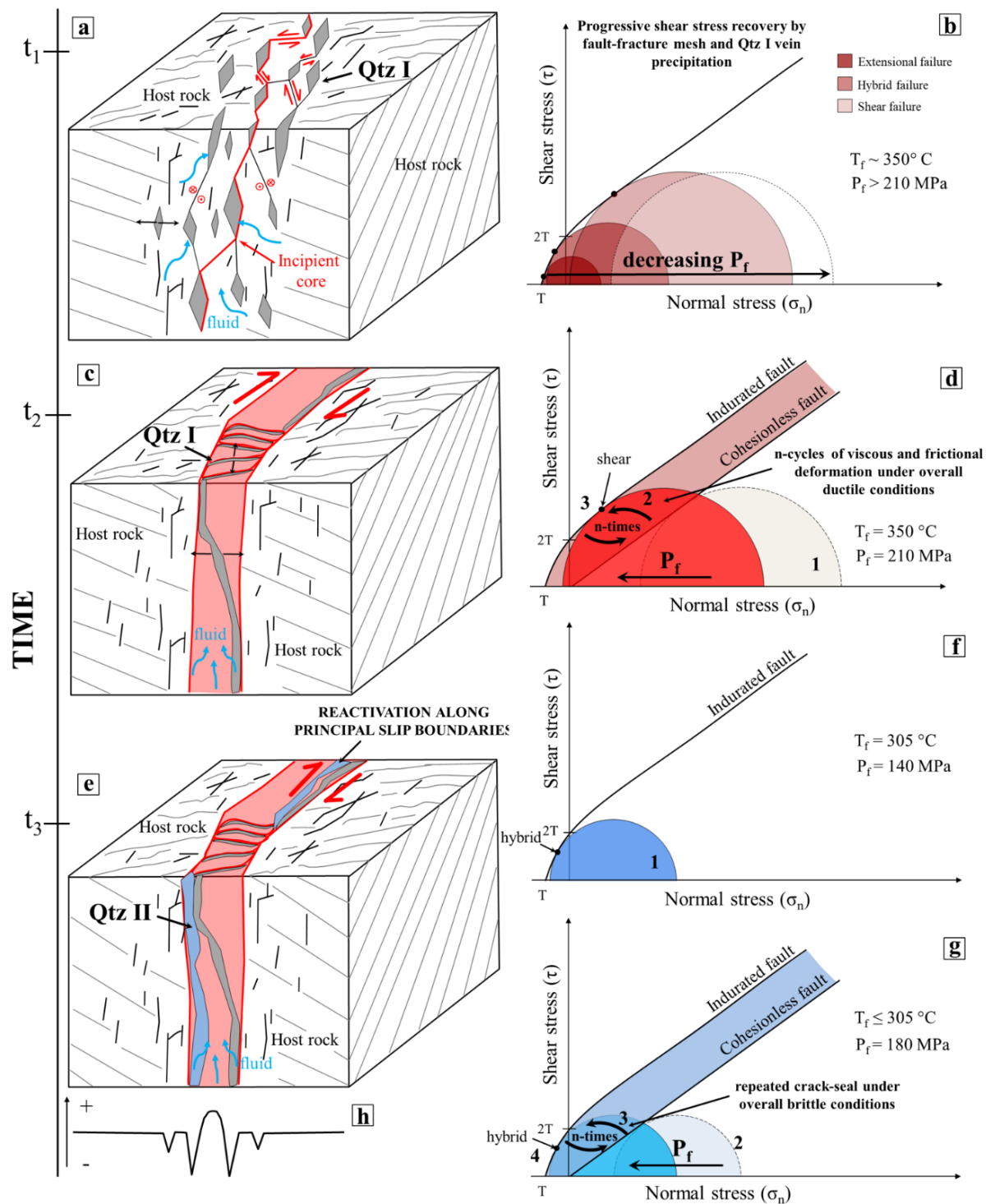
Figure 10.1. Conceptual model of the temporal and mechanical evolution of the BFZ300 fault zone (see text for more details). Grey lines: traces of metamorphic foliation. Black lines: fractures related to the BFZ300 structural development. (a) Initial embrittlement of the migmatitic basement occurred by fracture coalescence (red line) under (b) initial lower differential stress conditions and high fluid pressure and followed by a transient increase of differential stress. A first generation of quartz veins (Qtz I) precipitated inside the diffuse network of joints and hydrid/shear fractures which formed during this first deformation stage. (c) Progressive strain localization and fluid channeling within the fault core occurred by (d) episodically renewed fluid-pressure build-up driven by cycles of brittle and ductile deformation. (e-g) Progressive exhumation and cooling of the fault system occurred concomitant with several brittle reactivation episodes of the fault zone

under hybrid conditions and fluid pressure lower than during the previous deformational stages. Lastly, a second generation of quartz veins (Qtz II) was emplaced, mainly along the principal slip boundaries of the fault core, following the Qtz I vein as shown by (h) the strenght profile across the fault architecture, that suggests lower tensile strength values (and hence higher reactivation potential) along the Qtz I vein / host rock walls.

venting was likely associated with it, such that the system, once brittle failure in the core had occurred by hydrofracturing, moved back to a more diffuse deformation style typical of the still prevailing ductile conditions. Microscopic evidence of crystal-plastic deformation and dynamic recrystallization (Figs. 6.4a, b; Table 5) overprinting the early brittle structures of Qtz I in the fault core supports slow strain rate conditions during deformation. However, this ductile background deformation was punctuated by renewed and cyclically transient embrittlement as documented by healed fractures shown by trails of secondary fluid inclusions cutting across both the ductile fabrics and the earlier brittle deformational features (Figs. 6.4c, g). EBSD analysis of the new grains documented along healed microcracks also suggests that they likely nucleated from fluids circulating in the early fractures before being later deformed in the low-temperature plasticity regime (EBSD data are reported in Appendix A). Thus, we show that at the BDTZ 'neocrystallisation' by nucleation and growth in fractured fragments and dynamic recrystallisation (typically by bulging and subgrain rotation) coexist and compete in the overall microstructural evolution of quartz (e.g. Kjøll et al., 2015). Repeated fluid ingresses and related deformation would, in addition, also have caused some of the post-entrapment equilibration of the FI, as discussed above.

Mattila and Viola (2014) described a second brittle stage (referred to as Stage 2, their Fig. 18) during which a c. N-S to NNE-SSW-oriented episode of transpressional deformation affected southwestern Finland. Geometric and temporal relationships between structures of Stages 1 and 2 (see also Viola et al., 2009) were used to infer a clockwise rotation of the horizontal compression direction from NW-SE (Stage 1) to NNE-SSW (Stage 2). Consistent with the kinematic framework of Stage 2, we propose here that during progressive regional exhumation and cooling to entirely brittle conditions, the BFZ300 deformation continued through a further, distinct deformation phase (t_3 of Fig. 10.1e). This stage accommodated the selective reactivation of the BFZ300 core, with renewed dilation due to the rotated σ1 during Stage 2 acting subparallel to the strike of the Qtz I vein in the BFZ300 core. Localised dilation in a still fluid-rich system allowed the emplacement of the Qtz II vein (Fig. 10.1e). Our estimations indicate peak conditions of P_f 140 MPa and T ≈

305° C. The BFZ300 core was reactivated by an intermediate salinity fluid (in the range between 6 and 11 wt% NaCleq) under overall hybrid conditions (Fig. 10.1f), as suggested by the irregular thickness and curved geometry of the Qtz II vein therein, and by the synkinematic chlorite crystals that are stretched orthogonally to the vein boundaries (Fig. 5.5h). The Qtz II vein invariably localized along at the contact between Qtz I and the host rock (Figs. 5.5f, 10.1e) suggesting selective reactivation along the pre-existing principal slip zones, which represented the weakest part of the fault (Fig. 10.1h). Evidence for mesoscale hybrid fracturing and our P_f estimates (Fig. 9.2) suggest that P_f was lower than that of the earlier deformation stages during Qtz I emplacement.

BFZ300 underwent one or more events of brittle fracturing and induration (Fig. 10.1g), as suggested by the CL imaging of Qtz II crystals (Fig. 6.5c). The fluid pressure peak value for this structural stage is c. 180 MPa.

A possible, very late reactivation stage of unknown age is also documented by the secondary chlorite associated with Qtz I in the damage zone (Figs. 6.3a, d). Also, the stylolitic seams striking parallel to the BFZ300 fault zone (Fig. 6.6a) suggest a compression oriented c. E-W, i.e. subparallel to the inferred Sveconorwegian main shortening direction (e.g., Viola et al., 2011). The sphalerite-stannite mineral pairs arranged along these structures were possibly concentrated through a pression-solution during this deformational stage.

Skyttä and Torvela (2018) proposed that the BFZ300 is a brittle structure localized onto a zone of incomplete structural transposition inherited from the earlier ductile history of the Olkiluoto basement. However, in our mesoscale and microstructural analysis we did not find evidence of any ductile precursor, and we note that BFZ300 cuts the ductile structural grain at high angle, which excludes any reactivation of precursor ductile fabrics.

10.2 Implications for seismic deformation at the base of the BDTZ

In the previous paragraph we discussed the role of overpressured fluids on strain localization during the incipient stages of fault nucleation and subsequent reactivation(s) at the BDTZ. The maximum estimated fluid pressure and fluid temperature conditions derived in this study (peak conditions of 210 MPa and 350° C) are indeed realistic for the base of the seismogenic zone in the continental lithosphere (e.g., Scholz, 1990, and references therein) where the brittle-ductile transition for quartz occurs.

Mechanical models of long-term deformation (Rolandone and Jaupart, 2002) propose that deformation at the brittle-ductile transition can be reasonably described as being mostly accommodated by intermittent and concomitant coseismic slip and ductile flow. Hydrofracturing, as that documented in this study by the Qtz I and II veins, is possibly related in that context to seismic failure. Faults accommodating hydrofracturing are indeed commonly interpreted as seismogenic (e.g. Sibson, 1992a; Cox, 1995) particularly at depth.

Our study confirms this view because BFZ300 contains not only brittle fault rocks overprinting and overprinted by veins, but also clearcut evidence of mutually overprinting brittle and ductile deformation (Fig. 6.4). In light of the field observations discussed and of the constraints derived, we suggest therefore that BFZ300 behaved in a seismic way at least during the emplacement of the principal Qtz I and Qtz II veins. In this perspective, two possible scenarios can be considered to explain the genetic relationships between BFZ300 and a possible seismic behaviour of the crust during the Svecofennian orogeny. In a first scenario, the quartz veins of the fault core would represent the result of coseismic rupture during the mainshocks of a fully developed seismic cycle. Pore pressure fluctuations caused the repeated transient embrittlement of the rock mass, which was otherwise under overall ductile conditions. The documented brittle-ductile cycles are thus the expression of coseismic fracturing and aseismic creep between the individual shocks, as shown by viscous deformation overprinting the brittle features, guided by the residual differential stress.

A second possibility is that faulting occurred in the absence of a well-defined sequence of main- and aftershocks. As in the case of man-induced earthquakes triggered by high-pressure fluids during injection of fluids (e.g. Healy et al., 1968), where deformation is typically accommodated by diffuse swarms of low magnitude seismicity rather than well-defined mainshock-aftershock sequences (Cox, 2016), we propose that BFZ300 might have localised strain by diffuse veining with crack and seal textures (Cox, 2016). Breccias and cataclasites (Figs. 5.5, 6.6) mutually overprinting with veins show that failure and veining were indeed broadly coeval (e.g. Cox, 1995; Cox, 2016). Healing in fluid-rich environments can occur over short periods of time (days-months) when compared with recurrence time of large earthquakes (10-100 years) (Olsen et al., 1998; Tenthorey and Cox, 2006). Therefore, the documented repeated switches between brittle and ductile deformations would then be steered again by transient episodes of fluid overpressuring but in this case would express the accommodation of swarms of minor background earthquakes within overall ductile conditions. Microstructures of fault-rocks exhumed from the BDTZ elsewhere, are mostly in agreement with our hypotheses of seismic deformation. Moreover, microstructural analysis

of coeval BFZ045 has documented the occurrence of pseudotachylyte injection veins along the brittle slip zone that reworks the precursor ductile mylonite (Fig. 5.3d). For further details on the BFZ045 microstructures the reader is referred to the study of Prando et al. (under review), which is attached in Appendix D. Pseudotachylytes are among the few unambiguous evidence of seismic activity in the rock record (Cowan, 1999; Rowe and Griffith, 2015). The presence of pseudotachylites within the BFZ045 and hydrofractures in the BFZ300 supports the hypothesis of an overall seismic behaviour of the BFZ300-BFZ045 fault system.

Transient and short term high-stress deformation followed by phases of stress relaxation, which is prevalently characterized by recovery and recrystallization processes, has been documented by several authors in deformed quartz (Trepmann and Stöckhert, 2003; Trepmann et al., 2007; Bestmann et al., 2012; Trepmann and Stöckhert, 2013; Trepmann et al., 2017).

10.3 Summary and conclusions

This study demonstrates that a multi-scale and multi-technique approach leading to the generation of multiple and independent constraints offers the potential to reconstruct the details of the evolutionary history of fault zones that have experienced multiple events of reactivation. These events were triggered by fluid overpressure and were associated with intense fluid-rock re-equilibration processes. We have documented the localised, initial embrittlement of the Paleoproterozoic basement of southwestern Finland at the BDTZ, which occurred by brittle failure under overall ductile conditions in response to transiently high fluid pressure and temperature (peak conditions: $P_f > 210$ MPa; T~350° C).

The deformation stages experiences by the BFZ300 occurred at different depth within the seismogenic crust. A minimum depth for faulting can be estimated by assuming that the fluid pressures documented by the fluid inclusion analysis represent the pore fluid pressure within the fault at the timing of the hydrofracturing events. During hydrofracturing the pore fluid pressure equates the local least compressive stress σ_3, which is $\leq \sigma_2$, i.e. the vertical stress in a strike-slip fault like the BFZ300. Therefore, the fluid pressure under tensile extensional fracturing can be assumed to represent the minimum value of lithostatic stress.

Following these considerations and considering that the lithostatic load is given by $\sigma = \rho gh$, the minimum depth of deformation of the fault during time t_1 and t_2 (Fig. 10.1) can be estimated to between 8 and 13 km. This range reflects depths for baric gradient estimates between 27 MPa/km (dry overburden) and 17 MPa/km (hydrostatic pore fluid pressure in

the overburden). The minimum depth range estimates at the time of t_3 (Fig. 10.1) is between 5 and 8 km.

Our results further constrain the importance of recurrent seismicity and stress the importance of fluids in the fragmentation of Precambrian cratons when deformed at the BDTZ, something that is not yet that well understood in the case of the Fennoscandian Shield.

This study, moreover, provides important inputs to many modern geological applications, including site characterization studies for other deep geological disposal facilities for spent nuclear fuel.

Chapter 11. Deformation-controlled elemental mobility in naturally deformed hydrothermal pyrite

This chapter investigates the role of sulphides, specifically pyrite, in facilitating bulk strain accommodation and in enhancing the overall mass transport within the BFZ300 fault zone during its last, recorded deformation stages. Sulphides are present in the core of BFZ300 as multicrystalline aggregates with diameters ranging between 8 and 20 mm dispersed within the Qtz II vein (Fig. 6.3g, cfr. Chapter 6).

Sulphides in "wet" brittle deformation zones are commonly associated with the ingress of hydrothermal fluids within the dilatant volumes of faults, which generally localise significant slip during transient episodes of high fluid pressure (i.e., the "fluid-rich faults" of Cox, 2016). Sulphides are, additionally, of interest because it has been shown that they form good tracers of element mobility within brittle systems during deformation (e.g. Diehl et al., 2012) and thus offer the potential to better understand the micromechanics of strain localization and the feedbacks between deformation and phase chemistry.

Nodules of pyrite, in particular, are abundant in rocks affected by hydrothermal alteration related to magmatic intrusions and/or in many sedimentary rocks (e.g. Tvalchrelidze, 1980; Berner, 1970). They can thus be important constituents of fault rocks formed at the expense of these lithologies, possibly even contributing to the overall rheology of the fault zones hosting them. An integrated, detailed study of pyrite has thus the potential to clarify the nature of the processes of deformation-induced mass transport within chemically reactive fault zones and the effects and implications thereof. A few microstructural studies of pyrite have already suggested that microstructures produced by mineral deformation can cause the relative enrichment of certain elemental species that otherwise are not present in the host minerals (e.g. Reddy and Hough, 2013; Fougerouse at al., 2019, Dubosq et al., 2018; Dubosq et al., 2019). Understanding why this happens in naturally deformed pyrite might provide an insight into the capability and efficiency of faults to transport elements and fluids of different composition when slipping for the first time or during multiple, subsequent reactivations. In the perspective of deep nuclear waste repository studies, this can be thought of as an appropriate proxy of fluid and element transmissivity within and along brittle discontinuities affecting the rock volume hosting the repository, a topic of clear relevance to the long-term stability of these facilities.

Studies of grain-scale elemental mobility in pyrite and other sulphides has recently become of interest to also investigate the minor and trace element geochemistry of ore deposits (e.g. Reddy and Hough, 2013; Dubosq et al., 2018; Dubosq et al., 2019a; Dubosq et al., 2019b; Fougerouse et al., 2019). Detailed studies of element mobility within sulphides during deformation and metamorphism are, to date, still very few (e.g. Dubosq et al., 2018; Dubosq et al., 2019; Fougerouse et al., 2016). The study presented here was thus carried out aiming to contribute further to this interesting research topic. The very detailed reconstruction performed in this study of BFZ300, of its deformation history and of the boundary conditions that steered its multiple reactivations represents a very solid base to start the investigation of the details of how localization drives elemental mobility during "wet" brittle faulting at temperatures up to 305° C (see Chapter 10). Sulphide aggregates in the BFZ300 are mainly formed by a sulphide matrix made by pyrite, sphalerite, galena and chalcopyrite. Minor sulphide aggregates were characterised and studied by combining microstructural analysis, state-of-the-art laser ablation mapping and electron back-scattered diffraction to shed light through a comprehensive and multi-technique approach on the deformation mechanisms that deformed pyrite within the Qtz II vein. This, in turn, allows us to also better understand the sulphide net contribution to the overall elemental mobility and strain localization in a bi-phase system (i.e. quartz-sulphides). We believe that, given the general representativeness of BFZ300 for the processes of wet faulting in the BDTZ, results presented below are of general validity and may well apply to other fault zones worldwide.

11.1 Analytical Methods

This study is focussed on samples from drill core PH21. The core intercepts BFZ300 at ca. -421 m b.s.l. (Fig. 11.1a, see also Fig. 3 for drill core location along the fault). Two thin sections (one petrographic thin section, PH21_1, and one doubly polished section for fluid inclusion analysis, PH21_2) were prepared. They were cut orthogonally to the vein wall and parallel to the vein opening direction and used for petrographic analysis of the quartz-sulphide vein, for elemental imaging of the authigenic pyrite grains and for crystallographic orientation analysis on pyrite grains. Their accurate location within the drill core is shown by the yellow dashed line of Fig. 11.1b.

Multi-elemental 2D maps were acquired by means of laser-ablation inductively coupled plasma time-of-flight mass spectrometry (LA-ICP-TOFMS) at the Laboratory of Inorganic Chemistry of the ETH Zurich in Switzerland. For more details on the working conditions the Reader is referred to Chapter 4.
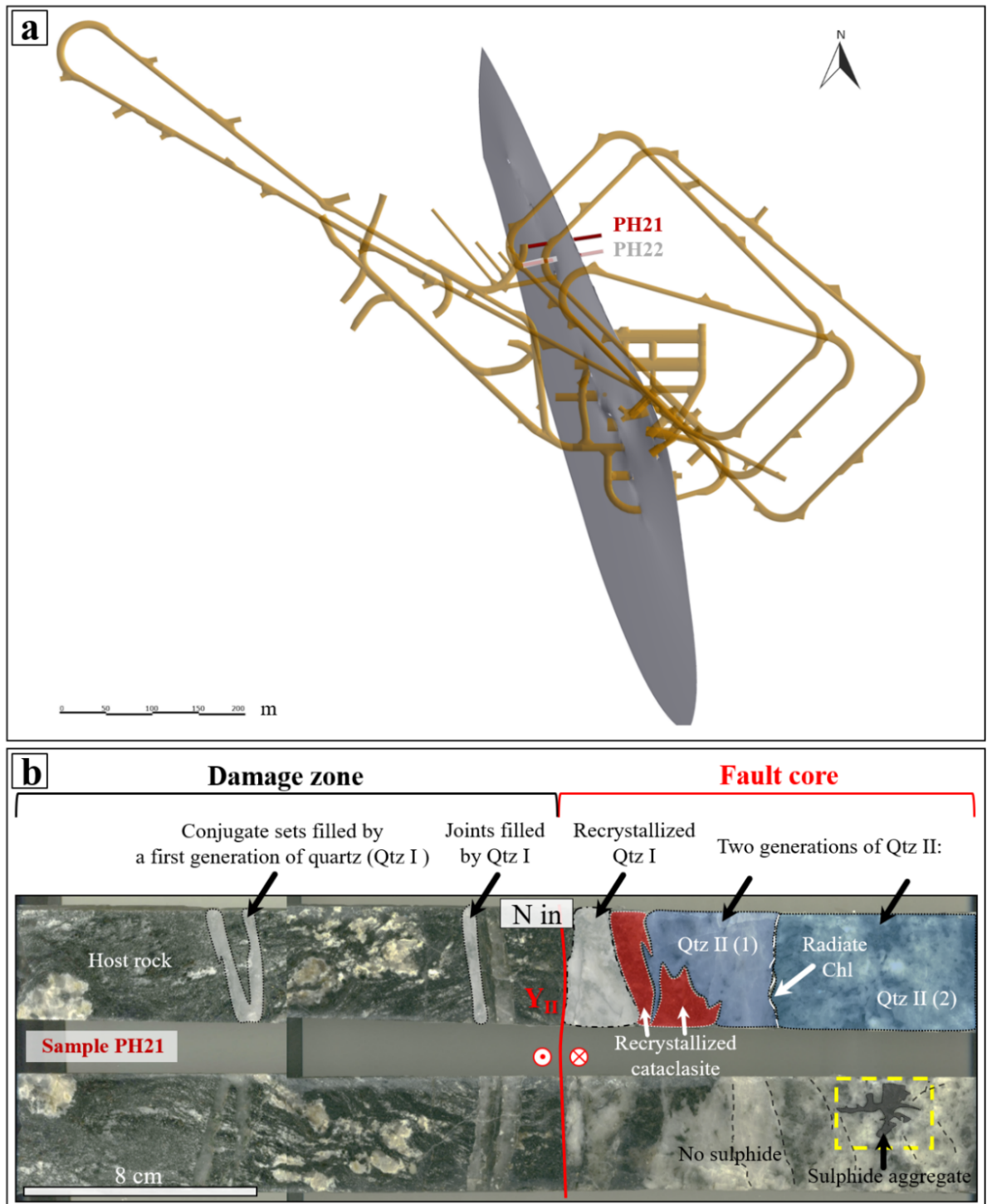
Figure 11.1. Location of drill core PH21, (a) which intercepts BFZ300 at ca. -421 m b.s.l. PH21 is horizontal and trends 080°. The grey 3D surface is the modelled BFZ300 fault plane, shown here as seen from above together with the yellow layout of the existing underground infrastructure. (b) Structural interpretation of drill core PH21, highlighting that the BFZ300 damage zone is characterized by Qtz I-filled conjugate sets of fractures and joints crosscutting the migmatitic host rock. The latter is characterized by geometrically irregular leucosome and melanosome layers. The internal, NS-trending principal slip zone (Y_{II}, indicated in red) separates the damage zone from the fault core, which is characterized by the recrystallized Qtz I vein and by two distinct Qtz II veinlets. Indeed, from detailed structural observations it appears that the Qtz II vein is characterized by two distinct, parallel veins, one made of quartz and a second containing also centimetric

sulphide aggregates enclosed within the quartz. The two veinlets are separated by a discrete surface decorated by radiate chlorite crystals stretched orthogonally to the vein boundaries. This evidence suggest that the Qtz II veins may have formed during a deformation history defined by incremental opening events (i.e. a crack-seal process). The yellow dashed line shows the location of the thin sections of Figure 11.3a and 11.4, which were used to study the details of Qtz II microstructures close to the sulphide aggregates.

For more details about the BFZ300 mesoscopic structures the reader is also referred to Chapter 5 and related figures.

Crystallographic orientation data were obtained from automatically indexed EBSD patterns collected on a JEOL 6610 VP-SEM at the Electron Microscopy Centre of the University of Plymouth, UK. Thin sections were SYTON polished before EBSD analysis. Working conditions during acquisition of EBSD patterns were 20 kV, 70° sample tilt, high vacuum mode, and a working distance between 17 and 23 mm. EBSD patterns were acquired on rectangular grids by moving the electron beam at a regular step size of 1 μm. EBSD maps were acquired next to the areas analysed with LA-ICP-TOFMS and include part of the same pyrite grain(s) analysed with LA-ICP-TOFMS, as well as a few adjacent grains. The acquired EBSD patterns were automatically indexed using the AZtec software and processed with the CHANNEL 5 software from Oxford Instruments.

11.2 Processing and presentation of EBSD data

Non-indexed solutions were replaced by the most common neighbour orientation to reduce data noise, following the procedure tested by Prior et al., (2002) and Bestmann and Prior (2003). Grains with an area smaller than 5 pixels were discarded from the dataset so as to minimize misindexing errors. EBSD data are presented in the form of:

1) Inverse Pole Figure (IPF) maps;

2) Equal area, lower hemisphere pole figures of crystallographic orientation;

3) Local misorientation (LM) maps, and

4) Texture component (TC) maps.

11.2.1 Inverse Pole Figure maps

IPF maps were oriented with respect to the direction perpendicular to the vein wall (direction X_0, with vein wall corresponding to direction Y_0). IPF maps are used to show the crystal orientation at each data point, according to the colour-coded inverse pole figure of cubic minerals (pyrite). These maps are used to plot all crystallographic directions that align with one of the sample's reference directions. In other words, the sample's X, Y or Z

directions are plotted in the crystallographic reference frame. Owing to crystal symmetry, only a portion of the crystallographic coordinate system needs to be shown.

On the IPF maps, misorientation angles between neighbouring data points were grouped into 1) low-angle boundaries, with misorientation between 1.5°and 10°, and 2) high-angle boundaries, with misorientation >10°. Low-angle boundaries are shown by white lines, whereas high-angle boundaries are shown in black.

11.2.2 Pole Figures

Pole figures were oriented parallel to the Y_0-X_0 plane. Crystallographic data in the pole figures are plotted as one-point-per-pixel. Considering the common slip system documented in naturally and experimentally deformed pyrite (Van Goethem et al. 1978; Cox et al., 1981; Graf et al., 1981; Levade et al., 1979; Barrie et al., 2008; Reddy and Hough, 2013; Dubosq et al., 2019), the following directions have been plotted: <100>, <111> and <110>. Slip planes were reconstructed by boundary trace analysis to identify the active slip system (see below).

11.2.3 Local misorientation maps

Local misorientation (LM) maps were used to highlight the distribution of angular misorientation within the analysed pyrite grains. These maps are colour-coded according to the degree of misorientation between each pixel and its neighbouring cluster of pixels within a radius of 7x7 pixels. The maximum misorientation used for this study is 3°, which corresponds to the red colour in the maps (e.g., Figs. 11.9b and 11.10b). This kind of map has the potential to highlight the presence of deformation substructures within the analysed grains, such as, for example, low-angle boundaries or the general distortion of a crystal lattice. The misorientation is computed across more pixels rather than just taking the misorientation angle between two neighbouring pixels. The algorithm calculates the average misorientation between each pixel and the surrounding pixels within an a priori established area and assigns a mean misorientation value to that pixel. The pixel is then colour-coded according to its mean misorientation value.

LM maps are crucial in order to detect and quantify even very minor bending and distortions (within 3° of resolution) of the crystal lattice.

11.2.4 Texture Component maps

This type of maps visualizes the relative misorientation (in this study up to 5°) of every analysed point with respect to a chosen reference point (reference orientation). The reference point is chosen by several trials, analysing different areas within the single grain. The map is colour-coded according to the misorientation angle, where the latter is calculated as the smallest angular difference (considering symmetry) between the chosen reference point and each other pixel of the same phase.

Texture component maps are useful to spatially visualize the degree of misorientations from the chosen reference point and, so, to investigate and quantify intracrystalline lattice distortions. Misorientation profiles have also been used to evaluate the mechanisms contributing to the intracrystalline distortions.

11.3 Boundary trace analysis

Boundary trace analysis (e.g. Prior et al., 2002; Reddy et al., 2007; Barrie et al., 2008; Piazolo et al., 2008; Menegon et al., 2011) is a method for determining the most feasible geometry of a low-angle boundary resulting from the operation of a specific slip system from the analysis of pole figure data. Given that a full analysis of the nature of a low-angle boundary would require information about the full 3D geometry of the boundary, ideal tilt or twist boundary models are generally implemented. These methods consider the dispersion of the crystallographic orientation data around a rotation axis within a sampled area or along a transect chosen from within an area containing the trace of a low-angle boundary as per the related textural component map. The rotation axis is identified on the pole figures as the direction associated with no or little dispersion (Lloyd and Freeman, 1994). In the case of a tilt boundary, the boundary plane must contain the 2D boundary trace and the rotation axis. The plane at high angle (ideally at 90°) to the boundary plane, and containing the rotation axis, represents the most likely active slip plane and thus contains the slip direction. On the contrary, in the case of a twist boundary, the rotation axis is orthogonal to the boundary plane.

In this study, we used boundary trace analysis to characterize the nature of low-angle boundaries in which misorientation profiles showed a progressive lattice strain at increments of <1° and we relied on an ideal tilt boundary model.

11.4 Drill core structural analysis

The general microstructural analysis of the Qtz II vein has already been presented in Chapter 6. In it, however, no distinction was made between quartz microstructures within domains immediately adjacent to the sulphide aggregates and microstructures recognized in quartz crystals located at several centimetres (c. 4-5 cm) from the sulphides. In the following, a more detailed structural analysis of the Qtz II vein is thus presented, documenting that there occurs an interesting and apparently systematic microstructural variability between microstructural sites in the proximity of minor sulphide aggregates and far away from them. We interpreted this variability as indeed correlated to the presence of the sulphides within the studied quartz-vein system.

Macroscopic observation of drill core PH21 (Fig. 11.1b) suggests that Qtz II is not a single massive vein but, instead, it is formed by at least two distinct generations of quartz arranged within two distinct veinlets (Fig. 11.1b). The first is adjacent to the Qtz I vein (Qtz II (1), Fig. 11.1b) and is characterized by a milky-white type of quartz, by abundant fluid inclusions, and by the absence of sulphides. This vein is cut across by a few fractures, mostly oriented parallel to the general BFZ300 strike (Fig. 11.1b).

The second vein (Qtz II (2), Fig. 11.1b) is right on the side of the Qtz II (1) vein. It is formed by a milky-white type of quartz containing minor sulphide aggregates with diameters ranging between 8 and 20 mm. Sulphide aggregates are mainly formed by pyrite, sphalerite, galena and chalcopyrite. Chalcopyrite is mainly present as part of "chalcopyrite disease" alteration textures within sphalerite crystals (e.g. Barton and Bethke, 1987, see also Chapter 6). Compared to the Qtz II (1) vein, the Qtz II (2) vein is pervasively affected by a dense network of fractures (Fig. 11.1b).

Chlorite along the surface separating the two veins has a radiate (euhedral) texture and single crystals have an average size ranging between 300 and 800 µm (Fig. 11.1b).

A schematic interpretation of the Qtz II vein is presented in Fig. 11.2a.

11.5 Microstructural analysis

11.5.1 Qtz II (2) vein: a closer look

Microstructural analysis of the second-generation vein (Qtz II (2)) demonstrates that quartz therein is characterised by varying grain size, distinct preservation of primary structures (i.e. growth structures and primary fluid inclusion trails) and different patterns of fractures as a function of its distance to the sulphide aggregates (Figs. 11.2 b-e).

In particular, parts of the Qtz II (2) vein located c. 5 cm or more away from sulphide aggregates are characterized by an average coarse grain size, with individual crystals ranging in size between 300 μm and 1 cm (Fig. 11.2b). Those grains contain well preserved and clear primary growth structures (Fig. 11.2c). Chlorite is present as an accessory phase generally with a radiate texture.

Other Qtz II (2) domains in proximity of the sulphide aggregates contain, instead, a more heterogeneous, yet generally finer, grain size ranging from 100 μm to 5 mm (Fig. 11.2d).
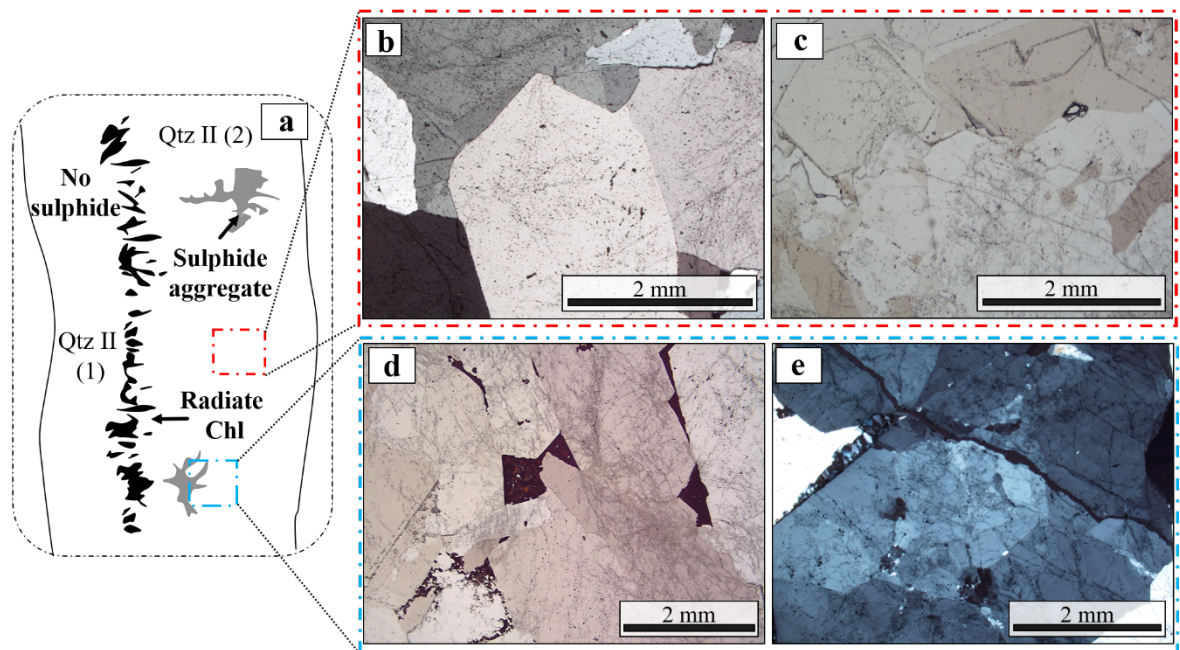
Figure 11.2. (a) Schematic representation of the Qtz II vein in the studied drillcore, where two different generations of quartz veins are recognizable (named Qtz II (1) and Qtz II (2)). Quartz of the second-generation vein, Qtz II (2), exhibits different microstructural features depending on its distance to the sulphide aggregates. (b) In the central part of the vein, 4-5 cm away from the sulphides, Qtz II (2) crystals exhibit a lower degree of fracturing and no evidence of crystal plasticity. (c) Well preserved primary growth structures are clearly visible. (d) Close to the mineralized areas, Qtz II (2) is pervasively deformed by a dense network of fractures. Most fractures are intergranular and/or transgranular, suggesting their secondary nature. (e) Close to the sulphides, Qtz II (2) also exhibits evidence of incipient crystal plasticity such as undulose extinction.

Here, quartz crystals also exhibit evidence of undulose extinction (Fig. 11.2e) and are also affected by a dense network of intergranular and intragranular fractures (Fig. 11.2d). In Qtz II (2) domains close to the sulphides, quartz primary growth structures are more difficult to discern as they are dismembered by the pervasive fracture network (Figs. 11.3a, b). Along these growth zones, however, fluid inclusions typically exhibit re-equilibrated textures (Fig.

11.3c, d), probably produced by repeated intracrystalline deformation and later brittle overprints.

In summary, the Qtz II (2) vein is characterized by numerous structural domains bearing evidence of different textures, each representative of a different deformation style.
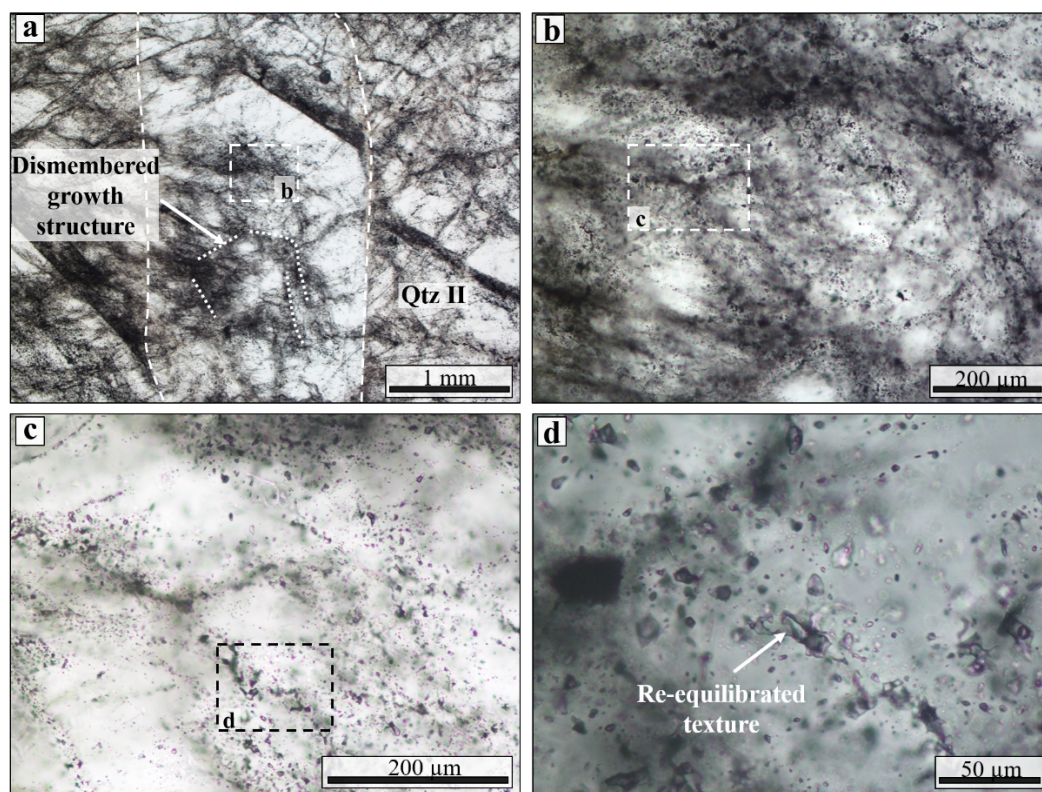
Figure 11.3. Petrographic analysis of fluid inclusions of Qtz II (2) crystals close to sulphide aggregates (sample: PH21_2). a) Optically continuous quartz crystal (highlighted by white dashed line) with an internal dismembered primary growth zone. b) Enlargement of one of the dismember growth surfaces within the hosting crystal. Intense brittle intracrystalline deformation accommodated by numerous fractures within the crystal is evident. c) Enlargement of a portion of a primary growth zone, showing (d) a re-equilibrated cluster of fluid inclusions.

11.5.2 Sulphide aggregates

At the microscale, sulphide aggregates appear as complex, composite and interdigitated bodies embedded within the host quartz vein. They are formed by a sulphide matrix made of pyrite, sphalerite and galena and chalcopyrite. Chalcopyrite is not very abundant and when presents it is in the form of alteration textures of largest sphalerite crystals. Because of its low abundance it is not treat in detail in the following petrographic description of sulphide aggregates.

At the scale of the thin section, pyrite, sphalerite and galena show variable grain size, different brittle deformation patterns and a distinct degree of chemical alteration. Textures

range from euhedral to anhedral, in accordance to their position from the Qtz II (2) vein boundaries. Several subdomains are therefore recognizable on the basis of petrographic differences.

One representative aggregate is described herewith in detail (Fig. 11.4) and we use this representative example to describe the standard petrographic features recognised in all the studied sulphide aggregates.
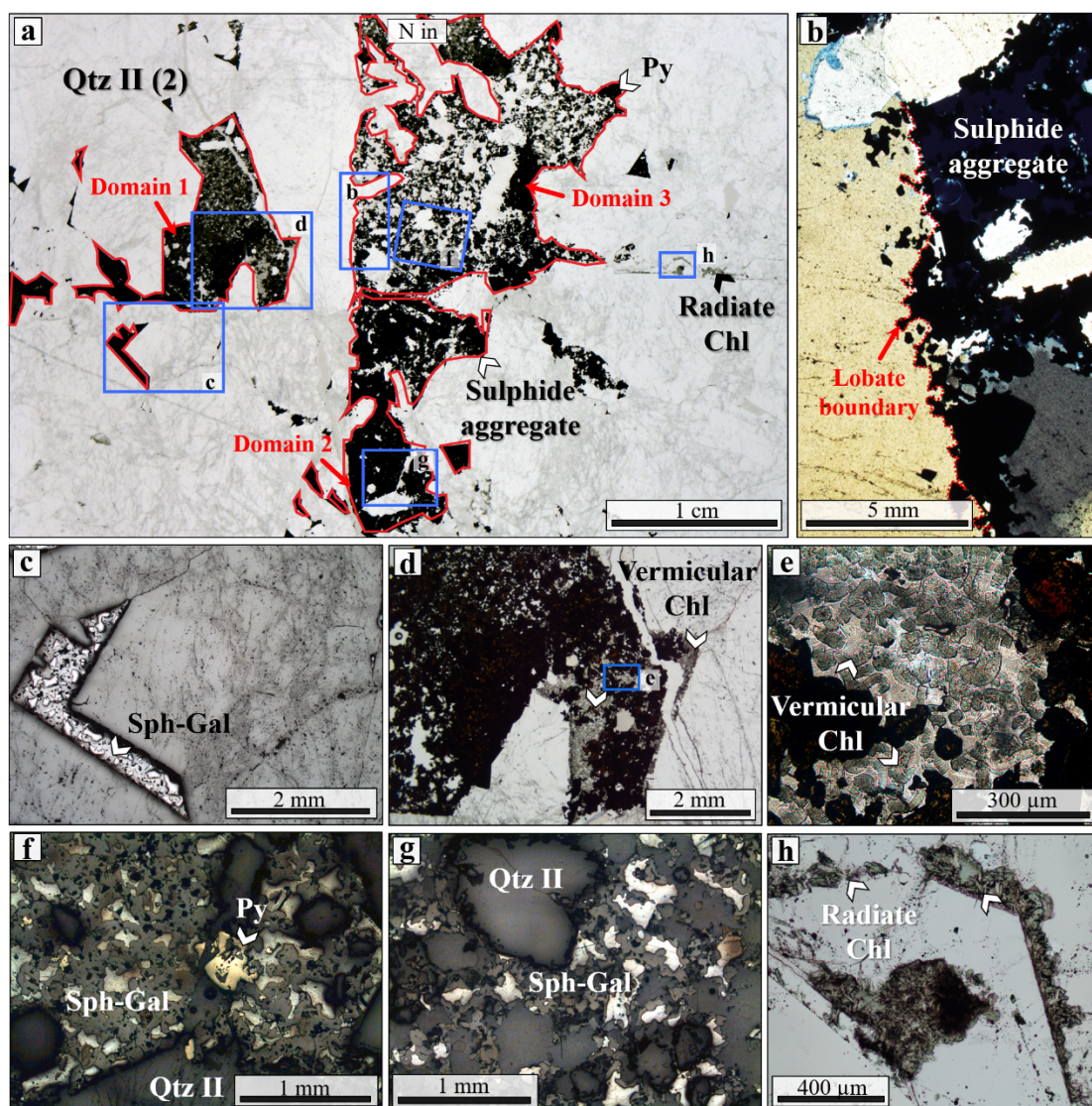
Figure 11.4. Microtextural characteristics of a representative aggregate of sulphides within a dilatant zone in the Qtz II (2) vein (sample: PH21_1). (a) Stitched photomicrographs of an aggregate of sulphides enclosed within quartz vein (parallel nicols). Thin section location is shown by the dashed yellow line in Fig. 11.1b. Subdomains (i.e. Domain 1, Domain 2 and Domain 3) are marked with red lines. (b) Domain 2 and Domain 3 are characterized by an irregular, lobate boundary, suggesting dissolution and local resorption along the quartz-sulphide interface. (c) Domain 1 is characterized by massive mineralization and it is mainly concentrated along the quartz crystal boundaries. (d) Vermicular chlorite associated with quartz-sulphides of Domain 1. (e) Vermicular chlorite is organized in small pockets (<1mm), which are mainly arranged along

intercrystalline fractures. (f) Massive sulphide mineralization of Domain 2. Euhedral quartz crystals are also visible within the sulphide matrix. (g) The mineralization within Domain 3 is dismembered in numerous smaller bodies with general anhedral textures. (h) Radiate chlorite associated with Qtz II (2) vein located in the proximity of the vein wall.

To the left of the Qtz II (2) vein in the analysed domain there occurs a first sulphide subdomain (Domain 1, Fig. 11.4a) that is about 10 mm long and has a massive texture. The mineralization therein is concentrated along the interface boundary to neighbouring quartz crystals (Fig. 11.4c). A few quartz crystals up to c. 2 mm in size are interspersed within the sulphide matrix (Fig. 11.4d). Small pockets (< 1 mm) of vermicular chlorite are locally visible along and close to the edges of the mineralized body (Fig. 11.4d), following the trace of thin intercrystalline fractures (Fig. 11.4d). Vermicular chlorite crystals have a grain size ranging between 50 μm and 100 μm (Fig. 11.4e). Vermicular chlorite associated with late fractures suggest that it precipitated from a late event of fluid ingress and chemical alteration likely induced by fault reactivation.

At the centre of the Qtz II (2) vein the sulphide aggregate is disarticulated into two distinct subdomains (Domain 2 and Domain 3, Fig. 11.4a). The mineralization within the two domains shows different degrees of deformation and even textures.

Domain 2 is located in the lower part of the sulphide aggregate (Fig. 11.4a) and it has small dimensions (5 mm in length). The sulphide mineralization exhibits a massive texture (Fig. 11.4f). There are also a few grains of euhedral quartz up to 3 mm in length included within the sulphide matrix (Fig. 11.4f). Quartz crystals included within the mineralized body are characterised by a heterogeneous grain size, ranging between 1 and 4 mm (Figs. 11.4a, f).

Domain 3 is located in the upper part of the sulphide aggregate and it is c. 15 mm in length (Fig. 11.4a). There, the mineralization is less massive than in the other domains as it appears to be dismembered into numerous smaller bodies (Fig. 11.4g), with general anhedral textures. Euhedral pyrite up to 3 mm in size is found in the interdigitated tips of the central main body (Fig. 11.4a).

The edges of Domain 2 and Domain 3 close to the centre of the quartz vein are characterized by an irregular and lobate morphology (Fig. 11.4b). Along their entire edge there are also several and smaller (< 2 mm) sulphide grains, which are isolated and appear to be apophyses of the main mineralized body (Fig. 10.4b). The lobate boundary follows a fracture trace (Fig. 11.4b).

Petrographic analysis of the host quartz shows that host quartz is affected by a diffuse network of fractures, many of them marked by trails of fluid inclusions (Figs. 11.4a, c).

Radiate chlorite also sporadically occurs within the host quartz, and it is localized along the boundaries of quartz grains (Fig. 11.4e). Chlorite crystals are less than 200 μm in length. Pyrite is one of the main constituent minerals of the studied sulphide aggregates (Fig. 11.5). It displays different textures and different degrees of deformation as well as variable chemical substitution by sphalerite and galena close to prominent fractures.
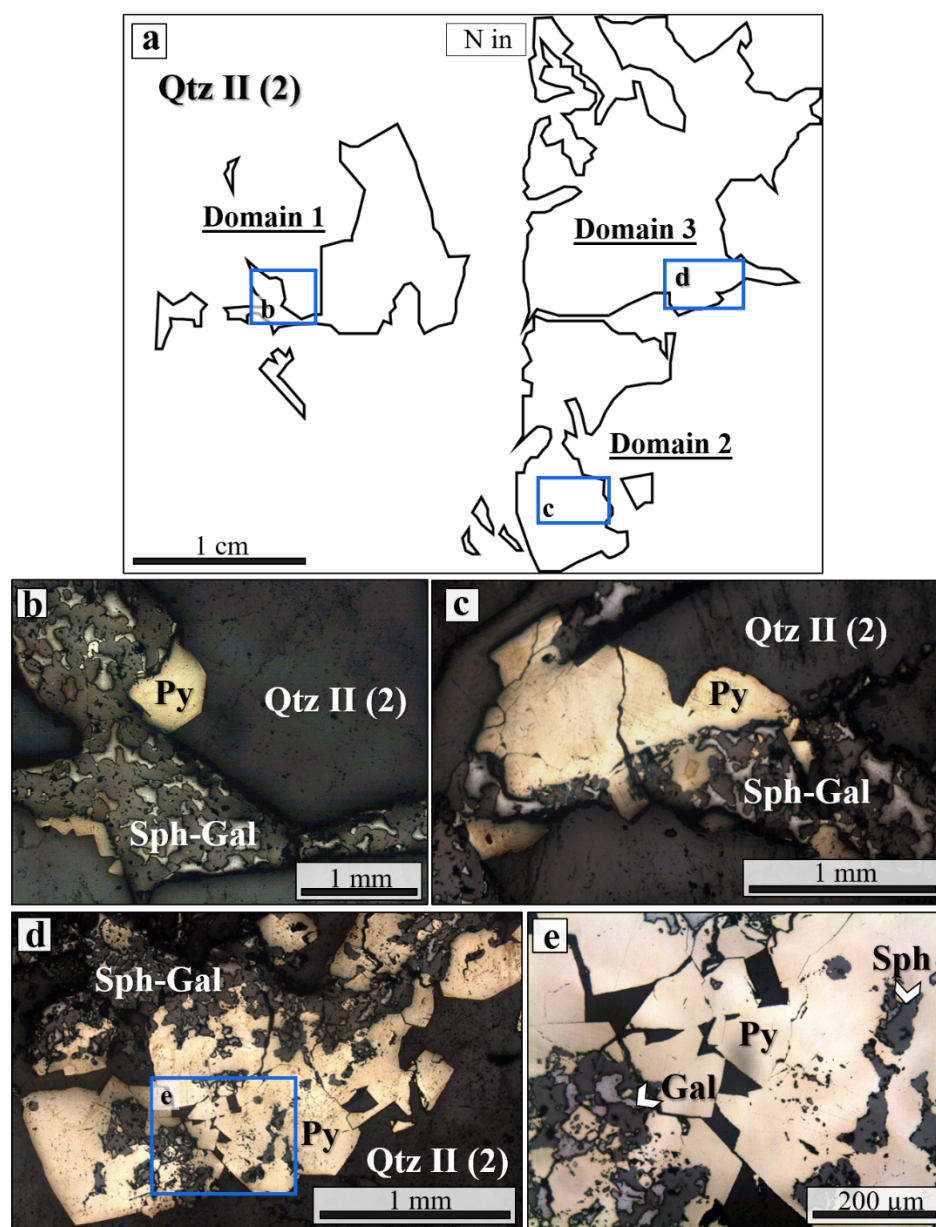
Figure 11.5. (a) Sketch of the sulphide aggregate shown in Fig. 11.4 and subdivision into different structural domains. Pyrite contains the results of different deformation episodes and styles, as indicated by microstructures that can be ascribed to the effects of mechanical comminution by cataclastic flow and those attesting to later events of replacement by sphalerite and galena. (b) In Domain 1, pyrite exhibits a general euhedral texture, with minor, only locally visible deformation (sphalerite and galena replacement in the left part of the crystal). (c) Pyrite within Domain 2 displays an anhedral texture. Replacement by sphalerite and galena is locally observed mainly along the pyrite crystal boundaries and follows the position of thin brittle

fractures. (d) Pyrite of Domain 3 displays instead the most intense deformation, as documented by cataclastic domains and severe replacement of pyrite by sphalerite and galena along discrete fractures. (e) Blown-up view of the replacement of pyrite by sphalerite and galena in the proximity of intragrain fractures and crystal edges. All panels except panels d and e are oriented bottom up with respect to the yellow rectangle in Fig. 11.1b.

Pyrite grains within Domain 1 show an euhedral texture and a grain size ranging between 600 and 800 μm (Fig. 11.5b). Petrographic analysis of that domain did not reveal the presence of intragrain brittle structural features within pyrite. Locally, pyrite is replaced by sphalerite and galena probably in response to late deformation and fluid flow, which caused irregular grain boundary geometries (for example, in the left side of the analysed pyrite grain of Fig. 11.5b).

Pyrite grains within Domain 2 are characterised by a slightly anhedral texture and average grain size in the 1.5-2 mm range (Fig. 11.5c). Pyrite contains several intragrain structures, with various orientations and dimensions but it also exhibits a higher degree of replacement by sphalerite and galena (Fig. 11.5c). Replacement mainly occurs along the edges of pyrite crystals (Fig. 11.5c).

Pyrite of Domain 3 is characterized by a higher degree of deformation and replacement.

Even if a general euhedral texture is still recognizable, large pyrite grains are comminuted into small grains creating a heterogenous grain size distribution, ranging between 200 μm and 800 μm (Fig. 11.5d). The smallest grains exhibit sharp edges contributing to their overall angular geometry. The largest pyrite grains are also affected by both intracrystalline and intergranular fractures. Some of these fractures are barren while others are filled by sphalerite and galena (Fig. 11.5d). Also, pyrite within Domain 3 contains more solid inclusions than that of the other subdomains, with most occurrences along fractures filled by a late event of mineralization.

In summary, petrographic analysis demonstrates that sulphide aggregates can be subdivided into at least three structural subdomains based on variable textures, grain size, brittle deformation patterns, style of intragrain strain accommodation and chemical alteration. Petrographic analysis also suggests that pyrite is cogenetic to quartz, while sphalerite and galena are the result of a late event of reactivation and fluid ingress within the system, probably as a result of strain localization during a later reactivation of BFZ300.

11.6 High resolution, elemental imaging of pyrite

Three distinct areas were identified in Domain 1, Domain 2 and Domain 3 to investigate in more detail the spatial distribution of trace elements within pyrite grains. Pyrite grains characterised by different degrees of deformation and replacement were therefore selected as representative examples for each of the described domains to map the intragrain elemental distribution induced by reactivation and strain accommodation. Pyrite was initially analysed by LA-ICP-TOFMS and the obtained semi-quantitative elemental images are presented below.
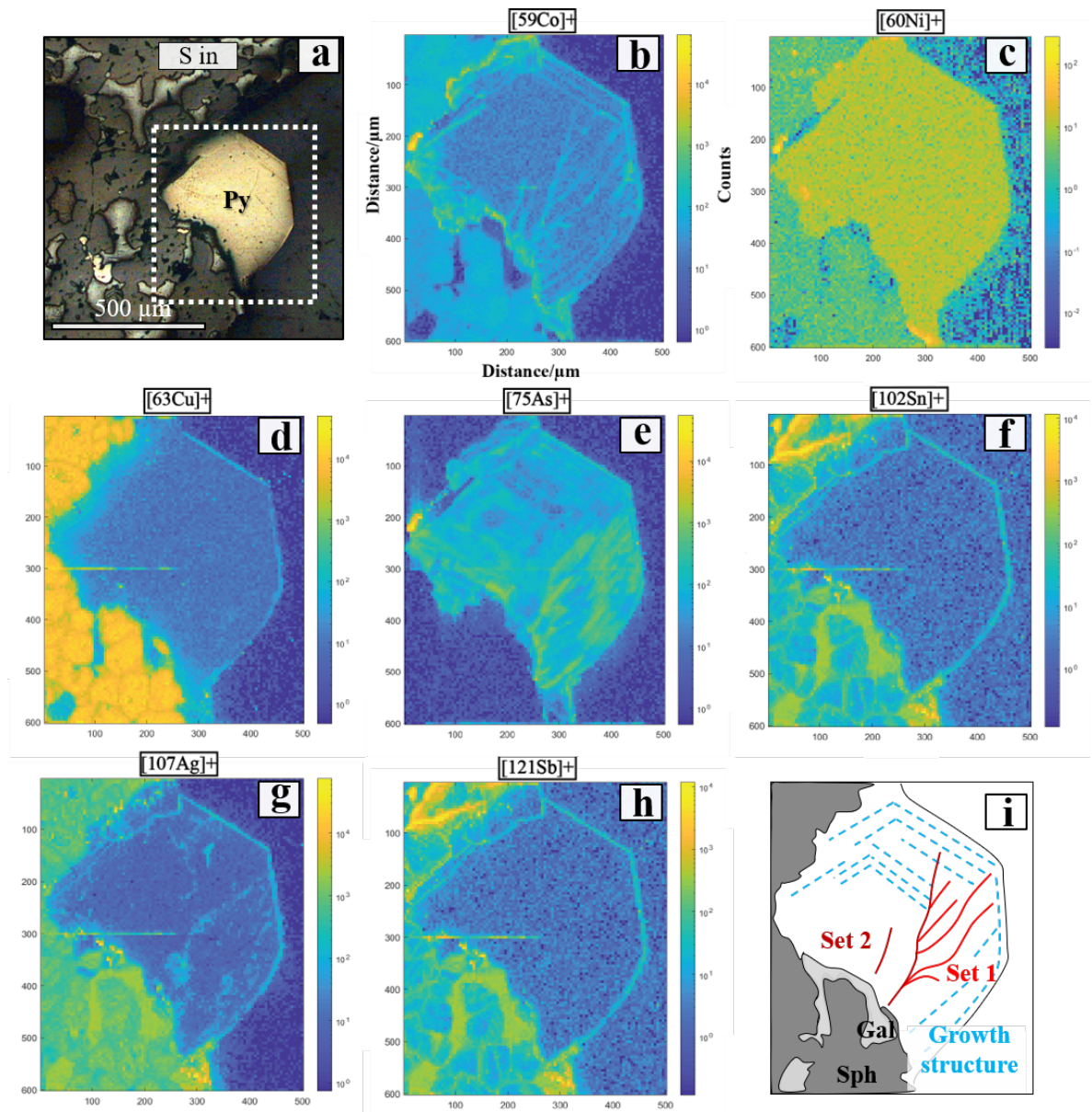
Figure 11.6. Example of LA-ICP-TOFMS elemental imaging of almost undeformed pyrite from Domain 1. (a) Reflected light photomicrograph of the pyrite crystal from Figure 11.4h. The white dashed line defines the area covered by laser ablation. (b-h) Chemical maps showing the qualitative elemental distribution of trace

elements within the analysed area. The signal intensity is in counts per second (Counts) while the dimensions of the analysed area are given in μm. The signal intensity follows the coloured reference bar. High counts are identified by shades of colour between dark green and yellow and lower counts are shown by shades of colour between dark blue and light blue. (i) Interpretation of the main spatial patterns highlighted by the distribution mapping of trace elements.

The acquired dataset on the spatial distribution of chemical species within pyrite grains shows that enrichment or depletion of specific elements within the studied grains produces peculiar features that can be resolved well at the scale of the performed analysis. In particular, the elemental distribution maps of Co ([59Co]+), Ni ([60Ni]+), Cu ([63Cu]+), As ([75As]+), Sn ([102Sn]+), Ag ([107Ag]+) and Sb ([121Sb]+) identify and highlight remarkably well both primary growth structures and fractures (Figs. 10.5a, 10.6a, 10.7a). Those elements were indeed selected for the characterization of trace elements spatial distribution within the selected pyrite grains from the distinct structural domains. Element relative concentrations are given in counts per second and follow a logarithmic scale. Semiquantitative elemental concentrations are here given in a logarithmic scale to widen the signal of trace elements that for definition are characterized by lower concentrations and, therefore, to make them and their spatial distribution more visible within the elemental images.

Figure 11.6 presents a selection of elemental maps acquired on a pyrite grain from Domain 1 (Fig. 11.6a). The chemical distribution of Co and As constrain the presence of well-preserved primary growth structures, with the typical banded growth features parallel to the crystal edges. Growth structures are remarkably well seen in the upper and central part of the pyrite grain (Figs. 11.6b, e).

These elemental maps also show that primary growth structures are locally crosscut by at least two distinct sets of fractures (Figs. 10.6b, e). One set of fractures are oriented at 60° (named Set 1, Fig. 10.6i) from the thin section horizontal plane, which is consistent with the direction of opening of Qtz II vein. A second set is oriented at 80° (named Set 2, Fig. 11.6i). Co also presents high counts in the external left boundary of the pyrite grain, close to the sphalerite-galena aggregate (Fig. 11.6b). Strikes were taken clockwise from the top of the figure.

The elemental distribution of Ni is characterized by a homogenously high signal within the pyrite grain whereas it drops to lower counts in the left-side of the analysed area,
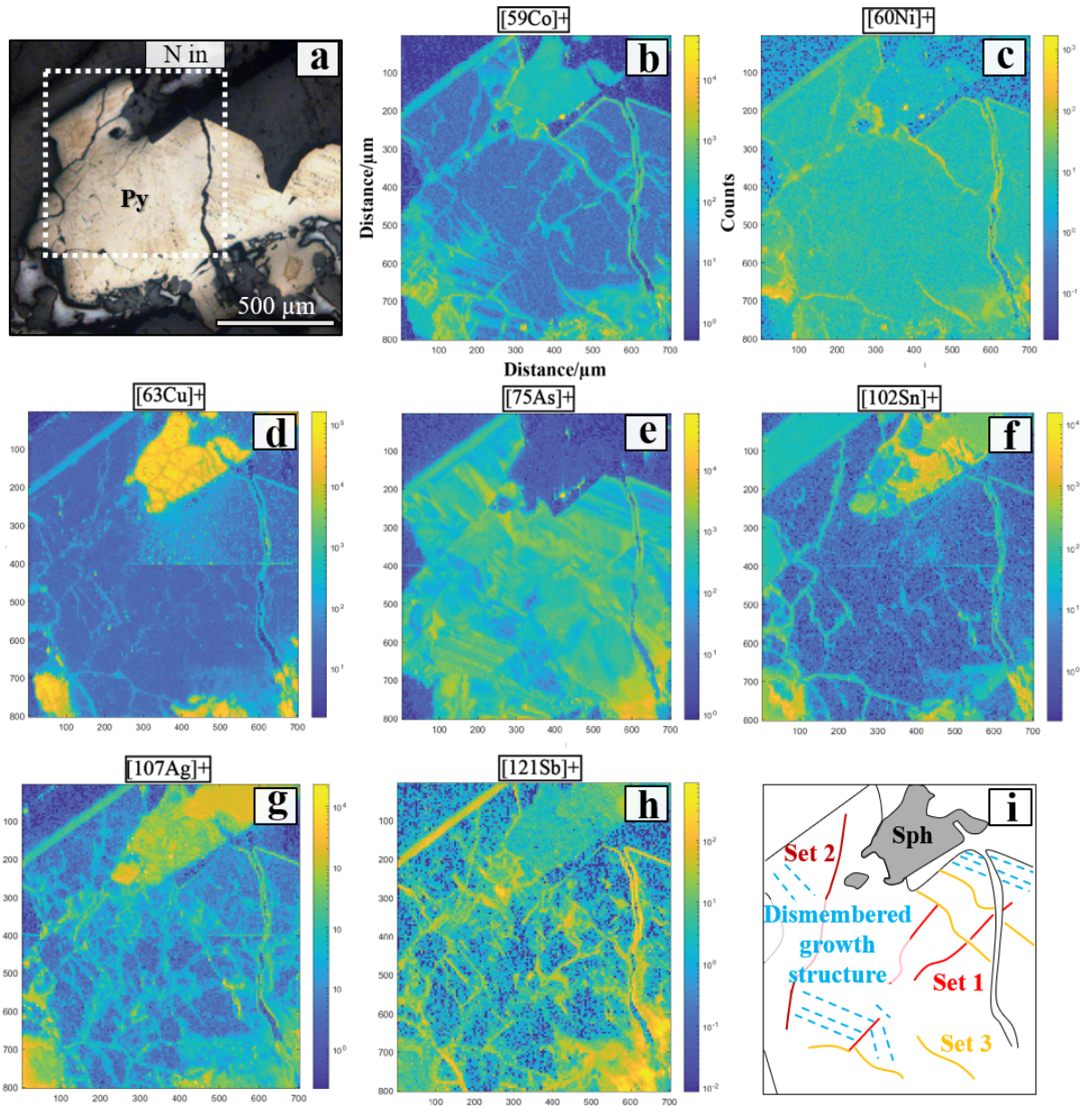
Figure 11.7. LA-ICP-TOFMS elemental imaging of slightly deformed pyrite in Domain 2. (a) Reflected light photomicrograph of the pyrite crystal from Figure 11.4f. South direction points upwards. The dashed white line defines the area analysed by laser ablation. (b-h) Chemical maps showing the qualitative elemental distribution of trace elements within the analysed area. The signal intensity is in counts per second (Counts) while the dimensions of the analysed area are given in µm. (i) Interpretation of the main spatial patterns highlighted by distribution mapping of trace elements.

close to the sphalerite-galena aggregate (Fig. 11.6c).

On the other side, the elemental distribution of Cu shows a homogenously high signal associated with the sphalerite-galena aggregate whereas counts are very low, or even zero, within the pyrite (Fig. 11.6d). Also, the Cu chemical map shows that the sphalerite-galena body is cut across by several fractures (Fig. 11.6d).

Chemical maps of Sn, Ag and Sb indicate that these elements are mainly concentrated on the left-side of the analysed area, in association with the sphalerite-galena aggregate and they also highlight a fracture network within the mineralized body (Figs. 11.6f-h), the same identified by Cu chemical map.

Figure 11.7 shows a selection of elemental maps based on the same elements of Fig. 11.6. These show the acquired data from pyrite within Domain 2. Pyrite is therein characterized by a slightly anhedral texture (Fig. 11.7a).
The chemical distribution of Co and As highlights the presence of primary growth structures, similar to what presented before (Figs. 11.7b and e). Nonetheless, primary growth structures are not that well defined and preserved here. They are, instead, discontinuous and dismembered within the mapped pyrite grain. Some broken-up fragments of primary growth structures are visible in the left lower side of the analysed area and in the upper part of the grain (Figs. 11.7b and e).

The relative concentration of Co, Ni, Cu and Sn highlights the presence of a pattern of fractures. Along the fracture traces the relative concentration of those elements increases with respect to the other parts of the grain. Chemical maps in summary show that the studied pyrite grains are invariably crosscut by at least three sets of fractures (Figs. 11.7b, c, d and f). A first set is oriented at55° (named Set 1, Fig. 10.7i). A second set of fractures is at 75° (named Set 2, Fig. 10.7i). Another set is oriented at 45° (named Set 3, Fig. 10.7i).

The elemental distribution of Ag and Sb indicates a more complex fracture pattern within the pyrite, with a chessboard distribution affecting the entire grain that leads to polygonization of the internal structure. Along these fractures, the Ag and Sb signal intensity remains higher than in the surroundings (Figs. 11.7g-h).

Figure 11.8 shows the selection of elemental maps collected from the highly deformed pyrite of Domain 3. Pyrite therein is characterized by a variable grain size, where the small grains are the results of the mechanical comminution of larger grains. An almost euhedral texture is locally still recognizable, despite the high degree of deformation (Fig. 11.8a).

Here, primary growth structures are only faintly outlined by the elemental distribution of Co and As (Figs. 11.8b, e). Primary growth structures are discontinuous and mainly located in the pyrite grains at the bottom of the analysed area.
Ni elemental distribution clearly highlights the fracture network running across pyrite grains (Fig. 11.8c). Along those fractures, Ni has a high signal intensity. It also displays a relatively high concentration within the central part of the central grain, highlighting a zone of interconnectivity between fractures.
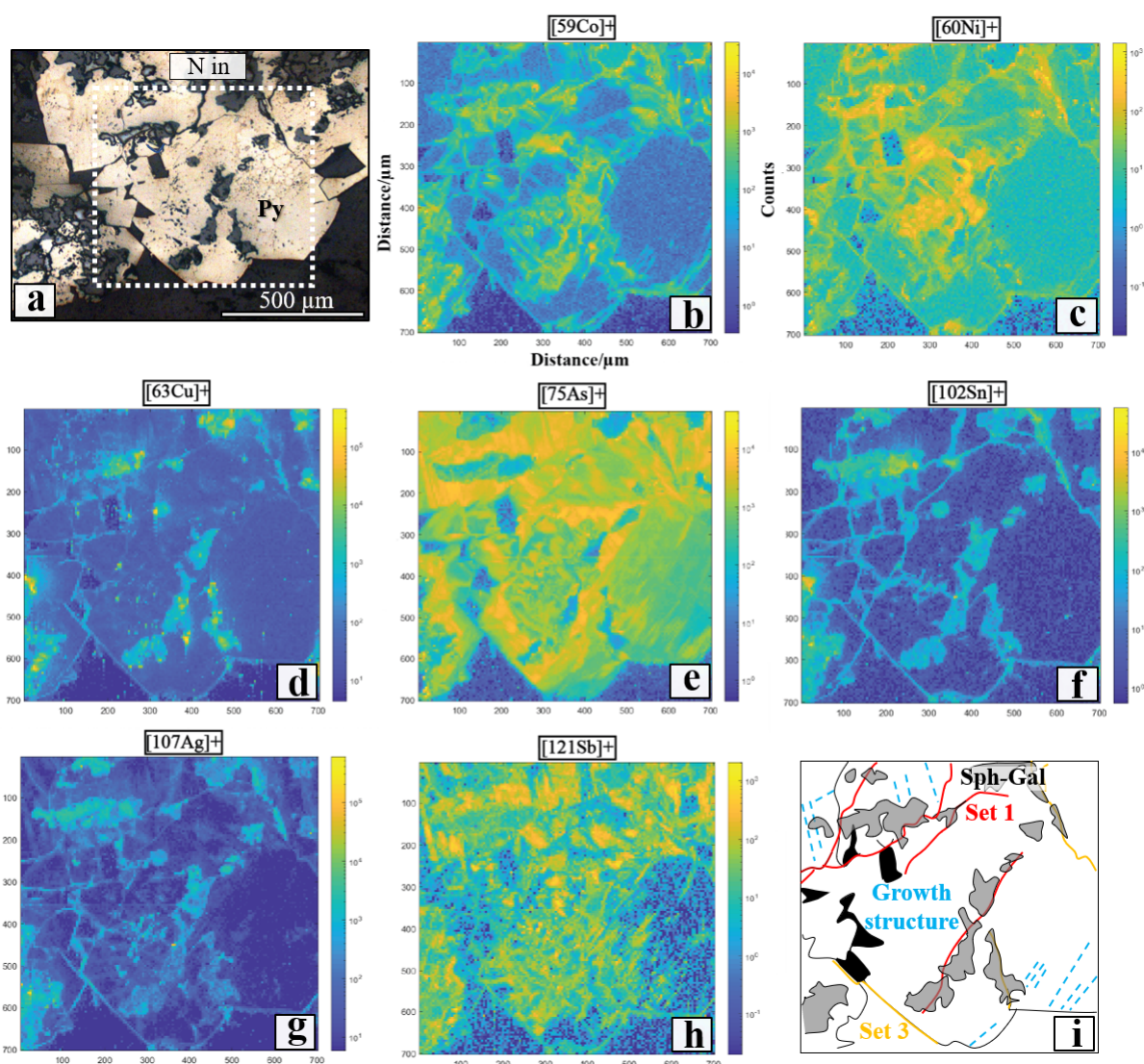
Figure 11.8. LA-ICP-TOFMS elemental imaging of deformed pyrite in Domain 3. (a) Reflected light photomicrograph of the pyrite crystal from Figure 10.4g. The dashed white line highlights the area covered by laser ablation. (b-h) Chemical maps showing semi-quantitative trace element distribution within the analysed area. The signal intensity is in counts per second (Counts) while the dimensions of the analysed area are given in μm. (i) Interpretation of the main spatial patterns highlighted by distribution mapping of trace elements.

The elemental distribution maps of Cu, Sn and Ag clearly highlight the grains edges and all the fractures extending across the analysed area (Fig. 11.8d, f and g). They also document a higher signal intensity of Cu, Sn and Ag in the proximity of anhedral grains of sphalerite.

Sphalerite is localized along the fracture mesh and pyrite crystal edges, suggesting that it is the result of chemical alteration of pyrite (Fig. 11.8d, f and g). Two main sets of fractures are identified. A first set is oriented at 50° (named Set 1, Fig. 10.7i). A second set is characterized by fractures at 45° (named Set 3, Fig. 10.7i).

The Sn chemical map shows an extremely heterogenous signal, which highlights an even more complex fracture network (Fig. 11.8h), whose constituent fractures are characterized on average by smaller dimensions and by a chaotic spatial distribution, reminiscent of the effects of dilatant hydrofracturing.

LA-ICP-TOFMS analysis thus clearly highlights the presence of several structural features within pyrite that were not identified during the standard petrographic analysis of the samples. Three main sets of fractures are identified from the analysis of the three pyrite types, each with different textures. A first set is oriented at 50°-60° (Set 1). A second set is oriented at 75°-80° (Set 2). Another set is at 45° (Set 3).

11.7 Electron back-scattered diffraction (EBSD) analysis of pyrite

With the aim to investigate in more detail the nature of the three main sets of structural features identified by means of the detailed analysis of the distribution of selected trace elements within the studied pyrite grains, we applied electron back-scattered (EBSD) analysis.

Because of the destructive nature of the LA-ICP-TOF mass spectrometry, EBSD analysis could unfortunately be performed only on areas located as close as possible to the actual pyrite grains mapped chemically (Fig. 11.9). For this reason, EBSD analysis was possible only in Domain 2 and Domain 3. The detailed and systematic studies of all sections, however, makes us confident of the representativeness of the data.
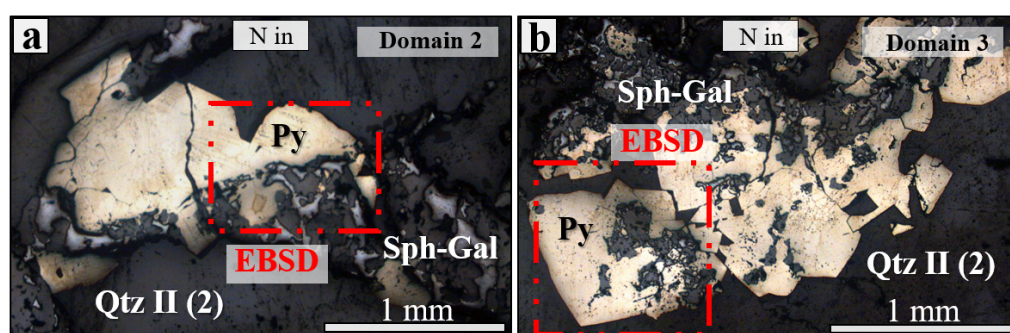
Figure 11.9. EBSD spot analysis on pyrite. Analyses were performed on areas as close as possible to the actual pyrite grains mapped chemically. (a) The dashed red box indicates the analysed area on a pyrite grain representative of Domain 2 whereas in (b) it highlights the analysed area in pyrite grains from Domain 3. Panel a is oriented bottom up with respect to the yellow rectangle in Fig. 11.1b.

EBSD maps are oriented with respect to the direction perpendicular to the vein wall (direction X_0, vein wall corresponds to direction Y_0). Pole figures (equal area, lower hemisphere) are oriented parallel to the Y_0-X_0 plane.

11.7.1 Domain 2

In the inverse pole figure (IPF) map, pyrite grains within Domain 2 document the presence of two different sets of low-angle boundaries (misorientation between 1.5 and 10°; low-angle boundaries are marked by white lines in Fig. 11.10a). Grain 1 in the figure displays low-angle boundaries oriented at 50°-55° from X_0, which corresponds to the direction of opening of the vein and therefore of maximum stretching. Another set of low-angle boundaries was mapped within Grain 2 and it is oriented at 10°-15° from X_0 (Fig. 11.10a) and it exhibits an irregular-lobate geometry (Fig. 11.10a).
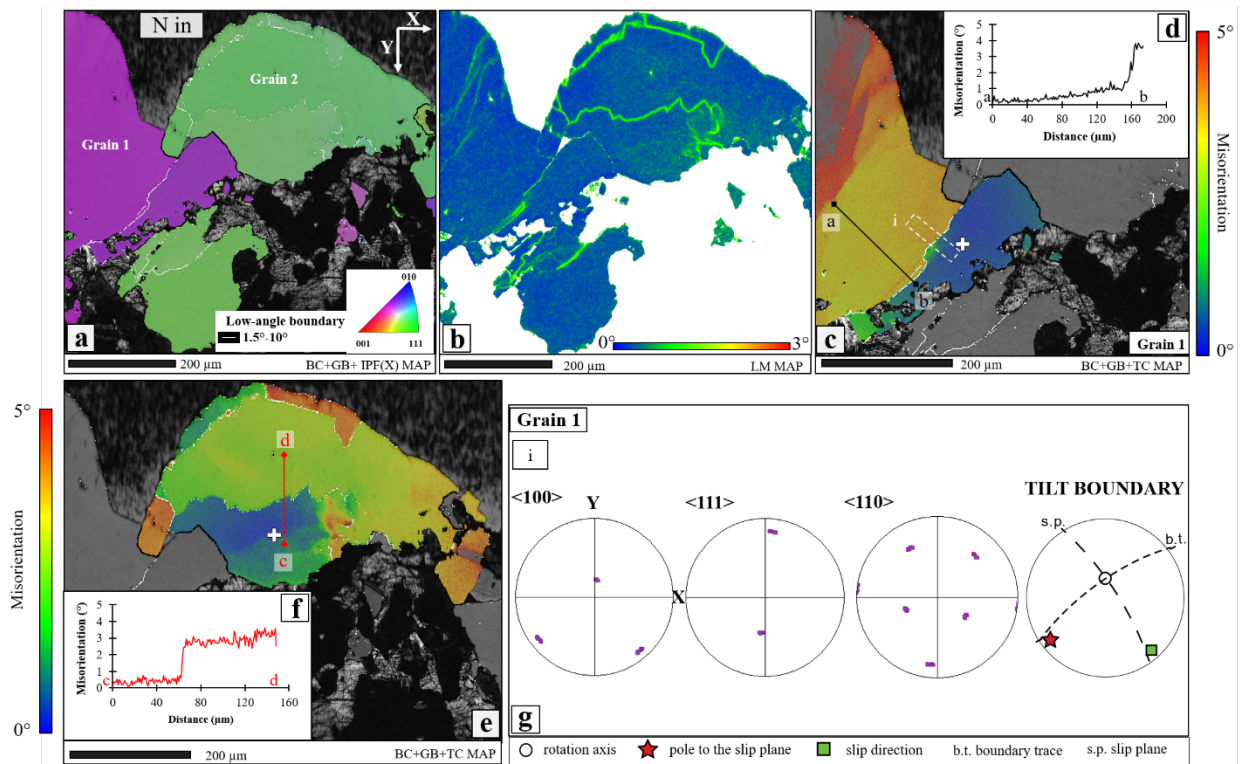
Figure 11.10. Processed EBSD Band Contrast (BC) of a region of pyrite within Domain 2 (Fig. 10.8a). The map is colour-coded according to the inverse pole figure (IPF) of pyrite. IPF reference map is shown at the bottom right side. Low-angle (1.5-10°) boundaries are marked with a white continuous line, while >10° grain boundaries are showed in black. Grey pixels are non-indexed points. (b) EBSD map of local misorientation (LM), colour coded according to the degrees of misorientation between each pixel and its neighbouring clusters of pixels within an area of 7x7 pixels. Colour scale is shown at the bottom right side. (c) Texture component map (TC) of Grain 1. The map is colour-shaded according to the angular misorientation from the reference point that is marked with a white cross. Trace of misorientation profile a-b oriented perpendicular

to the low-angle boundary is shown in black. White dashed rectangle encompasses the area of sampling of dataset 10.9e for boundary trace analysis. (d) Misorientation profile (a-b) shows a continuous increase in misorientation with a maximum value of 4°. (e) TC map of Grain 2. Trace of misorientation profile c-d perpendicular to a section of the low-angle boundary is shown in red. (f) Misorientation profile (c-d) shows a sharp step in the profile across sub-grain boundaries. (g) Upper hemisphere, equal angle stereographic projection of the sampled dataset and boundary trace analysis. All panels are oriented bottom up with respect to the yellow rectangle in Fig. 11.1b.

The misorientation map of the analysed area reveals the presence of several deformation substructures (such as subgrain walls) within the pyrite grains. The LM map shows a local misorientation of just a few degree (< 2.5°, Fig. 11.10b) across the deformation substructures.

The texture component (TC) map of Grain 1 shows that the mapped pyrite grain is characterized by distinct lattice misorientation across the low-angle boundary, with values of 1.5° on one side juxtaposed against misorientations of 3° on the other.

A misorientation profile across the low-angle boundary within Grain 1 (a-b, Fig. 11.10c) indicates the cumulative lattice misorientation or progressive lattice strain at increments of <1° (Fig. 10.10d).
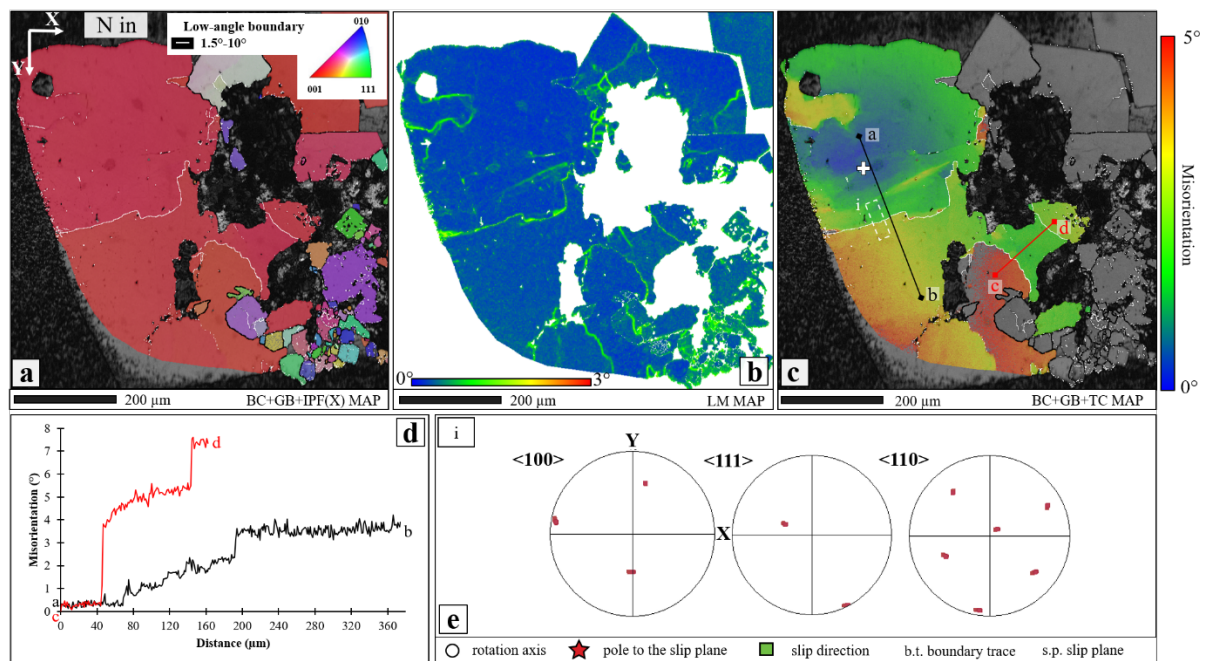
Figure 11.11. Processed EBSD Band Contrast (BC) of a region of pyrite within Domain 3 (Fig. 10.8b). The map is colour-coded according to the inverse pole figure (IPF) of pyrite. IPF map is shown at the bottom right side. Low-angle (1.5-10°) boundaries are marked with a white continuous line, while >10° grain boundaries are showed in black. Grey pixels are non-indexed points. (b) Local misorientation (LM) map of pyrite grain within Domain 3. Colour scale is shown at the bottom right side. (c) Texture component (TC) highlights the

spatial distribution of misorientation across the analysed area. The map is colour-shaded according to the angular misorientation from the reference point that is marked with a white cross. Traces of misorientation profiles a-b and c-d oriented perpendicular to the two sets of low-angle boundaries are shown in black and red lines respectively. White dashed rectangle encompasses the area of sampling of dataset 10.10e for boundary trace analysis. (d) Misorientation profiles across the two distinct sets of low-angle boundaries. (e) Upper hemisphere, equal angle stereographic projection of the sampled dataset and boundary trace analysis. All panels are oriented bottom up with respect to the yellow rectangle in Fig. 11.1b.

The TC Map of Grain 2 shows a more complex and variable misorientation distribution, where the maximum misorientation is about 4-4.5° and is mainly found along the pyrite grain external boundaries (Fig. 11.10e). The misorientation profile across one edge of the low-angle boundary within Grain 2 (c-d, Fig. 11.10e) shows that cumulative lattice misorientation is on average about 3° with sharp steps in the profile across the sub-grain boundaries (Fig. 11.10f).

In order to integrate the results from the cumulative misorientation profiles across the two pyrite grains, pole figures were plotted for a representative sample within a relatively small area across the low-angle boundary within Grain 1 (Fig. 11.10g). The location of the sampled area is highlighted by a dashed white rectangle in Fig. 11.10c.

The boundary trace analysis on Grain 1 highlights the orientation of the boundary plane as well as the most feasible slip plane and slip direction relative to the rotation axes (Fig. 11.10g). The dispersion paths on the pole figures identifies <100> as the rotation axis. A tilt boundary plane containing the boundary trace of the low-angle boundary and the rotation axis is consistent with these data (Fig. 11.10g). Because the (100), (010) and (001) planes in the cubic crystal system are symmetrically equivalent, which means that the pole figures are identical, such a tilt boundary can be explained by the activity of the {001}<100> slip system.

11.7.2 Domain 3

The inverse pole figure map of pyrite grain within Domain 3 documents two distinct sets of low-angle boundaries (Fig. 11.11a). The first set is oriented at 10-15° from X_0 (Fig. 11.11a), whereas the second set is at 45° (Fig. 11.11a).

The Local misorientation map shows that the maximum misorientation value of 1.5° is mainly distributed along the low-angle boundary traces (Fig. 11.11b).

Texture component (TC) mapping shows that the analysed pyrite grain has a different degree of misorientation across the low-angle boundaries (Fig. 11.11c).

Misorientation profiling across the first set of low-angle boundary within pyrite (a-b, Fig. 11.11d) shows that the cumulative lattice misorientation has a maximum value of 4° and a general progressive lattice strain at increments of <1° until 200 μm where there occurs a jump in the misorientation value from 3° to 4°. After c. 200 μm from the "c" point of origin, the misorientation maintains a constant value of 4° (Fig. 11.11d).

Another misorientation profile has also been produced across the second set of low-angle boundaries (c-d, Fig. 11.11c). Here, cumulative lattice misorientation has a maximum value of 7.5°. The profile shows a first sharp step from 0° to 4° at 40 μm, which is followed by a cumulative misorientation at increments of <1° until 150 μm and a second sharp transition from 5° to 7.5° (Fig. 11.11d).

The pole figures of Fig. 11.11e are related to the sampled dataset of the first set of low-angle boundaries (the sampled area is delimited by a white dashed rectangle in Fig. 11.11c).

The dispersion paths on the pole figures is low and in this case the boundary trace analysis is difficult to assess (Fig. 11.11e).

11.8 Pyrite microstructural features and relationship to trace element distribution

The deformation history of BFZ300 documented earlier is now further corroborated by the petrographic analysis of the sulphide aggregates and shows that also the Qtz II (2) vein was affected by different events of brittle deformation and fluid infiltration. In addition, the microstructural analysis of the sulphides has revealed that pyrite is cogenetic with quartz and that it was later deformed and partially replaced during a later event of fracturing and fluid-rock interaction, which precipitated sphalerite and galena.

Our comparative, integrated analysis of LA-ICP-TOFMS and EBSD data suggests that in the studied quartz-pyrite biphasic system several non-exclusive mechanisms of deformation can be responsible for elemental mobility within the pyrite lattice. This complex behaviour likely depends on the often transient boundary conditions that steered deformation. Additionally, the possibility that deformation was enhanced and partitioned by the competence contrast between sulphides and quartz should not be disregarded (e.g., structurally controlled tectonic overpressure in Mancktelow, 2008).

Our combined analytical approach allows us to discuss the details of the activated deformation mechanisms as a function of the enrichment or depletion of specific elements within specific structural domains, thus permitting to define specific and discrete stages of deformation.

Existing literature has already documented that intracrystalline deformation might induce differential element mobility, which in turn results in substantial gradients and abrupt changes of element concentrations within deforming crystals (e.g. Reddy and Hough, 2013; Piazolo et al., 2016; Dubosq et al., 2018; Peterman et al., 2016; Fougerouse et al., 2016; Fougerouse et al., 2019).

LA-ICP-TOFMS imaging on pyrite grains located within the three distinct sub-structural domains has shown that the relative enrichment or depletion of specific elements, such as Co, Ni, Cu, As, Ag, Sn, Sb (Figs. 11.5, 11.6, 11.7), can be correlated to the presence of three sets of intragrain substructures. These are: 1) a set of structural features oriented at 50°-60° from the direction of vein opening (named Set 1); 2) a set of structural features at 75°-80° (named Set 2); 3) a set of structural features oriented at 45° (named Set 3, Figs. 10.5i, 10.6i, 10.7i).

Considering the range of elements affected by deformation-controlled mobility in pyrite identified by previous studies (e.g. Reddy and Hough, 2013; Dubosq et al., 2019; Fougerouse et al., 2019), our dataset shows that pyrite deformation mechanisms involve a greater range of heavy elements than documented thus far. EBSD analysis demonstrates that mobility is indeed structurally controlled, and that in our samples low-angle boundaries accommodating lattice misorientations between 1.5° and 10° form combined chemical and structural features. In addition, EBSD analysis showed the presence of a fourth set of intragrain structures (named Set 4) found within Domain 2 and Domain 3 and oriented at 10°-15° from the direction of opening of the vein, X_0, (Figs. 11.10e, 11.11a) that was not clearly observed in the compositional maps.

Cumulative misorientation profiles and boundary trace analysis of the pole figure rotations for the four identified sets of low-angle boundaries suggest that these sets differ from each other. In particular, structures belonging to Set 3 are interpreted as healed fractures (Figs. 11.10a, d). Even if structures belonging to Set 2 were not identified with EBSD analysis, we interpret also these structural features as healed fractures. We interpret the enrichment in Sn, Sb and Ni along the healed fractures belonging to Set 2 and Set 3 indeed as resulting from a phase of later precipitation from a compositionally distinct fluid that percolated along a dense network of microfractures, deforming and substituting pyrite. (Fig. 11.11a).

The cumulative misorientation profile and the boundary trace analysis of Set 4 are instead interpreted as resulting from overgrowth or pressure-solution processes (i.e. Craig et al., 1998), even if the misorientation profile shows a continuous cumulative lattice

misorientation of up to 5° (Fig. 11.10d, a-b profile). This can be also interpreted as resulting from the presence of earlier precursor structures, which were later reactivated (Fig. 11.11a). On the other hand, misorientation profiles and boundary trace analysis of Set 1 suggests that it is a tilt boundary.

The boundary trace analysis indicates that rotation occurred along a single <100> axis and an active {001}<100> slip system. This inference is compatible with early work on naturally deformed pyrite from Van Goethem et al. (1987) that indicates the {001}<100> slip system as the primary slip system in pyrite. Later experimental work on pyrite (e.g. Cox, 1987; Barrie et al., 2008) confirmed that {001}<100> is the geometrically and energetically easiest slip system to activate between 600 and 700° C. Here, however, we have documented that this slip system can be activated also at lower temperature (<305° C, as per estimations from Fig. 8.4c).

The enrichment in Co, As and Ag along Set 1 is here interpreted as resulting from diffusion along the tilt boundary core. Our dataset is consistent with the so-called "pipe diffusion model" by Love (1964), proposed to account for enhanced diffusivity along tilt boundaries. This model suggests that the motion of vacancies and interstitials along a dislocation wall gives rise to a net flux parallel to the dislocation line itself (Fig. 11.12b).
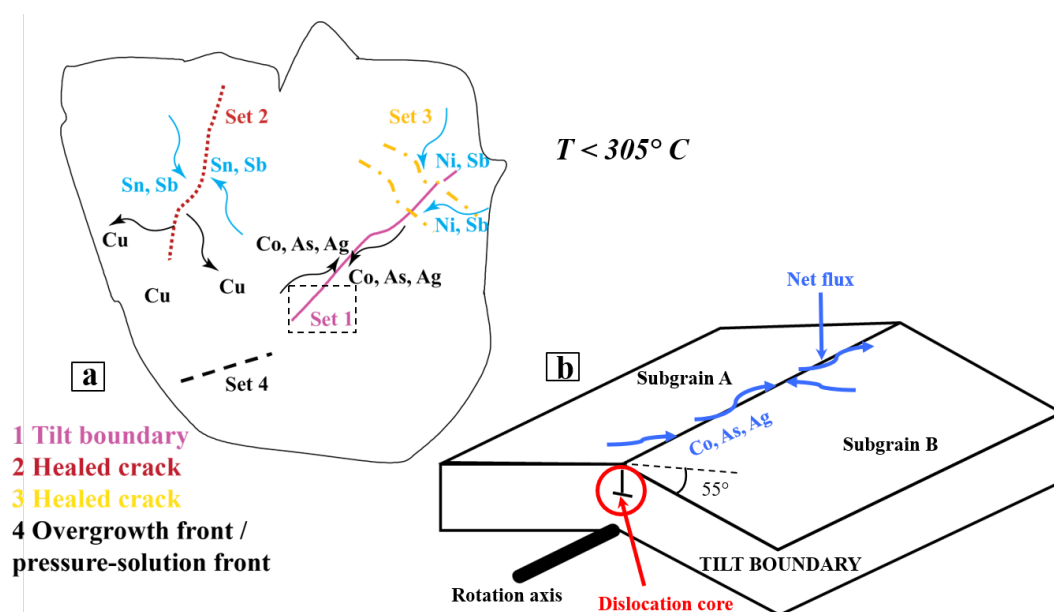
Figure 11.12 Interpretative model of trace element mobility within a naturally deformed hydrothermal pyrite. Temperature estimations derived from Fig. 8.4c. (a) Interpretation of the trace element mobility within several sets of structural features identified within the studied BFZ300 pyrite aggregates. (b) Schematic model of elemental mobility along Set 1. The boundary trace analysis suggests that Set 1 is compatible with a low-angle tilt boundary (modified from Reddy et al., 2007). The movement of dislocations creates a channel flux for the mobility and preferential entrapment of trace elements.

125

Pipe diffusion along dislocation lines as a viable mechanism controlling trace element mobility in naturally deformed pyrite was already documented in literature (e.g. Fougerouse at al., 2019; Dubosq et al., 2019). Nevertheless, previous studies showed that this mechanism was active in pyrite grains at temperatures well above 300-350° C, which is the temperature that we have constrained for the last stage of deformation of BFZ300.

11.9 Summary and conclusions

To summarise, the study of the BFZ300-intersecting PH21 drill core has shown that the Qtz II vein is itself composed of by at least two generations of quartz veins. One vein, named Qtz II (1), contains only quartz, whereas the second generation of quartz vein, named Qtz II (2), contains quartz in addition to sulphides and chlorite as minor phases. Sulphides are present as minor aggregates up to 20 mm in diameter, dispersed within the Qtz II (2) vein quartz.

Aggregates of sulphides are composed by pyrite, sphalerite, galena and chalcopyrite, with the latter present as small inclusions within larger grains of sphalerite ("chalcopyrite disease").

Petrographic analysis shows that quartz crystals found in the proximity of the sulphide aggregates are characterised by the highest degree of brittle deformation, as documented by intense fracture networks. This is also suggested by re-equilibrated textures of primary fluid inclusion assemblages hosted within the Qtz II (2) quartz close to the sulphide aggregates.

The petrographic study of a representative sulphide aggregate has shown that aggregates do not exhibit homogenous textures. Smaller structural subdomains characterized by different degrees of deformation are instead discernible. In each structural domain sulphide minerals and quartz crystals display a specific grain size, texture and a characteristic style and intensity of deformation, in addition to deformation-controlled replacement of pyrite. Pyrite generally exhibits an euhedral texture, even if some textural variability could be mapped as function of pyrite position within the structural subdomains. The different textures of pyrite are related to different levels of deformation and to the structural control on local chemical replacement by later fluids, which circulated within the fault during its renewed dilation connected with its latest deformation history documented herein. Replacement of pyrite by sphalerite and galena occurs along intracrystalline and intercrystalline fractures. Our interpretation considers pyrite as coeval with quartz during Qtz II (2) vein emplacement, whereas the replacement by sphalerite and galena along

fractures would represent the effect of a later stage of deformation and related fluid ingress within the system.

LA-ICP-TOFMS imaging on three pyrite grains representative of each of the structural subdomains, has very effectively documented the structurally controlled accumulation of Co, Ni, Cu, Sn, Ag, As, Sb, Pb along the three main sets of intragrain substructures. To define the nature of these substructures, EBSD analysis was conducted revealing that several, coexisting and non-exclusive deformation mechanisms contributed to the deformation of pyrite at <305° C. The documented deformation was accommodated by both brittle and low-temperature crystal-plastic processes. These deformation mechanisms caused strain that created short-circuit high diffusivity pathways (c.f. Lee, 1995) within the pyrite crystals. These governed elemental mobility at the pyrite lattice scale, contributing to the net transport of elements within the wet BFZ300 during its later stages of deformation. In detail, it can be show that a significant range of heavy elements (e.g. Co, Ni, Cu, Sn, Ag, As, Sb, Pb), potentially analogous to some radionuclides, were mobile during the latest stages of slip accommodated by the BFZ300. These occurred under overall brittle environmental conditions and coeval with the ingress of hydrothermal fluids. Ultimately, this study proves that intragrain microstructural features may provide efficient pathways for rapid elemental mobility through and along fault zones. This is of relevance to the risk assessment study of a deep repository built within heavily fractured and anisotropic rocks.

Chapter 12. Conclusive remarks and future perspectives

A wide range of mechanical and chemical parameters and processes control deformation and fault activity at the brittle-ductile transition zone (BDTZ). In this thesis, I have addressed specific aspects of this broad field of research in order to document and better constrain the case of BFZ300, a remarkable and representative "wet" brittle-ductile deformation zone that has undergone a complex and protracted structural history.

The obtained results have shown that fluid pressure, temperature and stress fluctuations, as much as their dynamic interplay, have a paramount importance in steering the structural evolution of fault systems operative at the BDTZ. Despite the numerous reactivations of BFZ300 and the obliterating character of its deformation episodes, it was possible to constrain in a quantitative fashion several of the parameters that guided its faulting history in space and through time. In particular, oscillations in fluid pressure between 210 and 80 have been shown to have triggered repeated and transient embrittlement by hydrofracturing even under overall ductile environmental conditions. Local temperatures in excess of c. 350° C coincided with multiple episodes of ingress into the dilatant BFZ300 fault system of hot fluids (Qtz I emplacement) and with the overall ductile environment of the BDTZ. This has led to significant cycles of deformation alternating brittle fracturing and plastic processes during repeated stress charge-discharge phases. In between brittle fracturing episodes, temperature and residual differential stress jointly guided the system towards a plastic accommodation and mechanical hardening of the fault rocks.

The BFZ300 fault continued to deform at shallower depth (e.g. the depth of emplacement of the Qtz II vein, between 5 and 8 km, see Chapter 10), when a renewed ingress of high-pressure (P_f c. 140 MPa) and hot hydrothermal fluids (T c. 300° C) caused further deformation by overall brittle processes. Even under shallow brittle conditions, the high-temperature of hydrothermal fluids promoted a semi-brittle behaviour of the minor phases, which developed both brittle and low-temperature crystal-plastic processes (Chapter 11). The detailed study of authigenic minor phases (in our case pyrite and other sulphides) has revealed that the elemental mobility of heavy trace elements is deeply controlled by this semi-brittle deformation style.

In the future, I would like to apply the adopted analytical techniques and the concepts developed during my Ph.D. to the characterization and study of the feedback mechanisms between deformation and fluid-controlled alteration. In particular, I think that important and

innovative insights into the mechanics of faults, both at the BDTZ and in the upper crust, can be derived from comparing chemical and physical aspects of fault rocks. "Chemical damage" zones could be identified and characterized by detailed analysis of minor and trace elements along transects of selected fault zones. Then, these could be compared with the more traditional physical-mechanical features (structural and microstructural aspects) of fault cores and damage zones, both in exhumed fossil and in active fault systems.

Acknowledgements

References

Aaltonen, I., Lahti, M., Engström, J., Mattila, J., Paananen, M., Paulamäki, S., Gehör, S., Kärki, A., Ahokas, T., Torvela, T. and Front, K.: Geological model of the Olkiluoto site, Version 2.0, Posiva Working Report 2010- 70, Posiva Oy, Eurajoki, 2010.

Aaltonen, I., Engström, J., Front, K., Gehör, S., Kosunen, P. and Kärki, A.: Geology of Olkiluoto. Posiva Working Report 2016- 16., Posiva Oy, Eurajoki., 2016.

Andersen, T., Austrheim, H. and Burke, E. A. J.: Fluid inclusions in granulites and eclogites from the Bergen Arcs, Caledonides of W. Norway, Mineral. Mag., 54, 145–158, 1990.

Aoya, M., Kouketsu, Y., Endo, S., Shimizu, H., Mizukami, T., Nakamura, D., & Wallis, S.: Extending the applicability of the Raman carbonaceous material geothermometer using data from contact metamorphic rocks. Journal of Metamorphic Geology, 28(9), 895-914, 2010.

Ault, A. K. and Selverstone, J.: Microtextural constraints on the interplay between fluid-rock reactions and deformation, Contrib. to Mineral. Petrol., 156(4), 501–515, doi:10.1007/s00410-008-0298-9, 2008.

Bakker, R.: Re-Equilibration Processes in Fluid Inclusion Assemblages, Minerals, 7(7), 117, doi:10.3390/min7070117, 2017.

Bakker, R. J. and Jansen, J. B. H.: Preferential water leakage from fluid inclusions by means of mobile dislocations, Nature, 345(6270), 58–60, doi:10.1038/345058a0, 1990.

Bakker, R. J. and Jansen, J. B. H.: Experimental post-entrapment water loss from synthetic CO2-H2O inclusions in natural quartz, Geochim. Cosmochim. Acta, 55(8), 2215–2230, doi:10.1016/0016-7037(91)90098-P, 1991.

Bakker, R. J. and Jansen, J. B. H.: A mechanism for preferential H2O leakage from fluid inclusions in quartz, based on TEM observations, Contrib. to Mineral. Petrol., 116(1–2), 7–20, doi:10.1007/BF00310686, 1994.

Barrie, C. D., Boyle, A. P., Cox, S. F., & Prior, D. J.: Slip systems and critical resolved shear stress in pyrite: an electron backscatter diffraction (EBSD) investigation. Mineralogical Magazine, 72(6), 1181-1199, 2008.

Barton, P. B. and Bethke, P. M.: Chalcopyrite disease in sphalerite: Pathology and epidemiologyt, Am. Mineral., 72(5–671 6), 451–467, 1987.

Basson, I. J. and Viola, G.: Passive kimberlite intrusion into actively dilating dyke-fracture arrays: Evidence from fibrous calcite veins and extensional fracture cleavage, Lithos, 76(1–4 SPEC. ISS.), 283–297, doi:10.1016/j.lithos.2004.03.041, 2004.

Behr, W. M., & Platt, J. P.: Brittle faults are weak, yet the ductile middle crust is strong: Implications for lithospheric mechanics. Geophysical Research Letters, 41(22), 8067-8075,

2014.

Beny-Bassez, C., & Rouzaud, J. N.: Characterization of carbonaceous materials by correlated electron and optical microscopy and Raman microspectroscopy, Scanning electron microscopy, 1, 119-132, 1985.

Ben-Zion, Y., & Sammis, C. G.: Characterization of fault zones. Pure and Applied Geophysics, 160(3-4), 677-715, 2003.

Berner, R. A.: Sedimentary pyrite formation. American journal of science, 268(1), 1-23, 1970.

Bestmann, M., Pennacchioni, G., Nielsen, S., Göken, M. and de Wall, H.: Deformation and ultrafine dynamic recrystallization of quartz in pseudotachylyte-bearing brittle faults: A matter of a few seconds, J. Struct. Geol., 38, 21–38, doi:10.1016/j.jsg.2011.10.001, 2012.

Bestmann, M., & Prior, D. J.: Intragranular dynamic recrystallization in naturally deformed calcite marble: diffusion accommodated grain boundary sliding as a result of subgrain rotation recrystallization. Journal of Structural Geology, 25(10), 1597-1613, 2003.

Beyssac, O., Goffé, B., Chopin, C. and Rouzaud, J. N.: Raman spectra of carbonaceous material in metasediments: a new geothermometer, Journal of Metamorphic Geology, 20(9), 859–871, doi:10.1046/j.1525-1314.2002.00408.x, 2002.

Bodansky, D.: Nuclear Energy: Principles. Practices, and Prospects (American Institute of Physics, Woodbury, NY), 246-273, 1996.

Bodnar, R. J.: The origin of fluid inclusions, in: Samson, I., Anderson, A. & Marshall, D. (eds.) Fluid inclusions: Analysis and Interpretation. Vancouver, Canada: Mineralogical Association of Canada, 11-18, 2003a.

Bodnar, R. J.: Re-equilibration of fluid inclusions, in: Samson, I., Anderson, A. & Marshall, D. (eds.) Fluid inclusions: Analysis and Interpretation. Vancouver, Canada: Mineralogical Association of Canada, 213-230, 2003b.

Bodvarsson, G. S., Boyle, W., Patterson, R., & Williams, D.: Overview of scientific investigations at Yucca Mountain—the potential repository for high-level nuclear waste. Journal of Contaminant Hydrology, 38(1-3), 3-24, 1999.

Boiron, M., Cathelineau, M., Banks, D. A., Fourcade, S. and Vallance, J.: Mixing of metamorphic and surficial fluids during the uplift of the Hercynian upper crust : consequences for gold deposition, Chem. Geol., 194, 119–141, 2003.

Bons, P. D.: The formation of large quartz veins by rapid ascent of fluids in mobile hydrofractures, Tectonophysics, 336(1–4), 1–17, doi:10.1016/S0040-1951(01)00090-7, 2001.

Bons, P. D., Elburg, M. A. and Gomez-Rivas, E.: A review of the formation of tectonic veins and their microstructures, J. Struct. Geol., 43, 33–62, doi:10.1016/j.jsg.2012.07.005, 2012.

Bourdelle, F. and Cathelineau, M.: Low-temperature chlorite geothermometry: a graphical representation based on a a T–R2+–Si diagram, Eur. J. Mineral., 27(5), 617–626,

doi:10.1127/ejm/2015/0027-2467, 2015.

Bourdelle, F., Parra, T., Chopin, C., & Beyssac, O.: A new chlorite geothermometer for diagenetic to low-grade metamorphic conditions. Contributions to Mineralogy and Petrology, 165(4), 723-735, 2013.

Brace, W. F., & Kohlstedt, D. L.: Limits on lithospheric stress imposed by laboratory experiments. Journal of Geophysical Research: Solid Earth, 85(B11), 6248-6252, 1980.

Burger, M., Schwarz, G., Gundlach-Graham, A., Käser, D., Hattendorf, B., & Günther, D.: Capabilities of laser ablation inductively coupled plasma time-of-flight mass spectrometry. Journal of Analytical Atomic Spectrometry, 32(10), 1946-1959, 2017.

Bürgmann, R., & Dresen, G.: Rheology of the lower crust and upper mantle: Evidence from rock mechanics, geodesy, and field observations. Annu. Rev. Earth Planet. Sci., 36, 531-567, 2008.

Caine, J. S., Evans, J. P. and Forster, C. B.: Fault zone architechture and permeability structure, Geology, 24(11), 1025–1028, doi:10.1130/0091-7613(1996)024<1025, 1996.

Chapman, N.: Geological disposal of radioactive wastes–concept, status and trends, Journal of Iberian Geology, 32(1), 7-14, 2006.

Compton, K. E., Kirkpatrick, J. D. and Holk, G. J.: Cyclical shear fracture and viscous flow during transitional ductile-brittle deformation in the Saddlebag Lake Shear Zone, California, Tectonophysics, 708, 1–14, doi:10.1016/j.tecto.2017.04.006, 2017.

Cowan, D. S.: Do faults preserve a record of seismic slip? A field geologist's opinion. Journal of Structural Geology, 8(21), 995-1001, 1999.

Cox, S. F.: Faulting processes at high fluid pressures: An example of fault valve behavior from the Wattle Gully Fault, Victoria, Australia, J. Geophys. Res., 100(B7), 841–859, 1995.

Cox S. F.: Coupling between deformation, fluid pressures and fluid flow in ore-producing hydrothermal environments, Econ. Geol., 100th Anniversary Volume, 39–75, 2005.

Cox, S. F.: Injection-driven swarm seismicity and permeability enhancement: Implications for the dynamics of hydrothermal ore systems in high fluid-flux, overpressured faulting regimes - An invited paper, Econ. Geol., 111(3), 559–587, doi:10.2113/econgeo.111.3.559, 2016.

Cox, S. F., Etheridge, M. A., & Hobbs, B. E.: The experimental ductile deformation of polycrystalline and single crystal pyrite. Economic Geology, 76(8), 2105-2117, 1981.

Cox, S., Knackstedt, M., & Braun, J.: Principles of structural control on permeability and fluid flow in hydrothermal systems, Reviews in Econ. Geol., 14, 1-24, 2001.

Craig, J. R., Vokes, F. M., & Solberg, T. N.: Pyrite: physical and chemical textures. Mineralium Deposita, 34(1), 82-101, 1998.

Crider, J. G. and Peacock, D. C. P.: Initiation of brittle faults in the upper crust: A review of field observations, J. Struct. Geol., 26(4), 691–707, doi:10.1016/j.jsg.2003.07.007, 2004.

De Paola, N., Collettini, C., Trippetta, F., Barchi, M. R. and Minelli, G.: A mechanical model for complex fault patterns induced by evaporite dehydration and cyclic changes in fluid pressure, J. Struct. Geol., 29(10), 1573–1584, doi:10.1016/j.jsg.2007.07.015, 2007.

Derez, T., Pennock, G., Drury, M. and Sintubin, M.: Low-temperature intracrystalline deformation microstructures in quartz, J. Struct. Geol., 71, 3–23, doi:10.1016/j.jsg.2014.07.015, 2015.

Diamond, L. W.: Introduction to gas-bearing, aqueous fluid inclusions, in : Fluid Inclusions: Analysis and Interpretation, edited by: I. Samson, A. Anderson, D. Marshall, eds., 363–372., 2003.

Diamond, L. W., Tarantola, A. and Stünitz, H.: Modification of fluid inclusions in quartz by deviatoric stress. II: Experimentally induced changes in inclusion volume and composition, Contrib. to Mineral. Petrol., 160(6), 845–864, doi:10.1007/s00410-010-0510-6, 2010.

Diehl, S. F., Goldhaber, M. B., Koenig, A. E., Lowers, H. A., & Ruppert, L. F.: Distribution of arsenic, selenium, and other trace elements in high pyrite Appalachian coals: evidence for multiple episodes of pyrite formation. International Journal of Coal Geology, 94, 238-249, 2012.

Dubessy, J., Buschaert, S., Lamb, W., Pironon, J. and Thiéry, R.: Methane-bearing aqueous fluid inclusions: Raman analysis, thermodynamic modelling and application to petroleum basins, Chem. Geol., 173(1–3), 193–205, doi:10.1016/S0009-2541(00)00275-8, 2001.

Dubosq, R., Lawley, C. J. M., Rogowitz, A., Schneider, D. A., & Jackson, S.: Pyrite deformation and connections to gold mobility: Insight from micro-structural analysis and trace element mapping. Lithos, 310, 86-104, 2018.

Dubosq, R., Rogowitz, A., Schweinar, K., Gault, B., & Schneider, D. A.: A 2D and 3D nanostructural study of naturally deformed pyrite: assessing the links between trace element mobility and defect structures. Contributions to Mineralogy and Petrology, 174(9), 72, 2019a.

Dubosq, R., Gault, B., Rogowitz, A., Schweinar, K., Zaefferer, S., & Schneider, D.: New Applications to Atom Probe Tomography: Insights on Trace Element Diffusion in Naturally Deformed Minerals. Microscopy and Microanalysis, 25(S2), 2498-2499, 2019b.

Ehlers, C., Lindroos, A. and Selonen, O.: The late Svecofennian granite-migmatite zone of southern Finland-a belt of transpressive deformation and granite emplacement., Precambrian Res., 64(1–4), 295–309, 1993.

European Commission (2004b): Euradwaste'04. Radioactive waste management community policy and research initiatives. Conference Summaries. 6th Commission Conference on the Management and Disposal of Radioactive Wastes.

Fall, A., Donald, R. and Bodnar, R. J.: The effect of fluid inclusion size on determination of homogenization temperature and density of liquid-rich aqueous inclusions, Am. Mineral., 94(11–12), 1569–1579, doi:10.2138/am.2009.3186, 2009.

Famin, V., Hébert, R., Philippot, P. and Jolivet, L.: Evolution of hydrothermal regime along a crustal shear zone , Tinos Island , Greece, Tectonics, 23, doi:10.1029/2003TC001509, 2004.

Famin, V., Hébert, R., Phillippot, P. and Jolivet, L.: Ion probe and fluid inclusion evidence for co-seismic fluid infiltration in a crustal detachment, Contrib. Mineral Petrol., 150, 354–367, doi:10.1007/s00410-005-0031-x, 2005.

Fossen, H., Structural geology, Cambridge University Press, 2016.

Fougerouse, D., Micklethwaite, S., Halfpenny, A., Reddy, S. M., Cliff, J. B., Martin, L. A., ... & Ulrich, S.: The golden ark: arsenopyrite crystal plasticity and the retention of gold through high strain and metamorphism. Terra Nova, 28(3), 181-187, 2016.

Fougerouse, D., Reddy, S. M., Kirkland, C. L., Saxey, D. W., Rickard, W. D., & Hough, R. M.: Time-resolved, defect-hosted, trace element mobility in deformed Witwatersrand pyrite. Geoscience Frontiers, 10(1), 55-63, 2019.

Goddard, J. V. and Evans, J. P.: Chemical changes and fluid-rock interaction in faults of crystalline thrust sheets, northwestern Wyoming, U.S.A., J. Struct. Geol., 17(4), 533–547, doi:10.1016/0191-8141(94)00068-B, 1995.

Goldstein, R. H.: Petrographic analysis of fluid inclusions, in: Fluid inclusions: Analysis and Interpretation: Mineralogical Association of Canada, edited by: Samson, I., Anderson, A., and Marshall, D., 1–45, 2003.

Goldstein, R. H. and Reynolds, T. J.: Fluid Inclusion Microthermometry, Syst. Fluid Inclusions Diagenetic Miner., 87–121, doi:10.2110/scn.94.31.0087, 1994.

Gorbatschev, R. and Bogdanova, S.: Frontiers in the Baltic Shield, Precambrian Res., 64(1–4), 3–21, doi:10.1016/0301-9268(93)90066-B, 1993.

Graf, J. L., Skinner, B. J., Bras, J., Fagot, M., Levade, C., & Couderc, J. J.: Transmission electron microscopic observation of plastic deformation in experimentally deformed pyrite. Economic Geology, 76(3), 738-742, 1981.

Grambow, B., Loida, A., & Smailos, E.: Long-term stability of spent nuclear fuel waste packages in Gorleben salt repository environments. Nuclear technology, 121(2), 174-188, 1998.

Griffith, A. A.: The Phenomena of Rupture and Flow in Solids, Philos. Trans. R. Soc. london, 221(582–893), 163–198, 1920.

Guermani, A. and Pennacchioni, G.: Brittle precursors of plastic deformation in a granite: An example from the Mont Blanc massif (Helvetic, western Alps), J. Struct. Geol., 20(2–3), 135–148, doi:10.1016/S0191-8141(97)00080-1, 1998.

Gundlach-Graham, A., & Günther, D.: Toward faster and higher resolution LA–ICPMS imaging: On the co-evolution of LA cell design and ICPMS instrumentation, Analytical and bioanalytical chemistry, 408(11), 2687-2695, 2016.

Hansen, F. D., & Leigh, C. D.: Salt disposal of heat-generating nuclear waste (p. 110). Albuquerque, NM: Sandia National Laboratories, 2011.

Healy, J. H., Rubey, W. W., Griggs, D. T. and Raleigh, C. B.: The Denver Earthquakes. Disposal of waste fluids by injection into a deep well has riggered earthquakes near Denver, Colorado., Science, 161(3848), 1301–1310, 1968.

Heinrich, C. A., Andrew, A. S., and Knill, M. D.: Regional metamorphism and ore formation: Evidence from stable isotopes and other fluid tracers, Reviews in Econ Geol, 11, 97–117, 2000.

Hey, M. H.: A new review of the chlorites., Mineral. Mag. J. Mineral. Soc., XXX(224), 1954.

Hirth, G., & Kohlstedt, D. L.: Experimental constraints on the dynamics of the partially molten upper mantle: Deformation in the diffusion creep regime, Journal of Geophysical Research: Solid Earth, 100(B2), 1981-2001, 1995.

Hudson, J. A. and Cosgrove, J.: Geological History and Its Impact on the Rock Mechanics Properties of the Olkiluoto Site, Posiva Working Report 2006, Posiva Oy, Eurajoki, 2006.

Hökmark, H., Loennqvist, M., & Fälth, B.: THM-issues in repository rock. Thermal, mechanical, thermo-mechanical and hydro-mechanical evolution of the rock at the Forsmark and Laxemar sites (No. SKB-TR--10-23). Swedish Nuclear Fuel and Waste Management Co, 2010.

Hökmark, H., & Fälth, B.: Approach to assessing the stability of Olkiluoto deformation zones during a glacial cycle. Posiva Oy, 2014.

Inoue, A., Meunier, A., Patrier-Mas, P., Rigault, C., Beaufort, D., & Vieillard, P. (2009). Application of chemical geothermometry to low-temperature trioctahedral chlorites. Clays and Clay Minerals, 57(3), 371-382, 2009.

Inoue, A., Kurokawa, K., & Hatta, T.: Application of chlorite geothermometry to hydrothermal alteration in Toyoha geothermal system, southwestern Hokkaido, Japan. Resource Geology, 60(1), 52-70, 2010.

Invernizzi, C., Vityk, M., Cello, G. and Bodnar, R.: Fluid inclusions in high pressure/low temperature rocks from the Calabrian Arc (Southern Italy): the burial and exhumation history of the subduction-related Diamante-Terranova unit, J. Metamorph. Geol., 16, 2, 247–258, 1998.

Jaeger, J. C. and Cook, N. G. W.: Foundamentals of Rock Mechanics, London: Chapman & Hall, 1976.

Jaques, L. and Pascal, C.: Full paleostress tensor reconstruction using quartz veins of Panasqueira Mine, central Portugal; part I: Paleopressure determination, J. Struct. Geol., 102, 58–74, doi:10.1016/j.jsg.2017.07.006, 2017.

Kaduri, M., Gratier, J. P., Renard, F., Çakir, Z. and Lasserre, C.: The implications of fault zone transformation on aseismic creep: Example of the North Anatolian Fault, Turkey, J. Geophys. Res. Solid Earth, 122(6), 4208–4236, doi:10.1002/2016JB013803, 2017.

Kerrich, R.: Some effects of tectonic recrystallisation on fluid inclusions in vein quartz, Contrib. to Mineral. Petrol., 59(2), 195–202, doi:10.1007/BF00371308, 1976.

Kim, J. S., Kwon, S. K., Sanchez, M., & Cho, G. C.: Geological storage of high level nuclear waste. KSCE Journal of Civil Engineering, 15(4), 721-737, 2011.

Kirilova, M., Toy, V., Rooney, J. S., Giorgetti, C., Gordon, K. C., Collettini, C. and

Takeshita, T. et al.: Structural disorder of graphite and implications for graphite thermometry., Solid Earth, 9(1), 2018.

Kjøll, H. J., Viola, G., Menegon, L. and Sørensen, B. E.: Brittle-viscous deformation of vein quartz under fluid-rich lower greenschist facies conditions, Solid Earth, 6(2), 681–699, doi:10.5194/se-6-681-2015, 2015.

Kohlstedt, D. L., Evans, B. and Mackwell, S. J.: Strength of the lithosphere: Constraints imposed by laboratory experiments, J. Geophys. Res., 100(B9), 587–602, 1995.

Korja, A., Heikkinen, P. and Aaro, S.: Crustal structure of the northern Baltic Sea palaeorift, Tectonophysics, 331(4), 341–358, doi:10.1016/S0040-1951(00)00290-0, 2001.

Kouketsu, Y., Mizukami, T., Mori, H., Endo, S., Aoya, M., Hara, H., Nakamura, D. and Wallis, S.: A new approach to develop the Raman carbonaceous material geothermometer for low-grade metamorphism using peak width, Island Arc, 23(1), 33–50, doi:10.1111/iar.12057, 2014.

Kukkonen, I. T. and Lauri, L. S.: Modelling the thermal evolution of a collisional Precambrian orogen: High heat production migmatitic granites of southern Finland, Precambrian Res., 168(3–4), 233–246, doi:10.1016/j.precamres.2008.10.004, 2009.

Kärki, A. and Paulamäki, S.: Petrology of Olkiluoto, Posiva Report 2006-02, Posiva Oy, Eurajoki., 2006.

Lahfid, A., Beyssac, O., Deville, E., Negro, F., Chopin, C., & Goffé, B.: Evolution of the Raman spectrum of carbonaceous material in low   grade metasediments of the Glarus Alps (Switzerland). Terra Nova, 22(5), 354-360, 2010.

Lahtinen, R., Korja, A., and Nironen, M: Palaeoproterozoic tectonic evolution, in: Precambrian Geology of Finland: Key to the Evolution of the Fennoscandian Shield, edited by: Lehtinen, M.,Nurmi, P. A., and Rämö, O. T., Developments in PrecambrianGeology, 2005.

Lloyd, G. E., & Freeman, B.: Dynamic recrystallization of quartz under greenschist conditions. Journal of Structural Geology, 16(6), 867-881, 1994.

Lambrecht, G. and Diamond, L. W.: Morphological ripening of fluid inclusions and coupled zone-refining in quartz crystals revealed by cathodoluminescence imaging: Implications for CL-petrography, fluid inclusion analysis and trace-element geothermometry, Geochimica et Cosmochimica Acta, 141, 381-406, 2014.

Laurich, B., Urai, J. L., Desbois, G., Vollmer, C., & Nussbaum, C.: Microstructural evolution of an incipient fault zone in Opalinus Clay: Insights from an optical and electron microscopic study of ion-beam polished samples from the Main Fault in the Mt-Terri Underground Research Laboratory. Journal of Structural Geology, 67, 107-128, 2014.

Lee, J. K.: Multipath diffusion in geochronology. Contributions to Mineralogy and Petrology, 120(1), 60-82, 1995.

Levade, C., Couderc, J. J., Bras, J., & Fagot, M.: Transmission electron microscopy study of experimentally deformed pyrite. Philosophical Magazine A, 46(2), 307-325, 1982.

Long, J. C., & Ewing, R. C.: Yucca Mountain: Earth-science issues at a geologic repository for high-level nuclear waste. Annu. Rev. Earth Planet. Sci., 32, 363-401, 2004.

Love, G. R.: Dislocation pipe diffusion. Acta Metallurgica, 12(6), 731-737, 1964.

Lund, B., Schmidt, P., Hieronymus, C., 2009: Stress evolution and fault stabilityduring the Weichselian glacial cycle. SKB TR-09-15, SvenskK€arnbr€anslehantering AB, 2009.

Mallants, D., Marivoet, J., & Sillen, X.: Performance assessment of the disposal of vitrified high-level waste in a clay layer. Journal of Nuclear Materials, 298(1-2), 125-135, 2001.

Mancktelow, N. S.: Tectonic pressure: Theoretical concepts and modelled examples. Lithos, 103(1-2), 149-177, 2008.

Mancktelow, N. S. and Pennacchioni, G.: The influence of grain boundary fluids on the microstructure of quartz-feldspar mylonites, J. Struct. Geol., 26, 47-69, doi:10.1016/S0191-8141(03)00081-6, 2004.

Mancktelow, N. S. and Pennacchioni, G.: The control of precursor brittle fracture and fluid-rock interaction on the development of single and paired ductile shear zones, J. Struct. Geol., 27(4), 645–661, doi:10.1016/j.jsg.2004.12.001, 2005.

Mattila, J., & Tammisto, E.: Stress-controlled fluid flow in fractures at the site of a potential nuclear waste repository, Finland, Geology, 40(4), 299-302, 2012.

Mattila, J. and Viola, G.: New constraints on 1.7Gyr of brittle tectonic evolution in southwestern Finland derived from a structural study at the site of a potential nuclear waste repository (Olkiluoto Island), J. Struct. Geol., 67(PA), 50–74, doi:10.1016/j.jsg.2014.07.003, 2014.

Menegon, L., Piazolo, S., & Pennacchioni, G.: The effect of Dauphiné twinning on plastic strain in quartz. Contributions to Mineralogy and Petrology, 161(4), 635-652, 2011.

Menegon, L., Pennacchioni G., Malaspina N., Harris K., and Wood E.: Earthquakes as Precursors of Ductile Shear Zones in the Dry and Strong Lower Crust, Geochem. Geophy. Geosy., 18(12), doi: 10.1002/2015GC006010, 2017.

Menegon, L., Marchesini, B., Prando, F., Garofalo, P. S., Viola, G., Anderson, M.and Mattila, J.: Brittle-viscous oscillations and different slip behaviours in a conjugate set of strike-slip faults, Geophysical Research Abstracts Vol. 20, EGU2018-14799, 2018.

Miller, S. A.: The Role of Fluids in Tectonic and Earthquake Processes, edited by R. Dmowska, Elsevier., 2013.

Mittempergher, S., Dallai, L., Pennacchioni, G., Renard, F. and Di Toro, G.: Origin of hydrous fluids at seismogenic depth: Constraints from natural and experimental fault rocks, Earth Planet. Sci. Lett., 385, 97–109, doi:10.1016/j.epsl.2013.10.027, 2014.

Moritz, R., Ghazban, F. and Singer, B. S.: Eocene Gold Ore Formation at Muteh, Sanandaj-Sirjan Tectonic Zone, Western Iran: A Result of Late-Stage Extension and Exhumation of Metamorphic Basement Rocks within the Zagros Orogen, Econ. Geol., 101, 1–28, 2006.

Morrison, J.: Meteoric water-rock interaction in the lower plate of the Whipple Mountain

metamorphic core complex , California, J. Metamorph. Geol.,12, 827–840, 1994.

Morrison, J. and Anderson, J. L.: Footwall Refrigeration Along a Detachment Fault : Implications for the Thermal Evolution of Core Complexes, Science, 279(January), 63–67, 1998.

Mulch, A., Mine, I. De, Cosca, M. A., Mine, I. De, Lausanne, D., Lausanne, C.-, Poincare, H. and Gr, U. M. R.: Reconstructing paleoelevation in eroded orogens, , (6), 525–528, doi:10.1130/G20394.1, 2004.

Munier, R.: Using observations in deposition tunnels to avoid intersections with critical fractures in deposition holes (No. SKB-R--06-54). Swedish Nuclear Fuel and Waste Management Co, 2006.

Munier, R., Hökmark, H., & Fälth, B.: Respect distances: rationale and means of computation. SKB, 2004.

Mänttäri, I., Engstroem, J., Lahaye, Y. and Pere, T.: U-Pb ages for PGR dykes, KFP, and adjacent older leucosomic PGRs from ONKALO underground research facility, Olkiluoto, Eurajoki, SW Finland, Posiva Oy., 2010.

Nekrasov, I. J., Sorokin, V. I. and Osadchii, E. G.: Fe and Zn partitioning between stannite and sphalerite and its application in geothermometry., Phys. Chem. Earth, 11(C), 739–742, doi:10.1016/0079-1946(79)90069-7, 1979.

Nemanich, R. J., & Solin, S. A., First-and second-order Raman scattering from finite-size crystals of graphite, Physical Review B, 20(2), 392, 1979.

Nussbaum, C., Bossart, P., Amann, F., & Aubourg, C.: Analysis of tectonic structures and excavation induced fractures in the Opalinus Clay, Mont Terri underground rock laboratory (Switzerland). Swiss Journal of Geosciences, 104(2), 187, 2011.

Oliver, N. H. S. and Bons P. D.: Mechanisms of fluid flow and fluid–rock interaction in fossil metamorphic hydrothermal systems inferred from vein–wallrock patterns, geometry and microstructure, Geofluids, 137–162, 2001.

Olsen, M. P., Scholz, C. H. and Léger, A.: Healing and sealing of a simulated fault gouge under hydrothermal conditions: Implications for fault healing, J. Geophys. Res., 103(B4), 7421, doi:10.1029/97JB03402, 1998.

Orellana, L. F., Scuderi, M. M., Collettini, C., & Violay, M.: Do scaly clays control seismicity on faulted shale rocks?. Earth and Planetary Science Letters, 488, 59-67, 2018.

Ortiz, L., Volckaert, G., & Mallants, D.: Gas generation and migration in Boom Clay, a potential host rock formation for nuclear waste storage, Engineering geology, 64(2-3), 287-296, 2002.

Passchier, C. W., & Trouw, R. A., Microtectonics. Springer Science & Business Media, 2005.

Pennacchioni, G., Di Toro, G., Brack, P., Menegon, L. and Villa, I. M.: Brittle-ductile-brittle deformation during cooling of tonalite (Adamello, Southern Italian Alps), Tectonophysics, 427(1–4), 171–197, doi:10.1016/j.tecto.2006.05.019, 2006.

Pere, T.: Fault-related local phenomena in the bedrock of Olkiluoto with particular reference to fault zone OL-BFZ100, Posiva Oy., 2009.

Peterman, E. M., Reddy, S. M., Saxey, D. W., Snoeyenbos, D. R., Rickard, W. D., Fougerouse, D., & Kylander-Clark, A. R.: Nanogeochronology of discordant zircon measured by atom probe microscopy of Pb-enriched dislocation loops. Science Advances, 2(9), e1601318, 2016.

Piazolo, S., Montagnat, M., & Blackford, J. R.: Sub structure characterization of experimentally and naturally deformed ice using cryo EBSD. Journal of Microscopy, 230(3), 509-519, 2008.

Piazolo, S., La Fontaine, A., Trimby, P., Harley, S., Yang, L., Armstrong, R., & Cairney, J. M.: Deformation-induced trace element redistribution in zircon revealed using atom probe tomography. Nature communications, 7, 10490, 2016.

Prando, F., Menegon, L., Anderson, M.W., Marchesini, B., Mattila, J. and Viola, G.: Fluid-mediated, brittle-ductile deformation at seismogenic depth- Part 2 – Stress history and fluid pressure variations in a shear zone in a nuclear waste repository (Olkiluoto Island, Finland)", doi.org/10.5194/se-2019-142, Solid Erath Discussion Forum (in review for Solid Earth).

Prior, D. J., Wheeler, J., Peruzzo, L., Spiess, R., & Storey, C.: Some garnet microstructures: an illustration of the potential of orientation maps and misorientation analysis in microstructural studies. Journal of Structural Geology, 24(6-7), 999-1011, 2002.

Ranalli, G.: Rheology of the Earth, Boston: Allen and Unwin, 1987.

Ranalli, G.: Rheology of the crust and its role in tectonic reactivation. Journal of geodynamics, 30(1-2), 3-15, 2000.

Ranalli, G., & Murphy, D. C.: Rheological stratification of the lithosphere. Tectonophysics, 132(4), 281-295, 1987.

Reddy, S. M., & Hough, R. M.: Microstructural evolution and trace element mobility in Witwatersrand pyrite. Contributions to Mineralogy and Petrology, 166(5), 1269-1284, 2013.

Reddy, S. M., Timms, N. E., Pantleon, W., & Trimby, P.: Quantitative characterization of plastic deformation of zircon and geological implications. Contributions to Mineralogy and Petrology, 153(6), 625-645, 2007.

Roedder, E. and Bodnar, R. J.: Geologic determinations from fluid inclusion studies., Annu. Rev. Earth Planet. Sci., 8(1953), 263–301, 1980.

Rolandone, F. and Jaupart, C.: The distributions of slip rate and ductile deformation in a strike-slip shear zone, Geophys. J. Int., 148(2), 179–192, doi:10.1046/j.1365-246X.2002.01574.x, 2002.

Rosso, K. M. and Bodnar, R. J.: Microthermometric and Raman spectroscopic detection limits of CO2 in fluid inclusions and the Raman spectroscopic characterization of CO2,

Geochim. Cosmochim. Acta, 59(19), 3961–3975, doi:10.1016/0016-7037(95)94441-H, 1995.

Rowe, C. D., & Griffith, W. A.: Do faults preserve a record of seismic slip: A second opinion. Journal of Structural Geology, 78, 1-26, 2015.

Rutter, E.H., Maddock, R.H., Hall, S.H. and White, S.H.: Comparative microstructures naturally and experimentally produced clay-bearing fault gouge, Pure and Applied Geophysics, 124, 3-30, 1986.

Saintot, A., Stephens, M., Viola, G. and Nordgulen, Ø.: Brittle tectonic evolution and paleostress field reconstruction in the southwestern part of the Fennoscandian Shield, Forsmark, Sweden, Tectonics, 30(4), 2011.

Scheffer, C., Tarantola, A., Vanderhaeghe, O., Rigaudier, T. and Photiades, A.: CO 2 flow during orogenic gravitational collapse : Syntectonic decarbonation and fl uid mixing at the ductile-brittle transition, Chem. Geol., 450, 248–263, doi:10.1016/j.chemgeo.2016.12.005, 2017a.

Scheffer, C., Tarantola, A., Vanderhaeghe, O., Voudouris, P., Rigaudier, T., Photiades, A., Morin, D. and Alloucherie, A.: The Lavrion Pb-Zn-Fe-Cu-Ag detachment-related district (Attica , Greece): Structural control on hydrothermal flow and element transfer-deposition, Tectonophysics, 717, 607–627, doi:10.1016/j.tecto.2017.06.029, 2017b.

Secor, D. T.: Role of fluid pressure in jointing. American Journal of Science, 263(8), 633-646, 1965.

Selverstone, J., Axen, G. J., Bartley, J. M: Fluid inclusion constraints on the kinematics of footwall uplift beneath the Brebber Line normal fault, estern Alps, Tectonics, 14(2), 264-278, 1995.

Selverstone, J., Franz, G., Thomas, S. and Getty, S.: Fluid variability in 2 GPa eclogites as an indicator of fluid behavior during subduction, Contrib to Mineral and Petrol, 112(2-3), 341-357, 1992.

Shimizu, M. and Shikazono, N.: Iron and zinc partitioning between coexisting stannite and sphalerite: a possible indicator of temperature and sulfur fugacity, Miner. Depos., 20, 314–320, 1985.

Scholz, C. H.: The Mechanics of Earthquakes and Faulting, Cambridge: Cambridge University Press, 1990.

Sibson, R. H.: Fault rocks and fault mechanisms. Journal of the Geological Society, 133(3), 191-213, 1977.

Sibson, R. H.: Transient discontinuities in ductile shear zones. Journal of Structural Geology, 2(1-2), 165-171, 1980.

Sibson, R. H.: Continental fault structure and the shallow earthquake source. Journal of the Geological Society, 140(5), 741-767, 1983.

Sibson, R. H.: Brecciation processes in fault zones: inferences from earthquake rupturing. Pure and Applied Geophysics, 124(1-2), 159-175, 1986.

Sibson, R. H.: Earthquake faulting as a structural process, J. Struct. Geol., 11(1–2), 1–14, doi:10.1016/0191-8141(89)90032-1, 1989.

Sibson, R. H.: Fault-valve behavior and the hydrostatic-lithostatic fluid pressure interface, Earth Sci. Rev., 32(1–2), 141–144, doi:10.1016/0012-8252(92)90019-P, 1992a.

Sibson, R. H.: Implications of fault-valve behaviour for rupture nucleation and recurrence., Tectonophysics, 211(1–4), 283–293., 1992b.

Sibson, R. H.: Load-strengthening versus load-weakening faulting, J. Struct. Geol., 15(2), 123–128, doi:10.1016/0191-8141(93)90090-W, 1993.

Sibson, R. H.: Structural permeability of fluid-driven fault-fracture meshes, J. Struct. Geol, 18(8), 1996.

Sibson, R. H., Robert, F. and Poulsen, K. H.: High-angle reverse faults, fluid-pressure cycling, and mesothermal gold-quartz deposits, Geology, 16(June 1988), 551–555, doi:10.1130/0091-7613(1988)016<0551:HARFFP>2.3.CO;2, 1988.

Siebenaller, L., Boiron, M. C., Vanderhaeghe, O., Hibsch, C., Jessell, M. W., Andre-Mayer, A. S., France-Lanord, C. and Photiades, A.: Fluid record of rock exhumation across the brittle-ductile transition during formation of a Metamorphic Core Complex (Naxos Island, Cyclades, Greece), J. Metamorph. Geol., 31(3), 313–338, doi:10.1111/jmg.12023, 2013.

Siebenaller, L., Vanderhaeghe, O., Jessell, M., Boiron, M. C. and Hibsch, C.: Syntectonic fluids redistribution and circulation coupled to quartz recrystallization in the ductile crust (Naxos Island, Cyclades, Greece), J. Geodyn., 101, 129–141, doi:10.1016/j.jog.2016.07.001, 2016.

Skyttä, P. and Torvela, T.: Brittle reactivation of ductile precursor structures: The role of incomplete structural transposition at a nuclear waste disposal site, Olkiluoto, Finland, J. Struct. Geol., 0–1, doi:10.1016/j.jsg.2018.06.009, 2018.Spruzeniece, L. and Piazolo, S.: Strain localization in brittle-ductile shear zones: Fluid-abundant vs. fluid-limited conditions (an example from Wyangala area, Australia), Solid Earth, 6(3), 881–901, doi:10.5194/se-6-881-2015, 2015.

Smith, S. A., Billi, A., Di Toro, G., & Spiess, R.: Principal slip zones in limestone: microstructural characterization and implications for the seismic cycle (Tre Monti Fault, Central Apennines, Italy). Pure and Applied Geophysics, 168(12), 2365-2393, 2011.

Staude, S., Bons, P. D., & Markl, G.: Hydrothermal vein formation by extension-driven dewatering of the middle crust: An example from SW Germany, Earth and Planetary Science Letters, 286(3-4), 387-395, 2009.

Steele-MacInnis, M., Lecumberri-Sanchez, P. and Bodnar, R. J.: HokieFlincs_H2O-NaCl: A Microsoft Excel spreadsheet for interpreting microthermometric data from fluid inclusions based on the PVTX properties of H2O-NaCl, Comput. Geosci., 49, 334–337, doi:10.1016/j.cageo.2012.01.022, 2012.

Sterner, S. M. and Bodnar J.: Synthetic fluid inclusions - VII. Re-equilibration of fluid inclusions in quartz during laboratory-simulated metamorphic burial and uplift, J. Metamorph. Geol., 7, 243–260, 1989.

Stipp, M., & Kunze, K.: Dynamic recrystallization near the brittle-plastic transition in naturally and experimentally deformed quartz aggregates. Tectonophysics, 448(1-4), 77-97, 2008.

Spruzeniece, L. and Piazolo, S.: Strain localization in brittle-ductile shear zones: fluid-abundant vs. fluid-limited conditions (an example from Wyangala area, Australia), Solid Earth, 6, 881-901, 2015.

Suominen, V.: The chronostratigraphy of southern Finland, with special reference to Postjotnian and Subjotnian diabases. Bull. Geol. Surv. Finl,. 356, 100, 1991.

Tarantola, A., Diamond, L. W. and Stünitz, H.: Modification of fluid inclusions in quartz by deviatoric stress I: Experimentally induced changes in inclusion shapes and microstructures, Contrib. to Mineral. Petrol., 160, 825–843, doi:10.1007/s00410-010-0509-z, 2010.

Tchalenko, J. S.: Similarities between Shear Zones of Different Magnitudes, Geol. Soc. Am. Bull., 81(6), 1625–1640, doi:10.1130/0016-7606(1970)81[1625:SBSZOD]2.0.CO;2, 1970.

Tenthorey, E. and Cox, S. F.: Cohesive strengthening of fault zones during the interseismic period: An experimental study, J. Geophys. Res. Solid Earth, 111(9), 1–14, doi:10.1029/2005JB004122, 2006.

Torvela, T. and Ehlers, C.: From ductile to brittle deformation: structural development and strain distribution along a crustal scale shear zone in SW Finland, International Journal of Earth Sciences, 99(5), 1133–1152, 2010.

Trepmann, C. A. and Stöckhert, B.: Quartz microstructures developed during non-steady state plastic flowat rapidly decaying stress and strain rate, J. Struct. Geol., 25(12), 2035–2051, doi:10.1016/S0191-8141(03)00073-7, 2003.

Trepmann, C. A. and Stöckhert, B.: Short-wavelength undulatory extinction in quartz recording coseismic deformation in the middle crust – An experimental study, Solid Earth, 4(2), 263–276, doi:10.5194/se-4-263-2013, 2013.

Trepmann, C. A., Stöckhert, B., Dorner, D., Moghadam, R. H., Küster, M. and Röller, K.: Simulating coseismic deformation of quartz in the middle crust and fabric evolution during postseismic stress relaxation - An experimental study, Tectonophysics, 442(1–4), 83–104, doi:10.1016/j.tecto.2007.05.005, 2007.

Trepmann, C. A., Hsu, C., Hentschel, F., Döhler, K., Schneider, C. and Wichmann, V.: Recrystallization of quartz after low-temperature plasticity – The record of stress relaxation below the seismogenic zone, J. Struct. Geol., 95, 77–92, doi:10.1016/j.jsg.2016.12.004, 2017.

Tuinstra, F. & Koenig, J. L.: Raman spectrum of graphite. Journal of Chemical Physics, 53, 1126–1130, 1970.

Tuisku, P. and Kärki, A.: Metamorphic petrology of Olkiluoto, Posiva Oy., 2010.

Tuinstra, F., & Koenig, J. L.: Raman spectrum of graphite, The Journal of Chemical Physics, 53(3), 1126-1130, 1970.

Turcotte, D. L. and Schubert G.: Geodynamics, Cambridge: Cambridge University Press,

2002.

Tvalchrelidze, G. A.: Types of pyrite deposits and provinces. International Geology Review, 22(2), 125-134, 1980.

Van den Kerkhof, A., Kronz, A. and Simon, K.: Deciphering fluid inclusions in high-grade rocks, Geosci. Front., 5(5), 683–695, doi:10.1016/j.gsf.2014.03.005, 2014.

Van Goethem, L., Van Landuyt, J., & Amelinckx, S.: Study of the glide elements in pyrite by means of electron microscopy and electron diffraction. American Mineralogist, 63(5-6), 548-550, 1978.

Van Noten, K., Muchez, P. and Sintubin, M.: Stress-state evolution of the brittle upper crust during compressional tectonic inversion as defined by successive quartz vein types (High-Ardenne slate belt , Germany), J. Geol. Soc. London, 168(2004), 407–422, doi:10.1144/0016-76492010-112.Stress-state, 2011.

Viola, G., Mancktelow, N. S. and Miller, J. A.: Cyclic frictional-viscous slip oscillations along the base of an advancing nappe complex: Insights into brittle-ductile nappe emplacement mechanisms from the Naukluft Nappe Complex, central Namibia, Tectonics, 25(3), 1–20, doi:10.1029/2005TC001939, 2006.

Viola, G., Venvik Ganerød, G. and Wahlgren, C. H.: Unraveling 1.5 Ga of brittle deformation history in the Laxemar-Simpevarp area, southeast Sweden: A contribution to the Swedish site investigation study for the disposal of highly radioactive nuclear waste, Tectonics, 28(5), 1–29, doi:10.1029/2009TC002461, 2009.

Viola, G., Mattila, J., Zwingmann, H., Todd, A. and Raven, M.: Structural and K / Ar Illite Geochronological Constraints on the Brittle Deformation History of the Olkiluoto Region, Southwest Finland, Posiva Working Report 2011, Posiva Oy, Eurajoki, 2011.

Viola, G., Scheiber, T., Fredin, O., Zwingmann, H., Margreth, A. and Knies, J.: Deconvoluting complex structural histories archived in brittle fault zones, Nat. Commun., 7, 1–10, doi:10.1038/ncomms13448, 2016.

Vityk, M. O. and Bodnar, R. J.: Textural evolution of synthetic fluid inclusions in quartz during reequilibration, with applications to tectonic reconstruction, Contrib. to Mineral. Petrol., 121(3), 309–323, doi:10.1007/BF02688246, 1995.

Vityk, M. O. and Bodnar, R. J.: Statistical microthermometry of synthetic fluid inclusions in quartz during decompression reequilibration, Contrib. to Mineral. Petrol., 132(2), 149–162, doi:10.1007/s004100050413, 1998.

Vityk, M. O., Bodnar, R. J. and Schmidt, C. S.: Fluid inclusion as a tectonothermobarometers: Relation between pressure-tempreture history and reequilibration morphology during crystal thickening, Geology, 22, 731–734, doi:10.1130/0091-7613(1994)022<0731:FIATRB>2.3.CO, 1994.

Wehrens, P., Berger, A., Peters, M., Spillmann, T. and Herwegh, M.: Deformation at the frictional-viscous transition: Evidence for cycles of fluid-assisted embrittlement and ductile deformation in the granitoid crust, Tectonophysics, 693, 66–84, doi:10.1016/j.tecto.2016.10.022, 2016.

Wileveau, Y., & Bernier, F.: Similarities in the hydromechanical response of Callovo-Oxfordian clay and Boom Clay during gallery excavation. Physics and Chemistry of the Earth, Parts A/B/C, 33, S343-S349, 2008.

Wilkins, R. W. T. and Barkas, J. P.: Fluid inclusions, Deformation and Recrystallization in Granite Tectonites, Contrib. Mineral. Petrol., 65, 293-299, 1978.

Witherspoon, P. A., & Bodvarsson, G. S.: Geological challenges in radioactive waste isolation: Third worldwide review, Geological Challenges in Radioactive Waste Isolation, 2001.

Wiewiora, A. & Weiss, Z.: Crystallochemical classifications of phyllosilicates based on the unified system of projection of chemical composition: II The chlorite group. Clay Miner., 25, 83–92, 1990.

Yang, F., Mao, J., Wang, Y., & Bierlein, F. P.: Geology and geochemistry of the Bulong quartz–barite vein-type gold deposit in the Xinjiang Uygur Autonomous Region, China. Ore Geology Reviews, 29(1), 52-76, 2006.

Appendix A

EBSD analysis of Qtz I from the fault core

Petrographic thin sections were later used at the Scanning Electron Microprobe (SEM) to investigate the crystallographic preferred orientation (CPO) of selected sites of the quartz veins from the fault core (sample name TPH-120-4, see Figure 2 for sample location). Samples were analysed with a JEOL 6610 SEM equipped with a Nordlys Nano EBSD detector, hosted at the Electron Microscopy Centre of the University of Plymouth, UK.

Before EBSD analysis, thin sections were chemically polished using colloidal silica. Thin sections were then carbon coated placed in a JEOL 6610 SEM equipped with a Nordlys Nano EBSD detector, at a 70° tilt to the horizontal (Prior et al., 1999). We used 20 kV of accelerating voltage, a working distance of 25 mm and a step size to 2 μm. The acquired EBSD patterns were automatically indexed using AZtec software and processed using CHANNEL 5 software from Oxford Instruments. Raw indexing of the two acquired maps was 96%. EBSD data were presented in the form of Inverse Pole Figure maps oriented with respect to the direction perpendicular to the vein wall (direction X0, vein wall corresponds to direction Y0), and of pole figures (equal area, lower hemisphere) oriented parallel to the Y0-X0 plane. Crystallographic data in the pole figures are plotted as one-point-per-pixel. In the IPF maps, low-angle boundaries (misorientation between 2°and 10°) are shown in cyan, high-angle boundaries (misorientation > 10°) are shown in black, and Dauphinétwin boundaries (misorientation of 60° around the c-axis) are shown in red.

Figure A1. EBSD analysis performed on fault core-Qtz I (sample TPH-120 4). a) Qtz I-fault core microstructures where EBSD map locations b) and c) are also reported. Also at the edge of intercrystalline bands we detected subgrains precursors of recrystallization. d) Intercrystalline bands are also marked by trails of fluid inclusions.

Appendix B

No. Analysis

No.	Na2O	TiO2	MnO	K2O	MgO	SiO2	Cr2O3	FeO	CaO	Al2O3	Cl	Total	Sample	Structural zone	Qtz type	Chl texture
1	0.02	0.03	0.50	0.04	7.57	25.00	0.05	32.30	0.03	25.21	0.03	90.99	PH22	FC	Qtz II	Rad
2	0.03	0.10	0.55	0.04	7.66	25.17	0.00	31.45	0.03	25.75	0.01	90.98	PH22	FC	Qtz II	Rad
3	0.00	0.12	0.59	0.04	7.55	24.98	0.00	31.63	0.01	25.38	0.01	90.45	PH22	FC	Qtz II	Rad
4	0.05	0.07	0.61	0.04	7.74	25.81	0.01	31.39	0.01	24.68	0.02	90.45	PH22	FC	Qtz II	Rad
5	0.00	0.12	0.54	0.00	8.09	25.10	0.00	31.22	0.01	25.56	0.02	90.83	PH22	FC	Qtz II	Rad
6	0.05	0.01	0.76	0.02	6.16	24.40	0.01	33.05	0.00	26.02	0.01	90.62	PH22	FC	Qtz II	Rad
7	0.08	0.08	0.98	0.04	5.10	25.75	0.04	32.54	0.05	24.67	0.01	89.48	PH22	FC	Qtz II	Rad
8	0.02	0.10	0.87	0.05	7.05	25.74	0.03	30.46	0.06	24.54	0.02	89.05	PH22	FC	Qtz II	Rad
9	0.07	0.10	0.78	0.08	7.10	25.91	0.02	30.73	0.08	24.76	0.01	89.81	PH22	FC	Qtz II	Rad

No.	XNa2O	XTiO2	XMnO	XK2O	XMgO	XSiO2	XCr2O3	Fe2+	Fe3+	XCaO	XAl2O3	XCl	Total
1	0.00	0.00	0.01	0.00	0.19	0.42	0.00	0.45	0.00	0.00	0.25	0.00	0.00
2	0.00	0.00	0.01	0.00	0.19	0.42	0.00	0.44	0.00	0.00	0.25	0.00	0.00
3	0.00	0.00	0.01	0.00	0.19	0.42	0.00	0.44	0.00	0.00	0.25	0.00	0.00
4	0.00	0.00	0.01	0.00	0.19	0.43	0.00	0.44	0.00	0.00	0.24	0.00	0.00
5	0.00	0.00	0.01	0.00	0.20	0.42	0.00	0.43	0.00	0.00	0.26	0.00	0.00
6	0.00	0.00	0.01	0.00	0.15	0.41	0.00	0.46	0.00	0.00	0.24	0.00	0.00
7	0.00	0.00	0.01	0.00	0.13	0.43	0.00	0.45	0.00	0.00	0.24	0.00	0.00
8	0.00	0.00	0.01	0.00	0.17	0.43	0.00	0.42	0.00	0.00	0.24	0.00	0.00
9	0.00	0.00	0.01	0.00	0.18	0.43	0.00	0.43	0.00	0.00	0.24	0.00	0.00

28/Tot

No.	Na2O	TiO2	MnO	K2O	MgO	SiO2	Cr2O3	Fe2+	Fe3+	CaO	Al2O3	Cl	Totale	Cl correction	28/Tot	
1	0.00	0.00	0.01	0.00	0.19	0.83	0.00	0.45	0.00	0.00	0.74	0.00	0.00	2.22	2.22	12.60 *Cl correction_ Clinohumite Analysis example pag.680 Zussman
2	0.00	0.00	0.01	0.00	0.19	0.84	0.00	0.44	0.00	0.00	0.76	0.00	0.00	2.24	2.23	12.53
3	0.00	0.00	0.01	0.00	0.19	0.83	0.00	0.44	0.00	0.00	0.75	0.00	0.00	2.22	2.22	12.63
4	0.00	0.00	0.01	0.00	0.19	0.86	0.00	0.44	0.00	0.00	0.73	0.00	0.00	2.23	2.23	12.58
5	0.00	0.00	0.01	0.00	0.20	0.84	0.00	0.43	0.00	0.00	0.75	0.00	0.00	2.23	2.23	12.54
6	0.00	0.00	0.01	0.00	0.15	0.81	0.00	0.46	0.00	0.00	0.77	0.00	0.00	2.20	2.20	12.71
7	0.00	0.00	0.01	0.00	0.13	0.86	0.00	0.45	0.00	0.00	0.73	0.00	0.00	2.18	2.18	12.83
8	0.00	0.00	0.01	0.00	0.17	0.86	0.00	0.42	0.00	0.00	0.72	0.00	0.00	2.20	2.19	12.76
9	0.00	0.00	0.01	0.00	0.18	0.86	0.00	0.43	0.00	0.00	0.73	0.00	0.00	2.21	2.21	12.66

No.	Na2O	TiO2	MnO	K2O	MgO	SiO2	Cr2O3	Fe2+	Fe3+	CaO	Al2O3	Cl	Total
1	0.00	0.00	0.01	0.00	0.19	0.42	0.00	0.45	0.00	0.00	0.49	0.00	1.56
2	0.00	0.00	0.01	0.00	0.19	0.42	0.00	0.44	0.00	0.00	0.51	0.00	1.56
3	0.00	0.00	0.01	0.00	0.19	0.42	0.00	0.44	0.00	0.00	0.50	0.00	1.55
4	0.00	0.00	0.01	0.00	0.19	0.43	0.00	0.44	0.00	0.00	0.48	0.00	1.56
5	0.00	0.00	0.01	0.00	0.20	0.42	0.00	0.43	0.00	0.00	0.50	0.00	1.56
6	0.00	0.00	0.01	0.00	0.15	0.41	0.00	0.46	0.00	0.00	0.51	0.00	1.54
7	0.00	0.00	0.01	0.00	0.13	0.43	0.00	0.45	0.00	0.00	0.48	0.00	1.51
8	0.00	0.00	0.01	0.00	0.17	0.43	0.00	0.42	0.00	0.00	0.48	0.00	1.53
9	0.00	0.00	0.01	0.00	0.18	0.43	0.00	0.43	0.00	0.00	0.49	0.00	1.54

No.	Na	Ti	Mn	K	Mg	Si	Cr	Fe2+	Fe3+	Ca	Al2	Cl	Total
1	0.01	0.01	0.09	0.01	2.37	5.24	0.00	5.67	0.00	0.00	6.23	0.01	19.64
2	0.01	0.02	0.10	0.01	2.38	5.25	0.00	5.48	0.00	0.00	6.33	0.01	19.59

Main table (rows 1–9):

	Na	Ti	Mn	K	Mg	Si	Cr2	Fe2+	Fe3+	Ca	Al2	Cl	Total
1	0.01	0.01	0.09	0.01	2.37	10.49	0.01	5.30	0.55	0.01	9.35	0.01	28.19
2	0.01	0.03	0.10	0.01	2.38	10.50	0.00	5.06	0.63	0.01	9.49	0.01	28.22
3	0.00	0.04	0.11	0.01	2.37	10.50	0.00	5.15	0.61	0.00	9.43	0.00	28.21
4	0.02	0.02	0.11	0.00	2.42	10.81	0.00	5.05	0.67	0.00	9.13	0.01	28.24
5	0.00	0.04	0.09	0.00	2.52	10.47	0.00	5.05	0.60	0.00	9.73	0.01	28.20
6	0.02	0.00	0.14	0.00	1.94	10.32	0.00	5.45	0.60	0.00	9.32	0.00	28.21
7	0.03	0.02	0.18	0.01	1.62	11.00	0.01	5.21	0.91	0.01	9.32	0.00	28.32
8	0.01	0.03	0.16	0.01	2.23	10.93	0.00	4.86	0.79	0.01	9.21	0.01	28.25
9	0.03	0.03	0.14	0.02	2.23	10.92	0.00	4.88	0.00	0.02	9.22	0.00	27.49

Partial table (rows 3–9):

	Na	Ti	Mn	K	Mg	Si	Fe3+	Fe2+	Ca	Al2	Cl		Total
3	0.00	0.01	0.11	0.01	2.37	5.25	0.00	5.56	0.00	6.28	0.00	0.00	19.60
4	0.02	0.03	0.11	0.01	2.42	5.40	0.00	5.49	0.00	6.09	0.00	0.01	19.56
5	0.00	0.04	0.09	0.00	2.52	5.24	0.00	5.45	0.00	6.28	0.00	0.01	19.61
6	0.02	0.02	0.14	0.01	1.94	5.16	0.00	5.85	0.00	6.49	0.01	0.00	19.61
7	0.03	0.04	0.18	0.01	1.62	5.50	0.00	5.81	0.00	6.21	0.01	0.00	19.40
8	0.01	0.00	0.16	0.02	2.23	5.46	0.00	5.41	0.00	6.14	0.01	0.01	19.46
9	0.03	0.03	0.14	0.02	2.23	5.46	0.00	5.41	0.00	6.15	0.02	0.00	19.47

correction throw the Na

	Na	Ti	Mn	K	Mg	Si	Cr	Fe2+	Fe3+	Ca	Al	Cl	OH	Total
1	0.02	0.01	0.09	0.02	2.35	5.21	0.00	5.26	0.37	0.01	6.19	0.02	0.01	15.98
2	0.02	0.02	0.10	0.02	2.36	5.21	0.00	5.02	0.42	0.01	6.28	0.01	0.01	15.99
3	0.00	0.02	0.10	0.02	2.35	5.21	0.00	5.11	0.40	0.00	6.24	0.01	0.00	15.99
4	0.04	0.01	0.11	0.00	2.39	5.36	0.00	5.00	0.44	0.00	6.04	0.01	0.00	15.99
5	0.00	0.02	0.09	0.00	2.50	5.20	0.00	5.01	0.40	0.00	6.24	0.01	0.00	15.99
6	0.04	0.00	0.14	0.01	1.93	5.12	0.00	5.41	0.39	0.01	6.44	0.01	0.00	15.99
7	0.06	0.01	0.18	0.02	1.61	5.44	0.00	5.15	0.60	0.01	6.14	0.01	0.01	15.99
8	0.02	0.02	0.15	0.03	2.21	5.42	0.00	4.82	0.52	0.02	6.08	0.01	0.01	15.99
9	0.06	0.02	0.14	0.04	2.27	5.56	0.00	4.97	0.00	0.02	6.26	0.01	0.01	15.99

F factor (Droop 1987) reported also in Zussman as the way to calculate the Fe^{3+} value

		F factor
1	35.52	0.99
2	35.45	0.99
3	35.46	0.99
4	35.42	0.99
5	35.46	0.99
6	35.48	0.99
7	35.22	0.99
8	35.28	0.99
9	35.34	1.02

Calculated using the suggestion of Prof. Andy Tindle Excel spreadsheet (Tindle 2014)

Fe3+	$Fe3+ = 0$ if $Fe2+ =$	$Fe3+ = t\ Fe2+ = 0$ if $Fe3+ >$ total Fe2+	
0.36852285	0.37	5.30	5.30
0.419760973	0.42	5.06	5.06
0.407046784	0.41	5.15	5.15
0.446394724	0.45	5.05	5.05
0.400374414	0.40	5.05	5.05
0.397546803	0.40	5.45	5.45
0.605463999	0.61	5.21	5.21
0.54775209	0.55	4.86	4.86
0.528924607	0.53	4.88	4.88

Based on Droop 1987

	FeO calc
1	30.20
2	29.04
3	29.31

4	28.84
5	28.92
6	30.80
7	29.15
8	27.47
9	30.73

Reformatted analysis with water_ Clinohumite Analysis example pag.680 Zussman

No.	Na2O	TiO2	MnO	K2O	MgO	SiO2	Cr2O3	FeO	CaO	Al2O3	Cl	H2O	Total
1	0.02	0.03	0.50	0.04	7.57	25.00	0.05	30.20	0.03	25.21	0.03	11.42	100.09
2	0.03	0.10	0.55	0.04	7.66	25.17	0.00	29.04	0.03	25.75	0.01	11.50	99.88
3	0.00	0.12	0.59	0.04	7.55	24.98	0.00	29.31	0.01	25.38	0.01	11.41	99.40
4	0.05	0.07	0.61	0.04	7.74	25.81	0.01	28.84	0.01	24.68	0.02	11.45	99.32
5	0.00	0.12	0.54	0.00	8.09	25.10	0.00	28.92	0.01	25.56	0.02	11.49	99.85
6	0.05	0.01	0.76	0.02	6.16	24.40	0.01	30.80	0.00	26.02	0.01	11.33	99.57
7	0.08	0.08	0.98	0.04	5.10	25.75	0.04	29.15	0.05	24.67	0.01	11.22	97.17
8	0.02	0.10	0.87	0.05	7.05	25.74	0.03	27.47	0.06	24.54	0.02	11.29	97.23
9	0.07	0.10	0.78	0.08	7.10	25.91	0.02	30.73	0.08	24.76	0.01	11.38	101.02

Si + Al per Al in ec Ottaedrico (tota vacanze ottaedriche

	Si+Al	Al			vacanze		R2+	Si		R3+
1	5.70	1.70	4.04	5.74	0.26	1.00	3.99	2.60	9.61	3.20
2	5.74	1.74	3.96	5.70	0.30	2.00	3.90	2.60	9.78	3.26
3	5.72	1.72	3.99	5.72	0.28	3.00	3.93	2.60	9.72	3.24
4	5.70	1.70	3.98	5.68	0.32	4.00	3.92	2.68	9.44	3.15
5	5.72	1.72	4.01	5.73	0.27	5.00	3.95	2.60	9.70	3.23
6	5.78	1.78	3.93	5.72	0.28	6.00	3.87	2.56	10.02	3.34
7	5.79	1.79	3.77	5.56	0.44	7.00	3.68	2.72	9.77	3.26
8	5.75	1.75	3.86	5.61	0.39	8.00	3.78	2.71	9.62	3.21
9	5.91	1.91	3.70	5.61	0.39	9.00	3.62	2.78	9.64	3.21

R2+ calculated assuming all Fe as Fe2+

$R3+= 28-2R2+-4Si/3$ Bourdelle and Cathelineau 2015

K2O+Na2O+CaO<1%wt Bourdelle et al., 2013 b*

1	0.09
2	0.09	*to exclude contaminated analysis
3	0.05
4	0.10
5	0.01
6	0.07
7	0.17
8	0.13
9	0.22

XFe=Fe/Fe+Mg

1	0.71
2	0.70

No. Analysis	
3	0.70
4	0.69
5	0.68
6	0.75
7	0.78
8	0.71
9	0.69

No. Analysis	Na2O	TiO2	MnO	K2O	MgO	SiO2	Cr2O3	FeO	CaO	Al2O3	Cl	Total	Sample	Structural zone	Qtz type	Chl texture
39	0.06	0.03	1.08	0.06	4.54	26.06	0.00	34.18	0.03	23.69	0.01	89.74	120-6	FC	Qtz II	Rad
40	0.04	0.03	0.64	0.03	4.85	25.63	0.00	34.26	0.01	24.23	0.03	89.75	120-6	FC	Qtz II	Rad
41	0.06	0.03	0.57	0.02	4.87	25.64	0.02	33.84	0.04	24.64	0.02	89.74	120-6	FC	Qtz II	Rad
42	0.00	0.06	0.52	0.01	9.26	25.82	0.00	29.04	0.02	24.84	0.02	89.60	120-6	FC	Qtz II	Rad
43	0.01	0.03	0.51	0.05	8.86	25.96	0.04	29.85	0.00	24.88	0.03	90.17	120-6	FC	Qtz II	Rad
44	0.01	0.04	0.71	0.05	8.73	26.50	0.01	30.08	0.04	24.49	0.02	90.69	120-6	FC	Qtz II	Rad
45	0.05	0.03	0.46	0.05	9.13	26.43	0.00	29.83	0.02	24.53	0.02	90.56	120-6	FC	Qtz II	Rad
46	0.01	0.13	0.60	0.01	8.05	26.13	0.00	30.47	0.02	25.02	0.01	90.45	120-6	FC	Qtz II	Rad
47	0.06	0.05	0.71	0.04	8.04	26.02	0.01	30.64	0.04	24.85	0.01	90.47	120-6	FC	Qtz II	Rad
48	0.03	0.04	0.65	0.03	8.32	26.57	0.00	30.47	0.00	24.53	0.03	90.67	120-6	FC	Qtz II	Rad
52	0.05	0.07	0.55	0.07	8.29	26.23	0.00	30.12	0.05	24.21	0.00	89.64	120-6	FC	Qtz II	Rad
53	0.06	0.09	0.57	0.05	9.17	26.57	0.05	29.86	0.02	24.49	0.03	90.95	120-6	FC	Qtz II	Rad
54	0.02	0.09	0.67	0.04	8.30	26.16	0.00	30.82	0.05	24.10	0.02	90.26	120-6	FC	Qtz II	Rad

	XNa2O	XTiO2	XMnO	XK2O	XMgO	XSiO2	XCr2O3	Fe2+	Fe3+	XCaO	XAl2O3	XCl
39	0.00	0.00	0.02	0.00	0.11	0.43	0.00	0.48	0.00	0.00	0.23	0.00
40	0.00	0.00	0.01	0.00	0.12	0.43	0.00	0.48	0.00	0.00	0.24	0.00
41	0.00	0.00	0.01	0.00	0.12	0.43	0.00	0.47	0.00	0.00	0.24	0.00
42	0.00	0.00	0.01	0.00	0.23	0.43	0.00	0.40	0.00	0.00	0.24	0.00
43	0.00	0.00	0.01	0.00	0.22	0.43	0.00	0.42	0.00	0.00	0.24	0.00
44	0.00	0.00	0.01	0.00	0.22	0.44	0.00	0.42	0.00	0.00	0.24	0.00
45	0.00	0.00	0.01	0.00	0.23	0.44	0.00	0.42	0.00	0.00	0.25	0.00
46	0.00	0.00	0.01	0.00	0.20	0.43	0.00	0.42	0.00	0.00	0.24	0.00
47	0.00	0.00	0.01	0.00	0.20	0.43	0.00	0.43	0.00	0.00	0.24	0.00
48	0.00	0.00	0.01	0.00	0.21	0.44	0.00	0.42	0.00	0.00	0.24	0.00
52	0.00	0.00	0.01	0.00	0.21	0.44	0.00	0.42	0.00	0.00	0.24	0.00
53	0.00	0.00	0.01	0.00	0.23	0.44	0.00	0.42	0.00	0.00	0.24	0.00
54	0.00	0.00	0.01	0.00	0.21	0.44	0.00	0.43	0.00	0.00	0.24	0.00

	Na2O	TiO2	MnO	K2O	MgO	SiO2	Cr2O3	Fe2+	Fe3+	CaO	Al2O3	Cl	Totale	Cl correction	28/Tot	
39	0.00	0.00	0.02	0.00	0.11	0.87	0.00	0.48	0.00	0.00	0.70	0.00	2.17	2.17	12.90	*Cl correction_ Clinohumite Analysis example pag.680 Zussman
40	0.00	0.00	0.01	0.00	0.12	0.85	0.00	0.48	0.00	0.00	0.71	0.00	2.17	2.17	12.88	
41	0.00	0.00	0.01	0.00	0.12	0.85	0.00	0.47	0.00	0.00	0.72	0.00	2.18	2.18	12.84	
42	0.00	0.00	0.01	0.00	0.23	0.86	0.00	0.40	0.00	0.00	0.73	0.00	2.23	2.23	12.53	
43	0.00	0.00	0.01	0.00	0.22	0.86	0.00	0.42	0.00	0.00	0.73	0.00	2.24	2.24	12.50	
44	0.00	0.00	0.01	0.00	0.22	0.88	0.00	0.42	0.00	0.00	0.72	0.00	2.25	2.25	12.44	
45	0.00	0.00	0.01	0.00	0.23	0.88	0.00	0.42	0.00	0.00	0.72	0.00	2.25	2.25	12.43	
46	0.00	0.00	0.01	0.00	0.20	0.87	0.00	0.42	0.00	0.00	0.74	0.00	2.24	2.24	12.49	
47	0.00	0.00	0.01	0.00	0.20	0.87	0.00	0.43	0.00	0.00	0.73	0.00	2.24	2.24	12.52	
48	0.00	0.00	0.01	0.00	0.21	0.88	0.00	0.42	0.00	0.00	0.72	0.00	2.25	2.25	12.46	
52	0.00	0.00	0.01	0.00	0.21	0.87	0.00	0.42	0.00	0.00	0.71	0.00	2.22	2.22	12.60	
53	0.00	0.00	0.01	0.00	0.23	0.88	0.00	0.42	0.00	0.00	0.72	0.00	2.26	2.26	12.38	
54	0.00	0.00	0.01	0.00	0.21	0.87	0.00	0.43	0.00	0.00	0.71	0.00	2.23	2.23	12.57	

	Na2O	TiO2	MnO	K2O	MgO	SiO2	Cr2O3	Fe2+	Fe3+	CaO	Al2O3	Cl	Total
39	0.00	0.00	0.02	0.00	0.11	0.43	0.00	0.48	0.00	0.00	0.46	0.00	1.51
40	0.00	0.00	0.01	0.00	0.12	0.43	0.00	0.48	0.00	0.00	0.48	0.00	1.51
41	0.00	0.00	0.01	0.00	0.12	0.43	0.00	0.47	0.00	0.00	0.48	0.00	1.51
42	0.00	0.00	0.01	0.00	0.23	0.43	0.00	0.40	0.00	0.00	0.49	0.00	1.56
43	0.00	0.00	0.01	0.00	0.22	0.43	0.00	0.42	0.00	0.00	0.49	0.00	1.56
44	0.00	0.00	0.01	0.00	0.23	0.44	0.00	0.42	0.00	0.00	0.48	0.00	1.57
45	0.00	0.00	0.01	0.00	0.23	0.44	0.00	0.42	0.00	0.00	0.49	0.00	1.57
46	0.00	0.00	0.01	0.00	0.20	0.43	0.00	0.42	0.00	0.00	0.49	0.00	1.56
47	0.00	0.00	0.01	0.00	0.20	0.43	0.00	0.43	0.00	0.00	0.49	0.00	1.57
48	0.00	0.00	0.01	0.00	0.21	0.44	0.00	0.42	0.00	0.00	0.48	0.00	1.55
52	0.00	0.00	0.01	0.00	0.21	0.44	0.00	0.42	0.00	0.00	0.47	0.00	1.58
53	0.00	0.00	0.01	0.00	0.23	0.44	0.00	0.42	0.00	0.00	0.48	0.00	1.56
54	0.00	0.00	0.01	0.00	0.21	0.44	0.00	0.43	0.00	0.00	0.47	0.00	1.56

	Na	Ti	Mn	K	Mg	Si	Cr	Fe2+	Fe3+	Ca	Al2	Cl	Total
39	0.03	0.01	0.20	0.02	1.45	5.59	0.00	6.13	0.00	0.00	5.99	0.01	19.43
40	0.02	0.01	0.12	0.01	1.55	5.49	0.00	6.14	0.00	0.00	6.12	0.01	19.46
41	0.03	0.01	0.10	0.01	1.55	5.48	0.00	6.05	0.00	0.00	6.20	0.01	19.43
42	0.00	0.02	0.09	0.01	2.88	5.39	0.00	5.07	0.00	0.00	6.11	0.01	19.56
43	0.00	0.01	0.09	0.00	2.75	5.40	0.00	5.19	0.00	0.00	6.10	0.01	19.55
44	0.00	0.01	0.13	0.01	2.69	5.49	0.00	5.21	0.00	0.00	5.98	0.01	19.53
45	0.02	0.01	0.08	0.01	2.82	5.47	0.00	5.16	0.00	0.00	5.98	0.01	19.56
46	0.01	0.04	0.11	0.00	2.49	5.43	0.00	5.30	0.00	0.00	6.13	0.00	19.49
47	0.03	0.02	0.12	0.01	2.50	5.42	0.00	5.34	0.00	0.00	6.10	0.01	19.54
48	0.01	0.01	0.11	0.01	2.57	5.51	0.00	5.28	0.00	0.00	5.99	0.00	19.50
52	0.02	0.02	0.10	0.02	2.59	5.50	0.00	5.28	0.00	0.00	5.98	0.01	19.52
53	0.02	0.03	0.10	0.01	2.82	5.48	0.00	5.15	0.00	0.00	5.95	0.00	19.55
54	0.01	0.03	0.12	0.01	2.59	5.47	0.00	5.39	0.00	0.00	5.94	0.01	19.56

F factor (Droop 1987) reported also in Zussman as the way to calculate the Fe3+ value

	Na	Ti	Mn	K	Mg	Si	Cr2	Fe2+	Fe3+	Ca	Al2	Cl	Total	F factor
39	0.03	0.01	0.20	0.02	1.45	11.19	0.00	5.56	0.87	0.00	8.99	0.01	28.31	0.99
40	0.02	0.01	0.12	0.01	1.55	10.99	0.00	5.59	0.83	0.00	9.18	0.01	28.29	0.99
41	0.03	0.01	0.10	0.01	1.55	10.96	0.00	5.47	0.86	0.00	9.31	0.01	28.30	0.99
42	0.00	0.02	0.09	0.00	2.88	10.77	0.00	4.62	0.68	0.00	9.16	0.01	28.23	0.99
43	0.00	0.01	0.09	0.01	2.75	10.80	0.00	4.73	0.69	0.00	9.15	0.01	28.23	0.99
44	0.00	0.01	0.13	0.01	2.69	10.97	0.00	4.71	0.72	0.00	8.96	0.01	28.25	0.99
45	0.02	0.01	0.08	0.00	2.82	10.94	0.00	4.71	0.67	0.00	8.97	0.01	28.25	0.99
46	0.01	0.04	0.11	0.00	2.49	10.86	0.00	4.78	0.77	0.00	9.19	0.00	28.26	0.99
47	0.03	0.02	0.12	0.01	2.50	10.84	0.00	4.87	0.70	0.00	9.15	0.01	28.25	0.99
48	0.01	0.01	0.11	0.02	2.57	11.02	0.00	4.78	0.76	0.00	8.99	0.01	28.27	0.99
52	0.02	0.02	0.10	0.01	2.59	11.00	0.00	4.80	0.73	0.00	8.97	0.00	28.26	0.99
53	0.02	0.03	0.10	0.01	2.82	10.95	0.01	4.69	0.69	0.00	8.92	0.01	28.24	0.99
54	0.01	0.03	0.12	0.01	2.59	10.94	0.00	4.94	0.68	0.00	8.91	0.01	28.24	0.99

	Na	Ti	Mn	K	Mg	Si	Cr	Fe2+	Fe3+	Ca	Al	Cl	OH	Total
39	0.05	0.01	0.19	0.03	1.44	5.53	0.00	5.50	0.57	0.01	5.93	0.01	0.01	35.25
40	0.03	0.01	0.12	0.01	1.53	5.44	0.00	5.53	0.54	0.00	6.06	0.00	0.02	35.27
41	0.05	0.00	0.10	0.01	1.53	5.42	0.00	5.41	0.57	0.01	6.14	0.01	0.01	35.25
42	0.00	0.01	0.09	0.01	2.86	5.34	0.00	4.58	0.45	0.01	6.06	0.01	0.01	35.39
43	0.01	0.00	0.09	0.03	2.72	5.35	0.00	4.69	0.46	0.01	6.05	0.01	0.02	35.38
44	0.00	0.01	0.12	0.03	2.67	5.44	0.00	4.69	0.47	0.01	5.92	0.02	0.02	35.37
45	0.04	0.01	0.08	0.03	2.79	5.42	0.00	4.67	0.44	0.01	5.93	0.01	0.01	35.42

No.															
46	0.01	0.02	0.10	0.01	0.02	2.47	5.38	0.00	4.74	0.51	0.00	6.07	0.01	15.99	35.31
47	0.05	0.01	0.12	0.02	0.01	2.47	5.37	0.00	4.83	0.46	0.01	6.05	0.01	15.99	35.40
48	0.02	0.01	0.11	0.02	0.01	2.55	5.46	0.00	4.73	0.50	0.00	5.94	0.02	15.98	35.33
52	0.04	0.01	0.10	0.04	0.01	2.57	5.45	0.00	4.75	0.48	0.01	5.93	0.00	16.00	35.37
53	0.05	0.01	0.10	0.02	0.01	2.79	5.43	0.00	4.65	0.45	0.00	5.90	0.02	15.98	35.41
54	0.01	0.01	0.12	0.02	0.00	2.57	5.43	0.00	4.90	0.45	0.01	5.89	0.01	15.99	35.40

Calculated using the suggestion of Prof. Andy Tindle' Excel spreadsheet (Tindle 2014)

Fe3+	Fe3+ = 0 if Fe2+ =	Fe3+ = t Fe2+ = 0 if Fe3+ > total Fe2+	
0.577159097	0.58	5.56	5.56
0.550488441	0.55	5.59	5.59
0.574682892	0.57	5.47	5.47
0.450169946	0.45	4.62	4.62
0.46091839	0.46	4.73	4.73
0.477561814	0.48	4.73	4.73
0.448354478	0.45	4.71	4.71
0.513236969	0.51	4.78	4.78
0.46949854	0.46	4.87	4.87
0.505553057	0.51	4.78	4.78
0.484377863	0.48	4.80	4.80
0.457991265	0.46	4.69	4.69
0.450851657	0.45	4.94	4.94

Based on Droop 1987

	FeO calc
39	30.96
40	31.19
41	30.62
42	26.46
43	27.20
44	27.32
45	27.24
46	27.52
47	27.97
48	27.55
52	27.36
53	27.20
54	28.24

Reformatted analysis with water_ Clinohumite Analysis example pag.680 Zussman

No.	Na2O	TiO2	MnO	K2O	MgO	SiO2	Cr2O3	FeO	Fe2O3	CaO	Al2O3	Cl	H2O	Total
39	0.06	0.03	1.08	0.06	4.54	26.06	0.00	30.96	0.00	0.03	23.69	0.01	11.17	97.70
40	0.04	0.04	0.64	0.03	4.85	25.63	0.00	31.19	0.00	0.01	24.23	0.03	11.18	97.86
41	0.06	0.03	0.57	0.02	4.87	25.64	0.02	30.62	0.00	0.04	24.64	0.02	11.22	97.74
42	0.00	0.06	0.52	0.02	9.26	25.82	0.00	26.46	0.00	0.02	24.84	0.02	11.49	98.51
43	0.01	0.03	0.51	0.01	8.86	25.96	0.04	27.20	0.00	0.00	24.88	0.03	11.52	99.04
44	0.01	0.04	0.71	0.05	8.73	26.50	0.01	27.32	0.00	0.04	24.49	0.02	11.57	99.50
45	0.05	0.03	0.46	0.05	9.13	26.43	0.00	27.24	0.00	0.02	24.53	0.01	11.59	99.56
46	0.01	0.13	0.60	0.01	8.05	26.13	0.00	27.52	0.00	0.02	25.02	0.01	11.54	99.03
47	0.06	0.05	0.71	0.04	8.04	26.02	0.01	27.97	0.00	0.04	24.85	0.03	11.51	99.31
48	0.03	0.04	0.65	0.03	8.32	26.57	0.00	27.55	0.00	0.00	24.53	0.00	11.56	99.31
52	0.05	0.07	0.55	0.07	8.29	26.23	0.00	27.36	0.00	0.05	24.21	0.03	11.44	98.32
53	0.06	0.09	0.57	0.05	9.17	26.57	0.05	27.20	0.00	0.02	24.49	0.03	11.63	99.92
54	0.02	0.09	0.67	0.04	8.30	26.16	0.00	28.24	0.00	0.05	24.10	0.02	11.46	99.14

	Si + Al per	Al in ec	Ottaedrico (tota	vacanze ottaedriche		R2+	R3+ cal Si	Si		R3+
39	5.73	1.73	3.85	5.58	0.42	39.00	3.75	3.25	2.77	9.43	3.14
40	5.75	1.75	3.87	5.61	0.39	40.00	3.80	3.30	2.72	9.52	3.17
41	5.78	1.78	3.81	5.59	0.41	41.00	3.76	3.35	2.71	9.65	3.22
42	5.70	1.70	3.99	5.69	0.31	42.00	3.94	3.25	2.67	9.44	3.15
43	5.70	1.70	3.98	5.69	0.31	43.00	3.94	3.25	2.68	9.42	3.14
44	5.68	1.68	3.98	5.66	0.34	44.00	3.92	3.20	2.72	9.29	3.10
45	5.67	1.67	4.00	5.67	0.33	45.00	3.95	3.19	2.71	9.25	3.08
46	5.73	1.73	3.92	5.65	0.35	46.00	3.86	3.29	2.69	9.52	3.17
47	5.71	1.71	3.95	5.66	0.34	47.00	3.88	3.25	2.69	9.49	3.16
48	5.70	1.70	3.95	5.64	0.36	48.00	3.89	3.22	2.73	9.31	3.10
52	5.69	1.69	3.95	5.64	0.36	52.00	3.90	3.20	2.72	9.30	3.10
53	5.66	1.66	4.01	5.67	0.33	53.00	3.95	3.18	2.71	9.25	3.08
54	5.66	1.66	4.02	5.68	0.32	54.00	3.96	3.17	2.71	9.24	3.08

K2O+Na2O+CaO<1%wt Bourdelle et al., ; $R2+$ calculated assuming all Fe as Fe^{2+}

$R3+= 28-2R2+-4Si)/3$ Bourdelle and Cathelineau 2015

39.00	0.15
40.00	0.08
41.00	0.12
42.00	0.04
43.00	0.02
44.00	0.10
45.00	0.13
46.00	0.04
47.00	0.14
48.00	0.06
52.00	0.17
53.00	0.12
54.00	0.10

*to exclude contaminated analysis

XFe=Fe/Fe+Mg

39.00	0.81
40.00	0.80
41.00	0.80
42.00	0.64
43.00	0.65
44.00	0.66
45.00	0.65
46.00	0.68
47.00	0.68
48.00	0.67
52.00	0.67
53.00	0.65
54.00	0.68
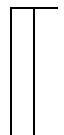
No. Analysis	Na2O	TiO2	MnO	K2O	MgO	SiO2	Cr2O3	FeO	CaO	Al2O3	Cl	Total	Sample	Structural zone	Qtz type	Chl texture
91	0.07	0.08	0.35	0.09	12.98	27.61	0.02	25.61	0.06	23.34	0.00	90.56	120-2	DZ	Qtz I	Verm
92	0.06	0.03	0.39	0.06	13.42	27.35	0.01	25.77	0.03	23.53	0.00	90.80	120-2	DZ	Qtz I	Verm
93	0.03	0.01	0.48	0.10	12.85	27.43	0.00	25.97	0.05	24.02	0.01	91.16	120-2	DZ	Qtz I	Verm
94	0.06	0.05	0.31	0.12	12.70	27.31	0.05	25.52	0.05	23.09	0.01	89.55	120-2	DZ	Qtz I	Verm
95	0.01	0.09	0.37	0.05	12.57	27.88	0.06	26.06	0.05	23.48	0.00	90.82	120-2	DZ	Qtz I	Verm
96	0.05	0.03	0.43	0.07	12.59	27.79	0.01	25.77	0.03	23.21	0.00	90.17	120-2	DZ	Qtz I	Verm
99	0.02	0.06	0.45	0.03	12.84	27.54	0.06	26.70	0.04	23.89	0.01	91.77	120-2	DZ	Qtz I	Verm
100	0.01	0.07	0.45	0.04	12.02	27.34	0.13	26.83	0.03	23.66	0.00	90.64	120-2	DZ	Qtz I	Verm
101	0.00	0.02	0.46	0.04	12.43	27.77	0.10	26.76	0.05	23.22	0.02	91.10	120-2	DZ	Qtz I	Verm
102	0.05	0.04	0.47	0.06	13.17	27.17	0.04	25.58	0.03	23.78	0.02	90.56	120-2	DZ	Qtz I	Verm
103	0.05	0.02	0.47	0.05	12.78	27.90	0.09	26.28	0.03	23.41	0.00	91.11	120-2	DZ	Qtz I	Verm

	XNa2O	XTiO2	XMnO	XK2O	XMgO	XSiO2	XCr2O3	Fe2+	Fe3+	XCaO	XAl2O3	XCl
91	0.00	0.00	0.00	0.00	0.32	0.46	0.00	0.36	0.00	0.00	0.23	0.00
92	0.00	0.00	0.01	0.00	0.33	0.46	0.00	0.36	0.00	0.00	0.23	0.00
93	0.00	0.00	0.01	0.00	0.32	0.46	0.00	0.36	0.00	0.00	0.24	0.00
94	0.00	0.00	0.00	0.00	0.32	0.45	0.00	0.36	0.00	0.00	0.23	0.00
95	0.00	0.00	0.01	0.00	0.31	0.46	0.00	0.36	0.00	0.00	0.23	0.00
96	0.00	0.00	0.01	0.00	0.31	0.46	0.00	0.36	0.00	0.00	0.23	0.00
99	0.00	0.00	0.01	0.00	0.32	0.46	0.00	0.37	0.00	0.00	0.23	0.00
100	0.00	0.00	0.01	0.00	0.30	0.46	0.00	0.37	0.00	0.00	0.23	0.00
101	0.00	0.00	0.01	0.00	0.31	0.46	0.00	0.37	0.00	0.00	0.23	0.00
102	0.00	0.00	0.01	0.00	0.33	0.45	0.00	0.36	0.00	0.00	0.23	0.00
103	0.00	0.00	0.01	0.00	0.32	0.46	0.00	0.37	0.00	0.00	0.23	0.00

28/Tot

	Na2O	TiO2	MnO	K2O	MgO	SiO2	Cr2O3	Fe2+	Fe3+	CaO	Al2O3	Cl	Totale	Cl correction	28/Tot
91	0.00	0.00	0.00	0.00	0.32	0.92	0.00	0.36	0.00	0.00	0.69	0.00	0.00	2.29	12.20
92	0.00	0.00	0.01	0.00	0.33	0.91	0.00	0.36	0.00	0.00	0.69	0.00	0.00	2.30	12.16
93	0.00	0.00	0.01	0.00	0.32	0.91	0.00	0.36	0.00	0.00	0.71	0.00	0.00	2.31	12.12
94	0.00	0.00	0.00	0.00	0.32	0.91	0.00	0.36	0.00	0.00	0.68	0.00	0.00	2.27	12.34
95	0.00	0.00	0.01	0.00	0.31	0.93	0.00	0.36	0.00	0.00	0.69	0.00	0.00	2.30	12.15
96	0.00	0.00	0.01	0.00	0.31	0.93	0.00	0.36	0.00	0.00	0.68	0.00	0.00	2.29	12.24
99	0.00	0.00	0.01	0.00	0.32	0.92	0.00	0.37	0.00	0.00	0.70	0.00	0.00	2.32	12.07
100	0.00	0.00	0.01	0.00	0.30	0.91	0.00	0.37	0.00	0.00	0.68	0.00	0.00	2.29	12.23
101	0.00	0.00	0.01	0.00	0.31	0.92	0.00	0.37	0.00	0.00	0.70	0.00	0.00	2.30	12.18
102	0.00	0.00	0.01	0.00	0.33	0.90	0.00	0.36	0.00	0.00	0.68	0.00	0.00	2.30	12.19
103	0.00	0.00	0.01	0.00	0.32	0.93	0.00	0.37	0.00	0.00	0.69	0.00	0.00	2.31	12.12

	Na2O	TiO2	MnO	K2O	MgO	SiO2	Cr2O3	Fe2+	Fe3+	CaO	Al2O3	Cl	Total	
91	0.00	0.00	0.00	0.00	0.32	0.46	0.00	0.36	0.00	0.00	0.46	0.00	0.00	1.61
92	0.00	0.00	0.01	0.00	0.33	0.46	0.00	0.36	0.00	0.00	0.46	0.00	0.00	1.62
93	0.00	0.00	0.01	0.00	0.32	0.46	0.00	0.36	0.00	0.00	0.47	0.00	0.00	1.62
94	0.00	0.00	0.00	0.00	0.32	0.45	0.00	0.36	0.00	0.00	0.45	0.00	0.00	1.59
95	0.00	0.00	0.01	0.00	0.31	0.46	0.00	0.36	0.00	0.00	0.46	0.00	0.00	1.61
96	0.00	0.00	0.01	0.00	0.31	0.46	0.00	0.36	0.00	0.00	0.46	0.00	0.00	1.60

Partial data (rows 99–103):

	Na	Ti	Mn	K	Mg	Si	Cr		Fe2+	Fe3+	Ca	Al2	Cl	Total	
99	0.00	0.00	0.01	0.00	0.32	0.46	0.00	0.00	0.37	0.00	0.00	0.47	0.00		1.63
100	0.00	0.00	0.01	0.00	0.30	0.46	0.00	0.00	0.37	0.00	0.00	0.46	0.00		1.60
101	0.00	0.00	0.01	0.00	0.31	0.46	0.00	0.00	0.37	0.00	0.00	0.46	0.00		1.61
102	0.00	0.00	0.01	0.00	0.33	0.45	0.00	0.00	0.36	0.00	0.00	0.47	0.00		1.61
103	0.00	0.00	0.01	0.00	0.32	0.46	0.00	0.00	0.37	0.00	0.00	0.46	0.00		1.62

	Na	Ti	Mn	K	Mg	Si	Cr		Fe2+	Fe3+	Ca	Al2	Cl	Total
91	0.03	0.01	0.06	0.02	3.93	5.61	0.00	0.00	4.35	0.00	0.00	5.59	0.00	19.61
92	0.02	0.01	0.07	0.01	4.05	5.53	0.00	0.00	4.36	0.00	0.00	5.53	0.00	19.67
93	0.01	0.00	0.08	0.02	3.87	5.54	0.00	0.00	4.38	0.00	0.00	5.71	0.00	19.63
94	0.03	0.01	0.05	0.03	3.89	5.61	0.00	0.00	4.38	0.00	0.00	5.59	0.00	19.61
95	0.01	0.01	0.06	0.01	3.79	5.64	0.00	0.00	4.41	0.00	0.00	5.60	0.00	19.55
96	0.02	0.00	0.07	0.02	3.82	5.66	0.00	0.00	4.39	0.00	0.00	5.57	0.00	19.57
99	0.01	0.01	0.08	0.01	3.84	5.53	0.01	0.01	4.48	0.00	0.00	5.65	0.00	19.63
100	0.00	0.01	0.08	0.01	3.65	5.56	0.01	0.02	4.57	0.00	0.00	5.68	0.01	19.57
101	0.00	0.00	0.08	0.01	3.76	5.63	0.01	0.01	4.54	0.00	0.00	5.55	0.01	19.59
102	0.02	0.01	0.08	0.02	3.98	5.51	0.00	0.01	4.34	0.00	0.00	5.68	0.01	19.65
103	0.02	0.00	0.08	0.01	3.84	5.63	0.01	0.01	4.43	0.00	0.00	5.56	0.00	19.59

F factor (Droop 1987) reported also in Zussman as the way to calculate the Fe3+ value

	Na	Ti	Mn	K	Mg	Si	Cr2		Fe2+	Fe3+	Ca	Al2	Cl	Total	F factor
91	0.03	0.02	0.06	0.02	3.93	11.21	0.00	0.00	3.96	0.58	0.01	8.38	0.00	28.22	0.99
92	0.02	0.03	0.07	0.01	4.05	11.07	0.00	0.00	4.03	0.49	0.01	8.42	0.00	28.18	0.99
93	0.01	0.01	0.08	0.02	3.87	11.07	0.00	0.00	4.01	0.56	0.01	8.57	0.00	28.21	0.99
94	0.03	0.02	0.05	0.03	3.89	11.22	0.01	0.01	3.99	0.59	0.01	8.38	0.00	28.22	0.99
95	0.01	0.03	0.06	0.01	3.79	11.28	0.01	0.01	3.96	0.68	0.01	8.40	0.00	28.23	0.99
96	0.02	0.01	0.07	0.01	3.82	11.32	0.00	0.00	3.96	0.65	0.01	8.36	0.00	28.23	0.99
99	0.01	0.02	0.08	0.01	3.84	11.06	0.01	0.01	4.11	0.55	0.01	8.48	0.00	28.19	0.99
100	0.00	0.02	0.08	0.01	3.65	11.13	0.02	0.02	4.14	0.64	0.02	8.51	0.00	28.21	0.99
101	0.00	0.01	0.08	0.01	3.76	11.26	0.01	0.01	4.11	0.63	0.01	8.32	0.01	28.21	0.99
102	0.02	0.01	0.08	0.02	3.98	11.02	0.01	0.01	3.99	0.53	0.01	8.53	0.01	28.19	0.99
103	0.02	0.01	0.08	0.01	3.84	11.25	0.01	0.01	4.02	0.61	0.01	8.34	0.00	28.21	0.99

correction throw the Na

	Na	Ti	Mn	K	Mg	Si	Cr		Fe2+	Fe3+	Ca	Al	Cl	OH	Total
91	0.06	0.01	0.06	0.05	3.90	5.56	0.00	0.00	3.93	0.39	0.01	5.54	0.00	16.00	35.51
92	0.04	0.01	0.07	0.03	4.02	5.50	0.00	0.00	4.01	0.33	0.01	5.58	0.00	16.00	35.58
93	0.02	0.00	0.08	0.05	3.84	5.49	0.00	0.00	3.98	0.37	0.01	5.67	0.00	16.00	35.51
94	0.05	0.01	0.05	0.06	3.86	5.57	0.00	0.00	3.96	0.39	0.01	5.55	0.01	15.99	35.51
95	0.01	0.01	0.06	0.03	3.76	5.59	0.00	0.00	3.92	0.45	0.01	5.55	0.00	16.00	35.41
96	0.04	0.00	0.07	0.04	3.79	5.61	0.00	0.00	3.92	0.43	0.01	5.52	0.00	16.00	35.44
99	0.02	0.01	0.08	0.02	3.82	5.49	0.00	0.00	4.09	0.37	0.01	5.62	0.00	16.00	35.52
100	0.01	0.01	0.08	0.02	3.62	5.52	0.01	0.01	4.11	0.42	0.01	5.63	0.00	16.00	35.44
101	0.00	0.00	0.08	0.02	3.73	5.59	0.01	0.01	4.08	0.42	0.01	5.51	0.01	15.99	35.44
102	0.04	0.01	0.08	0.03	3.96	5.47	0.00	0.00	3.96	0.35	0.01	5.65	0.01	15.99	35.55
103	0.04	0.00	0.08	0.03	3.81	5.58	0.01	0.01	3.99	0.41	0.01	5.52	0.00	16.00	35.48

Calculated using the suggestion of Prof. Andy Tindle' Excel spreadsheet (Tindle 2014)

Fe3+		Fe3+ = 0 if Fe2+ =		Fe3+ = t Fe2+ = 0 if Fe3+ > total Fe2+	
0.389727867	0.39	3.96	0.39	3.96	
0.328551527	0.33	4.03	0.33	4.03	
0.376325619	0.38	4.01	0.38	4.01	
0.393720215	0.39	3.99	0.39	3.99	
0.451710442	0.45	3.96	0.45	3.96	
0.431737316	0.43	3.96	0.43	3.96	
0.369747032	0.37	4.11	0.37	4.11	
0.427409555	0.43	4.14	0.43	4.14	
0.421869896	0.42	4.11	0.42	4.11	
0.352467212	0.35	3.99	0.35	3.99	
0.409037169	0.41	4.02	0.41	4.02	

Based on Droop 1987

	FeO calc	Fe2O3 calc
91	23.31	2.55
92	23.83	2.16
93	23.74	2.48
94	23.23	2.55
95	23.39	2.97
96	23.24	2.82
99	24.50	2.45
100	24.32	2.79
101	24.27	2.77
102	23.50	2.31
103	23.85	2.70

Reformatted analysis with water_ Clinohumite Analysis example pag.680 Zussman

No.	Na2O	TiO2	MnO	K2O	MgO	SiO2	Cr2O3	FeO	Fe2O3	CaO	Al2O3	Cl	H2O	Total
91	0.07	0.08	0.35	0.09	12.98	27.61	0.02	23.31	2.55	0.06	23.34	0.00	0.00	102.28
92	0.06	0.03	0.39	0.06	13.42	27.35	0.01	23.83	2.16	0.03	23.53	0.00	0.00	102.72
93	0.03	0.01	0.48	0.10	12.85	27.43	0.00	23.74	2.48	0.05	24.02	0.01	0.01	103.06
94	0.06	0.05	0.31	0.12	12.70	27.31	0.05	23.23	2.55	0.05	23.09	0.01	0.01	101.21
95	0.01	0.09	0.37	0.05	12.57	27.88	0.06	23.39	2.97	0.05	23.48	0.00	0.00	102.79
96	0.05	0.03	0.43	0.07	12.59	27.79	0.01	23.24	2.82	0.03	23.21	0.00	0.00	102.04
99	0.02	0.06	0.45	0.03	12.84	27.54	0.06	24.50	2.45	0.04	23.89	0.01	0.01	103.83
100	0.01	0.07	0.45	0.04	12.02	27.34	0.13	24.32	2.79	0.03	23.66	0.00	0.00	102.65
101	0.00	0.02	0.46	0.04	12.43	27.77	0.10	24.27	2.77	0.05	23.22	0.02	0.02	102.97
102	0.05	0.04	0.47	0.06	13.17	27.17	0.04	23.50	2.31	0.03	23.78	0.02	0.02	102.45
103	0.05	0.02	0.47	0.05	12.78	27.90	0.09	23.85	2.70	0.03	23.41	0.00	0.00	103.24

	Si + Al per Al in e Ottaedrico (tota vacanze ottaedriche						R2+	R3+ cal Si		R3+	
91	5.55	1.55	4.14	5.70	0.30	91.00	4.11	2.96	2.78	8.66	2.89

92	5.54	1.54	4.21	5.75	0.25		92.00	4.18	2.95	2.75	8.65	2.88
93	5.58	1.58	4.14	5.72	0.28		93.00	4.09	3.02	2.75	8.82	2.94
94	5.56	1.56	4.14	5.69	0.31		94.00	4.10	2.97	2.78	8.66	2.89
95	5.57	1.57	4.11	5.68	0.32		95.00	4.07	3.00	2.80	8.68	2.89
96	5.57	1.57	4.11	5.68	0.32		96.00	4.07	2.98	2.81	8.63	2.88
99	5.56	1.56	4.18	5.74	0.26		99.00	4.14	2.99	2.75	8.74	2.91
100	5.58	1.58	4.13	5.70	0.30		100.00	4.08	3.03	2.76	8.80	2.93
101	5.55	1.55	4.16	5.71	0.29		101.00	4.12	2.96	2.79	8.59	2.86
102	5.56	1.56	4.18	5.74	0.26		102.00	4.13	3.00	2.74	8.79	2.93
103	5.55	1.55	4.15	5.70	0.30		103.00	4.11	2.96	2.79	8.62	2.87

R2+ calculated assuming all Fe as Fe2+

K2O+Na2O+CaO<1%wt Bourdelle et al., 2013 b*

91.00	0.22
92.00	0.14
93.00	0.17
94.00	0.24
95.00	0.12
96.00	0.16
99.00	0.10
100.00	0.08
101.00	0.08
102.00	0.14
103.00	0.13

*to exclude contaminated analysis

XFe=Fe/Fe+Mg

91.00	0.53
92.00	0.52
93.00	0.53
94.00	0.53
95.00	0.54
96.00	0.53
99.00	0.54
100.00	0.56
101.00	0.55
102.00	0.52
103.00	0.54

No. Analysis	Na2O	TiO2	MnO	K2O	MgO	SiO2	Cr2O3	FeO	CaO	Al2O3	Cl	Total	Sample	Structural zone	Qtz type	Chl texture
10	0.04	0.02	0.59	0.06	13.66	25.49	0.00	27.86	0.03	22.04	0.00	89.78	120-4	FC	Qtz I	Verm
11	0.07	0.01	0.65	0.02	13.79	26.00	0.01	27.74	0.04	22.13	0.00	90.45	120-4	FC	Qtz I	Verm
12	0.00	0.00	0.62	0.04	13.74	25.83	0.04	27.87	0.05	22.00	0.01	90.20	120-4	FC	Qtz I	Verm
13	0.04	0.00	0.60	0.08	5.04	23.29	0.00	38.45	0.03	22.44	0.03	90.01	120-4	FC	Qtz I	Rad
14	0.02	0.08	0.55	0.04	7.69	24.79	0.00	35.04	0.03	22.10	0.03	90.38	120-4	FC	Qtz I	Rad
15	0.04	0.02	0.46	0.04	5.23	23.88	0.00	39.01	0.06	22.44	0.03	91.21	120-4	FC	Qtz I	Rad
16	0.08	0.00	0.53	0.07	6.61	23.62	0.00	36.61	0.00	22.89	0.03	90.44	120-4	FC	Qtz I	Rad
17	0.06	0.00	0.55	0.02	5.27	22.63	0.00	37.29	0.03	23.54	0.02	89.41	120-4	FC	Qtz I	Rad

	Na2O	TiO2	MnO	K2O	MgO	SiO2	Cr2O3	FeO	CaO	Al2O3	Cl	Total				
18	0.08	0.03	0.56	0.06	5.13	22.89	0.00	38.49	0.06	23.35	0.02	90.67	120-4	FC	Qtz I	Rad
20	0.03	0.01	0.48	0.04	6.75	23.91	0.06	36.75	0.03	22.98	0.04	91.09	120-4	FC	Qtz I	Rad

	XNa2O	XTiO2	XMnO	XK2O	XMgO	XSiO2	XCr2O3	Fe2+	Fe3+	XCaO	XAl2O3	XCl
10	0.00	0.00	0.01	0.00	0.34	0.42	0.00	0.00	0.39	0.00	0.22	0.00
11	0.00	0.00	0.01	0.00	0.34	0.43	0.00	0.00	0.39	0.00	0.22	0.00
12	0.00	0.00	0.01	0.00	0.13	0.43	0.00	0.00	0.54	0.00	0.22	0.00
13	0.00	0.00	0.01	0.00	0.19	0.39	0.00	0.00	0.49	0.00	0.22	0.00
14	0.00	0.00	0.01	0.00	0.13	0.41	0.00	0.00	0.54	0.00	0.22	0.00
15	0.00	0.00	0.01	0.00	0.16	0.40	0.00	0.00	0.51	0.00	0.22	0.00
16	0.00	0.00	0.01	0.00	0.13	0.39	0.00	0.00	0.52	0.00	0.22	0.00
17	0.00	0.00	0.01	0.00	0.13	0.38	0.00	0.00	0.54	0.00	0.23	0.00
18	0.00	0.00	0.01	0.00	0.13	0.38	0.00	0.00	0.54	0.00	0.23	0.00
20	0.00	0.00	0.01	0.00	0.17	0.40	0.00	0.00	0.51	0.00	0.23	0.00

	Na2O	TiO2	MnO	K2O	MgO	SiO2	Cr2O3	Fe2+	Fe3+	CaO	Al2O3	Cl	Totale	Cl correction	28/Tot
10	0.00	0.00	0.01	0.00	0.34	0.85	0.00	0.00	0.39	0.00	0.65	0.00	0.00	2.23	12.53
11	0.00	0.00	0.01	0.00	0.34	0.87	0.00	0.00	0.39	0.00	0.65	0.00	0.00	2.26	12.41
12	0.00	0.00	0.01	0.00	0.34	0.86	0.00	0.00	0.39	0.00	0.65	0.00	0.00	2.25	12.46
13	0.00	0.00	0.01	0.00	0.13	0.78	0.00	0.00	0.54	0.00	0.66	0.00	0.00	2.11	13.29
14	0.00	0.00	0.01	0.00	0.19	0.83	0.00	0.00	0.49	0.00	0.65	0.00	0.00	2.17	12.93
15	0.00	0.00	0.01	0.00	0.13	0.79	0.00	0.00	0.54	0.00	0.66	0.00	0.00	2.14	13.10
16	0.00	0.00	0.01	0.00	0.16	0.79	0.00	0.00	0.51	0.00	0.67	0.00	0.00	2.14	13.07
17	0.00	0.00	0.01	0.00	0.13	0.75	0.00	0.00	0.52	0.00	0.69	0.00	0.00	2.11	13.30
18	0.00	0.00	0.01	0.00	0.13	0.76	0.00	0.00	0.54	0.00	0.69	0.00	0.00	2.12	13.19
19	0.00	0.00	0.01	0.00	0.17	0.80	0.00	0.00	0.51	0.00	0.68	0.00	0.00	2.16	12.96

	Na2O	TiO2	MnO	K2O	MgO	SiO2	Cr2O3	Fe2+	Fe3+	CaO	Al2O3	Cl	Total
10	0.00	0.00	0.01	0.00	0.34	0.42	0.00	0.00	0.39	0.00	0.43	0.00	1.59
11	0.00	0.00	0.01	0.00	0.34	0.43	0.00	0.00	0.39	0.00	0.43	0.00	1.61
12	0.00	0.00	0.01	0.00	0.34	0.43	0.00	0.00	0.39	0.00	0.43	0.00	1.60
13	0.00	0.00	0.01	0.00	0.13	0.39	0.00	0.00	0.54	0.00	0.44	0.00	1.50
14	0.00	0.00	0.01	0.00	0.19	0.41	0.00	0.00	0.49	0.00	0.43	0.00	1.54
15	0.00	0.00	0.01	0.00	0.13	0.40	0.00	0.00	0.54	0.00	0.44	0.00	1.52
16	0.00	0.00	0.01	0.00	0.16	0.39	0.00	0.00	0.51	0.00	0.45	0.00	1.53
17	0.00	0.00	0.01	0.00	0.13	0.38	0.00	0.00	0.52	0.00	0.46	0.00	1.50
18	0.00	0.00	0.01	0.00	0.13	0.38	0.00	0.00	0.54	0.00	0.46	0.00	1.52
20	0.00	0.00	0.01	0.00	0.17	0.40	0.00	0.00	0.51	0.00	0.45	0.00	1.54

Na	Ti	Mn	K	Mg	Si	Cr	Fe2+	Fe3+	Ca	Al2	Cl	Total

Table 1 (cations normalised, Total ≈ 20)

#	Na	Ti	Mn	K	Mg	Si	Cr2	Fe2+	Fe3+	Ca	Al2	Cl		Total
10	0.02	0.00	0.10	0.01	4.25	5.32	0.00	4.86	0.00	0.01	5.42	0.00	0.00	19.99
11	0.03	0.00	0.11	0.00	4.25	5.37	0.00	4.79	0.00	0.01	5.39	0.00	0.00	19.95
12	0.00	0.00	0.11	0.01	4.25	5.36	0.00	4.83	0.00	0.01	5.38	0.00	0.00	19.95
13	0.02	0.00	0.11	0.02	1.66	5.15	0.00	7.11	0.00	0.01	5.85	0.01	0.00	19.95
14	0.01	0.01	0.10	0.01	2.47	5.34	0.00	6.31	0.00	0.01	5.61	0.01	0.00	19.86
15	0.02	0.03	0.09	0.02	1.70	5.21	0.00	7.11	0.00	0.00	5.77	0.01	0.00	19.93
16	0.03	0.00	0.10	0.01	2.14	5.14	0.00	6.66	0.00	0.01	5.87	0.01	0.00	19.96
17	0.02	0.00	0.10	0.01	1.74	5.01	0.00	6.90	0.00	0.01	6.14	0.01	0.00	19.94
18	0.03	0.01	0.10	0.02	1.68	5.02	0.00	7.06	0.00	0.01	6.04	0.01	0.00	19.98
20	0.01	0.00	0.09	0.01	2.17	5.16	0.01	6.63	0.00	0.01	5.84	0.01	0.00	19.93

Table 2 (Total ≈ 28)

#	Na	Ti	Mn	K	Mg	Si		Cr2	Fe2+	Fe3+	Ca	Al2	Cl		Total	F factor (Droop 1987) reported also in Zussman as the way to calculate the Fe3+ value
10	0.02	0.01	0.10	0.01	4.25	10.63		0.00	4.85	0.00	0.02	8.13	0.00	0.00	28.02	1.00
11	0.03	0.00	0.11	0.00	4.25	10.74		0.00	4.74	0.00	0.07	8.08	0.00	0.00	28.04	1.00
12	0.00	0.00	0.11	0.01	4.25	10.71		0.00	4.79	0.00	0.09	8.07	0.00	0.00	28.03	1.00
13	0.02	0.00	0.11	0.02	1.66	10.30		0.00	7.05	0.00	0.22	8.78	0.01	0.01	28.06	1.00
14	0.01	0.03	0.10	0.01	2.47	10.67		0.00	6.16	0.00	0.13	8.41	0.01	0.01	28.09	1.00
15	0.02	0.01	0.09	0.02	1.70	10.41		0.00	7.03	0.00	0.07	8.65	0.01	0.01	28.06	1.00
16	0.03	0.00	0.10	0.01	2.14	10.27		0.00	6.61	0.00	0.10	8.80	0.01	0.01	28.06	1.00
17	0.02	0.00	0.10	0.01	1.74	10.02		0.00	6.83	0.00	0.04	9.21	0.01	0.01	28.05	1.00
18	0.03	0.01	0.10	0.02	1.68	10.05		0.00	7.04	0.00	0.12	9.06	0.01	0.01	28.04	1.00
20	0.01	0.00	0.09	0.01	2.17	10.31		0.01	6.54	0.00		8.76	0.01	0.01	28.05	1.00

correction throw the Na (Total ≈ 16 / 36)

#	Na	Ti	Mn	K	Mg	Si		Cr	Fe2+	Fe3+	Ca	Al	Cl		OH	Total
10	0.03	0.00	0.10	0.03	4.24	5.31		0.00	4.84	0.01	0.01	5.41	0.00	0.00	16.00	36.00
11	0.06	0.00	0.11	0.01	4.24	5.36		0.00	4.74	0.05	0.05	5.38	0.00	0.00	16.00	35.96
12	0.00	0.00	0.11	0.02	4.24	5.35		0.00	4.78	0.05	0.06	5.37	0.01	0.01	15.99	35.94
13	0.04	0.00	0.11	0.05	1.66	5.14		0.00	7.04	0.06	0.15	5.84	0.02	0.02	15.98	35.94
14	0.01	0.01	0.10	0.02	2.46	5.32		0.00	6.14	0.15	0.08	5.59	0.02	0.02	15.98	35.81
15	0.03	0.00	0.08	0.02	1.70	5.20		0.00	7.01	0.08	0.05	5.75	0.02	0.02	15.98	35.90
16	0.07	0.00	0.10	0.04	2.14	5.13		0.00	6.60	0.05	0.07	5.85	0.02	0.02	15.98	35.97
17	0.05	0.00	0.10	0.01	1.74	5.00		0.00	6.82	0.07	0.03	6.13	0.02	0.02	15.98	35.92
18	0.07	0.00	0.10	0.03	1.68	5.02		0.00	7.03	0.03	0.01	6.03	0.02	0.02	15.98	35.99
20	0.03	0.00	0.09	0.02	2.17	5.15		0.01	6.53		0.08	5.83	0.03	0.03	15.97	35.91

Calculated using the suggestion of Prof. Andy Tindle 'Excel' spreadsheet (Tindle 2014)

Fe3+	Fe3+ = 0 if Fe2+ =	Fe3+ = t Fe2+ = 0 if Fe2+	Fe2+ = 0 if Fe3+ > total Fe2+
0.012808316	0.01	4.85	4.85
0.048857785	0.05	4.74	4.74
0.048241277	0.05	4.79	4.79
0.061907189	0.06	7.05	7.05
0.147006524	0.15	6.16	6.16
0.084359043	0.08	7.03	7.03
0.047962894	0.05	6.61	6.61
0.068522206	0.07	6.83	6.83
0.02568237	0.03	7.04	7.04

0.081466461   0.08   6.54   0.08   6.54

Based on Droop 1987

	FeO calc
10	27.79
11	27.46
12	27.59
13	38.12
14	34.22
15	38.55
16	36.35
17	36.92
18	38.35
20	36.30

Reformatted analysis with water_ Clinohumite Analysis example pag.680 Zussman

No.	Na2O	TiO2	MnO	K2O	MgO	SiO2	Cr2O3	FeO	CaO	Al2O3	Cl	H2O	Total
10	0.04	0.02	0.59	0.06	13.66	25.49	0.00	27.79	0.03	22.04	0.00	11.50	101.21
11	0.07	0.01	0.65	0.02	13.79	26.00	0.01	27.46	0.04	22.13	0.00	11.62	101.79
12	0.00	0.00	0.62	0.04	13.74	25.83	0.00	27.59	0.05	22.00	0.01	11.56	101.48
13	0.04	0.00	0.60	0.08	5.04	23.29	0.00	38.12	0.03	22.44	0.03	10.83	100.50
14	0.02	0.08	0.55	0.04	7.69	24.79	0.00	34.22	0.03	22.10	0.03	11.13	100.69
15	0.04	0.02	0.46	0.04	5.23	23.88	0.00	38.55	0.06	22.44	0.03	10.99	101.74
16	0.08	0.00	0.53	0.07	6.61	23.62	0.00	36.35	0.00	22.89	0.03	11.02	101.19
17	0.06	0.00	0.55	0.02	5.27	22.63	0.00	36.92	0.03	23.54	0.02	10.83	99.86
18	0.08	0.03	0.56	0.06	5.13	22.89	0.00	38.35	0.06	23.35	0.02	10.92	101.45
20	0.03	0.01	0.48	0.04	6.75	23.91	0.06	36.30	0.03	22.98	0.04	11.10	101.74

No.	Si + Al per	Al in e Ottaedrico (tota vacanze ottaedriche					R2+	R3+ calc	Si	R3+
10	5.36	1.36	4.60	5.97	0.03	10.00	4.55	2.71	2.66	2.76
11	5.37	1.37	4.57	5.94	0.06	11.00	4.51	2.71	2.68	2.75
12	5.36	1.36	4.59	5.95	0.05	12.00	4.54	2.71	2.68	2.74
13	5.49	1.49	4.43	5.92	0.08	13.00	4.38	2.95	2.57	2.99
14	5.45	1.45	4.43	5.88	0.12	14.00	4.37	2.87	2.66	2.87
15	5.47	1.47	4.44	5.91	0.09	15.00	4.40	2.92	2.60	2.94
16	5.49	1.49	4.44	5.93	0.07	16.00	4.39	2.95	2.56	2.99
17	5.56	1.56	4.36	5.93	0.07	17.00	4.31	3.10	2.50	3.13
18	5.52	1.52	4.42	5.94	0.06	18.00	4.36	3.03	2.51	3.08
20	5.49	1.49	4.44	5.92	0.08	20.00	4.39	2.96	2.57	2.98

R2+ calculated assuming all Fe as Fe2+

K2O+Na2O+CaO<1%wt Bourdelle et al., 2013 b*

10.00	0.13
11.00	0.13
12.00	0.09
13.00	0.16
14.00	0.09
15.00	0.14
16.00	0.15
17.00	0.11
18.00	0.20
20.00	0.11

*to exclude contaminated analysis

	$XFe=(Fe/Fe+Mg)$
10.00	0.53
11.00	0.53
12.00	0.53
13.00	0.81
14.00	0.72
15.00	0.81
16.00	0.76
17.00	0.80
18.00	0.81
20.00	0.75

Appendix C

Solid Earth

Fluid-mediated, brittle–ductile deformation at seismogenic depth – Part 1: Fluid record and deformation history of fault veins in a nuclear waste repository (Olkiluoto Island, Finland)

Barbara Marchesini[1], **Paolo Stefano Garofalo**[1], **Luca Menegon**[2,3], **Jussi Mattila**[4], **and Giulio Viola**[1]

[1]Dipartimento di Scienze Biologiche, Geologiche e Ambientali, Università di Bologna, Italy
[2]School of Geography, Earth and Environmental Sciences, University of Plymouth, PL48AA Plymouth, UK
[3]The Njord Centre, Department of Geoscience, University of Oslo, P.O. Box 1048 Blindern, Norway
[4]Geological Survey of Finland (GTK), Espoo, Finland

Correspondence: Barbara Marchesini (barbara.marchesini2@unibo.it, barbaramarchesini@hotmail.it)
and Giulio Viola (giulio.viola3@unibo.it)

Abstract. The dynamic evolution of fault zones at the seismogenic brittle–ductile transition zone (BDTZ) expresses the delicate interplay between numerous physical and chemical processes. Deformation and fluid flow at the BDTZ are closely related and mutually dependent during repeating and transient cycles of frictional and viscous deformation. Despite numerous studies documenting in detail seismogenic faults exhumed from the BDTZ, uncertainties remain as to the exact role of fluids in facilitating broadly coeval brittle and ductile deformation at that structural level. We combine structural analysis, fluid inclusion, and mineral chemistry data from synkinematic and authigenic minerals to reconstruct the temporal variations in fluid pressure (P_f), temperature (T), and bulk composition (X) of the fluids that mediated deformation and steered strain localization along BFZ300, a strike–slip fault originally active at the BDTZ. BFZ300 deforms the Paleoproterozoic migmatitic basement of southwestern Finland and hosts in its core two laterally continuous quartz veins formed by two texturally distinct types of quartz – Qtz I and Qtz II, with Qtz I older than Qtz II. Veins within the damage zone are formed exclusively by Qtz I. Mesostructural and microstructural analysis combined with fluid compositional data indicate recurrent cycles of mutually overprinting brittle and ductile deformation triggered by oscillations of fluid pressure peaking at 210 MPa. Fluid inclusion microthermometry and mineral pair geothermometry indicate that the two documented quartz types precipitated from different fluid batches, with bulk salinities in the 1 wt % NaCleq–5 wt % NaCleq range for Qtz I and in the 6 wt % NaCleq–11 wt % NaCleq range for Qtz II. The temperature of the fluids involved with initial strain localization and later fault reactivation evolved through time from > 350 °C during Qtz I precipitation to < 300 °C at the time of Qtz II crystallization. The peak fluid pressure estimates constrain pore pressure oscillations between 80 and 210 MPa during the recorded faulting episodes. Our results suggest variability of the physico-chemical conditions of the fluids steering deformation (P_f, T, X), reflecting the ingress and effects of multiple batches of fluid in the fault zone. Initial fluid-mediated embrittlement generated a diffuse network of joints and/or hybrid–shear fractures in the damage zone; subsequent strain localization led to more localized deformation within the fault core. Localization was guided by cyclically increasing fluid pressure and transient embrittlement of a system that was otherwise under overall ductile conditions.

Our analysis suggests that fluid overpressure at the BDTZ can play a key role in the initial embrittlement of the deforming rock and steer subsequent strain localization.

1 Introduction

The physical and chemical properties of fault systems play a fundamental role in controlling the rheological behaviour of the Earth's crust and in steering channelled fluid flow (e.g. Caine et al., 1996). Deformation and fluid flow are closely related and mutually dependent via a number of feedbacks, such as the control that fluids exert upon the effectiveness of deformation processes and the development of fault systems at all scales, and the control by rock heterogeneities and/or fracture system topology on the net fault transmissivity (e.g. Crider and Peacock, 2004). The nucleation and development of permeable fault systems and the mechanisms whereby individual faults may weaken and eventually fail are therefore complex functions of a number of processes. In this perspective, the interaction between fluid and mineral phases within fault rocks needs to be studied with a system approach in order to single out the role and importance of all processes involved (Kaduri et al., 2017).

An obvious effect of fluid involvement, particularly in crustal volumes that have experienced large deformation-controlled fluid fluxes, is the precipitation of authigenic and hydrothermal minerals within faults (Oliver and Bons, 2001; Viola et al., 2016) and their immediately adjacent host rock (Mancktelow and Pennacchioni, 2005; Garofalo, 2004). In the seismogenic region of the crust, where fluids may even be the primary driver of the seismic cycle (e.g. Miller, 2013), faults have been shown to have the potential to function like a "fluid-activated valve", whereby they experience transient and cyclic fluid pressure build-up before sudden fluid venting, pore pressure and mechanical strength drop concomitant with seismic failure (e.g. Sibson, 1989, 1992b, 1993; Cox, 1995; Viola et al., 2006; De Paola et al., 2007; Wehrens et al., 2016). Hydrothermal ore deposits, in which fault networks focus relatively large volumes of ore fluids and precipitate economic minerals (Cox et al., 2001; Boiron et al., 2003; Moritz et al., 2006; Scheffer et al., 2017a), are also pertinent examples of significant deformation-controlled fluid ingress.

The seismogenic depth down to 10–15 km (e.g. Kohlstedt et al., 1995) is thus a key region of the crust in which to study the whole range of fluid–rock interaction processes occurring within fault zones. Deformation at that depth might be accommodated under overall brittle–ductile conditions along fault systems crossing or rooting into the brittle–ductile transition zone (BDTZ). In detail, the deformation style in the BDTZ is generally characterized by the cyclicity, also at the short timescale, between brittle and ductile behaviour (Famin et al., 2004, 2005; Siebenaller et al., 2013). This is induced and regulated by the complex and transient interplay of numerous parameters, among which are the lithological composition and transient variation of temperature, pore pressure, and strain rate within the deforming system. Field studies have documented unequivocally that ductile and brittle deformation may even be simultaneously active during deformation as a function of the transient and spatially hetero-

geneous evolution of the chemical and physical parameters steering deformation, leading to the broad coexistence of geological features expressing frictional deformation and viscous creep and to mutual cross-cutting relationships thereof (e.g. Guermani and Pennacchioni, 1998; Kjøll et al., 2015; Pennacchioni et al., 2006; Wehrens et al., 2016; Scheffer et al., 2017b).

Veins are particularly important in this context because they attest to the relative abundance of aqueous fluids in the deformation history (e.g. Cox et al., 2001). Portions of the seismogenic crust that experience large fluid fluxes host pervasive and vertically extensive vein networks (Sibson et al., 1988), within which up to several million cubic metres of hydrothermal minerals may deposit from the flowing fluid (e.g. Heinrich et al., 2000; Cox, 2005; Bons, 2001; Garofalo et al., 2002). In contrast, portions of the crust deforming in the absence of significant fluid flow would show little to no evidence of veining, with only synkinematic H_2O-rich minerals within the fault rock attesting to hydrous conditions (Mancktelow and Pennacchioni, 2004; Menegon et al., 2017).

The physical–chemical conditions of fluid–rock interaction in the BDTZ have been studied within exhumed faults by applying a set of geochemical tools that include fluid inclusion analysis (e.g. Morrison, 1994; Morrison and Anderson, 1998; Mulch et al., 2004; Ault and Selverstone, 2008; Garofalo et al., 2014; Siebenaller et al., 2016; Compton et al., 2017), determination of the isotopic compositions of fault fluids, and mass transfer calculations between host rock and fault rocks (e.g. Goddard and Evans, 1995; Garofalo, 2004; Mittempergher et al., 2014; Spruzeniece and Piazolo, 2015). This approach yields important constraints on the P–T conditions of fluid–rock interaction within the BDTZ, on the source region of the fluids reaching and flowing within the deformation zones, and on element mobility during syntectonic fluid flow. These studies, however, do not specifically address the role of fluids in the mechanisms that trigger and permit the aforementioned cycles of brittle–ductile deformation. Open questions thus remain, such as what pressure, temperature, and composition (P, T, X) conditions are best for a fluid to trigger brittle–ductile deformation cycles in a fault system within the BDTZ and which fluid property is specifically most effective in controlling the cycles.

In this work, we follow a multidisciplinary approach by combining mesostructural and microstructural observations with the geochemical analysis of fluids, petrographic documentation of fault rocks and veins, microthermometric properties of fluid inclusion assemblages, electron probe microanalysis (EPMA) of fault minerals, Raman spectrometry of fluid inclusions, and electron probe cathodoluminescence imaging to study the effects of numerous cycles of fluid–rock interaction that have occurred in a vein-rich deformation zone at the seismogenic BDTZ and now exhumed as part of the Paleoproterozoic continental crust of southwestern Finland. The studied deformation zone belongs to an exhumed conjugate fault system that experienced a complex history
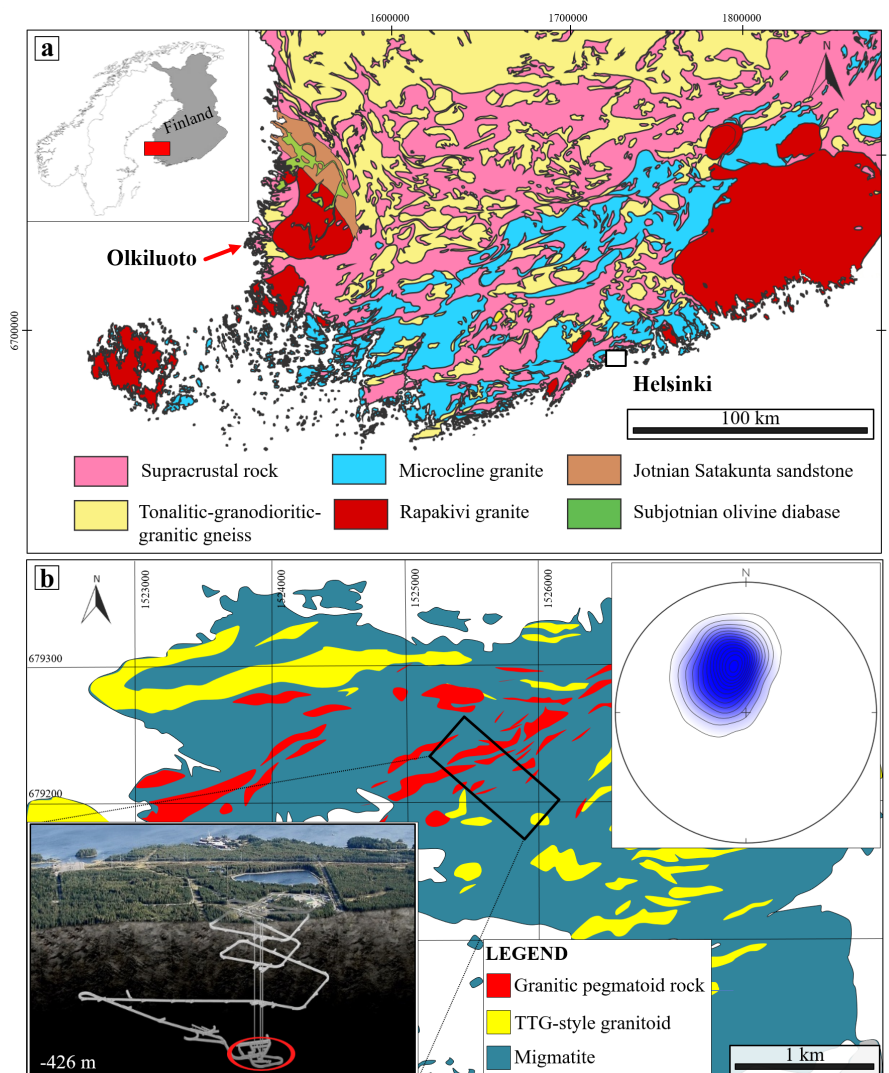
Figure 1. (a) Simplified geological map of southwestern Finland modified after Mattila and Viola (2014). **(b)** Geological sketch of Olkiluoto Island. The upper right inset shows the poles to foliation planes measured from all available Olkiluoto drill cores ($N = 4479$, equal area, lower hemisphere projection; Mattila and Viola, 2014). The lower left inset is a panoramic photograph with an overlay drawing of the underground infrastructure (photo courtesy of Posiva Oy, Finland). The red circle shows the depth location of BFZ300. Coordinates are given in the local KKJ1 coordinate system.

of structural reactivation and fluid flow. Deformation zone BFZ300, the target of our study, crops out at ca. 426 m below sea level within the deep Onkalo nuclear waste repository that is presently being built on the island of Olkiluoto (Fig. 1a).

Our results allow us to constrain and describe the progressive evolution of the deformation processes and the role of fluids involved both at fault initiation and during the subsequent reactivation phases. We propose that fluid pressure fluctuation cycles within an overall ductile environment at the BDTZ triggered brittle–ductile cyclicity encompassing fracturing, vein precipitation, and crystal–plastic deformation before renewed and fluid-induced embrittlement.

Our multi-technique approach made it possible to determine many of the actual chemical and physical properties of the fluids involved in the deformation process, leading to a well-constrained conceptual mechanical model for the fault nucleation and subsequent development.

2   Geological setting

The study area is located in southwestern Finland on the island of Olkiluoto (Fig. 1a) within the Paleoproterozoic Svecofennian orogenic province, which is formed by supracrustal high-grade metamorphic sequences and plu-

tonic rocks. The most abundant lithologies in the study area are variably migmatitic metasedimentary rocks interleaved with metavolcanic rocks up to several metres thick in addition to calc-alkaline synorogenic tonalite-trondhjemite-granodiorite-type (TTG) granitoids, as well as late orogenic leucogranites (Fig. 1a, b). For a detailed lithological characterization of the area, we refer the reader to Hudson and Cosgrove (2006) and Aaltonen et al. (2016).

Numerous studies carried out on Olkiluoto have highlighted the long geological evolution of the region, which is commonly summarized by tectonic models proposing either an evolution during a single and semi-continuous Svecofennian orogenic event (Gorbatschev and Bogdanova, 1993) or, alternatively, a sequence of up to five distinct accretion events leading to the amalgamation of several microcontinents and island arcs at the margin of the Archean craton between 1.92 and 1.79 Ga (e.g. Lahtinen et al., 2005). In this scenario, several subduction systems developed, and the collision of the involved microcontinents and island arc complexes resulted in conspicuous continental growth, forming the major part of the Paleoproterozoic domain of the Fennoscandian Shield (1.89–1.87 Ga). According to Lahtinen et al. (2005), this "Fennian accretionary event" ended with a phase of orogenic collapse associated with regional extension and remarkable crustal thinning between ca. 1.86 and 1.84 Ga. Renewed compression ensued during collision of the "Sarmatian Plate" with the previously consolidated Svecofennian Shield, causing major crustal shortening, high-temperature regional metamorphism (Kukkonen and Lauri, 2009), and the emplacement of S-type granites (e.g. Ehlers et al., 1993). Tectonic activity ascribable to this orogenic phase ceased with a distinct orogenic collapse phase at 1.79–1.77 Ga (Lahtinen et al., 2005).

Pervasive reworking of the Svecofennian domain took place in the Mesoproterozoic when the crust underwent significant stretching and was intruded by voluminous Rapakivi granites and diabase dykes resulting from the widespread melting of the lower crust at ca. 1.65–1.50 Ga. This tectonic phase was probably due to the development of a rift along the present Baltic Sea (Korja et al., 2001). Crustal thinning also caused the formation of the "Satakunta Graben", a NW–SE-trending graben located ca. 50 km to the north of Olkiluoto, which was later filled by Mesoproterozoic sandstone (Jotnian sandstones, Fig. 1a). The latest stage of crustal evolution in southern Finland is expressed by the intrusion of 1.27–1.25 Ga, N–S-striking olivine diabase dikes (Fig. 1a; e.g. Suominen, 1991).

As to the structural evolution of the study area, the bedrock was affected by complex, polyphase ductile deformation between 1.86 and 1.81 Ga. According to the evolutionary deformation scheme by Aaltonen et al. (2010) the results of up to five different phases, referred to as D_1–D_5, are preserved in the local structural record, each characterized by structures with distinctive mineral composition, metamorphic grade, geometry, and kinematics. The most relevant phases to our study are D_2 to D_4. During these ductile episodes, a regional and pervasive NE–SW-striking and moderately SE-dipping foliation developed, strain localized along mesoscopic shear zones parallel to subparallel to the foliation, and extensive migmatization occurred under amphibolite facies metamorphic conditions. NNE–SSW- and N–S-striking mylonitic shear zones also formed under those conditions, whereas later ductile events developed under progressively lower-grade metamorphism until ca. 1.7 Ga, when brittle deformation became the dominant deformation style in response to progressive regional exhumation and cooling (Mattila and Viola, 2014; Aaltonen et al., 2016). The penetrative, inherited ductile grain that by then characterized the crystalline basement and that was suitably oriented with regard to the prevailing stress field was invariably reactivated. This is the case for several NNE–SSW-striking faults mapped underground in the Onkalo repository, which clearly overprint earlier D_4 shear zones and fully exploit the pre-existing ductile precursors. Other faults, such as BFZ300, do not show any clear genetic relation to the older ductile fabric and cut it discordantly.

As shown in the following section, BFZ300 belongs to a set of subvertical, conjugate brittle–ductile to fully brittle strike–slip faults characterized by N–S-trending sinistral and NW–SE dextral faults. Both sets document a complex history of reactivation and contain evidence for cyclic and transient switches between brittle and ductile deformation at all scales. Mesostructural and microstructural studies show that the sinistral faults overprint and probably reactivate a dextral mylonitic precursor related to earlier localized ductile deformation (Prando et al., 2019). These faults locally contain pseudotachylyte injections, which suggests seismic behaviour during deformation (Menegon et al., 2018). In contrast, dextral faults cut across the foliation, do not exploit any ductile precursors, and do not host pseudotachylytes. BFZ300 belongs to this second group of faults. In the following, we describe its architecture, reconstruct its deformation history, and constrain the deformation mechanisms and faulting conditions that prevailed during its nucleation and subsequent development. The architecture and deformation history of the remarkably different conjugate structure to BFZ300, which is a sinistral brittle–ductile deformation zone, is described in the Part II companion paper (Prando et al., 2019).

3 Methods: fluid inclusion, mineral chemistry, and EBSD analysis

Field documentation and sampling were carried out at the underground Onkalo exposures of BFZ300 (Fig. 1b), which were necessarily limited in extent to the actual excavated volume of rock at the time of our study but that, together with the logged diamond drill cores from the underground exploration, allow for a well-constrained 3-D reconstruction of the local geology.

Fluid inclusion measurements were conducted on "fluid inclusion assemblages" (FIAs), i.e. on petrographically discriminated, cogenetic groups of fluid inclusions located along trails or (less commonly) within clusters (Bodnar, 2003a; Goldstein, 2003). By definition, FIAs are groups of inclusions that have been trapped together (i.e. they are cogenetic) at a specific stage of mineral formation and, as such, give the highest level of confidence when characterizing the properties of trapped fluids and discriminating possible stages of post-entrapment re-equilibration (Bodnar, 2003b, and references therein). We applied Roedder's identification criteria of FIAs according to the timing of entrapment (i.e. primary, secondary, pseudosecondary) in order to link stages of fluid entrapment with stages of brittle and ductile deformation of quartz. In this regard, we considered only FIAs that exhibited both similar orientation and petrographic characteristics at the scale of the thin section to be cogenetic and therefore representative of one specific stage of brittle deformation and fluid circulation.

In the selected samples, we studied 28 FIAs entrapped within two distinct generations of quartz (named Qtz I and Qtz II) forming two different generations of veins and exhibiting the least petrographic evidence of post-entrapment overprinting by later ductile and/or brittle deformation, which provided ca. 800 microthermometric properties. Due to the well-documented tendency of fluid inclusions to modify their shape, volume, and composition after their initial entrapment even under low deviatoric stress conditions (e.g. Diamond et al., 2010; Kerrich, 1976; Tarantola et al., 2010; Wilkins and Barkas, 1978), working on FIAs that show the least possible degree of textural re-equilibration is essential when aiming at constraining the physical and chemical properties of the fluid(s) involved in the fault activity.

Microthermometric properties of fluid inclusions were determined at the Department of Biological, Geological and Environmental Sciences of the University of Bologna using a Linkam THMSG 600 heating–freezing stage coupled with an Olympus BX51 polarizing microscope. The microthermometry stage was calibrated by using synthetic fluid inclusion samples at -56.6, 0.0, and $374\,°C$, which correspond to the melting of CO_2, ice melting, and final homogenization of H_2O inclusions, respectively. Obtained accuracies were $\pm0.3\,°C$ for final ice melting temperature (Tm_{ice}) and $\pm3\,°C$ for final homogenization temperature (Th_{tot}). In order to produce an internally consistent dataset, all phase transitions were exclusively collected for individual FIAs and measured with the same standard procedure. Samples were first rapidly cooled to ca. $-180\,°C$ and then slowly heated to detect the potential formation of a solid carbonic phase, eutectic phases, salt hydrates, ice, and clathrates. The Th_{tot} values were later determined in the FIAs by heating the samples from room temperature and recording the mode of homogenization (i.e. by bubble or liquid disappearance). All phase transitions were measured by using the cycling method described by Goldstein and Reynolds (1994), and care was

taken to also record the minimum and maximum values for each assemblage. Volume fractions of individual fluid inclusions, determined as a percentage of the ratio $\phi = V_v/V_{tot}$ (Diamond, 2003), were estimated optically at room temperature using calibrated charts. Salinity, bulk densities, and isochores were computed from the measured Tm_{ice} values using the HokieFlincs Excel spreadsheet (Steele-MacInnis et al., 2012, and references therein).

Fluid inclusions were also analysed using micro-Raman spectrometry. Analyses were carried out at the Department of Mathematical, Physical and Computer Sciences of the University of Parma (Italy) using a Jobin-Yvon Horiba LabRam spectrometer equipped with an He–Ne laser (emission line $632.8\,nm$) and motorized XY stage. The spectral resolution of the measurements was determined as nearly $2\,cm^{-1}$. The confocal hole was adjusted to obtain a spatial (lateral and depth) resolution of $1–2\,\mu m$. Most spectra were obtained with a $50\times$ objective (N.A. 0.75), although for shallow inclusions a $100\times$ objective (N.A. 0.90) was also used. The calibration was made using the $520.7\,cm^{-1}$ Raman line of silicon. A wide spectral range ($100–3600\,cm^{-1}$) was scanned for each inclusion for the presence of CO_2, N_2, CH_4, and H_2S, but the final acquisitions were made mainly between 1100 and $1800\,cm^{-1}$ for the study of CO_2 spectra and between 2500 and $3300\,cm^{-1}$ for CH_4 and H_2S. The acquisition time for each spectral window was $120–240\,s$, with two accumulations. The power on the sample surface is nearly $1\,mW$, but the power on the analysed inclusions has to be considered lower due to reflections and scattering. Analyses were carried out on the vapour bubbles of the fluid inclusions.

After the calculation of representative fluid inclusion isochores for each FIA, the pressure corrections were assessed by using the crystallization temperatures of two mineral pairs – namely chlorite–quartz and stannite–sphalerite – as independent input parameters. Chlorite–quartz temperatures were calculated by using the method of Bourdelle and Cathelineau (2015), which assumes quartz–chlorite equilibrium and uses ratios of chlorite endmember activities to link the chlorite compositions with the corresponding formation temperatures through the quartz–chlorite equilibrium constants. This method is based on the measurements of the concentrations of the major chlorite components (Si, Fe, Mg) and can only be applied to chlorites with ($K_2O + Na_2O + CaO$) $< 1\,wt\%$, which is indeed the case of our chlorites. To estimate the formation temperature of cogenetic sulfides associated with Qtz II we used the stannite–sphalerite formation temperature following the method proposed by Shimizu and Shikazono (1985). This geothermometer uses the temperature dependency of iron and zinc partitioning between stannite and sphalerite (Nekrasov et al., 1979) as a temperature indicator of the association of Qtz II stannite and sphalerite.

Electron probe microanalysis (EPMA) of fault minerals was carried out with a JEOL-8200 wavelength-dispersive electron microprobe housed at the Department of Earth Sciences of the University of Milan, Italy. The instrument fits

five wavelength dispersive spectroscopy (WDS) spectrometers utilizing lithium fluoride (LiFH), pentaerythritol (PETJ and PETH), and thallium acid phthalate (TAP) analysing crystals and an optical microscope. Samples were probed with a beam size of $\sim 1\,\mu m$ at a 15 keV and 5 nA beam current. Synthetic and natural materials were used as calibration standards at the beginning of each session. Analytical 1σ errors are typically $< 4\%$ for major elements and for the minor elements.

Panchromatic cathodoluminescence (CL) imaging was also performed by using the CL CCD detector adjacent to the optical microscope of the JEOL-8200 on the sections used for microstructural work. The electron beam was focused on the sections with an accelerating voltage of 15 kV and a 30 nA beam current. Black-and-white digital images were collected with a $40\times$ magnification by beam mapping with the CCD detector at a spatial resolution of 1 µm (beam resolution), which resulted in imaged areas of 27.8×22.2 mm. The exposure time for image acquisition was 120 s.

Petrographic thin sections were later studied with the scanning electron microprobe (SEM) to investigate the crystallographic preferred orientation (CPO) of selected sites of the quartz veins from the fault core (sample name TPH-120-4; see Fig. 2 for sample location). Samples were analysed with a JEOL-6610 SEM equipped with a Nordlys Nano electron backscatter diffraction (EBSD) detector, hosted at the Electron Microscopy Centre of the University of Plymouth, UK. EBSD detailed results are reported in the Supplement.

4   Results

4.1   BFZ300 fault architecture

The studied BFZ300 section is located at a depth of 426 m b.s.l. and is about 8 m long (Fig. 2a). It strikes NNW–SSE and dips very steeply to subvertically to the southwest (Fig. 2b). It cuts through high-grade veined migmatite, interlayered with gneiss and pegmatitic granite. The fault is a strike–slip fault system formed by two main subparallel fault segments connected by a mesoscopic sinistral step-over zone. Subhorizontal striae defined by elongated trails of chlorite grains and kinematic indicators, such as chlorite slickensides (Fig. 2c) and R and R' planes, invariably indicate dextral strike–slip kinematics. The most striking mesoscopic characteristic of BFZ300 is the presence in the fault core of a composite set of almost continuous quartz veins (between 1 and 20 cm in thickness) along the entire exposed strike length. A schematic representation of the fault zone is shown in Fig. 3.

The fault contains a 0.5–2 m thick damage zone separated from the undeformed host rock by two discrete bounding surfaces (Y_I planes according to Tchalenko, 1970; Fig. 2a). The damage zone can be defined in the field on the basis of the presence of a fractured volume containing sets of conjugate

dextral and sinistral hybrid fractures (Fig. 3a) intersecting to form a tight acute angle of ca. 38° (Figs. 2b, 3a). Laterally continuous, NNW–SSE-striking Mode I fractures (joints) invariably bisect this angle (Fig. 2b), helping to constrain the stress field orientation at the time of fracture formation, with the greatest compressive stress axis σ_1 parallel to the Mode I fracture strike and oriented ca. NNW–SSE. Joints are sharp and have a regular spacing of ca. 10 cm. The joints and the hybrid fractures of the damage zone contain quartz, referred to as Qtz I hereinafter, forming veins up to 1–1.5 cm thick (Fig. 3a). Fractures and faults decorated by Qtz I have a translucent look that reflects the generally fine grain size of Qtz I (< 1 cm, Fig. 3b). Locally they are formed by en echelon tensional segments connected by shear planes not decorated by any quartz infill (Fig. 3b). Joints occur also as barren fractures defining a penetrative sympathetic fracture cleavage (sensu Basson and Viola, 2004; green lines in Fig. 2b). Field evidence also suggests that fracture density within the damage zone tends to increase towards the fault core.

The fault core is bounded by two main discrete slip surfaces (Y_{II}; Figs. 2a, 3d, f, h). It contains, and is defined by, two distinct generations of quartz veins (Fig. 3c) that are interrupted and offset laterally by a metric sinistral step-over zone (Fig. 3d–f). The main quartz vein of the core is infilled by quartz exhibiting the same mesoscopic appearance of Qtz I in the damage zone; we therefore refer to it as a Qtz I vein. It is accompanied by a younger, subparallel vein formed by a milky-white type of quartz with a significantly larger grain size than Qtz I (> 1 cm) that we refer to as Qtz II (Fig. 3c). Locally, pockets of cataclasite and breccia formed at the expense of the host migmatitic gneiss are also observed along and between the two veins (Fig. 3g, i). The Qtz II vein exhibits a quite irregular, curved geometry (Fig. 3c, h) and a variable thickness up to a maximum of ca. 20 cm. The minimum Qtz II vein thickness coincides spatially with an apparent lateral displacement of the vein. The BFZ300 core varies in thickness between 20 and 30 cm along most of the exposed fault length but becomes thicker (up to 50 cm) in the compressional step-over zone that connects the two fault segments that are offset laterally by ca. 1 m. The sinistral step-over zone is defined by synthetic T fractures (Fig. 3d, e) and contains a decimetric brecciated lens (Fig. 3d). T fractures are filled by Qtz I veins (Fig. 3e).

Chlorite is present as a secondary phase, with a modal abundance between 5 % vol and 10 % vol in both Qtz I and Qtz II veins. In Qtz I veins it occurs as euhedral–subhedral crystals up to 1–2 mm in size (Fig. 3g). Chlorite is present mostly as a disseminated, interstitial phase concentrated mainly in the internal part of the Qtz I veins (Fig. 3g). In the Qtz II vein, however, it occurs as elongated crystals (5–8 mm in length) arranged perpendicularly to the walls of the vein, which suggests orthogonal dilation at the time of opening (Fig. 3h). The Qtz II vein also contains small (1–2 cm) aggregates of sulfides (sphalerite, pyrite, galena, and chal-
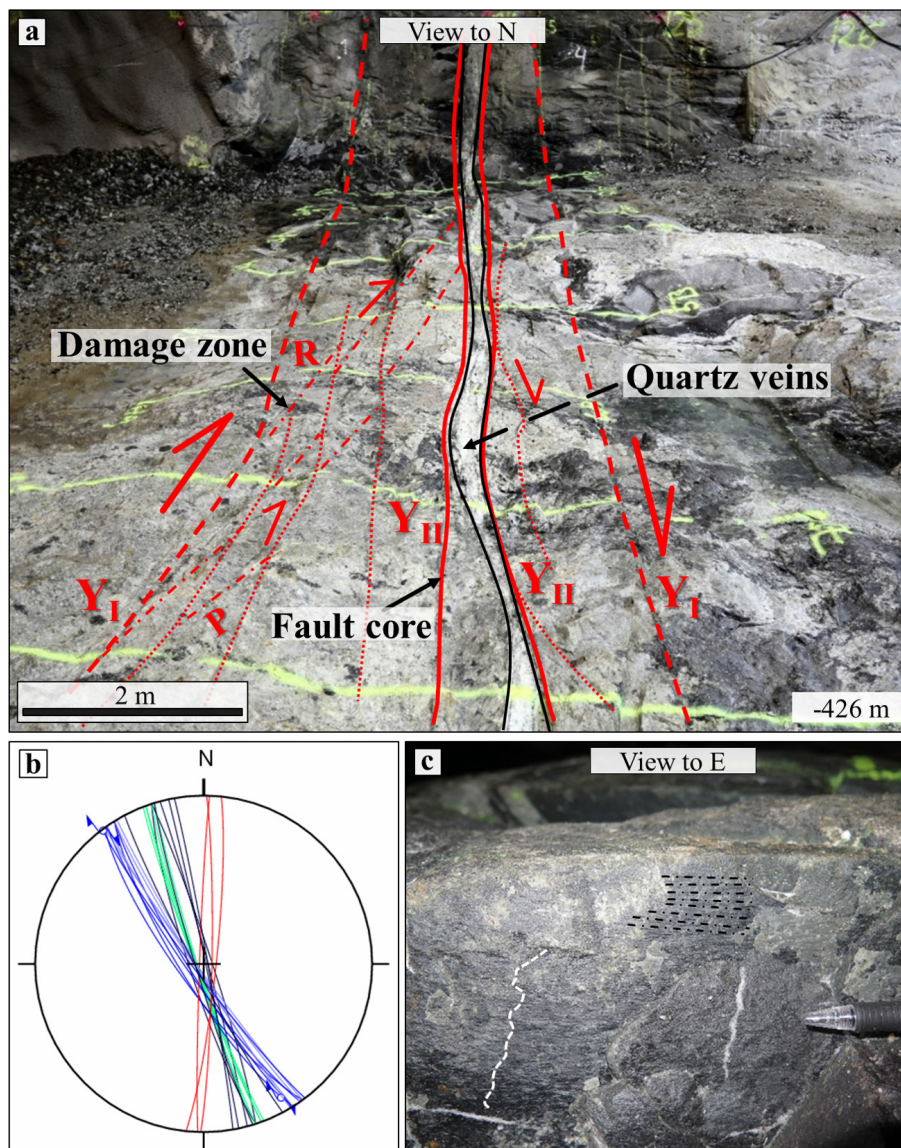
Figure 2. (a) View to the north and interpretation of the structural elements of BFZ300. **(b)** Lower hemisphere, equiangular projection of conjugate fault segments (blue: dextral faults; red: sinistral faults), cleavage (green), and Qtz I chlorite veins infilling joints (black). **(c)** Slickensides (white dashed line) and slickenlines (black dashed lines) on a chlorite-decorated, NW–SE-striking fracture plane at the vein–host interface, indicating dextral strike–slip kinematics.

copyrite) mainly concentrated in the central part of the vein (Fig. 3g).

As observed in the field, the presence of Qtz I veins along the joints in the damage zone and the continuity of the fault core Qtz I vein suggest Mode I fracturing during Qtz I emplacement (Figs. 2a, 3a, c). The semi-continuous parallelism of Qtz I and Qtz II veins in the fault core, combined with the location of the Qtz II vein along the walls of the Qtz I vein, suggests the partial reactivation of the Qtz I vein during Qtz II emplacement. Dilation leading to Qtz II emplacement exploited and further reworked the Qtz I host-rock contact, which seemingly had a lower tensile strength than the pristine

migmatite. The reconstructed time relationship between the two vein generations is also consistent with local evidence of the Qtz II vein partly cross-cutting the Qtz I vein (Fig. 3f).

4.2 BFZ300 microstructural analysis

To constrain the spatial and temporal association of fault rocks and the type of fluid involved in the deformation, several outcrop samples, each representative of a specific structural domain, were collected (TPH-120-2, TPH-120-3, TPH-120-4, TPH-120-5, and TPH-120-6), in addition to samples PH21 and PH22 from diamond drill cores that intersect
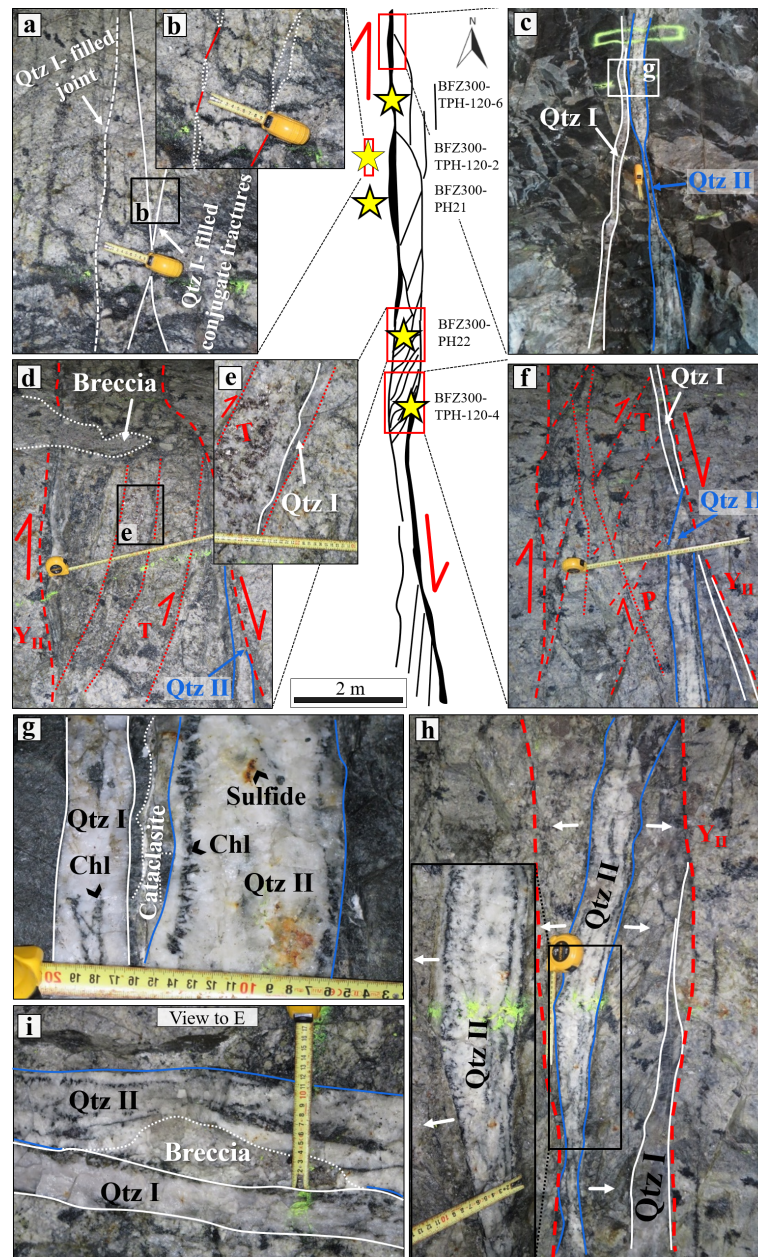
Figure 3. BFZ300 architecture with examples of representative structural features. The red rectangles locate the areas where detailed outcrop photos were taken. Stars locate hand and drill core samples. Stars with a black outline identify samples used for the microthermometric study. Note that the fault is made of two main segments offset laterally at a sinistral compressive step-over zone. Fault core quartz veins are shown by thicker black lines in the schematic model (centre of figure), while blue and white lines highlight the positions of the two types of quartz veins in the outcrop pictures. **(a)** Damage zone made of millimetre-thick, en echelon veins connected by conjugate shear segments. **(b)** Detail of **(a)** showing fractures filled by the first quartz generation (Qtz I). **(c)** Two distinct generations of quartz–chlorite veins recognized in the fault core (Qtz I and Qtz II). **(d)** Detail of the sinistral compressional step-over zone characterized by multiple and parallel T fractures, filled by Qtz I. A brecciated body is cross-cut by the Y planes. **(e)** Tensional fracture infilled by Qtz I. **(f)** Compressional structures (P shears) from the step-over zone and relationships between Qtz I and Qtz II. The Riedel geometry suggests that the Qtz II vein formed due to the reactivation of the internal principal slip zones (Y_{II}). Note the Qtz II vein cutting the Qtz I vein. **(g)** Juxtaposed Qtz I and Qtz II veins. Qtz I veins are thinner and made of a translucent, small-grained quartz. In contrast, Qtz II veins, which contain pockets of sulfide aggregates, are thicker and made of larger and euhedral quartz. Chlorite occurs as a minor phase in both veins. Notice the presence of a cataclastic band between the two veins. **(h)** Spatial continuity of the chlorite aggregates within the Qtz II veins, which always grow orthogonal to the vein boundaries. This open-space filling texture suggests hybrid conditions of reactivation of the older Qtz I veins. **(i)** Small quartz breccia formed between the two generations of quartz veins.

BFZ300 at the same depth in an area that is currently not excavated. From these samples we prepared 10 petrographic thin sections (samples TPH-120-2, TPH-120-4, TPH-120-6, PH21, and PH22) and 9 doubly-polished sections for fluid inclusion analysis (thickness ∼ 150 μm; samples TPH-120-2, TPH-120-4, TPH-120-6, PH21, and PH22). Due to the extensive reactivation of the fault zone and the consequent obliteration of the fluid inclusion (FI) record, the FI study was carried out only in samples TPH-120-4, TPH-120-6, and PH21. Hand samples and drill cores localities are shown in Fig. 3.

The microstructural work was carried out on oriented petrographic thin sections cut orthogonally to the migmatitic foliation and parallel to the slickenlines.

In the following we provide a description of the microstructural characteristics of BFZ300 by detailing our findings and observations separately for the main structural domains of the fault zone.

4.2.1 Damage zone

Qtz I veins within the damage zone cut across the migmatitic host rock and form the infill of conjugate sets of hybrid fractures, which, when studied at the microscale, appear to be formed by dilatant segments joined by cataclastic shear fractures (Fig. 4a). Shearing on the latter is well documented by the asymptotic bending into the shear surfaces of foliation planes formed by the alignment of chlorite and muscovite, both partly altered to sericite and chlorite, respectively (Fig. 4a). Qtz I infilling the tensional segments has an average grain size between 200 μm and 3 mm and exhibits a rather heterogeneous texture, from purely blocky to mixed elongated–blocky (Fig. 4b, c). The largest crystals (800 μm to 1 mm) are elongated and stretched from the vein walls towards the inner part of the vein (Figs. 4c, 5a). At least two episodes of vein growth and renewed dilation, as indicated by the presence of median lines (MLs), are visible within one of the studied veins and confirm a syntaxial growth mechanism for the vein (Fig. 5; e.g. Bons et al., 2012). Medial lines are defined by the alignment of chlorite, sericite, and carbonate aggregates (Fig. 5a, b, d). Blocky euhedral quartz crystals are also found varying in grain size between 300 and 600 μm. These crystals are juxtaposed against very-fine-grained quartz (< 200 μm) within sericite-rich cataclastic bands (Fig. 4b). These cataclasites contain also hydrothermally altered host-rock fragments including pervasively altered K-feldspar-bearing lithic fragments and phyllosilicates.

With the exception of the blocky variety, Qtz I crystals exhibit various degrees of crystal–plastic deformation and recovery. They contain widespread evidence of undulose extinction and extinction bands (Fig. 5b), and incipient bulging along grain boundaries is also evident (Fig. 5c). Millimetric intracrystalline barren fractures are also recognized (e.g. Fig. 5c). Cathodoluminescence imaging of Qtz I from the damage zone also shows the presence of a dense network of

healed quartz microfractures (Fig. 4d), which demonstrates healing subsequent to brittle deformation and fracturing.

Chlorite occurs along the ML of the veins, secondary cracks, along grain boundaries, and as inclusions within quartz crystals. It has a vermicular texture (Fig. 5d) and crystal dimensions up to 50 μm.

4.2.2 Fault core

In the fault core, Qtz I grain size reaches the smallest observed value (range: 30–800 μm; Fig. 6a), although it is strongly variable within the vein, suggesting the presence of heterogeneous and complex structural sub-domains. The earliest post-vein emplacement deformation stage is reflected by the low-temperature, intracrystalline deformation of the largest crystals (400–800 μm in size). Undulose extinction, wide extinction bands (WEBs; Derez et al., 2015), and bulging along grain boundaries are the most common microstructures ascribable to this deformation stage (Fig. 6a, b). A first brittle deformation event is documented by narrow, intracrystalline fractures that cross-cut the largest quartz crystals (Fig. 6c) and which locally contain new grains of quartz ranging in size between 20 and 100 μm (Fig. 6d). In more detail, these new grains form parallel bands that are oriented at a low angle (< 30°) to the vein walls and that can be up to 2 mm in length and 200 μm in thickness. Plastically deformed Qtz I crystals hosting these intracrystalline bands of new grains are cut across by another later set of subparallel intercrystalline fractures, which are interpreted as the expression of yet another deformation event that occurred under overall brittle conditions. These fractures are parallel to the strike of BFZ300 and are in turn sealed by partly recrystallized new quartz grains (grain size: 50–150 μm; Fig. 6e). The cathodoluminescence imaging of these fractures shows that they are sealed, yielding a homogeneous dark signal (Fig. S1 in the Supplement). They are locally decorated by trails of fluid inclusions (Fig. S2a, d) and can be up to 2.5 cm in length and up to 500 μm in width (Fig. 6a). EBSD maps were acquired along some of these intercrystalline bands, and results suggest that the new grains sealing the fractures reflect the combined effect of initial cracking, grain nucleation, and subsequent partial dynamic recrystallization (Fig. S2b, c).

Qtz II within the fault core is typically coarse grained (individual crystals: 300 μm–1 cm in size) and exhibits a regular blocky texture devoid of any shape or crystal preferred orientation (Fig. 7a). Locally, these large crystals display primary growth textures, such as primary FIAs oriented parallel to specific crystallographic planes. With the exception of undulose extinction, Qtz II does not show clear evidence of plastic deformation, although cathodoluminescence imaging of optically continuous Qtz II has also shown that a dense network of healed quartz microfractures locally cross-cuts Qtz II crystals (Fig. 7c). These are relatively thin (hundreds of micrometres thick) networks that are poorly visible to invisible by standard petrographic analysis. The only petrographic ev-
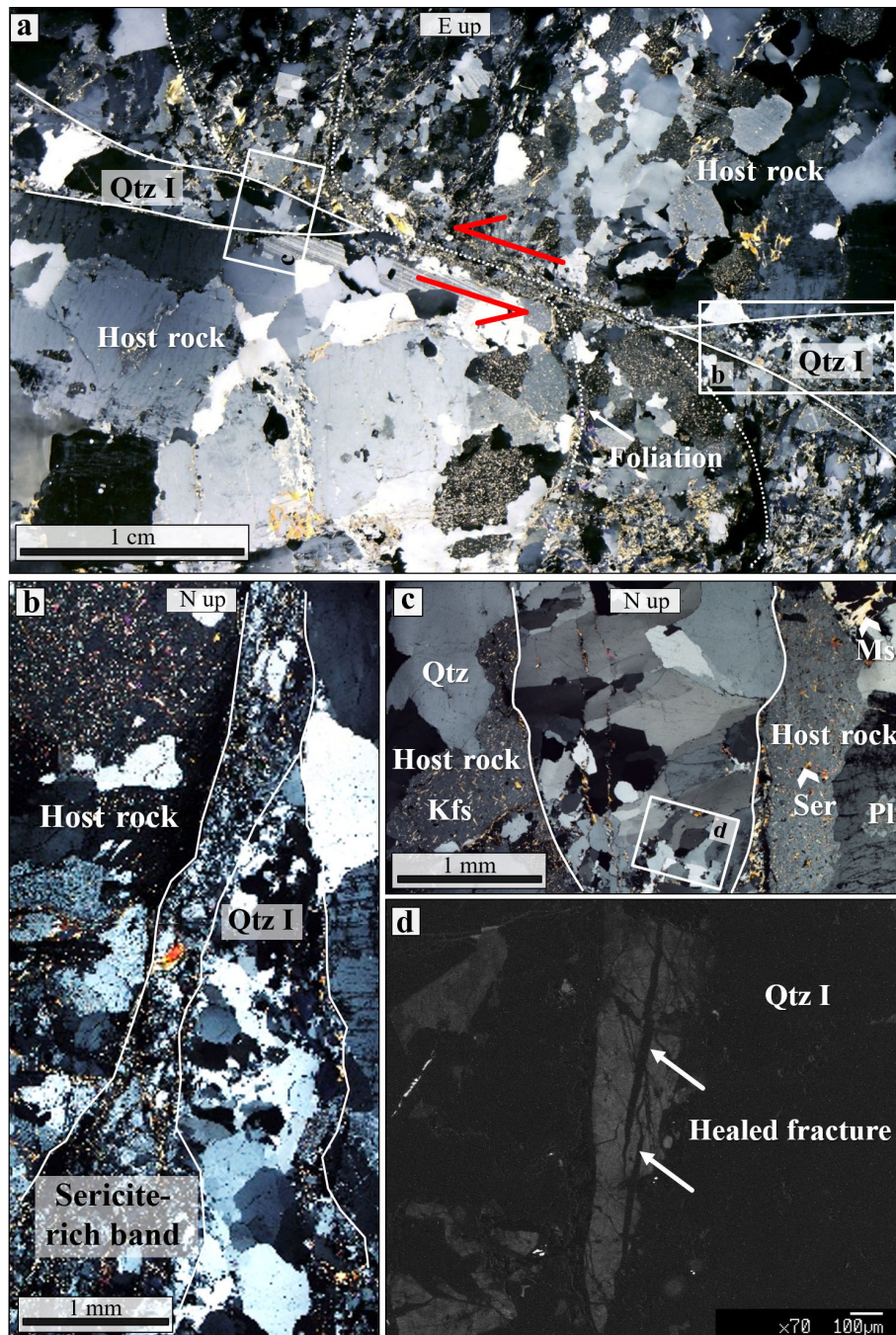
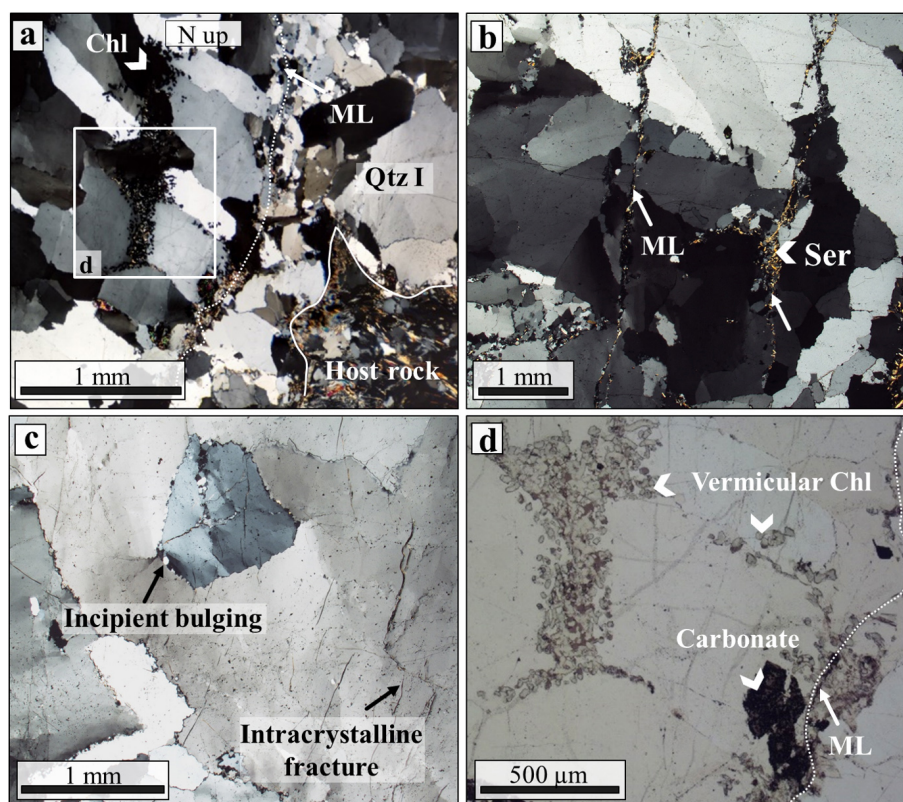**Figure 4.** Microtextural characteristics of Qtz I from the damage zone of BFZ300 (sample: TPH-120-2). **(a)** Stitched photomicrographs of a Qtz I vein interconnecting with a sinistral shear band (crossed nicols). Faulting kinematics is suggested by drag folds in the host rock. **(b)** Tip of Qtz I vein hosted by a sericite-rich cataclastic band of the host rock. **(c)** Detail of panel **(a)** showing open-space filling texture in the Qtz I vein. Notice the sericite microfractures cross-cutting Qtz I. **(d)** Panchromatic cathodoluminescence image of Qtz I showing healed microfractures cross-cutting the crystal.

idence for these healed microfractures within quartz is represented by well-defined trails of fluid inclusions cross-cutting primary growth bands (Fig. 7d).

Chlorite is the second most abundant phase within the fault core Qtz I and Qtz II veins and occurs with a variety of textures. Aggregates of vermicular chlorite similar to that occurring in the damage zone are also present in Qtz I from the core (Fig. 8e), although chlorite with flaky and radiate textures (Fig. 8f) is also present. The latter is generally 100–300 μm in size and is in textural equilibrium with quartz and

Figure 5. Microtextural characteristics of Qtz I from the damage zone of BFZ300 (samples PH21 and TPH-120-2). **(a)** Stitched microphotographs of a Qtz I vein showing elongated–blocky texture with crystals growing obliquely with respect to the vein boundaries, which suggests growth under oblique dilatation. A series of median lines (MLs) are marked by **(b)** sericite crystals suggesting repeated crack and seal. Quartz crystals show low-temperature crystal–plastic deformation by undulose extinction and extinction bands. **(c)** Detail of plastic deformation in damage zone quartz veins: distorted crystals showing incipient bulging and intracrystalline fracturing. **(d)** Detail (plane-polarized light) of an ML and secondary fractures both decorated by vermicular chlorite and aggregates of rare-earth-element-bearing carbonate.

rare calcite. Radiate chlorite overgrowing fractured Qtz II (Fig. 7b) suggests late Qtz II precipitation.

Associated with Qtz II, a sulfide assemblage made of pyrite, sphalerite, galena, and chalcopyrite (Fig. 7d, e; see also Fig. 3g) forms aggregates that are commonly located along quartz grain boundaries. These aggregates have dimensions between 10 and 600 μm.

Multiply reworked breccias and cataclasites occur within and cross-cut BFZ300. In the studied sections, a cataclastic band between 5 and 8 mm thick cross-cuts both Qtz I and Qtz II veins (Fig. 8a), but it is in turn cross-cut by a different quartz–radiate–chlorite vein displaying evidence of syntaxial growth. This cataclasite contains poorly sorted and angular quartz clasts between 8 and 12 mm in size set in a finer (20–200 μm in size) white mica–quartz matrix. The largest quartz fragments show irregular, lobate grain boundaries and are affected by undulose extinction. We interpret these textures as the product of dissolution and cataclastic reworking of Qtz I.

Parallel sets of stylolitic seams trend ca. N–S, parallel to the strike of BFZ300, and mark the two sides of the cataclastic band (Fig. 8a, c). They host anhedral sphalerite, stannite,

galena, pyrite, and chalcopyrite (Fig. 8d), which are coeval with the formation of the Qtz II vein. We interpret the presence of these anhedral sulfide minerals along the stylolite as the product of passive concentration by pressure solution.

4.3 Fluid inclusion data

4.3.1 Fluid inclusion petrography

The studied FIAs invariably contain a two-phase fluid (liquid–vapour) and are mainly arranged in secondary trails within Qtz I crystals in the damage zone (Type S1) and also within Qtz I fault core, where they form dismembered (Type S2) trails and also appear as individual clusters inside the crystals affected by crystal–plastic deformation (Type S3). Within Qtz II, FIAs are arranged as pseudosecondary (Type PS) and secondary (Type S4) trails. Representative examples of FI petrographic features are shown for each structural domain in Fig. 9. Table 1 provides a schematic representation of the location of the FI types, in addition to their location within the fault architecture and their fluid properties.
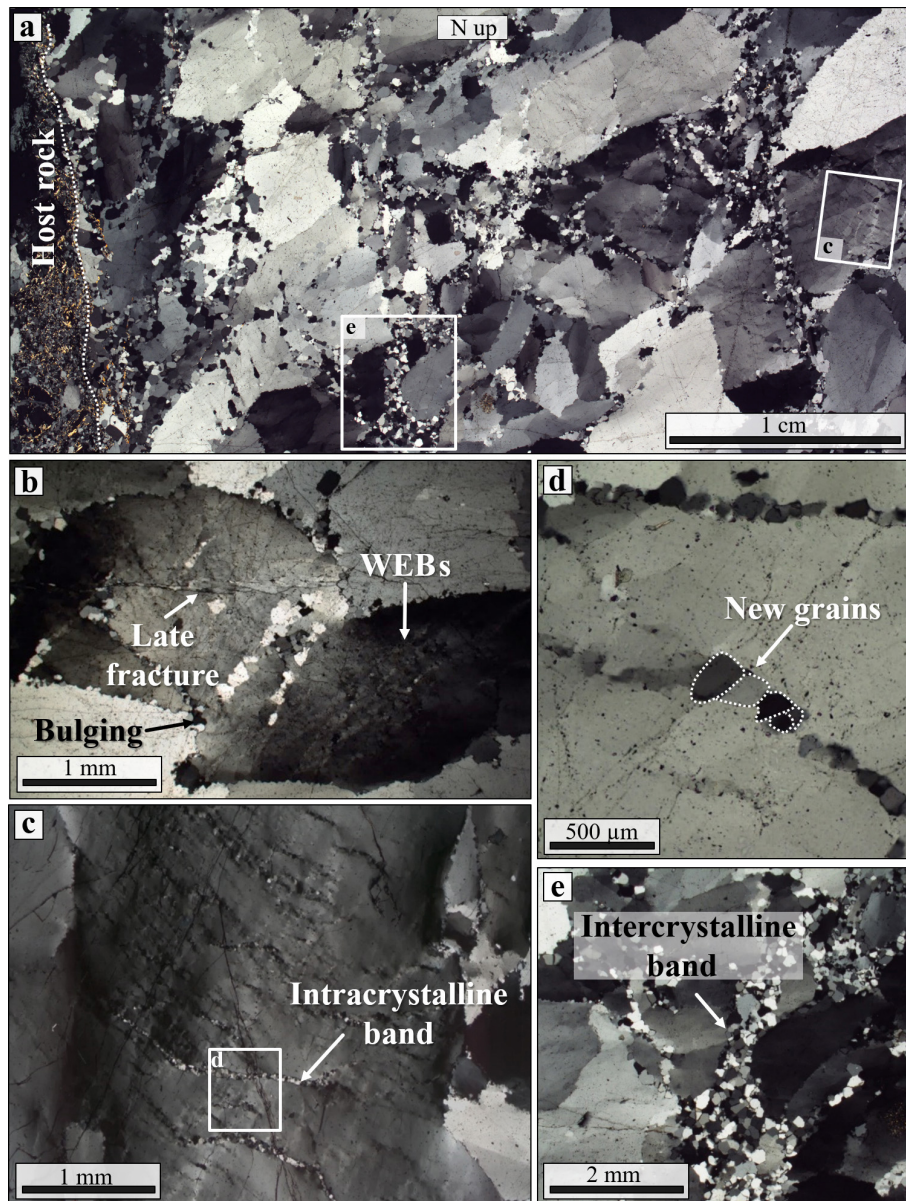
Figure 6. Microtextural characteristics of Qtz I from the BFZ300 core (sample TPH-120-4). **(a)** Stitched photomicrographs showing the typical heterogeneous grain size of Qtz I (30–800 μm). **(b)** Evidence of plastic deformation of Qtz I from the fault core given by bulging of the largest crystals, wide extinction bands, and undulose extinction. Note the late brittle fractures cross-cutting all the previously formed plastic features. **(c)** Intracrystalline deformation bands within a large crystal. **(d)** Detail of **(c)** showing the typical grain size of the band (50–250 μm). Intracrystalline deformation bands are oriented at $< 30°$ with respect to the BFZ300 vein walls and can be up to 2 mm in length. **(e)** Intercrystalline deformation band showing a thickening at the triple junction of larger grains. These intercrystalline bands are parallel to the strike of BFZ300.

Damage zone. Within Qtz I grains (Fig. 9a, b), secondary FIAs are found as trails (Fig. 9a) that parallel what we interpret as healed, old microfractures. In these assemblages, FIs have a maximum size between 2 and 20 μm, a regular equi-dimensional shape (i.e. negative crystal morphology), and a volume fraction, ϕ ($\phi = V_v / V_{tot}$, see Sect. 3), ranging between 5 and 15 % (Fig. 9b).

Fault core. Qtz I grains host secondary FIAs (Type S2), which are transgranular trails (Fig. 9c) along healed joints and hybrid fractures. These trails are locally interrupted and dismembered by aggregates of new, fine-grained quartz grains (Fig. 9c) and generate a texture that is indeed typical of Qtz I from the fault core (Fig. 6a). Fluid inclusions vary in size between 1 and 10 μm, have a ϕ of 10 %–20 %, and show a negative crystal morphology (Fig. 9d). Fluid in-
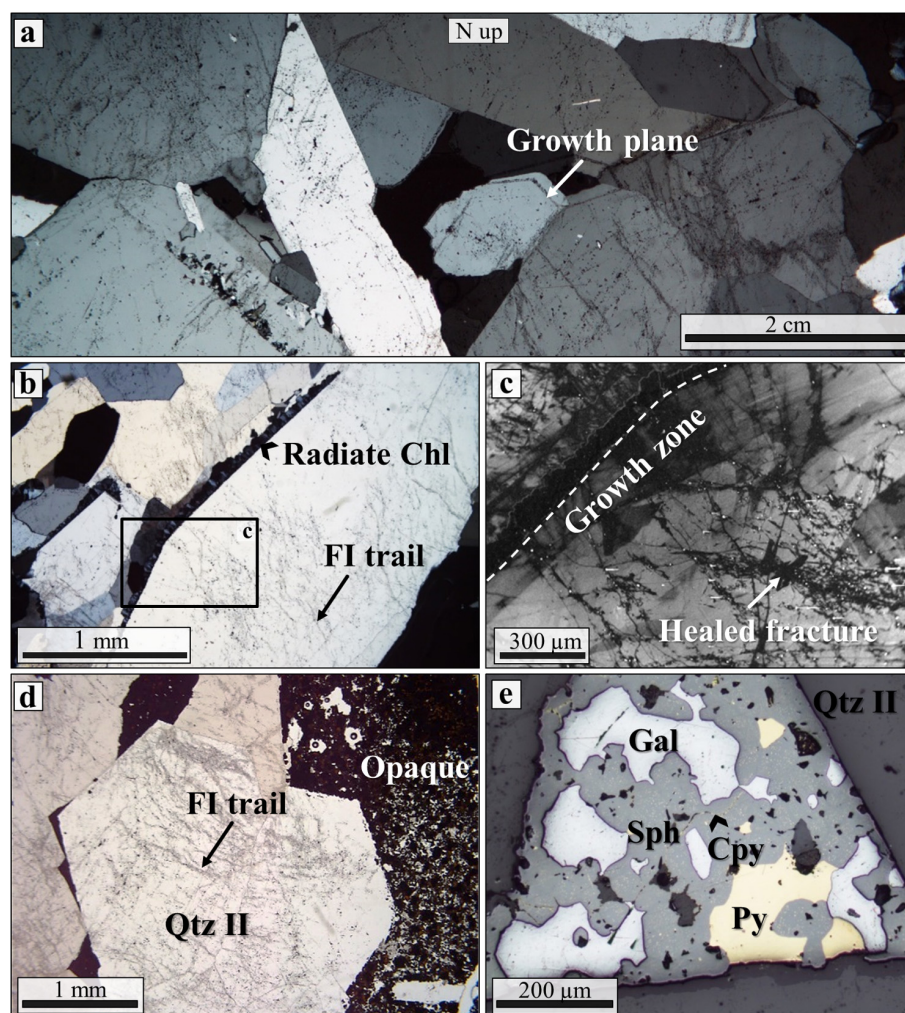
Figure 7. Microstructural characteristics of Qtz II from BFZ300 (samples TPH-120-6, PH22). **(a)** Stitched photomicrographs of Qtz II vein from the fault core. Notice the coarse quartz crystals and their elongated–blocky texture. Primary growth textures are sometimes visible and are marked by solid inclusions and decrepitated FIAs. **(b)** Radiate chlorite crystals along a prismatic Qtz II crystal boundary. Note that Qtz II is cross-cut by numerous trails of FIs. **(c)** Panchromatic cathodoluminescence image of the same large Qtz II crystal from panel **(b)**, showing radiate chlorite along the crystal boundary and a primary growth zone cut by a set of healed fractures. **(d)** Euhedral quartz crystals set within opaque phases and cross-cut by a network of thin microfractures. **(e)** Reflected-light photomicrograph showing the opaque mineral assemblage typically associated with Qtz II, i.e. subhedral to anhedral sphalerite, pyrite, and galena. Chalcopyrite is a minor phase and occurs as small round inclusions within sphalerite (chalcopyrite "disease") or as large subhedral–anhedral masses together with galena.

clusions are also found as isolated clusters inside intensely recrystallized quartz domains (Fig. 9c). FIAs inside these recrystallized quartz domains were pervasively obliterated during later episodes of ductile deformation. The development of WEBs, intercrystalline bands, and bulging resulted in the remobilization (i.e. "transposition" sensu Anderson et al., 1990) of these assemblages. This is regularly observed and is documented, for instance, by the presence of short, secondary trails of regularly shaped inclusion oriented at a high angle with respect to a longer parent trail (Fig. 9c). Morphologically, these trails resemble the transposed trails documented in high-grade metamorphic rocks (Andersen et al., 1990; Van den Kerkhof et al., 2014). Different types of

fluid inclusion morphologies are found within the intensely recrystallized quartz domains (Fig. 9f). Negative crystal morphology is observed in some areas of the selected samples, but it is uncommon. The "dismembered" morphology is instead more typical (Vityk and Bodnar, 1995; Tarantola et al., 2010), and is observed in the relatively large inclusions (> 20 μm). This morphology is made of a central (often empty) inclusion, showing several tails and re-entrants, surrounded by three-dimensional clusters of small "satellite" inclusions. These clusters might be arranged with a quasi-planar geometry inside the host (i.e. in a trail-like fashion). Another typical texture found in most assemblages is the "scalloped" morphology of small- to medium-sized inclu-
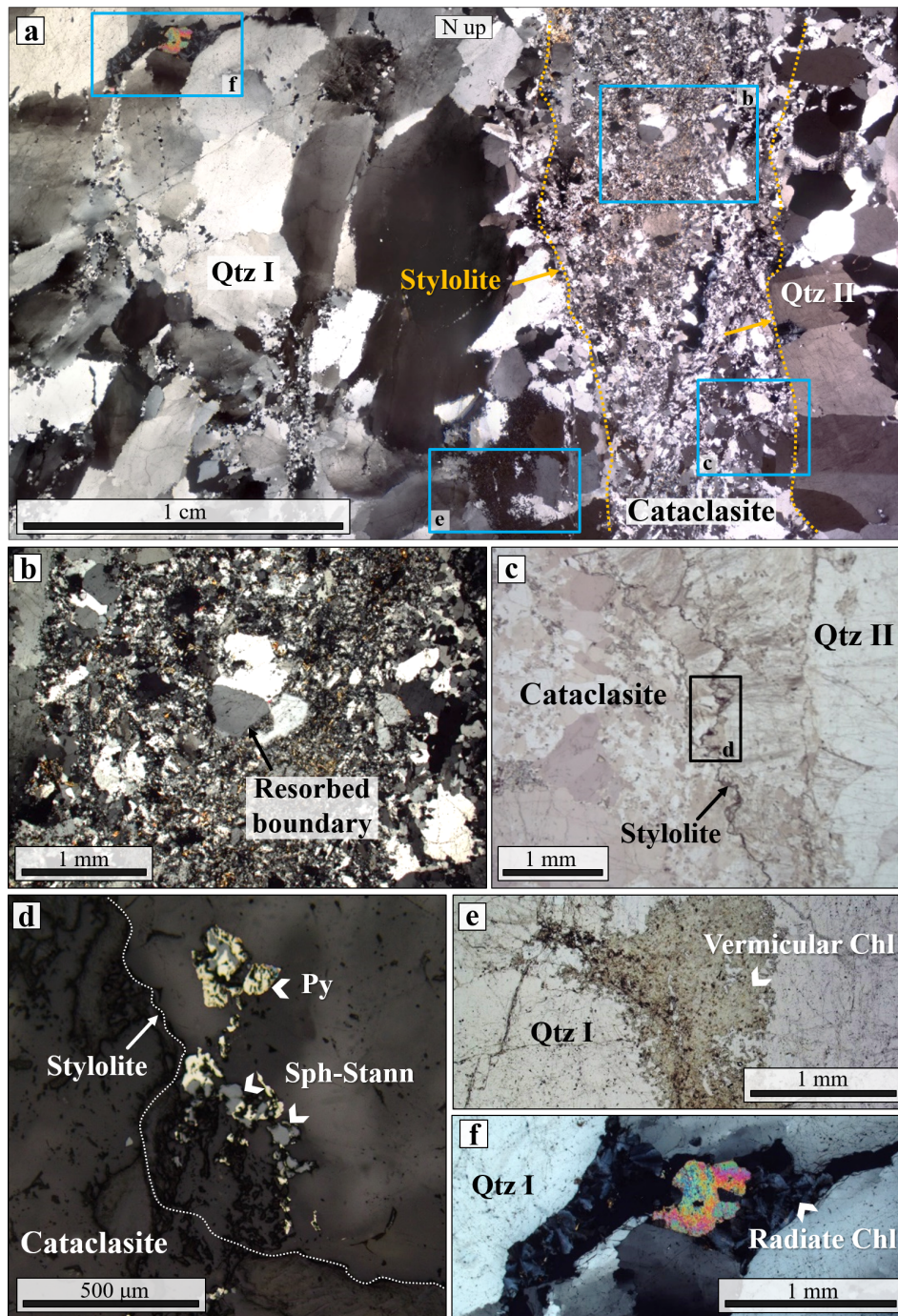
Figure 8. Microstructures of the cataclasite juxtaposing Qtz I and Qtz II veins (sample TPH-120-4). **(a)** Stitched photomicrographs covering the contact between the two quartz veins and the intervening 5 mm thick cataclastic band. **(b)** Cataclastic band containing large Qtz I fragments (8–12 mm) embedded within a finer matrix (20–200 μm in size) of sericite and recrystallized quartz. The largest crystals show lobate boundaries, suggesting dissolution and local resorption along the clast–matrix interface. **(c)** Stylolite seams at the boundary of the cataclasite that strike parallel to the BFZ300. **(d)** Reflected-light photomicrograph showing anhedral to subhedral pyrite, chalcopyrite, stannite, and sphalerite arranged along the stylolite as residual products of pressure solution. **(e)** Vermicular and radiate **(f)** chlorite aggregates associated with Qtz I close to the cataclastic band.

Figure 9. Characteristic textures of FIAs hosted within the BFZ300 quartz (samples PH21, TPH-120-4, TPH-120-6). **(a)** Secondary trails cross-cutting large Qtz I crystals of the damage zone. **(b)** Detail of **(a)** showing the phase ratios of one of the studied secondary assemblages (FIA 3), most representative of Type S1 FIA. **(c)** Long secondary transgranular trails cross-cutting Qtz I of the fault core, dismembered by intercrystalline fractures, infilled by quartz new grains. Qtz I fault core also hosts a set of short sub-trails developed at a high angle with respect to the long trails. **(d)** Detail of Type S2 FIA entrapped along a preserved secondary fracture trail. **(e)** Small inclusions (< 1 μm) arranged along the boundaries of new polygonal quartz. **(f)** Example of Type S3 FIA arranged as isolated clusters inside ductile-deformed fault core Qtz I. These trails formed during a brittle deformation stage that predates ductile re-crystallization. **(g)** Pseudosecondary FIA associated with Qtz II chlorite (FIA 11). The enlargement shows the phase ratio details. **(h)** Small-scale view of secondary FIAs cross-cutting Qtz II. **(i)** Detail of secondary trails cross-cutting euhedral Qtz II (FIA 13). In all photographs north points up.

Table 1. Schematic summary of main microstructures, fluid properties, and $P-T$ deformation conditions in the quartz veins of the BFZ300 fault.

Structural zone and sample	Qtz type	Deformation type	Microstructures	Microthermometric properties	Fluid pressure (P_f) and mineral pair thermometry
Damage zone (PH-21)	Qtz I	Brittle–ductile		Tm_{ice} S1: -5.9 to $-0.1\,°C$ Th_{tot} S1: $150-400\,°C$	$T_{Chl\text{-}QtzI\,(DZ)}$: $175-240\,°C$ P_f (S1): $50-80\,MPa$
Fault core (TPH120-4A)	Qtz I	Cyclic Brittle–ductile		Tm_{ice} S2: -8.2 to $-0.4\,°C$ Th_{tot} S2: $130-410\,°C$	$T_{Chl\text{-}QtzI\,(FC)}$: $350\,°C$ P_f (S2): $30-210\,MPa$
Fault core (TPH120-6) (TPH120-4)	Qtz II	Brittle		Tm_{ice} PS: -13.6 to $-0.1\,°C$ Th_{tot} PS: $150-440\,°C$ Tm_{ice} S4: -11 to $0\,°C$ Th_{tot} S4: $130-430\,°C$	$T_{Chl\text{-}QtzII}$: $160-220\,°C$ $T_{Sph\text{-}Stann\text{-}Qtz\,II}$: $250-305\,°C$ P_f (PS): $50-140\,MPa$ P_f (S4): $40-180\,MPa$

Note: microstructures are coupled with the corresponding FI types and $P-T$ constraints derived from the collected dataset. See text for a further explanation. Note that we combine structural and geochemical data to constrain the relationships between stages of mineral-scale deformation and fluid circulation, which in turn defines the relative chronology of stages of fluid flow during faulting. ML: median line; Blg: bulging.

sions (< 10–$15\,\mu m$), which is defined by the presence of indentations, embayments, irregularities, and sharp tips of the inclusion walls (Fig. 9f). Small inclusions ($< 1\,\mu m$) are also found at the edge of the straight, regular boundaries of new quartz grains; they are mostly dark, i.e. they are vapour-rich or empty, and are equant in shape (Fig. 9e). Although small inclusions do not allow for a microthermometric study of the fluid-phase behaviour in this structural domain, they confirm the complex reactivation history of BFZ300.

Qtz II contains both pseudosecondary (Type PS) and secondary (Type S4) assemblages (Fig. 9g, i, h). The first type is arranged in trails that cut at a low angle the hosting quartz but not the neighbouring phases (e.g. chlorite). In these assemblages, FIs are relatively large (2–$45\,\mu m$) and exhibit an elongated shape and ϕ values between 15 % and 30 % (Fig. 9g). Type S4 FIAs (Fig. 9h) host two-phase inclusions whose size (5–$35\,\mu m$) is similar to that of PS trails but show a ϕ between 30 % and 40 % (Fig. 9i).

Primary FIAs are also present along growth planes of Qtz II, where they have a relatively large size (20–$50\,\mu m$; Fig. S3a, b, c). They present irregular and dismembered textures, which suggest intense post-entrapment re-equilibration.

In summary, our microtextural study shows that the FIAs to be selected for the microthermometric study are only those hosted within Qtz I and Qtz II crystals with little to no recrystallization and whose inclusions have textures corresponding to the least intense post-entrapment re-equilibration (Bodnar, 2003b, and references therein; Tarantola et al., 2010). These are the pseudosecondary and secondary FIAs in which dendritic or transposed inclusions are absent and in which the host quartz exhibits only undulose extinction (S1, S2, S4, and PS).
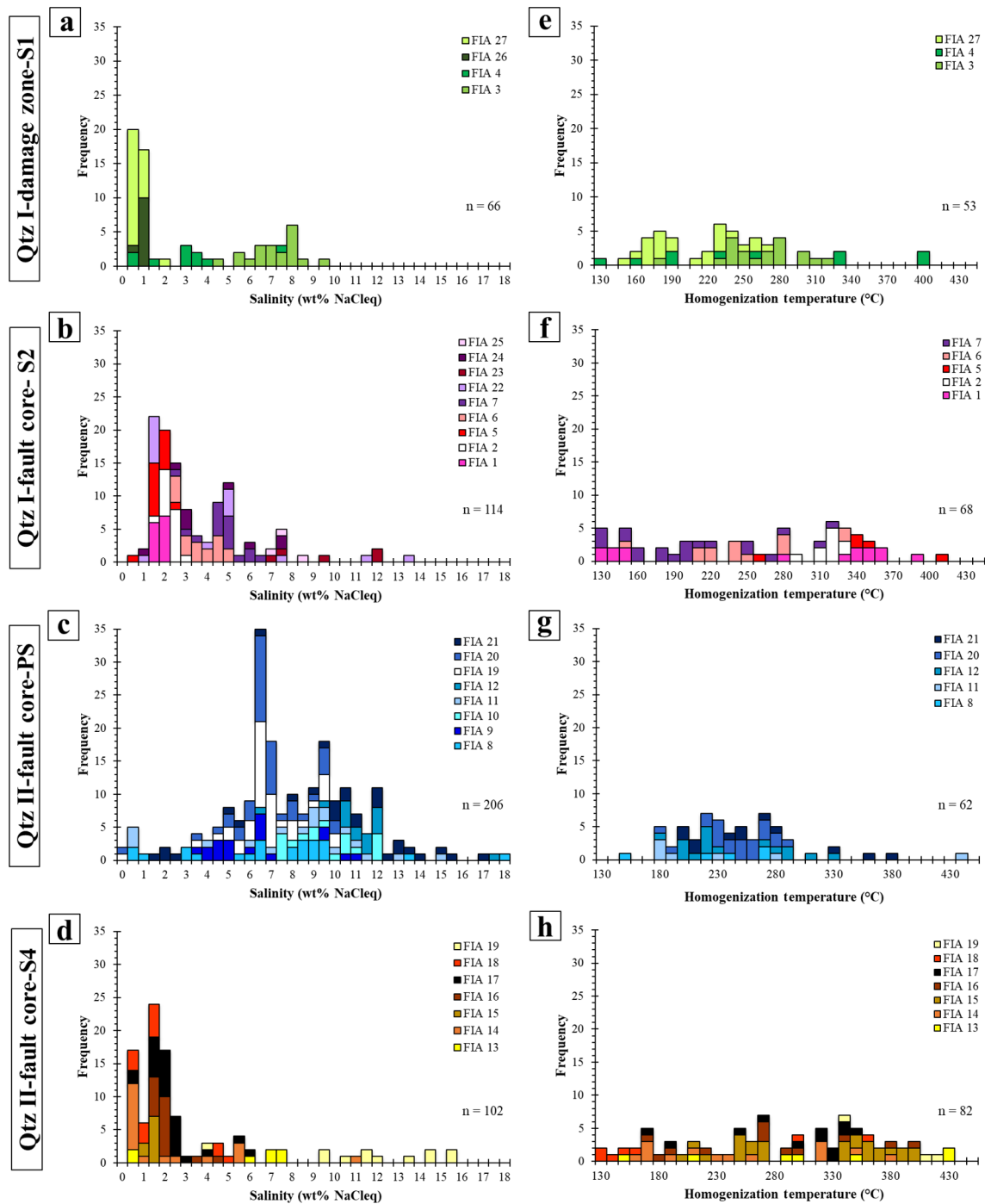
Figure 10. Microthermometric data of the studied FIAs. Panels **(a)**–**(d)** show the bulk salinities of individual FIAs calculated from the Tm_{ice} data, while panels **(e)**–**(h)** refer to the temperatures of final homogenization in the same assemblages. Notice that the data report the properties of individual FIAs according to their occurrence within Qtz I of the damage zone, Qtz I from the fault core, and Qtz II from the fault core. Notice that pseudosecondary (PS) and secondary (S) FIAs identify progressive later stages of fluid entrapment and can be used to constrain the fluid properties in the fault zone. Notice also that the measured ranges of Th_{tot} spread across T intervals that are too large to represent entrapment at equilibrium (e.g. FIA 7 of Qtz I from fault core: 130–320 °C), which suggests post-entrapment re-equilibration of the inclusions. Fluid bulk composition is expressed as salinity, which is conventionally reported as weight percent of NaCl equivalents (wt % NaCleq; Roedder, 1984).

4.3.2 Microthermometry

Damage zone. Secondary FIAs hosted within Qtz I from the damage zone (Type S1) show a range of Tm_{ice} between -5.9 and $-0.1\,°C$, which corresponds to a salinity of 0 wt % NaCleq–9 wt % NaCleq (Fig. 10a). In these FIAs, final homogenization (Th_{tot}) occurs into the liquid phase (i.e. by disappearance of the vapour bubble) and mainly between 150 and 400 °C (Fig. 10e).

Fault core. The secondary FIAs hosted within Qtz I in the fault core (Type S2) show a range of Tm_{ice} between -8.2 and $-0.4\,°C$, which corresponds to salinities between 0 wt % NaCleq and 14 wt % NaCleq (Fig. 10b), and final homogenization occurs into the liquid phase between 130 and 410 °C (Fig. 10f).

Pseudosecondary FIAs entrapped within Qtz II (Type PS) show a range of Tm_{ice} between -13.6 and $-0.1\,°C$, which corresponds to a salinity range between 0 wt % NaCleq and 18 wt % NaCleq (Fig. 10c); final homogenization occurs into the liquid phase and between 150 and 440 °C (Fig. 10g). Secondary FIAs in Qtz II (Type S4) show a range of Tm_{ice} between -11 and $0\,°C$, which corresponds to a 0 wt % NaCleq–15 wt % NaCleq range of salinity (Fig. 10d), while final homogenization into the liquid phase is between 130 and 430 °C (Fig. 10h).

As no gases were determined during microthermometric analysis (i.e. melting of carbonic-phase or clathrate hydrates was not detected during the freezing experiments), additional micro-Raman analysis was performed on a set of representative FIAs (samples: TPH-120-4; TPH-120-6; PH21; PH22). Aqueous fluid inclusions hosted by both Qtz I and Qtz II show peaks at the characteristic wavenumbers of CH_4 ($2917\,cm^{-1}$) and CO_2 ($1388\,cm^{-1}$). These peaks were determined as weak in all spectra, and CO_2 detection was sporadic in a few inclusions of only one sample of the fault core (TPH-120-4). Although spectroscopic detections, the CO_2- and CH_4-bearing inclusions are not systematically associated with specific quartz vein generations or microstructures (i.e. intracrystalline healed cracks, WEB planes, intercrystalline fractures). We therefore cannot associate the presence of CO_2 and/or CH_4 to any specific deformation stage of the fault.

Such spectroscopic determinations are consistent with the lack of microthermometric evidence of carbonic-phase or clathrate hydrates during the freezing experiments (Rosso and Bodnar, 1995; Dubessy et al., 2001). The impossibility of detecting CO_2- and CH_4-bearing fluids during the freezing experiments indicate a gas pressure that is systematically lower than that required to observe clathrate dissociation (e.g. 1.4 MPa in CO_2–H_2O fluids; Rosso and Bodnar, 1995); i.e. it shows low gas concentrations. As a consequence, we have modelled the fluid phases as simple H_2O–NaCl systems.

4.4 Chlorite and sulfide geothermometry

Chlorite composition has been determined for several generations of chlorites in association with Qtz I and II, namely vermicular chlorite associated with Qtz I from the damage zone, vermicular and radiate chlorite associated with Qtz I from the fault core, and radiate chlorite associated with Qtz II from the fault core (Table 2). Chlorite compositions are shown in Fig. 11a and are expressed as a function of the $Fe/(Fe + Mg)$ ratio. Chlorite compositional data are presented according to the structural domain of the fault they are associated with and to the corresponding texture. Vermicular chlorite associated with Qtz I in the damage zone has an XFe range between 0.50 and 0.55, while vermicular chlorite associated with Qtz I from the fault core has an XFe of 0.53. Radiate chlorite associated with Qtz I from the fault core has an XFe range between 0.71 and 0.81, while radiate chlorite associated with Qtz II from the fault core is between 0.65 and 0.80, constraining compositions within the ripidolite and aphrosiderite endmembers.

Temperature–composition relationships for the quartz–chlorite pair portrayed in the T–R^{2+}–Si diagram of Bourdelle and Cathelineau (2015) show that, in the hypothesis of quartz–chlorite equilibrium, the precipitation of vermicular chlorite within the Qtz I of the damage zone took place in the 175–240 °C range (green diamonds in Fig. 11a). This range is distinct from that of the vermicular and radiate chlorite from Qtz I of the fault core, which is probably ca. 350 °C because the measured R^{2+}–Si compositional parameters ($R^{2+} = Mg+Fe$) plot at the edge of, or slightly outside, the calibrated region of the Bourdelle and Cathelineau plot (red diamonds in Fig. 11a). We stress that the high-T chlorite plots parallel to the 350 °C isotherm, suggesting that it most probably precipitated at the same or at a similar temperature. Radiate chlorite associated with Qtz II from the fault core is instead compatible with an equilibrium precipitation at 160–220 °C (light blue diamonds in Fig. 11a).

The collected EPMA data show that the sulfides associated with Qtz II have compositions that approach those of pure phases (Table 3). Pyrite has trace element concentrations (Cu, As, Pb, Ni, Zn) that are in general below the EPMA detection limit, while galena, sphalerite, and chalcopyrite show only some significant trace contents of Fe and Zn (e.g. Fe: 0.22 wt %–1.00 wt % in galena; Zn: 0.11 wt %–3.95 wt % in chalcopyrite). Pyrite and sphalerite from the Qtz II veins (Fig. 7e) have trace element concentrations that are, again, mostly below detection limits.

The stylolites bordering the cataclasite bands described above and formed at the contact between the Qtz I and Qtz II vein contain pyrite, galena, and the sphalerite–stannite pair (Fig. 8a, c, d), with the latter showing the largest compositional variation. This pair represents a mineral geothermometer because the partitioning of Zn and Fe between sphalerite and stannite was demonstrated to be temperature dependent but pressure independent (Nekrasov et al., 1979; Shimizu and

Table 2. Representative chlorite EPMA from various structural zones of BFZ300.

Sample	4A	4A	4A	4A	4A	4A	PH21	PH21	PH21	2	2	2	6	6	6	6
Structural zone	FC	FC	FC	FC	FC	FC	DZ	DZ	DZ	DZ	DZ	DZ	FC	FC	FC	FC
Quartz type	Qtz I	Qtz I	Qtz I	Qtz I	Qtz I	Qtz I	Qtz I	Qtz I	Qtz I	Qtz I	Qtz I	Qtz I	Qtz II	Qtz II	Qtz II	Qtz II
Textural type	Verm	Verm	Verm	Rad	Rad	Rad	Verm	Verm	Verm	Verm	Verm	Verm	Rad	Rad	Rad	Rad
Na_2O	0.04	0.07	0.00	0.08	0.08	0.03	0.05	0.02	0.04	0.03	0.01	0.05	0.04	0.06	0.01	0.01
TiO_2	0.02	0.01	0.00	0.00	0.03	0.01	0.09	0.04	0.01	0.01	0.01	0.03	0.03	0.03	0.04	0.13
MnO	0.59	0.65	0.62	0.53	0.56	0.48	0.24	0.24	0.30	0.48	0.37	0.43	0.64	0.57	0.71	0.60
K_2O	0.06	0.02	0.04	0.07	0.04	0.04	0.01	0.01	0.03	0.10	0.05	0.07	0.03	0.02	0.05	0.01
MgO	13.66	13.79	13.74	6.61	5.13	6.75	13.95	14.06	13.29	12.85	12.57	12.59	4.85	4.87	8.73	8.05
SiO_2	25.49	26.00	25.83	23.62	22.89	23.91	27.24	27.02	27.49	27.43	27.88	27.79	25.63	25.64	26.5	26.13
Cr_2O_3	0.00	0.01	0.04	0.00	0.00	0.06	0.04	0.03	0.06	0	0.06	0.01	0	0.02	0.01	0
FeO	27.86	27.74	27.87	36.61	38.49	36.75	24.68	25.21	26.07	25.97	26.06	25.77	34.26	33.84	30.08	30.47
CaO	0.03	0.04	0.05	0.00	0.06	0.03	0.01	0.02	0	0.05	0.05	0.03	0.01	0.04	0.04	0.02
Al_2O_3	22.04	22.13	22.00	22.89	23.35	22.98	24.13	24.75	24.91	24.02	23.48	23.21	24.23	24.64	24.49	25.02
Cl	0.00	0.00	0.01	0.03	0.02	0.04	0.01	0	0	0.01	0	0	0.03	0.02	0.02	0.01
Total	89.78	90.45	90.20	90.44	90.67	91.09	90.69	91.42	92.23	91.12	90.81	90.08	89.82	89.94	90.78	90.48
No. ions in formula based on 28 (O,OH)																
Na	0.02	0.03	0	0.03	0.03	0.01	0.02	0.01	0.01	0.01	0.01	0.02	0.02	0.03	0	0.01
Ti	0	0	0	0	0	0	0.01	0.01	0	0	0.01	0	0.01	0.0	0.01	0.02
Mn	0.10	0.11	0.11	0.10	0.10	0.09	0.04	0.04	0.05	0.08	0.06	0.07	0.12	0.10	0.12	0.11
K	0.01	0	0.01	0.02	0.02	0.01	0	0	0.01	0.02	0.01	0.02	0.01	0	0.01	0
Mg	4.25	4.25	4.25	2.14	1.68	2.17	4.18	4.19	3.93	3.86	3.79	3.82	1.55	1.55	2.69	2.49
Si	5.32	5.37	5.36	5.14	5.02	5.15	5.48	5.40	5.46	5.53	5.64	5.66	5.49	5.47	5.48	5.43
Cr	0	0	0.01	0	0	0.01	0.01	0	0.01	0	0.01	0	0	0	0	
Fe^{2+}	4.86	4.79	4.83	6.66	7.06	6.62	4.15	4.21	4.33	4.38	4.40	4.39	6.14	6.04	5.20	5.29
Ca	0.01	0.01	0.01	0	0.01	0.01	0	0	0	0.01	0.01	0.01	0	0.01	0.01	0
Al	5.42	5.39	5.38	5.86	6.04	5.84	5.72	5.83	5.83	5.71	5.59	5.57	6.12	6.20	5.97	6.13
Cl	0	0	0	0.01	0.01	0.01	0	0	0	0	0	0	0.01	0.01	0.01	0
Fe	4.86	4.79	4.83	6.66	7.06	6.62	4.15	4.21	4.33	4.38	4.40	4.39	6.14	6.04	5.20	5.29
Al tetr.	2.68	2.63	2.64	2.86	2.98	2.85	2.52	2.60	2.54	2.47	2.37	2.34	2.51	2.53	2.52	2.57
Al oct.	2.73	2.76	2.73	3.00	3.06	2.99	3.20	3.22	3.29	3.24	3.23	3.23	3.61	3.67	3.45	3.56
Fe/(Fe + Mg)	0.53	0.53	0.53	0.76	0.81	0.75	0.50	0.50	0.52	0.53	0.54	0.53	0.80	0.79	0.66	0.68
Based on 28 (O,OH)																
R^{2+}	9.11	9.04	9.08	8.80	8.74	8.79	8.33	8.40	8.26	8.24	8.19	8.21	7.69	7.59	7.90	7.79
Si	5.32	5.37	5.36	5.14	5.02	5.15	5.48	5.40	5.46	5.53	5.64	5.66	5.49	5.47	5.48	5.43
Based on 14 (O,OH)																
R^{2+}	4.55	4.52	4.54	4.40	4.37	4.40	4.17	4.20	4.13	4.12	4.10	4.10	3.84	3.79	3.95	3.89
Si	2.66	2.68	2.68	2.57	2.51	2.58	2.74	2.70	2.73	2.77	2.82	2.83	2.75	2.74	2.74	2.71

Shikazono, 1985). In the 14 analysed pairs, stannite shows a range of Zn concentrations varying between 0.48 wt % and 3.25 wt %, while those of Fe, Cu, and Sn vary within narrow ranges (Fe: 12.74 ± 0.56 wt %; Cu: 28.30 ± 0.33 wt %; Sn: 27.65 ± 0.71 wt %). Sphalerite in the pair has concentrations of Fe and Zn of 7.63 ± 0.87 wt % and 56.68 ± 1.17 wt %, respectively. These ranges allow for the calculation of the partition coefficient (K_D) of the following reaction: Cu_2FeSnS_4 (in stannite) + ZnS (in sphalerite) = Cu_2ZnSnS_4 (in stannite) + FeS (in sphalerite). We have used the $\log k_D – T$ relationship of Shimizu and Shikazono (1985) to calculate the formation temperature of the pair, which is portrayed in the $(C_{Cu_2FeSnS_4}/X_{Cu_2ZnSnS_4}) – (X_{FeS}/X_{ZnS})$ plot of Shimizu and Shikazono (Fig. 11b). The resulting 220–305 °C interval lies at the low end of, or slightly outside, the 250–350 °C interval of the geothermometer.

Therefore, we consider the 250–305 °C interval as the best estimation of the formation T of sphalerite–stannite in the stylolite.

5 Discussion

Our work constrains the architecture and the environmental conditions at which BFZ300 deformation took place. Field and petrographic observations support the idea of transiently elevated fluid pressures, cyclic frictional–viscous deformation and progressive, and discrete strain localization (Figs. 2, 3). Analytical data suggest that these deformation cycles took place at the BDTZ. In the following, we discuss these constraints by systematically considering our different analytical results.
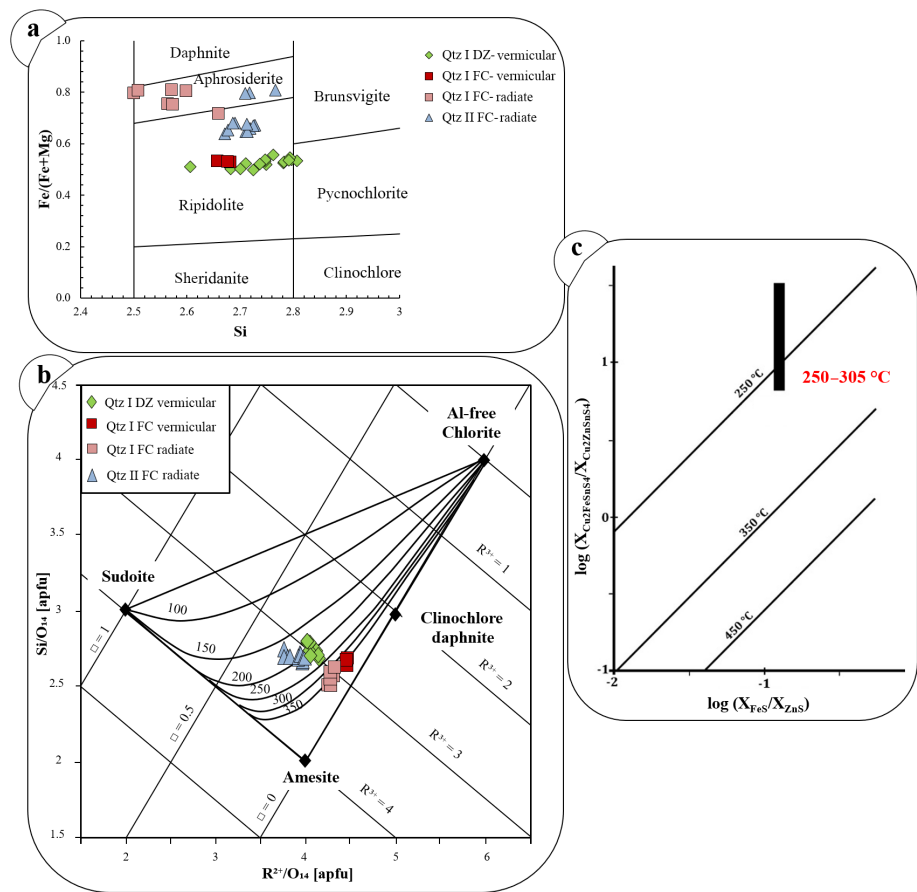
Figure 11. Chlorite chemical composition diagram and mineral pair geothermometry applied to the assemblages of the Qtz I and Qtz II veins. **(a)** Chlorite compositional diagram based on Hey (1954). Green, red, pink, and light blue symbols indicate distinct chlorite textures in association with Qtz I and Qtz II veins. **(b)** Chlorite–quartz formation temperature estimated using the method of Bourdelle and Cathelineau (2015). The maximum temperature is from the Qtz I chlorite pair from the fault core. **(c)** Estimated temperature of formation of sphalerite–stannite in association with the Qtz II vein (based on Shimizu and Shikazono, 1985). The region of the plot that was calibrated with this geothermometer lies between the 250 and 450 °C isotherms.

Table 3. Representative EPMA of sulfides associated with Qtz II.

Analysis	Structural zone	Qtz type	Mineral	S	Fe	Cu	As	Pb	Ni	Zn	Ti	Sn	Total
TPH120-6-14	Core	II	pyrite	55.02	47.50	0.01	0.00	0.00	0.02	0.00	0.00		102.55
TPH120-6-17	Core	II	pyrite	54.08	47.19	0.00	0.01	0.00	0.00	0.00	0.00		101.28
TPH120-6-18	Core	II	sphalerite	34.46	6.46	0.09	0.01	0.00	0.03	59.62	0.02		100.69
TPH120-6-19	Core	II	sphalerite	34.48	6.24	0.08	0.06	0.00	0.04	59.61	0.02		100.53
TPH120-4A-34	Core	II	pyrite	54.49	47.40	0.05	0.00	0.00	0.00	0.00	0.00		101.94
TPH120-4A-35	Core	II	pyrite	54.13	47.26	0.02	0.04	0.00	0.00	0.01	0.55		102.01
TPH120-4A-38	Core	II	galena	13.40	0.00	0.00	0.00	86.63	0.00	0.32	0.01		100.36
TPH120-4A-59	Core	II	galena	13.50	0.06	0.00	0.01	87.04	0.00	0.10	0.01		100.72
TPH120-4A-40	Core*	II	sphalerite	35.06	9.46	0.05	0.00	0.00	0.00	56.74	0.01		101.32
TPH120-4A-43	Core[a]	II	sphalerite	34.69	9.04	0.01	0.03	0.00	0.00	57.51	0.01		101.28
TPH120-4A-41	Core	II	chalcopyrite	35.40	30.53	33.51	0.00	0.00	0.00	1.32	0.00		100.76
TPH120-4A-42	Core	II	chalcopyrite	35.78	30.78	33.59	0.03	0.00	0.01	1.22	0.01		101.42
TPH120-4A-19	Core[b]	II	stannite	29.79	12.53	28.41	0.07	0.08	0.00	0.92	0.000	27.86	99.66
TPH120-4A-22	Core[b]	II	sphalerite	33.82	8.15	0.06	0.00	0.03	0.02	57.27	0.006	0.00	99.36

[a] Located within cataclastic band and close to stylolite. [b] Located along stylolite. Sphalerite and stannite compositions from locations indicated by [b] have been used to calculate the temperatures of sphalerite–stannite equilibrium following the geothermometer of Shimizu and Shikazono (1985). See text for a further explanation.

5.1 Fluid inclusion data and mineral pair geothermometry

Field evidence combined with microstructural observations, fluid inclusion analyses, and the documented distinct generations of synkinematic chlorites confirm that Qtz I and Qtz II veins precipitated from distinct batches of aqueous fluid (i.e. H_2O–NaCl) that infiltrated the fault zone during different stages of its evolution.

We documented a wide range of bulk salinity for each FIA entrapped within the quartz veins in each structural domain (Fig. 10a–d). This suggests post-entrapment re-equilibration of fluid inclusions (Bakker and Jansen, 1990; Diamond et al., 2010). The Th_{tot} varies between ca. 130 and 440 °C without a clear mode or a skew (Fig. 10e, h), indicating that no common range of entrapment temperature can be identified in the dataset. Therefore, we conclude that even the properties of petrographically intact FIAs do not correspond to chemically well-preserved assemblages. Indeed, the ranges of Th_{tot} in individual FIAs are typically of the order of 150–200 °C (Fig. 10e–h), i.e. a value that is much higher than the ~ 10 °C range expected for homogeneous FIAs entrapped isochorically and isoplethically (Fall et al., 2009; Vityk and Bodnar, 1998) and that demonstrates post-entrapment re-equilibration (Vitik and Bodnar, 1998; Bodnar, 2003b; Sterner and Bodnar, 1989; Invernizzi et al., 1998). A major implication of fluid inclusion re-equilibration in our study is that the calculated fluid properties do not rigorously reflect those of the pristine fluid originally entrapped within BFZ300, but rather those of a fluid that modified its properties during the fault activity.

Then, a possible approach to interpret our FI dataset is a comparison with experimental work on synthetic fluid inclusions subjected to a range of post-entrapment re-equilibration conditions (Bakker, 2017; Bakker and Jansen, 1990, 1991, 1994; Vityk and Bodnar, 1995, 1998; Vityk et al., 1994; Invernizzi et al., 1998). A straight comparison to the experiments is in our case difficult because most experimental work was carried out at high P–T conditions (500–900 °C; 90–300 MPa), and also only few experiments were carried out under deviatoric stress conditions that approach those of natural rocks (Diamond et al., 2010; Tarantola et al., 2010). Despite these limitations, however, some key experimental results provide fundamental constraints on our dataset. First, both hydrostatic and uniaxial compression experiments showed that in each re-equilibrated FIA a number of inclusions survive the modified post-entrapment P–T conditions virtually intact, showing that only severe deformation leads to total re-equilibration and complete obliteration of pristine inclusions (i.e. $\Delta\sigma > 100$ MPa in uniaxial compression experiments; > 400 MPa change of confining P in hydrostatic experiments). Second, under conditions leading to only low to moderate re-equilibration, the bulk chemical composition of the fluid inclusions does not change significantly from that of the pristine inclusions.

All of this implies that natural quartz samples with microstructures typical of moderate T deformation, such as deformation lamellae, deformation bands, undulose extinction and bulging, and hosting FIAs with moderately re-equilibrated textures, should still contain a number of inclusions whose properties resemble those of the pristine fluid. In this scenario, our microthermometric dataset can be used to constrain the more probable salinity ranges of the fluid batches which triggered the BZ300 reactivation stages. Two possible interpretations of the microthermometric dataset can follow and we can give the corresponding different salinity ranges for the fluids.

One possibility is that the different quartz veins and the fluids trapped within fluid inclusions originated from multiple pulses of a single low-salinity fluid, with a salinity between 0 wt % NaCleq and 7 wt % NaCleq, as shown by the distribution of > 70 % of the bulk salinities skewed towards values of 7 wt % NaCleq or less (Fig. 10a–d). Thus, it is possible that aliquots of the 0 wt % NaCleq–7 wt % NaCleq FIAs from Qtz I and II crystals from both the damage zone and fault core are still representative of the pristine sampled fluid. These inclusions would be those that survived or were relatively less affected by deformation events postdating their entrapment. Inclusions falling outside the most typical 0 wt % NaCleq–7wt % NaCleq salinity range would instead correspond to those which progressively modified their properties as a consequence of fluid–rock interaction during faulting and that experienced significant H_2O loss and consequent salinity increase during the successive stages of fault deformation (Bakker and Jansen, 1990; Diamond et al., 2010). The large documented range of Th_{tot} lacking a specific mode observed in individual FIAs is the product of fluid density changes caused by fluid inclusion re-equilibration during post-entrapment deformation. This would have happened repeatedly and cyclically within the host quartz during all ductile and brittle stages of deformation of the multistage deformation history of BFZ300.

Alternatively, multiple batches of fluids with different salinities (from low to intermediate salinity) may have infiltrated and evolved within BFZ300 during its activity. In fact, considering the salinity dataset presented for each structural domain, fluid salinity can be seen clustering in restricted ranges typical for each domain: (1) the salinity of 60 % of secondary fluid inclusions in Qtz I from the damage zone is between 0 wt % NaCleq and 1 wt % NaCleq; (2) > 80 % of the secondary inclusions in Qtz I from the fault core preserve a salinity in the 1 to 5 wt % NaCleq range; (3) 75 % of pseudosecondary inclusions in Qtz II show salinity values between 6 wt % NaCleq and 11 wt % NaCleq; and (4) ~ 70 % of the secondary inclusions trapped within Qtz II show salinity values between 0 wt % NaCleq and 3 wt % NaCleq. These clusters may best represent the original compositional ranges of different batches of fluids, each involved during a different faulting stage. Salinities outside these ranges may instead be explained again as resulting from the post-entrapment re-

equilibration of those fluids with different salinities. This hypothetical scenario, in which chemically distinct fluids entered into the fault and interacted with the rock at different times (e.g. Selverstone et al., 1992; Boiron et al., 2003; Famin et al., 2005), is also reinforced by several lines of observations, such as the variation of chlorite composition, the slight change in paragenesis–redox state within Qtz II and Qtz I veins (i.e. the absence of massive sulfides in Qtz I), and the prolonged history of faulting (see below).

Fully aware of the interpretative uncertainties of our dataset, we have combined the microthermometric data of the studied FIAs with the independent quartz–chlorite and sphalerite–stannite geothermometers to constrain the most probable fluid pressure during the faulting events. With this approach, we use the formation temperatures of the mineral pairs as independent geothermometers and consider the intersection between these values and the FIA isochores to derive the ranges of trapping pressure (Roedder and Bodnar, 1980). In Fig. 12, we present the ranges of the possible pressure (P_f) of the fluids involved during faulting as calculated by combining the fluid inclusion data with the constraints provided by the mineral pair geothermometry, the hydrostatic and lithostatic pressure gradients, and a possible geothermal gradient (e.g. Van Noten et al., 2011; Selverstone et al., 1995; Jaques and Pascal, 2017). The reconstructed regional gradients at the time of vein emplacement are derived from peak metamorphic conditions (4–5 kbar; 650–700 °C, leading to ca. 40 °C km^{-1}; from Kärki and Paulamäki, 2006). Hydrostatic and lithostatic pressures are then calculated by using pure water density and assuming a rock density of 2700 kg m^{-3}, respectively. These gradients are used to constrain the upper and lower bounds to physically possible fluid pressures. We computed the maximum and minimum isochores by using the entire salinity and Th$_{tot}$ ranges obtained from the FIAs in each structural domain (Fig. 10). We also computed the isochores of the inclusions with the most representative salinity estimates for each structural domain obtained by comparing the frequency diagrams (Fig. 10) with the Th$_{tot}$ vs. salinity plots (Fig. S4). Considering the peak temperature of each structural zone from the geothermometric estimations in combination with the computed isocores, the estimated peak conditions of the fluid pressure are (1) 80 MPa for Qtz I from the damage zone, (2) 210 MPa for Qtz I from the fault core, (3) 140 MPa from pseudosecondary inclusions in Qtz II from the core, and (4) 180 MPa from secondary inclusions in Qtz II, still from the core (Fig. 12; Table 1).

In addition to the P_f peak conditions we can also constrain the physically possible fluid pressure ranges for each stage of fluid ingress, which are derived by considering the temperature range estimated for each structural domain. Thus, for the damage zone, a P_f interval of 50–80 MPa (Fig. 12a) can be derived by intersecting the range of T obtained from the chlorite–quartz pair in the Qtz I from the damage zone with the range of isochores from the same quartz. As to the fault

core, we combine the 350 °C constraint from the chlorite–quartz pair from Qtz I in the fault core with the isochores from the same quartz, which yields P_f between ca. 30 and 210 MPa (Fig. 12b). Similarly, the intersection between the equilibrium T of the sphalerite–stannite pair in the Qtz II from the fault core and the range of isochores of the pseudosecondary FIAs of Qtz II defines P_f values between 50 and 140 MPa (Fig. 12c). Estimations from secondary FIAs in Qtz II constrain a range between 40 and 180 MPa (Fig. 12d).

As also supported by the microstructures described above, we propose that these values are sufficiently accurate to constrain at least four stages of fault reactivation, each triggered by a fluid with distinct physical and compositional properties.

As shown by the T vs. P plots in Fig. 12, the secondary FIAs entrapped in Qtz I from the damage zone constrain the lowest value of P_f (i.e. 50–80 MPa) of the entire dataset. We interpret this not as representative of the early BFZ300 localization, but rather as possibly resulting from fluid entrapment during a later stage of fault reactivation at $T \sim 200$ °C. This is also consistent with the calculated temperature of crystallization of the vermicular chlorite associated with Qtz I from the damage zone (175–240 °C, Fig. 11b) and with the secondary nature of the entrapped FIAs. Also, the most abundant salinities observed in the Qtz I from the damage zone (0 wt % NaCl$_{eq}$–1 wt % NaCl$_{eq}$) coincide with the lowest Th$_{tot}$ measured in the same structural domain. Later fracturing of Qtz I in the damage zone may thus have been coeval with the formation of vermicular chlorite preserved therein, which is found along secondary cracks and median lines (Fig. 5d).

In light of these considerations, we propose that initial BFZ300 localization occurred in the presence of a fluid with T and P of at least 350 °C and 210 MPa, respectively. Later faulting continued by cyclic brittle–ductile switches induced and assisted by fluid batches at progressively lower temperature and pressure.

5.2 Structural evolution and fluid flow: a conceptual model

Based on the integration of field, microstructural, thermometric, and fluid inclusion constraints (Table 1), we propose a conceptual model for the structural evolution of BFZ300 (Fig. 13). The fault's finite strain results from several slip episodes mediated by multiple events of fluid ingress and fluid–rock interaction. A first constraint provided by our study is that the analysis of the bulk chemical composition of the fluids that cyclically ingressed the fault suggests the likely presence of several batches of fluids of varying salinity and composition.

The embrittlement of the Olkiluoto metamorphic basement (time t_1 in Fig. 13a, b) represents the initial stage of the deformational history of BFZ300, when conditions for brittle dilation and fracturing of the Paleoproterozoic base-
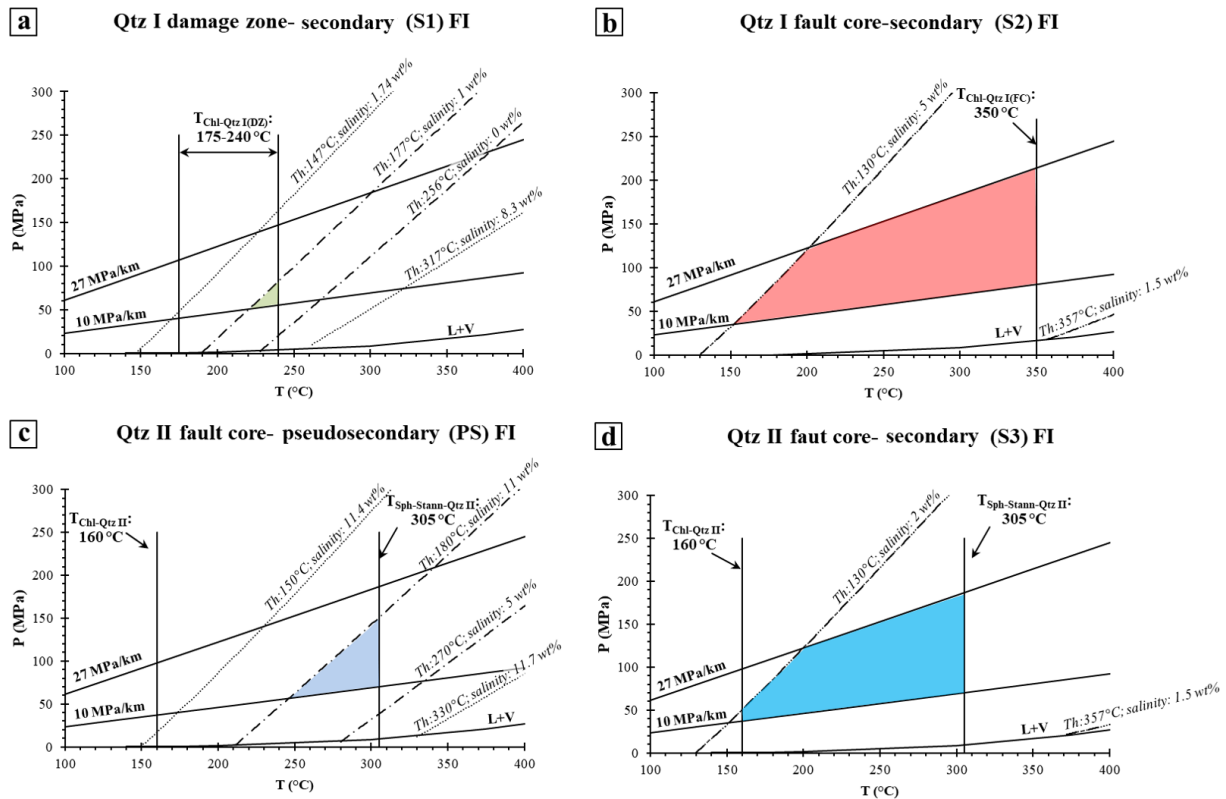
Figure 12. P–T diagrams showing the ranges of P–T trapping conditions of the analysed fluid inclusions: **(a)** secondary inclusions in Qtz I from the fault damage zone; **(b)** secondary inclusions from Qtz I in the fault core; **(c)** pseudosecondary inclusions trapped in Qtz II in the fault core; and **(d)** secondary inclusions in the Qtz II. Thin dashed lines indicate maximum and minimum isochores of FIAs in each structural domain. The coloured areas identify the probable P–T trapping ranges defined by (i) the slope and position of the fluid inclusion isochores as determined by the most representative salinity and homogenization temperature range (see the Supplement for details); (ii) mineral pair geothermometry and (iii) hydrostatic and lithostatic fluid pressures computed assuming a regional geothermal gradient of ca. $40\,°C\,km^{-1}$ (assuming retrograde conditions of 4 kbar and $650\,°C$; from Kärki and Paulamäki, 2006). The liquid–vapour equilibrium curve for the H_2O–NaCl modelled fluid is also indicated.

ment were first met in a transient fashion. We propose that brittle failure under still ductile environmental conditions was caused by transiently elevated P_f ($> 210\,MPa$), as also demonstrated by field evidence of hydrofracturing (pure tensional en echelon veins at the BDTZ depth). Hydrofracturing of the host basement is also indicated by the emplacement of Qtz I veins within the diffuse network of joints and conjugate hybrid–shear fractures of the damage zone (Figs. 13a, 3a, b). These brittle features are quite broadly distributed, suggesting an initial volumetrically diffuse strain distribution. Their formation caused the overall mechanical weakening of the host-rock volume, which in turn facilitated later strain localization. Brittle structures formed during this stage are discordant to the ENE–WSW-striking metamorphic foliation (Fig. 1b), which they cut at a high angle (Fig. 13a). Conditions for tensional and hybrid failure require low differential stress, i.e. $\sigma_1 - \sigma_3 \leq 4T$, where T is the tensional strength of the rock. Opening of fractures caused a stress drop, sudden increase in permeability, fluid venting, and inhibited further build-up of P_f. Dilatant fractures were partially infilled by

Qtz I, which precipitated from a first fluid with inferred low salinity (in the range between 1 wt % NaCl$_{eq}$ and 5 wt % Na-Cl$_{eq}$). Precipitation of Qtz I and formation of veins within these fractures caused hardening of the system. The progressive recovery of shear stresses altered the overall background stress conditions such that failure, after causing initial pure dilation, was later accommodated by hybrid extensional and, eventually, by shear fracturing (Fig. 13b), thus forming laterally continuous and interconnected shear fractures associated with breccia pockets and cataclasites (Fig. 3d, g, i). Conjugate shear fractures connected the previously formed extensional fractures through fracture coalescence (e.g. Griffith, 1920; Sibson, 1996; Fig. 13a). At the microscale this is demonstrated by the elongated–blocky texture of Qtz I crystals from the damage zone (Figs. 4c and 5a), where crystals grew at a high angle to the vein boundaries (thus suggesting initial near-orthogonal dilation) that are physically connected by cataclastic shear bands to form a fault-fracture mesh (e.g. Sibson, 1996). Cataclastic bands formed at the expense of the migmatitic host rock are enriched in authi-

Figure 13. Conceptual model of the temporal and mechanical evolution of the BFZ300 fault zone (see text for more details). Grey lines: traces of metamorphic foliation. Black lines: fractures related to the BFZ300 structural development. **(a)** Initial embrittlement of the migmatitic basement occurred by fracture coalescence (red line) under **(b)** initial lower differential stress conditions and high fluid pressure, followed by a transient increase in differential stress. A first generation of quartz veins (Qtz I) precipitated inside the diffuse network of joints and hybrid–shear fractures which formed during this first deformation stage. **(c)** Progressive strain localization and fluid channelling within the fault core occurred by **(d)** episodically renewed fluid pressure build-up driven by cycles of brittle and ductile deformation. **(e–g)** Progressive exhumation and cooling of the fault system occurred concomitant with several brittle reactivation episodes of the fault zone under hybrid conditions and fluid pressure lower than during the previous deformational stages. Lastly, a second generation of quartz veins (Qtz II) was emplaced, mainly along the principal slip boundaries of the fault core, following the Qtz I vein as shown by **(h)** the strength profile across the fault architecture, which suggests lower tensile strength values (and hence higher reactivation potential) along the Qtz I vein and host-rock walls.

genic, synkinematic sericite, likely due to the interaction between K feldspar and fluids circulating in the dilatant fault zone (Fig. 4b). Shear fractures thus deformed the migmatitic host rock to connect dilatant and mostly Qtz-I-filled tension gashes during a continuum of deformation. The conjugate shear fractures ascribable to this stage invariably define tight acute angles (Figs. 2b, 3a), which we take as further evidence

of overall low differential stress conditions at the time of failure (Fig. 13b).

In synthesis, Qtz I veins from the damage zone are interpreted as the expression of the earliest stage of fault nucleation, before strain localization affected a progressively narrower rock volume to eventually form the main fault core. Indeed, the mesoscale and microscale features observed in the

damage zone Qtz I, lacking the pervasive crystal–plastic deformation that otherwise occurred in the fault core Qtz I, are used to document the initial stage of embrittlement. Based on geometric, kinematic, and deformation style characteristics, we tentatively assign this deformation episode to Stage 1 by Mattila and Viola (2014, their Fig. 18), i.e. to a discrete brittle episode considered the expression of the earliest onset of brittle conditions in southwestern Finland ca. 1.75 Ga, under overall NW–SE to NNW–SSE transpressive conditions.

Further deformation of the BFZ300 (time t_2 in Fig. 13c) occurred by progressive inward strain localization and narrowing of the actively deforming volume of the deformation zone (from a wide damage zone to a narrow fault core). The early BFZ300 core, consisting of the main Qtz I vein, is interpreted as having formed at this stage within an overall dextral strike–slip kinematic framework. Emplacement of the Qtz I vein in the core represents the last pulse of this brittle deformational episode (Fig. 13b). Major fluid venting was likely associated with it such that the system, once brittle failure in the core had occurred by hydrofracturing, moved back to a more diffuse deformation style typical of the still prevailing ductile conditions. Microscopic evidence of crystal–plastic deformation and dynamic recrystallization (Fig. 6a, b; Table 1) overprinting the early brittle structures of Qtz I in the fault core supports slow strain rate conditions during deformation. However, this ductile background deformation was punctuated by renewed and cyclically transient embrittlement as documented by healed fractures shown by trails of secondary fluid inclusions cutting across both the ductile fabrics and the earlier brittle deformational features (Figs. 6c, S2a, b). EBSD analysis of the new grains documented along healed microcracks also suggests that they likely nucleated from fluids circulating in the early fractures before being later deformed in the low-temperature plasticity regime. Thus, we show that at the BDTZ "neocrystallization" by nucleation and growth in fractured fragments and dynamic recrystallization (typically by bulging and subgrain rotation) coexist and compete in the overall microstructural evolution of quartz (e.g. Kjøll et al., 2015). Repeated fluid ingress and related deformation would, in addition, have also caused some of the post-entrapment equilibration of the FI, as discussed above.

Mattila and Viola (2014) describe a second brittle stage (referred to as Stage 2, their Fig. 18) during which a ca. N–S to NNE–SSW-oriented episode of transpressional deformation affected southwestern Finland. Geometric and temporal relationships between structures of Stage 1 and 2 (see also Viola et al., 2009) were used to infer a clockwise rotation of the horizontal compression direction from NW–SE (Stage 1) to NNE–SSW (Stage 2). Consistent with the kinematic framework of Stage 2, we propose here that during progressive regional exhumation and cooling to entirely brittle conditions, the BFZ300 deformation continued through a further, distinct deformation phase (t_3 in Fig. 13e). This stage accommodated the selective reactivation of the BFZ300 core, with

renewed dilation due to the rotated σ_1 during Stage 2 acting subparallel to the strike of the Qtz I vein in the BFZ300 core. Localized dilation in a still fluid-rich system allowed for the emplacement of the Qtz II vein (Fig. 13e). Our estimations indicate peak conditions of P_f 140 MPa and $T \approx 305\,°C$. The BFZ300 core was reactivated by an intermediate-salinity fluid (in the range between 6 wt % NaCleq and 11 wt % NaCleq) under overall hybrid conditions (Fig. 13f), as suggested by the irregular thickness and curved geometry of the Qtz II vein therein and by the synkinematic chlorite crystals that are stretched orthogonally to the vein boundaries (Fig. 3h). The Qtz II vein invariably localized along at the contact between Qtz I and the host rock (Figs. 3f, 13e), suggesting selective reactivation along the pre-existing principal slip zones, which represented the weakest part of the fault (Fig. 13h). Evidence for mesoscale hybrid fracturing and our P_f estimates (Fig. 12) suggest that P_f was lower than that of the earlier deformation stages during Qtz I emplacement.

BFZ300 underwent one or more events of brittle fracturing and induration (Fig. 13g), as suggested by the CL imaging of Qtz II crystals (Fig. 7c). The fluid pressure peak value for this structural stage is ca. 180 MPa.

A possible, very late reactivation stage of unknown age is also documented by the secondary chlorite associated with Qtz I in the damage zone (Fig. 5a, d). Also, the stylolitic seams striking parallel to the BFZ300 fault zone suggest compression oriented ca. E–W, i.e. subparallel to the inferred Sveconorwegian main shortening direction (e.g. Viola et al., 2011). The sphalerite–stannite mineral pairs arranged along these structures were possibly concentrated through pressure solution during this deformational stage.

Skyttä and Torvela (2018) proposed that the BFZ300 is a brittle structure localized onto a zone of incomplete structural transposition inherited from the earlier ductile history of the Olkiluoto basement. However, in our mesoscale and microstructural analysis we did not find evidence of any ductile precursor, and we note that BFZ300 cuts the ductile structural grain at a high angle, which excludes any reactivation of precursor ductile fabrics.

5.3 Implications for seismic deformation at the base of the BDTZ

This study demonstrates the role of overpressured fluids in strain localization during the incipient stages of fault nucleation and subsequent reactivation(s) at the BDTZ. The maximum estimated fluid pressure and fluid temperature conditions derived in this study (peak conditions of 210 MPa and 350 °C) are indeed realistic for the base of the seismogenic zone in the continental lithosphere (e.g. Scholz, 1990, and references therein) where the brittle–ductile transition for quartz occurs.

Mechanical models of long-term deformation (Rolandone and Jaupart, 2002) propose that deformation at the brittle–ductile transition can be reasonably described as mostly ac-

commodated by intermittent and concomitant coseismic slip and ductile flow. Hydrofracturing, as documented in this study by the Qtz I and II veins, is possibly related in that context to seismic failure. Faults accommodating hydrofracturing are indeed commonly interpreted as seismogenic (e.g. Sibson, 1992a; Cox, 1995), particularly at depth.

Our study confirms this view because BFZ300 contains not only brittle fault rocks overprinting and overprinted by veins, but also clear-cut evidence of mutually overprinting brittle and ductile deformation (Fig. 6). In light of the field observations discussed and the constraints derived, we suggest that BFZ300 behaved in a seismic way at least during the emplacement of the principal Qtz I and Qtz II veins. In this perspective, two possible scenarios can be considered to explain the genetic relationships between BFZ300 and a possible seismic behaviour of the crust during the Svecofennian orogeny. In a first scenario, the quartz veins of the fault core would represent the result of coseismic rupture during the mainshocks of a fully developed seismic cycle. Pore pressure fluctuations caused the repeated transient embrittlement of the rock mass, which was otherwise under overall ductile conditions. The documented brittle–ductile cycles are thus the expression of coseismic fracturing and aseismic creep between the individual shocks, as shown by viscous deformation overprinting the brittle features, guided by the residual differential stress.

A second possibility is that faulting occurred in the absence of a well-defined sequence of mainshocks and aftershocks. As in the case of man-induced earthquakes triggered by high-pressure fluids during injection of fluids (e.g. Healy et al., 1968), whereby deformation is typically accommodated by diffuse swarms of low-magnitude seismicity rather than well-defined mainshock–aftershock sequences (Cox, 2016), we propose that BFZ300 might have localized strain by diffuse veining with crack-and-seal textures (Cox, 2016). Breccias and cataclasites (Figs. 3, 8) mutually overprinting with veins show that failure and veining were indeed broadly coeval (e.g. Cox, 1995, 2016). Healing in fluid-rich environments can occur over short periods of time (days to months) when compared with the recurrence time of large earthquakes (10–100 years) (Olsen et al., 1998; Tenthorey and Cox, 2006). Therefore, the documented repeated switches between brittle and ductile deformations would then be steered by transient episodes of fluid overpressuring but in this case would express the accommodation of swarms of minor background earthquakes within overall ductile conditions.

Microstructures of fault rocks exhumed from the brittle–ductile transition in other geological settings are mostly in agreement with our hypotheses of seismic deformation. Transient and short-term high-stress deformation followed by phases of stress relaxation, which is prevalently characterized by recovery and recrystallization processes, has been documented by several authors in deformed quartz (Trep-

mann and Stöckhert, 2003, 2013; Trepmann et al., 2007, 2017; Bestmann et al., 2012).

6 Conclusions

This study shows that a multi-scale and multi-technique approach leading to the generation of independent constraints offers the potential to reconstruct in detail the evolutionary history of fault zones that have experienced multiple events of reactivation triggered by fluid overpressure and in which intense fluid–rock re-equilibration processes have taken place. We document the localized, initial embrittlement of the Paleoproterozoic basement of southwestern Finland at the BDTZ, which occurred by brittle failure under overall ductile conditions in response to transiently high fluid pressure and temperature (peak conditions: $P_f > 210 \, \text{MPa}$; $T \sim 350 \, ^\circ\text{C}$). Our results further constrain the importance of cyclic seismicity and fluids in the fragmentation of Precambrian cratons when deformed at the BDTZ, something that is not yet that well understood for the Fennoscandian Shield. Our study, moreover, provides potentially important inputs to many modern geological applications, including site characterization of deep geological disposal facilities for spent nuclear fuel. Results from the detailed geological characterization of faults at the Olkiluoto site can thus be used for continuously updating the geological site description and yield further constraints on the mechanics of faulting at the BDTZ.

Review statement. This paper was edited by Bernhard Grasemann and reviewed by Olivier Vanderhaeghe and two anonymous referees.

References

Aaltonen, I., Lahti, M., Engström, J., Mattila, J., Paananen, M., Paulamäki, S., Gehör, S., Kärki, A., Ahokas, T., Torvela, T., and Front, K.: Geological model of the Olkiluoto site, Version 2.0, Posiva Working Report 2010-70, Posiva Oy, Eurajoki, 2010.

Aaltonen, I., Engström, J., Front, K., Gehör, S., Kosunen, P., and Kärki, A.: Geology of Olkiluoto, Posiva Working Report 2016-16, Posiva Oy, Eurajoki, 2016.

Andersen, T., Austrheim, H., and Burke, E. A. J.: Fluid inclusions in granulites and eclogites from the Bergen Arcs, Caledonides of W. Norway, Mineral. Mag., 54, 145–158, 1990.

Ault, A. K. and Selverstone, J.: Microtextural constraints on the interplay between fluid-rock reactions and deformation, Contrib. Mineral. Petr., 156, 501–515, https://doi.org/10.1007/s00410-008-0298-9, 2008.

Bakker, R.: Re-Equilibration Processes in Fluid Inclusion Assemblages, Minerals, 7, 1–19, https://doi.org/10.3390/min7070117, 2017.

Bakker, R. J. and Jansen, J. B. H.: Preferential water leakage from fluid inclusions by means of mobile dislocations, Nature, 345, 58–60, https://doi.org/10.1038/345058a0, 1990.

Bakker, R. J. and Jansen, J. B. H.: Experimental post-entrapment water loss from synthetic CO_2-H_2O inclusions in natural quartz, Geochim. Cosmochim. Ac., 55, 2215–2230, https://doi.org/10.1016/0016-7037(91)90098-P, 1991.

Bakker, R. J. and Jansen, J. B. H.: A mechanism for preferential H_2O leakage from fluid inclusions in quartz, based on TEM observations, Contrib. Mineral. Petr., 116, 7–20, https://doi.org/10.1007/BF00310686, 1994.

Basson, I. J. and Viola, G.: Passive kimberlite intrusion into actively dilating dyke-fracture arrays: Evidence from fibrous calcite veins and extensional fracture cleavage, Lithos, 76, 283–297, https://doi.org/10.1016/j.lithos.2004.03.041, 2004.

Bestmann, M., Pennacchioni, G., Nielsen, S., Göken, M., and de Wall, H.: Deformation and ultrafine dynamic recrystallization of quartz in pseudotachylyte-bearing brittle faults: A matter of a few seconds, J. Struct. Geol., 38, 21–38, https://doi.org/10.1016/j.jsg.2011.10.001, 2012.

Bodnar, R. J.: The origin of fluid inclusions, in: Fluid inclusions: Analysis and Interpretation, edited by: Samson, I., Anderson, A., and Marshall, D., Vancouver, Canada: Mineralogical Association of Canada, 11–18, 2003a.

Bodnar, R. J.: Re-equilibration of fluid inclusions, in: Fluid inclusions: Analysis and Interpretation, edited by: Samson, I., Anderson, A., and Marshall, D., Vancouver, Canada: Mineralogical Association of Canada, 213–230, 2003b.

Boiron, M., Cathelineau, M., Banks, D. A., Fourcade, S., and Vallance, J.: Mixing of metamorphic and surficial fluids during the uplift of the Hercynian upper crust: consequences for gold deposition, Chem. Geol., 194, 119–141, 2003.

Bons, P. D.: The formation of large quartz veins by rapid ascent of fluids in mobile hydrofractures, Tectonophysics, 336, 1–17, https://doi.org/10.1016/S0040-1951(01)00090-7, 2001.

Bons, P. D., Elburg, M. A., and Gomez-Rivas, E.: A review of the formation of tectonic veins and their microstructures, J. Struct. Geol., 43, 33–62, https://doi.org/10.1016/j.jsg.2012.07.005, 2012.

Bourdelle, F. and Cathelineau, M.: Low-temperature chlorite geothermometry: a graphical representation based on a a T–R2+–Si diagram, Eur. J. Mineral., 27, 617–626, https://doi.org/10.1127/ejm/2015/0027-2467, 2015.

Caine, J. S., Evans, J. P., and Forster, C. B.: Fault zone architechture and permeability structure, Geology, 24, 1025–1028, https://doi.org/10.1130/0091-7613(1996)024<1025, 1996.

Compton, K. E., Kirkpatrick, J. D., and Holk, G. J.: Cyclical shear fracture and viscous flow during transitional ductile-brittle deformation in the Saddlebag Lake Shear Zone, California, Tectonophysics, 708, 1–14, https://doi.org/10.1016/j.tecto.2017.04.006, 2017.

Cox, S., Knackstedt, M., and Braun, J.: Principles of structural control on permeability and fluid flow in hydrothermal systems, Rev. Econ. Geol., 14, 1–24, 2001.

Cox, S. F.: Faulting processes at high fluid pressures: An example of fault valve behavior from the Wattle Gully Fault, Victoria, Australia, J. Geophys. Res., 100, 841–859, 1995.

Cox, S. F.: Coupling between deformation, fluid pressures and fluid flow in ore-producing hydrothermal environments, Econ. Geol., 100th Anniversary Volume, 39–75, 2005.

Cox, S. F.: Injection-driven swarm seismicity and permeability enhancement: Implications for the dynamics of hydrothermal ore systems in high fluid-flux, overpressured faulting regimes – An invited paper, Econ. Geol., 111, 559–587, https://doi.org/10.2113/econgeo.111.3.559, 2016.

Crider, J. G. and Peacock, D. C. P.: Initiation of brittle faults in the upper crust: A review of field observations, J. Struct. Geol., 26, 691–707, https://doi.org/10.1016/j.jsg.2003.07.007, 2004.

De Paola, N., Collettini, C., Trippetta, F., Barchi, M. R., and Minelli, G.: A mechanical model for complex fault patterns induced by evaporite dehydration and cyclic changes in fluid pressure, J. Struct. Geol., 29, 1573–1584, https://doi.org/10.1016/j.jsg.2007.07.015, 2007.

Derez, T., Pennock, G., Drury, M., and Sintubin, M.: Low-temperature intracrystalline deformation microstructures in quartz, J. Struct. Geol., 71, 3–23, https://doi.org/10.1016/j.jsg.2014.07.015, 2015.

Diamond, L. W.: Introduction to gas-bearing, aqueous fluid inclusions, in: Fluid Inclusions: Analysis and Interpretation, edited by: Samson, I., Anderson, A., and Marshall, D., 363–372, 2003.

Diamond, L. W., Tarantola, A., and Stünitz, H.: Modification of fluid inclusions in quartz by deviatoric stress. II: Experimentally induced changes in inclusion volume and composition, Contrib. Mineral. Petr., 160, 845–864, https://doi.org/10.1007/s00410-010-0510-6, 2010.

Dubessy, J., Buschaert, S., Lamb, W., Pironon, J., and Thiéry, R.: Methane-bearing aqueous fluid inclusions: Raman analysis, thermodynamic modelling and application to petroleum basins,

Chem. Geol., 173, 193–205, https://doi.org/10.1016/S0009-2541(00)00275-8, 2001.

Ehlers, C., Lindroos, A., and Selonen, O.: The late Svecofennian granite-migmatite zone of southern Finland-a belt of transpressive deformation and granite emplacement, Precambrian Res., 64, 295–309, 1993.

Fall, A., Donald, R., and Bodnar, R. J.: The effect of fluid inclusion size on determination of homogenization temperature and density of liquid-rich aqueous inclusions, Am. Mineral., 94, 1569–1579, https://doi.org/10.2138/am.2009.3186, 2009.

Famin, V., Hébert, R., Philippot, P., and Jolivet, L.: Evolution of hydrothermal regime along a crustal shear zone, Tinos Island, Greece, Tectonics, 23, TC5004, https://doi.org/10.1029/2003TC001509, 2004.

Famin, V., Hébert, R., Phillippot, P., and Jolivet, L.: Ion probe and fluid inclusion evidence for co-seismic fluid infiltration in a crustal detachment, Contrib. Mineral Petrol., 150, 354–367, https://doi.org/10.1007/s00410-005-0031-x, 2005.

Garofalo, P. S.: Mass transfer during gold precipitation within a vertically extensive vein network (Sigma deposit – Abitibi greenstone belt – Canada). Part II. Mass transfer calculations, Eur. J. Mineral., 16, 761–776, https://doi.org/10.1127/0935-1221/2004/0016-0761, 2004.

Garofalo, P. S., Matthäi, S. K., and Heinrich, C. A.: Three-dimensional geometry, ore distribution, and time-integrated mass transfer through the quartz-tourmaline-gold vein network of the Sigma deposit (Abitibi belt – Canada), Geofluids, 2, 217–232, 2002.

Garofalo, P. S., Fricker, M. B., Günther, D., Bersani, D., and Lottici, P.: Physical-chemical properties and metal budget of Au-transporting hydrothermal fluids in orogenic deposits, Geol. Soc. London, Spec. Publ., 402, 71–102, https://doi.org/10.1144/SP402.8, 2014.

Goddard, J. V. and Evans, J. P.: Chemical changes and fluid-rock interaction in faults of crystalline thrust sheets, northwestern Wyoming, USA, J. Struct. Geol., 17, 533–547, https://doi.org/10.1016/0191-8141(94)00068-B, 1995.

Goldstein, R. H.: Petrographic analysis of fluid inclusions, in: Fluid inclusions: Analysis and Interpretation: Mineralogical Association of Canada, edited by: Samson, I., Anderson, A., and Marshall, D., 1–45, 2003.

Goldstein, R. H. and Reynolds, T. J.: Fluid inclusion microthermometry, in: Systematics of fluid inclusions in diagenetic minerals – SEPM Short Course 31. SEPM (Society for Sedimentary Geology), edited by: Goldstein, R. H., Tulsa, Oklahoma, 87–121, 1994.

Gorbatschev, R. and Bogdanova, S.: Frontiers in the Baltic Shield, Precambrian Res., 64, 3–21, https://doi.org/10.1016/0301-9268(93)90066-B, 1993.

Griffith, A. A.: The Phenomena of Rupture and Flow in Solids, Philos. T. Roy. Soc. Lond., 221, 163–198, 1920.

Guermani, A. and Pennacchioni, G.: Brittle precursors of plastic deformation in a granite: An example from the Mont Blanc massif (Helvetic, western Alps), J. Struct. Geol., 20, 135–148, https://doi.org/10.1016/S0191-8141(97)00080-1, 1998.

Healy, J. H., Rubey, W. W., Griggs, D. T., and Raleigh, C. B.: The Denver Earthquakes. Disposal of waste fluids by injection into a deep well has riggered earthquakes near Denver, Colorado, Science, 161, 1301–1310, 1968.

Heinrich, C. A., Andrew, A. S., and Knill, M. D.: Regional metamorphism and ore formation: Evidence from stable isotopes and other fluid tracers, Rev. Econ. Geol., 11, 97–117, 2000.

Hey, M. H.: A new review of the chlorites, Mineral. Mag. J. M. Soc., 224, 277–292, https://doi.org/10.1180/minmag.1954.030.224.01, 1954.

Hudson, J. A. and Cosgrove, J.: Geological History and Its Impact on the Rock Mechanics Properties of the Olkiluoto Site, Posiva Working Report 2006, Posiva Oy, Eurajoki, 2006.

Invernizzi, C., Vityk, M., Cello, G., and Bodnar, R.: Fluid inclusions in high pressure/low temperature rocks from the Calabrian Arc (Southern Italy): the burial and exhumation history of the subduction-related Diamante-Terranova unit, J. Metamorph. Geol., 16, 2, 247–258, 1998.

Jaques, L. and Pascal, C.: Full paleostress tensor reconstruction using quartz veins of Panasqueira Mine, central Portugal; part I: Paleopressure determination, J. Struct. Geol., 102, 58–74, https://doi.org/10.1016/j.jsg.2017.07.006, 2017.

Kaduri, M., Gratier, J. P., Renard, F., Çakir, Z., and Lasserre, C.: The implications of fault zone transformation on aseismic creep: Example of the North Anatolian Fault, Turkey, J. Geophys. Res.-Sol. Ea., 122, 4208–4236, https://doi.org/10.1002/2016JB013803, 2017.

Kärki, A. and Paulamäki, S.: Petrology of Olkiluoto, Posiva Report 2006-02, Posiva Oy, Eurajoki, 2006.

Kerrich, R.: Some effects of tectonic recrystallisation on fluid inclusions in vein quartz, Contrib. Mineral. Petr., 59, 195–202, https://doi.org/10.1007/BF00371308, 1976.

Kjøll, H. J., Viola, G., Menegon, L., and Sørensen, B. E.: Brittle-viscous deformation of vein quartz under fluid-rich lower greenschist facies conditions, Solid Earth, 6, 681–699, https://doi.org/10.5194/se-6-681-2015, 2015.

Kohlstedt, D. L., Evans, B., and Mackwell, S. J.: Strength of the lithosphere: Constraints imposed by laboratory experiments, J. Geophys. Res., 100, 587–602, 1995.

Korja, A., Heikkinen, P., and Aaro, S.: Crustal structure of the northern Baltic Sea palaeorift, Tectonophysics, 331, 341–358, https://doi.org/10.1016/S0040-1951(00)00290-0, 2001.

Kukkonen, I. T. and Lauri, L. S.: Modelling the thermal evolution of a collisional Precambrian orogen: High heat production migmatitic granites of southern Finland, Precambrian Res., 168, 233–246, https://doi.org/10.1016/j.precamres.2008.10.004, 2009.

Lahtinen, R., Korja, A., and Nironen, M: Palaeoproterozoic tectonic evolution, in: Precambrian Geology of Finland: Key to the Evolution of the Fennoscandian Shield, edited by: Lehtinen, M., Nurmi, P. A., and Rämö, O. T., Developments in Precambrian Geology, 2005.

Mancktelow, N. S. and Pennacchioni, G.: The influence of grain boundary fluids on the microstructure of quartz-feldspar mylonites, J. Struct. Geol., 26, 47–69, https://doi.org/10.1016/S0191-8141(03)00081-6, 2004.

Mancktelow, N. S. and Pennacchioni, G.: The control of precursor brittle fracture and fluid-rock interaction on the development of single and paired ductile shear zones, J. Struct. Geol., 27, 645–661, https://doi.org/10.1016/j.jsg.2004.12.001, 2005.

Mattila, J. and Viola, G.: New constraints on 1.7 Gyr of brittle tectonic evolution in southwestern Finland derived from a structural study at the site of a potential nuclear waste

repository (Olkiluoto Island), J. Struct. Geol., 67, 50–74, https://doi.org/10.1016/j.jsg.2014.07.003, 2014.

Menegon, L., Pennacchioni G., Malaspina N., Harris K., and Wood E.: Earthquakes as Precursors of Ductile Shear Zones in the Dry and Strong Lower Crust, Geochem. Geophy. Geosy., 18, 4356–4374, https://doi.org/10.1002/2015GC006010, 2017.

Menegon, L., Marchesini, B., Prando, F., Garofalo, P. S., Viola, G., Anderson, M., and Mattila, J.: Brittle-viscous oscillations and different slip behaviours in a conjugate set of strike-slip faults, Geophys. Res., Abstracts Vol. 20, EGU2018-14799, 2018.

Miller, S. A.: The Role of Fluids in Tectonic and Earthquake Processes, edited by: Dmowska, R., Elsevier, 2013.

Mittempergher, S., Dallai, L., Pennacchioni, G., Renard, F., and Di Toro, G.: Origin of hydrous fluids at seismogenic depth: Constraints from natural and experimental fault rocks, Earth Planet. Sc. Lett., 385, 97–109, https://doi.org/10.1016/j.epsl.2013.10.027, 2014.

Moritz, R., Ghazban, F., and Singer, B. S.: Eocene Gold Ore Formation at Muteh, Sanandaj-Sirjan Tectonic Zone, Western Iran: A Result of Late-Stage Extension and Exhumation of Metamorphic Basement Rocks within the Zagros Orogen, Econ. Geol., 101, 1–28, 2006.

Morrison, J.: Meteoric water-rock interaction in the lower plate of the Whipple Mountain metamorphic core complex, California, J. Metamorph. Geol., 12, 827–840, 1994.

Morrison, J. and Anderson, J. L.: Footwall Refrigeration Along a Detachment Fault: Implications for the Thermal Evolution of Core Complexes, Science, 279, 63–67, 1998.

Mulch, A., Teyssier, C., Cosca, M. A., Vanderhaeghe, O., and Vennemann, T. W.: Reconstructing paleoelevation in eroded orogens, 6, 525–528, https://doi.org/10.1130/G20394.1, 2004.

Nekrasov, I. J., Sorokin, V. I., and Osadchii, E. G.: Fe and Zn partitioning between stannite and sphalerite and its application in geothermometry, Phys. Chem. Earth, 11, 739–742, https://doi.org/10.1016/0079-1946(79)90069-7, 1979.

Oliver, N. H. S. and Bons P. D.: Mechanisms of fluid flow and fluid–rock interaction in fossil metamorphic hydrothermal systems inferred from vein–wallrock patterns, geometry and microstructure, Geofluids, 1, 137–162, 2001.

Olsen, M. P., Scholz, C. H., and Léger, A.: Healing and sealing of a simulated fault gouge under hydrothermal conditions: Implications for fault healing, J. Geophys. Res., 103, 7421, https://doi.org/10.1029/97JB03402, 1998.

Pennacchioni, G., Di Toro, G., Brack, P., Menegon, L., and Villa, I. M.: Brittle-ductile-brittle deformation during cooling of tonalite (Adamello, Southern Italian Alps), Tectonophysics, 427, 171–197, https://doi.org/10.1016/j.tecto.2006.05.019, 2006.

Prando, F., Menegon, L., Anderson, M. W., Marchesini, B., Mattila, J., and Viola, G.: Fluid-mediated, brittle-ductile deformation at seismogenic depth: Part 2 – The microstructural record of oscillations of differential stress and fluid pressure in a shear zone in a nuclear waste repository (Olkiluoto Island, Finland), Solid Earth, in preparation, 2019.

Roedder, E.: Fluid Inclusions, Mineralogical Society of America, 1984.

Roedder, E. and Bodnar, R. J.: Geologic determinations from fluid inclusion studies, Annu. Rev. Earth Planet. Sc., 8, 263–301, 1980.

Rolandone, F. and Jaupart, C.: The distributions of slip rate and ductile deformation in a strike-slip shear zone, Geophys. J. Int., 148, 179–192, https://doi.org/10.1046/j.1365-246X.2002.01574.x, 2002.

Rosso, K. M. and Bodnar, R. J.: Microthermometric and Raman spectroscopic detection limits of CO_2 in fluid inclusions and the Raman spectroscopic characterization of CO_2, Geochim. Cosmochim. Ac., 59, 3961–3975, https://doi.org/10.1016/0016-7037(95)94441-H, 1995.

Scheffer, C., Tarantola, A., Vanderhaeghe, O., Rigaudier, T., and Photiades, A.: CO_2 flow during orogenic gravitational collapse: Syntectonic decarbonation and fl uid mixing at the ductile-brittle transition, Chem. Geol., 450, 248–263, https://doi.org/10.1016/j.chemgeo.2016.12.005, 2017a.

Scheffer, C., Tarantola, A., Vanderhaeghe, O., Voudouris, P., Rigaudier, T., Photiades, A., Morin, D., and Alloucherie, A.: The Lavrion Pb-Zn-Fe-Cu-Ag detachment-related district (Attica, Greece): Structural control on hydrothermal flow and element transfer-deposition, Tectonophysics, 717, 607–627, https://doi.org/10.1016/j.tecto.2017.06.029, 2017b.

Selverstone, J., Franz, G., Thomas, S., and Getty, S.: Fluid variability in 2 GPa eclogites as an indicator of fluid behavior during subduction, Contrib. Mineral. Petr., 112, 341–357, 1992.

Selverstone, J., Axen, G. J., and Bartley, J. M: Fluid inclusion constraints on the kinematics of footwall uplift beneath the Brebber Line normal fault, estern Alps, Tectonics, 14, 264–278, 1995.

Shimizu, M. and Shikazono, N.: Iron and zinc partitioning between coexisting stannite and sphalerite: a possible indicator of temperature and sulfur fugacity, Miner. Deposita, 20, 314–320, 1985.

Scholz, C. H.: The Mechanics of Earthquakes and Faulting, Cambridge, Cambridge University Press, 1990.

Sibson, R. H.: Earthquake faulting as a structural process, J. Struct. Geol., 11, 1–14, https://doi.org/10.1016/0191-8141(89)90032-1, 1989.

Sibson, R. H.: Fault-valve behavior and the hydrostatic-lithostatic fluid pressure interface, Earth Sci. Rev., 32, 141–144, https://doi.org/10.1016/0012-8252(92)90019-P, 1992a.

Sibson, R. H.: Implications of fault-valve behaviour for rupture nucleation and recurrence, Tectonophysics, 211, 283–293, 1992b.

Sibson, R. H.: Load-strengthening versus load-weakening faulting, J. Struct. Geol., 15, 123–128, https://doi.org/10.1016/0191-8141(93)90090-W, 1993.

Sibson, R. H.: Structural permeability of fluid-driven fault-fracture meshes, J. Struct. Geol, 18, 1031–1042, https://doi.org/10.1016/0191-8141(96)00032-6, 1996.

Sibson, R. H., Robert, F., and Poulsen, K. H.: High-angle reverse faults, fluid-pressure cycling, and mesothermal gold-quartz deposits, Geology, 16, 551–555, https://doi.org/10.1130/0091-7613(1988)016<0551:HARFFP>2.3.CO;2, 1988.

Siebenaller, L., Boiron, M. C., Vanderhaeghe, O., Hibsch, C., Jessell, M. W., Andre-Mayer, A. S., France-Lanord, C., and Photiades, A.: Fluid record of rock exhumation across the brittle-ductile transition during formation of a Metamorphic Core Complex (Naxos Island, Cyclades, Greece), J. Metamorph. Geol., 31, 313–338, https://doi.org/10.1111/jmg.12023, 2013.

Siebenaller, L., Vanderhaeghe, O., Jessell, M., Boiron, M. C., and Hibsch, C.: Syntectonic fluids redistribution and circulation coupled to quartz recrystallization in the ductile crust

(Naxos Island, Cyclades, Greece), J. Geodyn., 101, 129–141, https://doi.org/10.1016/j.jog.2016.07.001, 2016.

Skyttä, P. and Torvela, T.: Brittle reactivation of ductile precursor structures: The role of incomplete structural transposition at a nuclear waste disposal site, Olkiluoto, Finland, J. Struct. Geol., 116, 253–259, https://doi.org/10.1016/j.jsg.2018.06.009, 2018.

Spruzeniece, L. and Piazolo, S.: Strain localization in brittle-ductile shear zones: fluid-abundant vs. fluid-limited conditions (an example from Wyangala area, Australia), Solid Earth, 6, 881–901, https://doi.org/10.5194/se-6-881-2015, 2015.

Steele-MacInnis, M., Lecumberri-Sanchez, P., and Bodnar, R. J.: HokieFlincs_H2O-NaCl: A Microsoft Excel spreadsheet for interpreting microthermometric data from fluid inclusions based on the PVTX properties of H_2O-NaCl, Comput. Geosci., 49, 334–337, https://doi.org/10.1016/j.cageo.2012.01.022, 2012.

Sterner, S. M. and Bodnar J.: Synthetic fluid inclusions – VII. Re-equilibration of fluid inclusions in quartz during laboratory-simulated metamorphic burial and uplift, J. Metamorph. Geol., 7, 243–260, 1989.

Suominen, V.: The chronostratigraphy of southern Finland, with special reference to Postjotnian and Subjotnian diabases, Bull. Geol. Surv. Finl., 356, 100, 1991.

Tarantola, A., Diamond, L. W., and Stünitz, H.: Modification of fluid inclusions in quartz by deviatoric stress I: Experimentally induced changes in inclusion shapes and microstructures, Contrib. Mineral. Petr., 160, 825–843, https://doi.org/10.1007/s00410-010-0509-z, 2010.

Tchalenko, J. S.: Similarities between Shear Zones of Different Magnitudes, Geol. Soc. Am. Bull., 81, 1625–1640, https://doi.org/10.1130/0016-7606(1970)81[1625:SBSZOD]2.0.CO;2, 1970.

Tenthorey, E. and Cox, S. F.: Cohesive strengthening of fault zones during the interseismic period: An experimental study, J. Geophys. Res.-Sol. Ea., 111, 1–14, https://doi.org/10.1029/2005JB004122, 2006.

Trepmann, C. A. and Stöckhert, B.: Quartz microstructures developed during non-steady state plastic flowat rapidly decaying stress and strain rate, J. Struct. Geol., 25, 2035–2051, https://doi.org/10.1016/S0191-8141(03)00073-7, 2003.

Trepmann, C. A. and Stöckhert, B.: Short-wavelength undulatory extinction in quartz recording coseismic deformation in the middle crust – an experimental study, Solid Earth, 4, 263–276, https://doi.org/10.5194/se-4-263-2013, 2013.

Trepmann, C. A., Stöckhert, B., Dorner, D., Moghadam, R. H., Küster, M., and Röller, K.: Simulating coseismic deformation of quartz in the middle crust and fabric evolution during postseismic stress relaxation – An experimental study, Tectonophysics, 442, 83–104, https://doi.org/10.1016/j.tecto.2007.05.005, 2007.

Trepmann, C. A., Hsu, C., Hentschel, F., Döhler, K., Schneider, C., and Wichmann, V.: Recrystallization of quartz after low-temperature plasticity – The record of stress relaxation below the seismogenic zone, J. Struct. Geol., 95, 77–92, https://doi.org/10.1016/j.jsg.2016.12.004, 2017.

Van Noten, K., Muchez, P., and Sintubin, M.: Stress-state evolution of the brittle upper crust during compressional tectonic inversion as defined by successive quartz vein types (High-Ardenne slate belt, Germany), J. Geol. Soc. London, 168, 407–422, https://doi.org/10.1144/0016-76492010-112.Stress-state, 2011.

Van den Kerkhof, A., Kronz, A., and Simon, K.: Deciphering fluid inclusions in high-grade rocks, Geosci. Front., 5, 683–695, https://doi.org/10.1016/j.gsf.2014.03.005, 2014.

Viola, G., Mancktelow, N. S., and Miller, J. A.: Cyclic frictional-viscous slip oscillations along the base of an advancing nappe complex: Insights into brittle-ductile nappe emplacement mechanisms from the Naukluft Nappe Complex, central Namibia, Tectonics, 25, 1–20, https://doi.org/10.1029/2005TC001939, 2006.

Viola, G., Venvik Ganerød, G., and Wahlgren, C. H.: Unraveling 1.5 Ga of brittle deformation history in the Laxemar-Simpevarp area, southeast Sweden: A contribution to the Swedish site investigation study for the disposal of highly radioactive nuclear waste, Tectonics, 28, 1–29, https://doi.org/10.1029/2009TC002461, 2009.

Viola, G., Mattila, J., Zwingmann, H., Todd, A., and Raven, M.: Structural and K/Ar Illite Geochronological Constraints on the Brittle Deformation History of the Olkiluoto Region, Southwest Finland, Posiva Working Report 2011, Posiva Oy, Eurajoki, 2011.

Viola, G., Scheiber, T., Fredin, O., Zwingmann, H., Margreth, A., and Knies, J.: Deconvoluting complex structural histories archived in brittle fault zones, Nat. Commun., 7, 1–10, https://doi.org/10.1038/ncomms13448, 2016.

Vityk, M. O. and Bodnar, R. J.: Textural evolution of synthetic fluid inclusions in quartz during reequilibration, with applications to tectonic reconstruction, Contrib. Mineral. Petr., 121, 309–323, https://doi.org/10.1007/BF02688246, 1995.

Vityk, M. O. and Bodnar, R. J.: Statistical microthermometry of synthetic fluid inclusions in quartz during decompression reequilibration, Contrib. Mineral. Petr., 132, 149–162, https://doi.org/10.1007/s004100050413, 1998.

Vityk, M. O., Bodnar, R. J., and Schmidt, C. S.: Fluid inclusion as a tectonothermobarometers: Relation between pressure-tempreture history and reequilibration morphology during crystal thickening, Geology, 22, 731–734, https://doi.org/10.1130/0091-7613(1994)022<0731:FIATRB>2.3.CO, 1994.

Wehrens, P., Berger, A., Peters, M., Spillmann, T., and Herwegh, M.: Deformation at the frictional-viscous transition: Evidence for cycles of fluid-assisted embrittlement and ductile deformation in the granitoid crust, Tectonophysics, 693, 66–84, https://doi.org/10.1016/j.tecto.2016.10.022, 2016.

Wilkins, R. W. T. and Barkas, J. P.: Fluid inclusions, Deformation and Recrystallization in Granite Tectonites, Contrib. Mineral. Petrol., 65, 293–299, 1978.

Solid Earth

Open Access

EGU

Supplement of

Fluid-mediated, brittle–ductile deformation at seismogenic depth – Part 1: Fluid record and deformation history of fault veins in a nuclear waste repository (Olkiluoto Island, Finland)

Barbara Marchesini et al.

Correspondence to: Barbara Marchesini (barbara.marchesini2@unibo.it, barbaramarchesini@hotmail.it)
and Giulio Viola (giulio.viola3@unibo.it)

EBSD analysis

Before EBSD analysis, thin sections were chemically polished using colloidal silica. Thin sections were then carbon coated placed in a JEOL 6610 SEM equipped with a Nordlys Nano EBSD detector, at a 70° tilt to the horizontal (Prior et al., 1999). We used 20 kV of accelerating voltage, a working distance of 25 mm and a step size to 2 µm. The acquired EBSD patterns were automatically indexed using AZtec software and processed using CHANNEL 5 software from Oxford Instruments. Raw indexing of the two acquired maps was 96%. EBSD data were presented in the form of Inverse Pole Figure maps oriented with respect to the direction perpendicular to the vein wall (direction X0, vein wall corresponds to direction Y0), and of pole figures (equal area, lower hemisphere) oriented parallel to the Y0-X0 plane. Crystallographic data in the pole figures are plotted as one-point-per-pixel. In the IPF maps, low-angle boundaries (misorientation between 2°and 10°) are shown in cyan, high-angle boundaries (misorientation > 10°) are shown in black, and Dauphinétwin boundaries (misorientation of 60° around the c-axis) are shown in red.

12   **Supplementary Figures:**

13
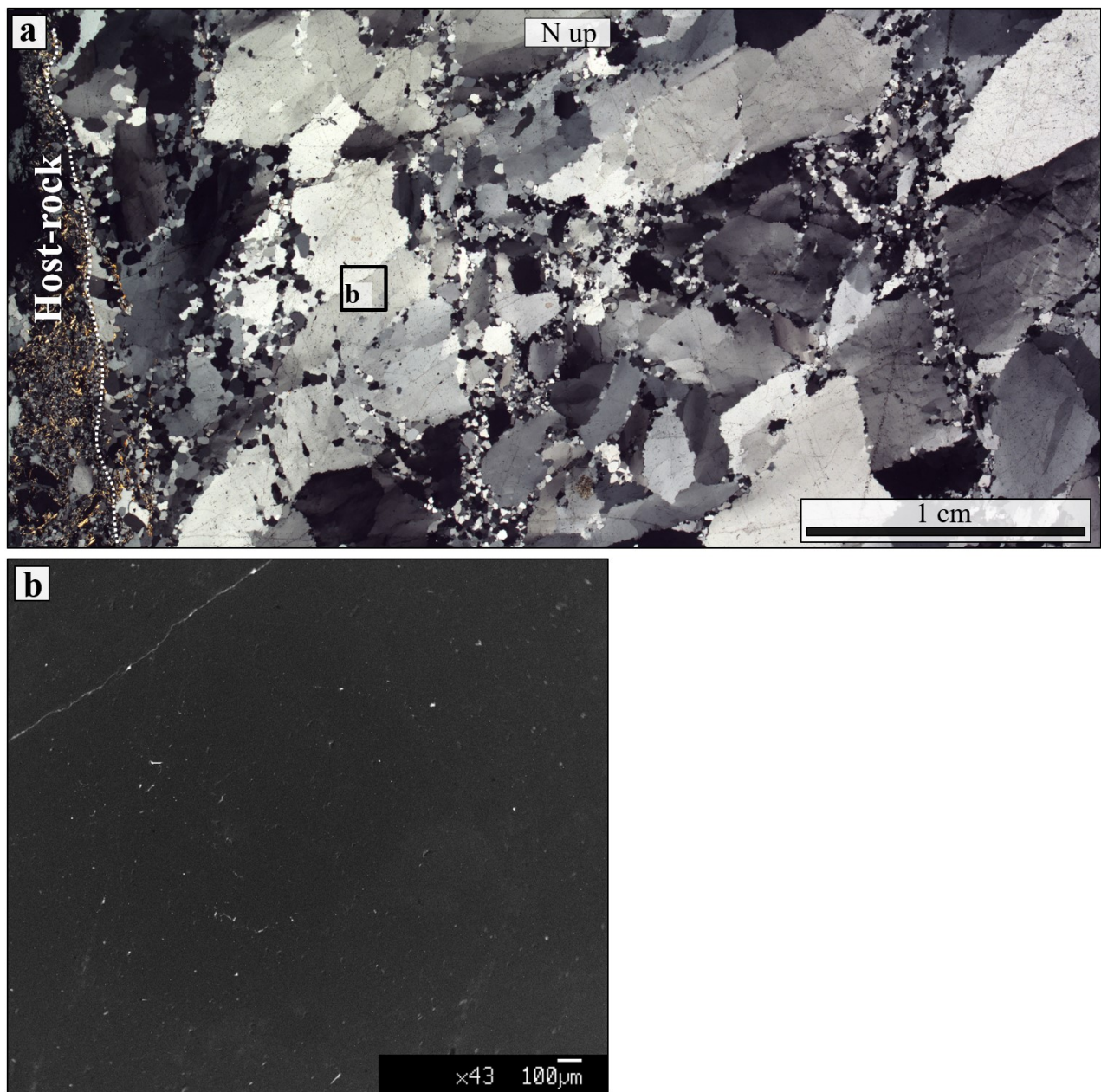
14   **Figure S1**. Stitched photomicrographs of fault core Qtz I where the location of the catodoluminescence imaging is reported. b) Panchromatic

15   cathodoluminescence image of intercrystalline fracture occurring within Qtz I from the fault core, showing homogeneous-dark signal.
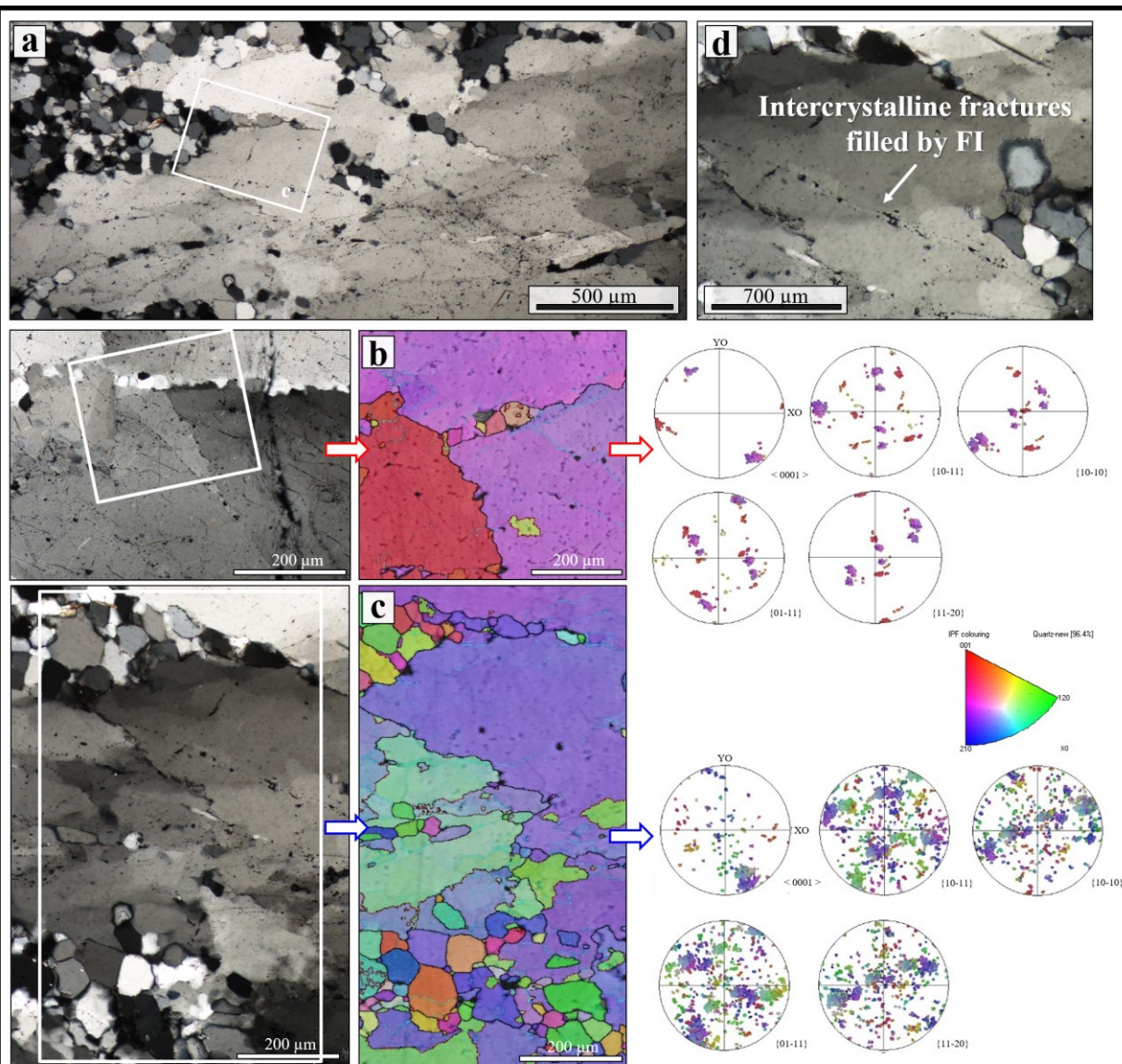
Figure S2. EBSD analysis performed on fault core-Qtz I (sample TPH-120 4). a) Qtz I-fault core microstructures where EBSD map locations b) and c) are also reported. Also at the edge of intercrystalline bands we detected subgrains precursors of recrystallization. d) Intercrystalline bands are also marked by trails of fluid inclusions
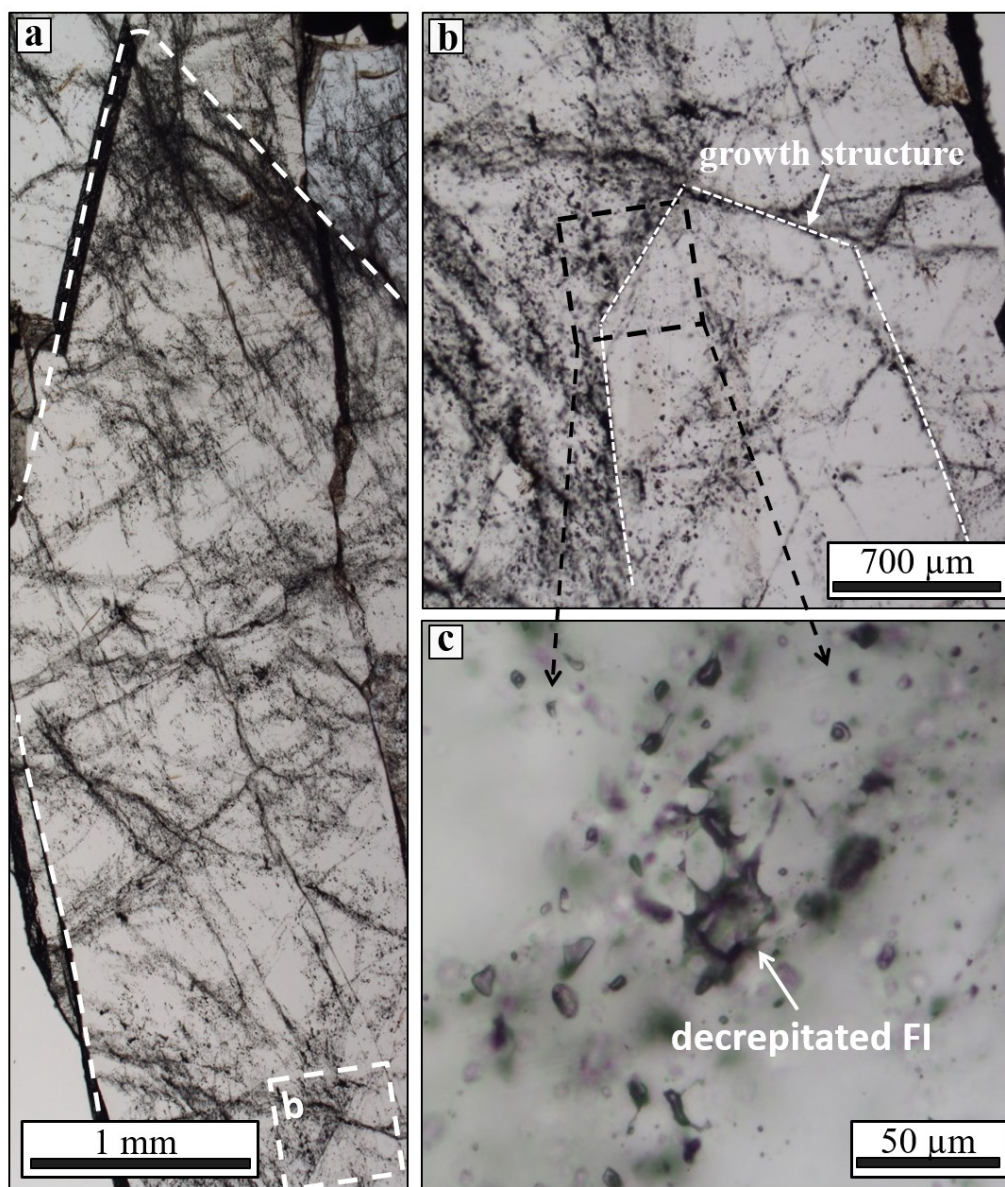
Figure S3. Petrographic relationships between fluid inclusions and Qtz II (sample TPH-120-6). a) Optically continuous, single crystal (highlighted). The white dashed square at the bottom right corner marks a possibly primary FIA entrapped during crystal growth. b) Enlargement of the growth structure. c) Enlargement of a portion of the primary growth zone, showing a re-equilibrated cluster of fluid inclusions along the primary growth zone. Note that the largest fluid inclusion is decrepitated and is surrounded by planes of tiny and irregular FIs (satellite inclusions). In the light of this structures, microthermometric estimations from this thype of assemblages are excluded.

28
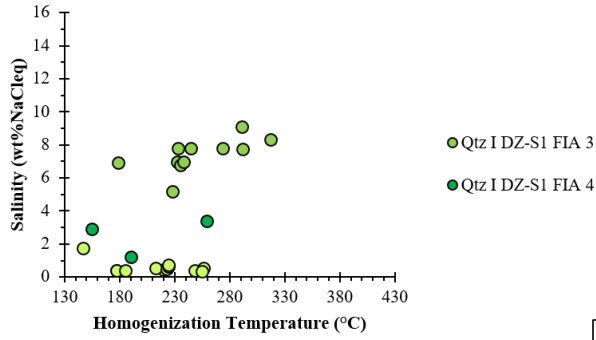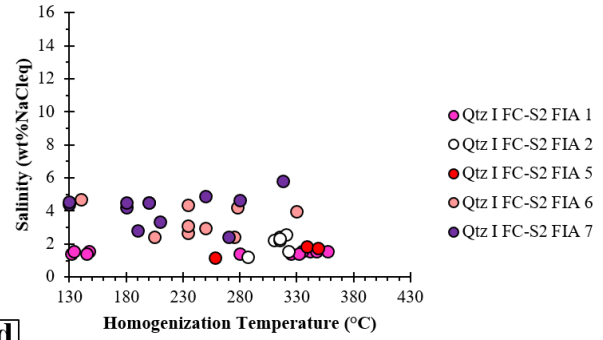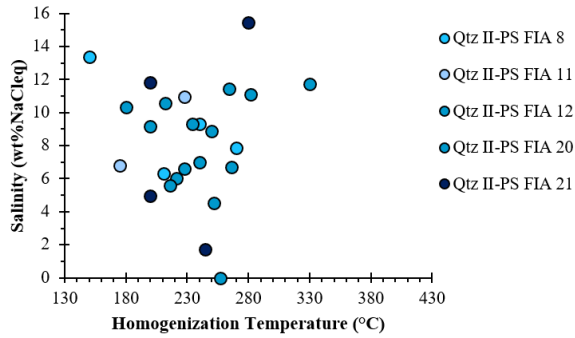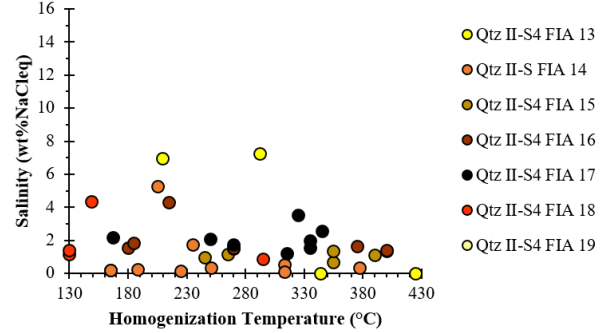
29 **Figure S4**. Homogenization Temperature vs. Salinity plots for fluid inclsuions types identified in each structural domain: a) Qtz I-damage

30 zone; b) Qtz I-fault core; c) Pseudosecondary FI in Qtz II-fault core; d) secondary FI entrapped within Qtz II vein. These plots are used to

31 estimate the most probable composition of the fluids.

32

33

Appendix D

Fluid-mediated, brittle-ductile deformation at seismogenic depth: Part II – Stress history and fluid pressure variations in a shear zone in a nuclear waste repository (Olkiluoto Island, Finland)

5   Francesca Prando[1], Luca Menegon[1,2], Mark. W. Anderson[1], Barbara Marchesini[3], Jussi Mattila [4,5] and Giulio Viola[3]

[1] School of Geography, Earth and Environmental Sciences, University of Plymouth, PL48AA Plymouth, UK
[2]The Njord Centre, Department of Geoscience, University of Oslo, P.O. Box 1048 Blindern, Norway
10   [3]Dipartimento di Scienze Biologiche, Geologiche e Ambientali, Università di Bologna, Italy
[4] Geological Survey of Finland, Espoo, Finland
[5] Currently at: Rock Mechanics Consulting Finland Oy (RMCF), Vantaa, Finland

Correspondence to: Francesca Prando (francesca.prando@plymouth.ac.uk) and Luca Menegon
15   (luca.menegon@plymouth.ac.uk)

Abstract. Microstructural record of fault rocks active at the brittle ductile transition zone (BDTZ) may retain information on the rheological parameters driving the switch in deformation mode, and on the role of stress and fluid pressure in controlling different fault slip behaviours. In this study we analysed the deformation microstructures of the strike-slip fault zone BFZ045

20   in Olkiluoto (SW Finland), located in the site of a deep geological repository for nuclear waste. We combined microstructural analysis, electron backscatter diffraction (EBSD), and mineral chemistry data to reconstruct the variations in pressure, temperature, fluid pressure and differential stress that mediated deformation and strain localization along BFZ045 across the BDTZ. BFZ045 exhibits a mixed ductile-brittle deformation, with a narrow (< 20 cm thick) brittle fault core with cataclasites and pseudotachylytes that overprint a wider (60-100 cm thick) quartz-rich mylonite. Ductile deformation took place at 400-

25   500° C and 3-4 kbar, typical of the greenschist facies metamorphism at the base of the seismogenic crust. Cataclastic deformation occurred under lower T conditions down to T ≥ 320° C and was not further overprinted by mylonitic creep. We used the recrystallized grain size piezometry for quartz to document a progressive increase in differential stress during mylonitization, from ca. 50 MPa to ca. 120 MPa. The increase in differential stress was localised towards the shear zone centre, which was eventually overprinted by brittle deformation in a narrowing shear zone. Synkinematic quartz veins emplaced along

30   the mylonitic foliation during an early, low stress creep event, and were overprinted by dynamic recrystallization and mylonitic creep at increasing differential stress. We propose a conceptual model in which the ductile-brittle deformation cycle was

controlled by transient oscillations in fluid pressure in a narrowing shear zone deforming at progressively higher differential stress during cooling.

1 Introduction

35

The change from fracturing and frictional sliding to dominant thermally activated creep processes accommodating viscous flow in mylonitic rocks occurs at the brittle–ductile transition zone (BDTZ; e.g. Kohlstedt et al., 1995; Handy et al., 2007). Conventional strength envelopes localize the BDTZ at a depth of 10-15 km in the continental crust (Kohlstedt et al., 1995, Ranalli, 1997, Bos and Spiers, 2002), corresponding to the base of the seismogenic zone (Sibson, 1982). Strength envelopes

40 also predict that the BDTZ coincides with a peak strength in the crust, between the brittle upper crust and the ductile middle- and lower crust. Naturally constrained stress profiles through exhumed mid-crustal rocks are consistent with this picture (Behr and Platt, 2011).

However, field evidence of seismic behaviour followed by solid-state viscous creep below the brittle-ductile transition in the continental crust (Austrheim, 2013, Menegon et al., 2017; White 1996, 2012), as well as of the cyclical interplay between

45 brittle and ductile deformation during the evolution of mid-crustal shear zones (e.g. Pennacchioni and Mancktelow, 2007; Fusseis and Handy, 2008; Wehrens et al., 2016; Melosh et al., 2018), demonstrate that the BDTZ occupies a depth interval that can vary transiently reflecting changes in, e.g., stress and fluid pressure, as well as changes in shear zone- and fault microstructures (Handy et al., 2007). More specifically, different deformation mechanisms (dislocation creep, diffusion creep, fluid-assisted veining, dissolution-precipitation creep, fracturing and cataclasis) overlap in space and time at the BDTZ as a

50 function of lithology, P-T conditions, and oscillating stress, strain rate and fluid pressure. Thus, the BDTZ occurs over a relatively wide range of conditions in a depth interval marked by significant fluctuations in strength (Hirth and Tullis, 1994; Scholz, 1998; Fossen and Cavalcante, 2017; Melosh et al., 2018) and fluid pressure (Cox, 2010; Kjøll et al, 2015; Sibson and Rowland, 2003; Yardley and Baumgartner, 2007; Marchesini et al., 2019) that steer the overall short- and long-term rheological behaviour of the crust. Given that shear zones at the BDTZ act as rheologically weak detachment horizons within the crust

55 (Handy and Brun, 2004; Gueydan et al., 2003; Pfiffner, 2016), understanding the effects of stress-, strain rate- and fluid pressure fluctuations on the rheological evolution of shear zones at the BDTZ is an important goal in tectonics research. In particular, it is important to assess whether evidence of such cyclical fluctuations are preserved in the geological record, and whether the extent of such variations can be estimated by examining natural fault rocks.

Microstructures can record crucial information on the parameters steering deformation cycles at the BDTZ, and are an

60 invaluable tool that enables derivation of rheological parameters of shear zones (e.g. Stipp et al., 2002; Behr and Platt, 2011; Ceccato et al., 2018). However, the mutual overprinting relationships between brittle and ductile deformation and associated fault rocks at the BDTZ typically result in only partial microstructural records, in which the youngest deformation event might have completely overprinted the evidence of earlier deformation episodes. Recent deformation experiments have, however,

opened up new avenues for the detailed investigations of natural deformation microstructures in quartz-rich rocks that result

65 from stress variations during brittle-ductile deformation. The 'kick and cook' experiments have documented quartz microstructures formed during transient high stress deformation followed by stress relaxation (Trepmann et al., 2007). Similar microstructures found in natural shear zones formed below the BDTZ were interpreted to results from seismic loading from the overlying brittle crust, followed by either static grain growth or dislocation creep deformation at relaxing stress (Trepmann and Stöckhert, 2003, 2013; Trepmann et al., 2017). Deformation experiments conducted by Kidder et al. (2016) show that the

70 microstructure associated with a stress increase in quartzite is a bimodal distribution of recrystallized grain size. The smaller grains accurately record the stress increase, whereas the surviving coarser grains formed during earlier, lower stress deformation. The smaller grains can be used to constrain differential stresses during the most recent (high stress) deformation event using a recrystallized grain size palaeopiezometer (Stipp and Tullis, 2003; Cross et al., 2017).

Fluids can also play a fundamental role in triggering a transient switch from dominantly ductile to brittle deformation, as

75 demonstrated for example by the synkinematic emplacement of quartz veins subsequently overprinted by crystal-plastic deformation (Handy et al., 2007; Kjøll et al., 2015; Trepmann and Seybold 2019; Marchesini et al., 2019). Cyclical ductile-brittle-ductile deformation associated with high fluid fluxes involving a fault-valve behaviour (Sibson, 1990) implies cycles of fluid pressure build-up followed by fluid venting and pressure drop, and has been related to seismic fault behaviour (Sibson, 1992; Cox, 1995; Nguyen at al., 1998; Viola et al., 2006). Near lithostatic values of fluid pressure are required to facilitate

80 synkinematic vein emplacement in a shear zone at the BDTZ (Cox, 1995; Streit and Cox, 2001; Cox, 2007; Hirth and Beeler, 2015).

Given the fundamental interplay between variations in P-T conditions, fluid pressures, stress and strain rate occurring at the BDTZ, fault modelling and field studies must attempt to quantify the thermal and structural history of fault rocks, as well as the fluid activity in faults in order to untangle the relative contribution of different rheological parameters in controlling the

85 dominant deformation mode and mechanisms active at seismogenic depths. This study investigates the microstructural record of the deformation behaviour at the BDTZ of a subvertical sinistral strike-slip fault hosted in granitoids of the Paleoproterozoic Baltic Shield in Finland. The fault occurs within the deep ONKALO spent nuclear fuel repository that is currently being built on the island of Olkiluoto in SW Finland (Fig. 1a). The present-day structure of the fault consists of a narrow (< 20 cm thick) brittle fault zone core that exploits a wider (ca. 1 m thick) ductile, mylonitic precursor. We constrain the deformation history

90 of the fault zone and use quartz microstructure to estimate the stress history of the mylonitic precursor. We propose a conceptual model of the evolution of fault slip behaviour that incorporates the constraints on differential stress and fluid pressure derived from our microstructural analysis, and that favours the scenario of a narrowing shear zone that progressively localizes strain when deforming across the BDTZ.

2 Geological Setting

95   The island of Olkiluoto in SW Finland (Fig. 1a) is located in the Paleoproterozoic bedrock of the Baltic shield. The region is dominated by high grade metasediments and by plutonic rocks, emplaced during the latest accretionary stages of the Svecofennian Orogeny between 1.89 and 1.80 Ga (Lahtinen et al 1994, Nironen et al. 1997, Lahtinen et al 2005, Pajunen et al. 2008). In the study area, the dominant rock types consist of amphibolite facies migmatitic metasediments, calc-alkaline synorogenic TTG-type granitoids, and late-orogenic leucogranites and pegmatites. The migmatisation occurred between 1.84-

100   1.82 Ga (Aaltonen et al. 2016), during the collisional stage of the Svecofennian Orogeny characterized by considerable crustal thickening and high-grade metamorphism (Kukkonen and Lauri, 2009). Stable mineral assemblages constrain the formation of the migmatite at 3.7-4.2 Kbar and 660-700° C (Tuisku and Karki, 2010). Tonalite and granodiorite intrusions were emplaced prior to the metamorphic peak, between 1.89 and 1.85 Ma (Mänttäri et al., 2006), while leucogranites intrusions emplaced during the high-grade metamorphism and late orogenic stages, between 1.85 to 1.79 Ga (Mänttäri et al., 2010). Retrograde

105   metamorphism under greenschist facies conditions affected the rocks soon after the peak conditions, and continued throughout the orogenic collapse, dated at 1.79-1.77 Ga for SW Finland (Lahtinen et al., 2005). Approximately 150 Ma later, during an extensional tectonic phase, Southern Finland was intruded by Rapakivi granites (1.65-1.54 Ga), with the Laitila and Eurajoki plutons located at 15 and 4 km eastern of Olkiluoto, respectively. Crustal extension also caused the formation of an NW–SE trending graben 50 km north of Olkiluoto, later filled with Mesoproterozoic sandstones. Olkiluoto bedrock was affected by the

110   emplacement of NE-SW striking diabase dykes (1.56 Ga) and Greisen veins associated with the Rapakivi batholiths intrusions and graben formation. The intrusion of olivine diabase sills occurred during a phase of regional compression at c. 1.27-1.25 Ga (Suominen 1991).

The study area was affected by a polyphase ductile deformation between 1.86 and 1.79 Ga (Aaltonen et al., 2016), followed by a complex brittle deformation history, as a result of exhumation and cooling. Aaltonen et al. (2010) identified characteristic

115   structures for three (D_2-D_4) deformation stages, which overprint a pre-migmatite, poorly preserved deformation stage (D_1). At 1.86-1.83 Ga, D_2 deformation affected progressively the bedrock of Olkiluoto, developing a pervasive NE-SW striking high-grade (locally migmatitic) foliation dipping moderately towards SE, as well as NE–SW striking mesoscopic shear zones (Aaltonen et al. 2010). The following D_3 stage (1.83 to 1.81 Ga) was more localized and occurred under amphibolite facies conditions. It resulted in NNE-SSW striking foliations, observed in the central part of Olkiluoto, and E-W to NE-SW trending,

120   S to SE dipping shear zones (Aaltonen at al. 2010). The latest stage, D_4, developed under greenschist facies retrograde metamorphism around 1.81–1.79 Ga according to U/Pb dating of syn-kinematic pegmatites (Mänttäri et al., 2010). D_4 structures consist of NNE-SSW and N-S striking subvertical ductile shear zones, varying in width from ~ 0.5 m to 200 m (Fig.1a).

The progressive regional exhumation led to a switch in deformation style, with the onset of brittle deformation in Olkiluoto at

125   ~ 1.75 Ga (Mattila and Viola, 2014, Aaltonen et al., 2016). Mattila and Viola (2014) used paleostress inversion of fault slip data to identify seven distinct brittle stages that developed in the time span from 1.75 to 0.8 Ga. These brittle deformation

stages are characterized by both the reactivation of optimally oriented pre-existing ductile structures, and by the formation of new Andersonian-type faults and joints. The dominant brittle structures in the study area can be grouped into two main sets: (1) an E-W to NE-SW trending set of low angle faults exploiting the regional migmatitic foliation, and (2) a set of subvertical faults striking N-S to NW-SE (Fig.1; Aaltonen et al., 2016). We assumed that, previous to the brittle stage, the crust in Olkiluoto had been passively exhumed during the late- to post-orogenic deformation stages of the Svecofennian orogeny (Lahtinen et al., 2005). Low angle faults cross-cut the subvertical faults and attest to a later stage of exhumation (Aaltonen et al., 2016).

The subvertical faults have orientation compatible with the first stage of brittle deformation identified by Mattila and Viola (2014), and they typically form conjugate systems of NNW–SSE sinistral and NW–SE dextral strike-slip faults (Mattila and Viola, 2014). This conjugate system has been interpreted to result from the NW–SE to NNW–SSE compression proposed for the late- to post- Svecofennian orogeny (Viola et al., 2009; Torvela and Ehlers, 2010; Saintot at al., 2011).

A network of vertical N-S and NW-SE faults has been mapped and investigated at the repository scale with underground surveys and boreholes (Aaltonen et al. 2016, Fig 1b). N-S faults are typically localized on mica-rich precursor ductile shear zones (Pere, 2009). The role of subvertical, N-S striking ductile precursor zones in controlling the localization of faults at the disposal site was investigated by Skyttä and Torvela (2018), who identified the ductile precursor structures as short limbs of D_4 asymmetric folds and as anastomosing networks of discrete retrograde (greenschist facies) ductile shear zones. Skyttä and Torvela (2018) proposed that the subvertical N-S faults formed as a result of progressive strain localisation during the late stage of D_4 deformation, which culminated in the development of faults through linkage of individual fault segments that preferentially exploited optimally oriented branches of the anastomosing network of localised ductile high strain zones. As such, the faults exploiting D_4 shear zones represent ideal targets to investigate the deformation processes and mechanisms at the brittle-ductile transition, and the associated rheological parameters recorded in the fault rock microstructures. This study uses the N-S sinistral strike-slip fault BFZ045 as a natural laboratory to investigate the stress history of the ductile precursor and the role of fluids on the deformation processes active at the brittle-ductile transition. The companion paper by Marchesini et al. (2019) has thoroughly described the deformation history of the conjugate (yet very different) dextral BFZ300 fault.

3 Methods

Samples were obtained from two sub-horizontal drill cores from the underground facilities that intersect the BFZ045 fault (Fig. 2a). The analysed samples were selected from (i) a 2 m continuous section along drill core PH28, which was drilled at a depth of 433 m b.s.l. and is oriented ESE-WNW, and (ii) drill core PH16 from the Demonstration Facilities tunnels at 420 m depth, described in Aaltonen et al. (2016). The PH28 samples were selected from the 99-101m interval of the drill core, with core distance measured from ESE to WNW, which includes the fault core and the proximal damage zone. The drill core was cut in half parallel to the stretching lineation and perpendicular to the mylonitic foliation and subsampled at regular intervals of 2 cm. Nineteen polished thin sections cut parallel to the stretching lineation were added to three samples from PH16

previously described in Aaltonen et al. (2016). An additional thin section from drill core PH21 (drilled at the same depth of
160 PH16) was used to estimate the T of the fabric formation in the host rock using Raman spectroscopy of carbonaceous material
(see 3.2 and 4.5).

3.1 Microstructural observations and Electron Backscatter Diffraction (EBSD) analysis

Deformation microstructures were investigated using petrographic microscopy and scanning electron microscopy (SEM). SEM
and EBSD analysis was performed at the Plymouth University Electron Microscopy Centre using a JEOL LV6610 SEM and
165 a JEOL 7001 FEG-SEM. Thin sections used for Electron Backscatter Diffraction (EBSD) analysis were polished with colloidal
silica before being carbon coated. Data were acquired on a NordlysNano and a NordlysMax EBSD detector (Oxford
Instruments). Working conditions during acquisition of the EBSD patterns were 20 kV, 20 mm working distance, 70° sample
tilt and high vacuum. AZtec software was used for pattern indexing on rectangular grids with step size of 0.7 μm, 1 μm and
1.8 μm. EBSD patterns were processed with the Channel 5 software (Oxford Instruments), and noise reduction was performed
170 following the procedure suggested in Bestmann and Prior (2003). The EBSD data are presented as grain size maps, with a 10°
misorientation threshold to define grain boundaries (in black), while low-angle boundaries are defined as having misorientation
> 2° and < 10° and are displayed as white or cyan lines. The grain size was measured as the diameter of a circle with equivalent
area to the grain. The spread of the internal orientation of each grain was shown as Grain Orientation Spread (GOS) maps and
was considered as a measure of the internal strain of the grain. A trade-off curve was used to calculate a threshold GOS value,
175 which separates recrystallized grains from relict grains, following the procedure outlined in Cross et al. (2017). The average
recrystallized grain size, calculated as root mean square (RMS), was used to apply the EBSD calibrated recrystallized grain
size piezometer for quartz (Cross et al., 2017). Grain reference orientation deviation angle maps (GROD) were used to visualise
subgrains only partially outlined by low-angle boundaries and to estimate their size. GROD maps are colour coded to show
the angular deviation at each point of a grain from the average orientation of the grain. Quartz c-axis orientation is presented
180 as pole figures on equal area, lower hemisphere projections, and one point per grain. The XY plane of the pole figure is parallel
to the shear zone foliation, X is parallel to the stretching lineation, and Z is normal to the foliation.

3.2 Mineral chemistry and Raman spectroscopy

A first semi-quantitative chemical composition point analysis was conducted using a JEOL 7001 FEG-SEM equipped with
energy-dispersive spectrometer (EDS) at the Electron Microscopy Centre of the University of Plymouth. Major element
185 mineral chemistry of chlorite and white mica was measured with Electron Microprobe Analysis (EMPA), at the Department
of Earth Sciences, University of Milan, Italy. Carbon coated thin sections were probed with a JEOL 8200 Super Probe equipped
with 5 wavelength-dispersive spectrometer (WDS). Working conditions were set to 15 kV of probe current, 5nA current on
sample, 1 μm beam diameter. Natural minerals were used for standardization, measurement times were 30s on peaks and 10s
on backgrounds of the X-ray lines.

190   Raman spectroscopy was applied for feldspar and opaque phase identification and for carbonaceous material (CM) characterization. Data acquisition was conducted at the Department of Chemistry, University of Padua (Italy), using a Thermo Scientific DXR MicroRaman spectrometer, equipped with a 532 nm depolarised laser. Spectra were acquired from polished thin section, using a laser power of 5 mW, spectrograph aperture 25 μm pinhole, and a 50X low distance objective. The estimate spot size was 1.1 μm in diameter and spectral resolution of 4.4 cm-1, with acquisition time of 30–90s. Feldspars composition

195   was classified on the basis of the acquired Raman spectra, as suggested in Freeman et al. (2008), using a comparison with standard Raman spectra from the RRUFF Project database (Lafuente et al. 2015). To assure a good statistical analysis of the CM structural heterogeneity, only samples with > 10 CM spectra were taken in consideration. Omnic software (Thermo Fisher Scientific) was used for Raman spectrum decomposition, using the software Lorentian/Gaussian function, following the procedure described in Koeketsu et al. (2009). A linear relationship between temperature and the Raman parameter R2 (derived

200   from the area of the defect band relative to the ordered graphite band) forms the basis of the CM geothermometer (Beyssac et al., 2002). Temperature can be estimated to ± 50 °C in the range 330–650 °C. Deformation can affect the internal disorder and underestimate the temperature obtained from the spectra analysis (Kirilova et al., 2017). To consider the possible role of deformation, analysis of CM both in the host rock and along the D$_4$ mylonitic foliation were collected. Care was taken to avoid CM within cracks, and to prevent altered measurement from CM damaged during the thin section polishing, we performed

205   measurements by focusing the laser beam on CM beneath the surface of a transparent adjacent grain as suggested in Beyssac et al. (2002).

4 Results

4.1 BFZ045 fault zone structure

Underground field observations and measurements indicate that BFZ045 is a strike-slip fault, with an average orientation of

210   87/095 (dip/dip direction, Fig. 2b) and with a mixed ductile-brittle deformation style that manifests itself as a 10-100 cm wide mylonite with a sinistral sense of shear, overprinted by cataclasites, fault breccias cemented by quartz, chlorite and sulphides, and by a network of veins typically filled with chlorite, quartz, and calcite. Slickensides with chlorite mineral striations are abundant throughout BFZ045 and the average orientation of the striations is 07/169 (plunge/trend, Fig. 2c). Stepped slickensides indicate a dominant sinistral sense of shear, although striations associated with dextral kinematics have also been

215   observed. The damage zone is typically 0-5 m thick and is characterized by an increased fracture density towards the fault core. Fractures are mostly filled by chlorite (Aaltonen et al, 2016).

The structure and the fault rocks of BFZ045 were characterized in detail from the two cores PH28 and PH16, both drilled approximately at the depth of 420 meters. The horizontal drill core PH28 provides a cross section of BFZ045, where a 2 m thick damage zone surrounds a 60 cm thick fault core characterised by a sub-vertical network of cohesive cataclasites and

220   veins that overprint a mylonite oriented 61/075 (dip/dip direction, Figs. 2a, b, d). A schematic representation of the fault

geometry along PH28 is represented in Fig. 2a. The host rock is a coarse-grained veined migmatite consisting of 40 vol% of quartz, 50 vol% of feldspars, and 10 vol% of muscovite (Fig. 2d, I).

The damage zone of BFZ045 consists of an asymmetrical (~20 cm east side of the core and ~ 60 cm on the west side) fractured host rock surrounding a mylonitic fault core (Fig 2a). Its boundaries were defined by the farthest occurrence of chlorite filled

225 fractures, identified microscopically as deformation band as they are associated with visible slip. A total of 12 fractures longer than 5 cm were observed along the core, of which 7 within a distance of 10 cm from the fault core (west side of the core). Fracture density increases towards the contact with the brittle fault core, with the average spacing between fractures decreasing from 3 cm to ca. 0.5 cm. Chlorite and calcite are the most common minerals partially filling the fractures oriented variably with respect to the mylonitic foliation. The contact between the damage zone and the mylonite is sharp.

230 The millimetre-spaced mylonitic foliation is defined by a compositional layering of alternating quartz-feldspathic domains and mica-rich domains (Fig. 2b, II). Rodding of quartz and feldspar defines a stretching lineation, with average orientation of 10/168 (plunge/trend) (Fig. 2b,c). Multiple slip surfaces marked by 0.5 – 10 cm thick cataclastic domains overprint the mylonite along the foliation (Fig. 2d, III). Locally, phyllosilicates and trails of opaque minerals define thin (<1mm thick) anastomosing foliation planes within the cataclasites, which wrap around sub-angular fragments of the mylonitic precursor.

235 Along a thin (<5 mm thick) slip surface, two pseudotachylyte injection veins intruding the mylonite at a high angle have been observed, which demonstrates the transient seismogenic behaviour of BFZ045. The pseudotachylyte main generation surface is less than 1 mm thick and is parallel to the mylonitic foliation (Fig. 3c). Calcite veins (1-3 mm thick) overprint the fault core either at high angle to the foliation or along the slip surfaces. Representative micrographs of samples taken from the fault core and from its damage zone are shown in figure 3.

240 **4.2 Microstructures and petrography**

The migmatitic host rock mineral assemblage observed in the PH28 samples consists of 50 % of quartz (qtz), 40 % K-feldspar (kf), and plagioclase (pl) and the remaining 10% of white mica (wm), alteration minerals of plagioclase (sericite) and secondary chlorite and calcite veins. Coarse-grained (1-2mm) quartz and feldspars are homogeneously distributed in an equigranular texture and show mostly straight grain boundaries. K-feldspar occurs as orthoclase, with a well-developed veined perthitic texture. Plagioclase, albitic in composition as determined from Raman analysis, has lamellar twinning and is commonly altered

245 into sericite. Both types of feldspar locally show bent twin lamellae and undulose extinction. White mica was observed occasionally as millimetric sub-euhedral grains.

The damage zone retains the same mineral assemblage of the host rock, except along the chlorite filled shear bands and fractures (Fig 3a). Shear bands appear as cohesive micro-cataclasites, with fine grained (< 10 μm) chlorite surrounding angular

250 feldspar and quartz clasts. Calcite veins are preferentially oriented at high angle to the mylonitic foliation (60° to 85°). Microfractures in feldspars are preferentially oriented parallel and at low angle (≤ 20°) to the foliation. Both orientations correspond to the orientation of fluid inclusion trails observed in quartz (section 4.3.1).

The relative mineral abundances in the mylonite are slightly different from those in the host rock, and consist of 50% quartz, 20% white mica + chlorite, and 30% K-feldspar + plagioclase. Accessory phases are rutile, anatase, and apatite, which are

255 typically found associated with chlorite to form black seams. The spaced mylonitic foliation is defined by a compositional banding between alternating millimetre-thick quartz bands and narrower (0.2 to 1 mm thick) mica- and feldspars-rich bands (Fig. 3b). Porphyroclasts of K-feldspar are up to 7 mm in size and show asymmetric pressure shadows filled with chlorite + muscovite ± feldspars (albite and K-feldspar), with a geometry indicative of a sinistral sense of shear. Veins of radiate chlorite are observed cutting the mylonitic foliation at a high angle (~60°).

260 The brittle overprint in the fault core occurs mostly as 3 to 10 cm thick protocataclasites, with chlorite rich C' shear bands cutting the mylonitic foliation and indicative of a sinistral sense of shears. The protocataclasite transitions to 0.5 - 2 cm thick cataclasite bands in the fault core. Compared to the host rock the cataclasite bands are richer in chlorite and opaque minerals, which occur as fine-grained (2-10 μm) flaky aggregates within the quartz + feldspars + muscovite rich matrix. Clasts are predominantly angular fragments of the mylonite, ranging in size from 100 μm to 5 mm, and surrounded by a variable

265 proportion of fine grained (<50 μm) matrix (Fig. 3c). Foliation in the matrix is defined by aligned phyllosilicates and anastomosing dark seams of opaque minerals. Veins with radiate chlorite that typically overprint the mylonite were also observed within mylonitic clasts inside the cataclasite.

A fine grained pseudotachylyte generation surface is observed subparallel to a cataclastic band (Fig. 3c), identified from characteristic centimetric injection veins, branching in the mylonitic rock at high angle to the foliation. The matrix of the

270 pseudotachylyte is completely altered to a fine-grained, <2 μm, chlorite and muscovite rich matrix that surrounds survivor clasts of quartz and rutile (Fig. 3d).

In the following section, we present a detailed description of quartz deformation and recrystallisation microstructures in the mylonite and in the cataclasite. We used the varying deformation microstructure of quartz as a proxy for the variation of differential stress and fluid pressure during the deformation of BFZ045 at the brittle-ductile transition.

275 **4.3 Quartz microstructures**

4.3.1 Damage zone

The damaged host rock shows large sub-euhedral quartz grains (> 3mm) with lobate to straight grain boundaries. Quartz displays intracrystalline deformation features such as undulatory extinction, wide extinction bands (WEBs, following the terminology of Derez et al., 2015; Fig. 4a), and bulges resulting in sutured grain boundaries (Fig. 4b; Stipp and Kunze, 2008).

280 WEBs are locally bounded by fluid inclusion trails with different orientations, which give them a blocky or slightly elongated aspect (Figs. 4a-b). Two main sets of intracrystalline fluid inclusion trails are observed, one at a low angle with respect to the mylonitic foliation and the other perpendicular to the foliation. Fine bulges (10-20 μm in size) occur along grain boundaries and intercrystalline fractures (Fig. 4a). Quartz grains in the proximity of the mylonite (sample PH28-2, Fig. 2b) develop intracrystalline bands of recrystallized grains sub- parallel to the foliation, with grain size of ~ 30-60 μm.

4.3.2 Fault core

Quartz in the mylonite presents various degrees of recrystallization (Figs. 5a-c). In zones where ductile deformation is less prominent (e.g. samples PH28_3, PH16_1, Fig. 2), quartz retains a coarser grain size (1-5 mm), and forms slightly asymmetric (sigmoidal-shaped) grains. Internally, the grains display patchy undulatory extinction, well-developed blocky to elongated WEBs (100-300 μm wide), and discrete intracrystalline bands (< 200 μm wide) of bulges and recrystallized grains preferentially oriented sub-parallel to the foliation and at ca. 45° from the foliation, measured clockwise (Fig. 5a). The host grains contain small subgrains (< 60μm), which, towards the boundaries of the host grain, make transition to aggregates of recrystallized grains of size comparable to the subgrains, forming typical core-and-mantle microstructures (Fig. 5a).

In zones of complete recrystallization at a distance >2 cm from the cataclastic fault zone core, quartz forms highly elongated polycrystalline ribbons (up to 0.5 – 1 mm thick, and up to 2 cm long) parallel to the foliation (Fig. 5b). The recrystallized grains locally define a shape preferred orientation (SPO in Fig. 5b) inclined with 10° to 30° with respect to the trace of the foliation, consistently with the bulk sinistral sense of shear.

Adjacent to the cataclastic unit, at a distance < 1 cm (sample PH16_3, Fig. 2), ataxial/unitaxial (i.e. with no visible median line; Bons, 2012) quartz veins are observed (Fig. 5c). They occur parallel to the mylonitic foliation (and to the layers of recrystallized quartz) and contain grains elongated normal to the vein boundary (i.e. normal to the foliation). The vein crystals range in length from 200-400 μm and have a maximum thickness of 150 μm measured parallel to the vein. Quartz in the veins shows undulatory extinction and bulges at the grain boundaries (Fig. 5d) indicative of crystal plastic deformation. The recrystallized quartz in the mylonite surrounding the vein has a finer grain size than the one in the mylonite described in Figs. 5a-b, which is located farther away from the cataclastic core.

Quartz in the mylonite at distances < 2 cm from the cataclasites occurs in almost entirely recrystallized ribbons with a finer grain size (ca. 10 μm) than the one observed at higher distances from the brittle fault core (Fig. 5e). The quartz clasts in the cataclasite (Fig. 5f) preserve the deformation and recrystallization microstructures observed in the mylonite in close proximity to the cataclasite (Fig. 5e).

4.4 EBSD and grain size analysis of quartz

4.4.1 Mylonite

EBSD analysis of the mylonite was conducted on sample PH16_1, which is located at the mylonitic shear zone boundary at a distance of 4 cm from the brittle fault core (Fig. 2a). EBSD maps were acquired from intracrystalline bands of recrystallized grains within an elongated mm- sized quartz grain (Fig. 6a), and from a highly recrystallized quartz layer along the mylonitic foliation (Fig. 7a).

The recrystallized grain size within the intracrystalline bands ranges from 5 to 60 μm (Fig. 6b, c). The Grain Orientation Spread (GOS) within the recrystallized bands varies between 0° and 8.4°, with a threshold value of 1° between the recrystallized grains

and the relict grains when analysing the trade-off curve proposed by Cross et al. (2017). The average grain size of recrystallized grains (GOS < 1°) is 16 ± 7 µm whereas relict grains (GOS > 1°) have an average grain size of 25 ± 9 µm. Relict grains contain subgrains of an average size of 17 ± 7 µm (Fig. 6f).

320 Quartz grain hosting the intracrystalline band shows subgrains of approximately 25-50 µm in size, which is comparable to the size of the coarser recrystallized grains observed in the intracrystalline bands (Fig. 6c). The size of the subgrains in the host quartz was estimated visually with the aid of Grain Relative Orientation Distribution maps (GROD, Fig. 6g).

In the recrystallized quartz layer (Fig. 7a), quartz grain shape ranges from equant to elongate parallel to the foliation, with grain size ranging from 5 to 87 µm (Figs. 7b, c). Grain Orientation Spread (GOS analysis identified a threshold value of 1.56°

325 to separate recrystallized- and relict grains (Fig. 7d). Average grain size of the recrystallized grains is 18 ± 8 µm, while relict grains have an average size of 28 ± 11 µm (Fig. 7e).

The relict grains contain subgrains of an average size of 17 ± 7 µm (Figs. 7c, f). The crystallographic preferred orientation (CPO) of the c-axis of the relict grains and recrystallized grains forms a single girdle consistently inclined with the sinistral sense of shear of the sample (Fig. 7g). The EBSD-calibrated recrystallized grain size piezometer for quartz of Cross et al.

330 (2017) was used to estimate the differential stresses during plastic flow in the mylonite. The estimated differential stress is 73-80 MPa for the average recrystallized grain size of 16-18 µm.

4.4.2 Vein parallel to the mylonitic foliation

The quartz vein parallel to the foliation shown in Fig. 5c and 8a was analysed to identify possible evidence of crystal-plastic deformation and dynamic recrystallization. Grain shape varies from fibrous with elongation perpendicular to the vein wall, to

335 more equant/less elongate. Grain boundaries of vein crystals are straight to lobate, the latter most commonly observed in association with fine recrystallized grains and bulges (<15 µm in size) (Figs. 8 b, c). Irrespective of their shape, most of the grains contain low-angle boundaries and Dauphiné twins. The low-angle boundaries are typically arranged to define polygonal to slightly elongated domains of ~10 µm in size, comparable to that of the surrounding recrystallized grains in the mylonite (Fig 8c).

340 Quartz in the mylonite flanking the vein shows fine grain size (<20 µm), with only a small fraction of coarser grains (30-60 µm). Grain Orientation Spread (GOS) analysis indicates that dynamic recrystallization is pervasive. The mean recrystallized grain size is 10 ± 3 µm, and the relict average grain size is 20 ± 9 µm, with a GOS threshold value of 1.94° (Figs. 8d, e). Selected relict grains (size> 40 µm) in the mylonite contain subgrains with size between 5 to 25 µm range (Fig. 8f). Finer grains observed within the vein also present a GOS value below the threshold, which suggests they represent the recrystallized

345 fraction in the quartz vein (Figs. 8c, f). In the vein quartz, GOS analysis indicates that the average subgrain size is 24 ± 7 µm, although the largest fraction of subgrains is smaller than 15 µm, i.e., similar in size to the recrystallized grains in the flanking mylonite and in the vein itself. The c-axis CPO of the recrystallized grains in the mylonite forms a single girdle synthetically inclined with the sinistral sense of shear (Fig. 8h). The c-axis CPO of recrystallized grains in the veins overlaps with the one

of the relict grains (Fig. 8i). The differential stress estimated from the average recrystallized grain size in the mylonite (10 μm)
350   is 106 MPa.

4.4.3 Cataclasite

We analysed a largely recrystallized quartz clast in the cataclasite from sample PH28_10 (Fig. 9a). The selected clast is rotated
of less than 10° with respect to the adjacent mylonitic foliation. Quartz grain size in the clast ranges from 4 to 60 μm. The
coarser grains are elongated parallel to the foliation, show bulges and fine recrystallized grains at their boundaries, and contain
355   a high density of low-angle boundaries (Fig. 9b). The low-angle boundaries define small polygonal domains of a size
comparable to the one of the recrystallized grains found at the grain boundaries (Fig. 9c). The GOS map in figure 9d identifies
two grain size distributions, separated by a GOS threshold value of 3.23°. The recrystallized grains (average grain size: 8 ± 4
μm) form equigranular aggregates at the boundaries of the coarser (average grain size: 17 ± 10 μm) elongated relict grains.
The c-axis CPO of the recrystallized grains and of the relict grains is the same, showing two maxima at an intermediate position
360   between the centre of the pole figure and its periphery, and consistently inclined with the sinistral sense of shear of the sample
(Fig. 9f). The differential stress estimated from the average recrystallized grain size in the clast (8 μm) is 123 MPa. Although
the map has been acquired from a clast, these microstructures and recrystallized grain size are representative of the mylonite
in the immediate vicinity (< 2 cm) of the brittle fault core (Figs. 5e, f).

4.5. Mineral chemistry, Raman spectroscopy, and pressure-temperature (P-T) conditions of deformation

365   We estimated the P-T conditions of mylonitic and cataclastic deformation using Raman spectroscopy of carbonaceous material
(RSCM), chlorite thermometry, and phengite barometry. Carbonaceous material was observed as grains and aggregates
ranging in size from ~50 to ~200 μm in the host rock (sample PH21_1, Fig. 10a) and as smaller grains (20- 50 μm) along the
mylonitic foliation, (sample PH16_1-2, Fig. 10b) along chlorite and muscovite rich layers. We estimated a peak metamorphic
temperature of 530°± 50° for the carbonaceous material in the host rock (using the thermometer calibration for a laser
370   wavelength of 514 nm, Beyssac et al. 2002), and a lower T of 436° ± 50° for the mylonite (Aoya et al., 2010, using the
thermometer calibration for a laser wavelength of 532 nm) (Fig. 11a).

The average compositions of white mica are listed in Table 1. The full dataset of chemical compositions of white micas is
reported in the Supplementary Material (S1). White mica composition was measured for grains parallel to the foliation
associated with stable K-feldspar (Figs. 10c, d) and structural formulae were calculated assuming 11 oxygens. The range of Si
375   apfu in the probed muscovite grains is 3.12 –3.16. This compositional range indicates a pressure of 2-4 Kbar using the Si-in-
phengite geobarometer (Fig. 11b, Massonne and Schreyer, 1987), considering the average temperature of 440°C derived with
the graphite thermometry.

Chlorite composition was determined for i) chlorite grains intergrown with quartz and muscovite in the strain shadows around
feldspar porphyroclasts in the mylonite (Fig. 10c, d), ii) chlorites flakes aggregate in the cataclasite quartz matrix (Fig. 10e),
380   and iii) radiate chlorites filling veins at high angle to the mylonitic foliation (Fig. 10f). The structural formula of chlorite was

Solid Earth
Discussions
Open Access
EGU

calculated based on 14 oxygens, and representative composition are shown in Table 2. The full dataset of chemical compositions for chlorite is reported in the Supplementary Material (S2).

Chlorites along the mylonitic foliation and in the cataclasite have similar Si content (2.54 - 2.75 apfu), Al between 2.48- 2.82 apfu, and are moderately Fe-rich with a XFe (XFe=Fe/(Fe+Mg)) between 0.62 and 0.82. Chlorites in the mylonitic sample
385   from PH_16 have a more narrow range of XFe, between 0.5 and 0.6. The radial chlorite filling the veins has Si content between 2.51 and 2.780 apfu, Al between 2.74 and 3.00 apfu, and smaller XFe variations, between 0.69 and 0.81. In general, BFZ045 chlorites have a aphrosiderite-ripidolite composition and the microprobe results show that the composition of distinct chlorite generations is similar (Fig. 11c). The CHL(2) semi-empirical thermometer of Lanari et al. (2014) was applied to each EMPA analysis of chlorite with Si<3 apfu and (Na + K + Ca) < 0.1apfu. FeO was used as Fe total, and $aH_2O=1$ and $aSiO_2=1$ were
390   assumed. The estimated temperature for the mylonite ranges from 380 °C to 500 °C (limit of the used thermometer), with an average T of 440 °C for an assumed P of 3.5 kbar (Fig. 11d). Mean temperatures estimated for the cataclasite matrix (414 °C) and for the radiated chlorite in the veins (424 °C) are slightly lower than those of the mylonite, and compositions yielding T lower than 400 °C are more frequent, especially in the cataclasite (Fig 11d). The estimated temperature varied by 10 °C every 0.5 kbar increment.

5. Discussion

Our observations constrain the details of the structure and the deformation history of BFZ045. In particular, the microstructures of fault rocks indicate a sequence of deformation events where ductile deformation (mylonitisation) was punctuated by brittle deformation (veining), and eventually culminated in the formation of the brittle, cataclastic fault core. We interpret this sequence to result from the evolving stress history and fluid pressure variations along the fault. In the following, we discuss
400   the constraints provided by our microstructural analysis, and derive a conceptual model of fault slip behaviour of BFZ045 at the brittle-ductile transition.

5.1 The sequence of deformation events in BFZ045: ductile-brittle deformation cycles in the middle crust

Our microstructural observations are consistent with the general conclusion that brittle deformation along BFZ045 exploited
405   a ductile (mylonitic) precursor (Nordbäck and Mattila al., 2018; Skytta and Torvela, 2018). Veins, cataclasites and pseudotachylytes are localised along the mylonitic fabric of BFZ045, and only minor evidence of brittle deformation (mostly in the form of fractures filled by chlorite) is present outside of the mylonitic fault core (Figs. 2a, 3a). The analysed samples document a switch from dominant ductile to brittle deformation mode, via a transitional deformation stage where overall ductile conditions were punctuated by veining.
410   The first stage of deformation of BFZ045 is represented by the development of a localized N-S trending mylonitic foliation in the migmatites (Figs. 2, 3b, 5a, 5b). Mylonitic creep was punctuated by transient brittle events, with the opening of extensional

fractures along the mylonitic foliation filled by quartz veins (Figs. 5c, d). Veining was again followed by mylonitic deformation, as indicated by dislocation creep and dynamic recrystallization microstructures of quartz in the veins. Mylonite and veins were then overprinted by brittle deformation that formed cm- thick cataclasites (Figs. 3c, 5e, 5f) and a <0.5 cm thick

415 pseudotachylyte that, together, form the brittle fault core of BFZ045. The pseudotachylyte is recognizable from injection vein intruding the mylonitic precursor (Fig. 3c,d).

The parallelism between stretching lineation in the mylonite and chlorite slickenlines in the cataclasites indicates that the ductile-brittle deformation history of BFZ045 occurred under a constant strike-slip regime with sinistral kinematics, as shown by the kinematic indicators in the mylonites and by the stepped slickensides observed in the field. This conclusion is consistent

420 with the model of the brittle evolution of SW Finland proposed by Mattila and Viola (2014), which attributes the sinistral kinematics of NNW-SSE trending subvertical faults to the ductile-brittle transition stage of the basement at 1.75 Ga (stage 1 of deformation in Mattila and Viola, 2014). BFZ045 experienced later reactivations during the prolonged brittle history of the SW Finland basement, as indicated by calcite veins cutting the brittle fault core and by (rare) slickenlines with dextral kinematics observed in the underground exposures (Aaltonen et al. 2016). Local dextral kinematics along BFZ045 is

425 potentially consistent with the stage 2 of deformation of Mattila and Viola (2014) at 1.7-1.6 Ga. These later features, however, are not discussed further in this paper as they are subordinate to, and did not obliterate the earlier history.

The sequence of deformation events recorded along BFZ045 is estimated to have occurred in the middle crust under slightly decreasing T from 450-500 °C to 320-400 °C (Fig. 11). We note that cataclasites and pseudotachylytes are not overprinted by mylonitic creep, which might indicate that they formed when the temperature was sufficiently low to favour predominantly

430 brittle deformation along BFZ045.

A temperature of 440 ± 50 °C is derived from graphite thermometry along the mylonitic foliation, which is approximately 100° degrees lower than the T of 530 ± 50 °C estimated from the graphite thermometry in the host rock fabric (Fig. 11a). This is consistent with the retrograded greenschist facies conditions attributed to the final stages of D$_4$ deformation in the SW Finland basement at 1.81-1.77 Ga (Lahtinen et al., 2005; Mänttäri et al., 2010). If the graphite analysed in BFZ045 represents

435 carbonaceous material that was mobilized after the D$_2$-D$_3$ deformation phases that formed the main foliation in the host rock, then the T of 440 ± 50 °C indicates the T of graphite crystallization during the D$_4$ greenschist facies metamorphic overprint and mylonitization of BFZ045. However, the difference in temperature between the host rock fabric and the shear zone can also be explained as the result of strain-induced disorder in the crystal lattice of the analysed graphite, which might result in an underestimation of the temperature of formation of the graphite (Kirilova et al., 2018). Considering the 50° error range of

440 the thermometer and the difference in estimate due to the use of two different calibrations that for the same R2 values can determine different temperatures (Fig. 12c) (Beyssac et al. 2002; Aoya et al. 2010), a temperature estimate of 440 ± 50 °C for the mylonite is acceptable.

A T of 440° was considered to constrain the P at the time of deformation along BFZ045 using the phengite geobarometer (Massonne et al, 1987) (Fig. 12d). The peak metamorphic temperatures obtained from the mylonite suggest a P of 3-4 kbar,

445 which overlaps with the P estimates based on stable mineral assemblages of Tuisku et al. (2010) of 3.7 – 4.2 kbar at the

culmination of regional metamorphism in Olkiluoto (phase D_2-D_3). We interpret this result as representative of the conditions during mylonitic deformation along BFZ045 in the middle crust after peak metamorphism.

Our estimate of P-T conditions of mylonitization of BFZ045 (~450 °C, 3-3.5 kbar) are consistent with the late Svecofennian orogeny and the emplacement and cooling of pegmatitic granites in SW Finland (Aaltonen et al. 2010). The pegmatitic granites

450   emplaced at 15-12 km depth, were then affected by the last stage of ductile deformation D_4 and cooled below 300 °C ca. 1.75 Ga ago (Aaltonen et al. 2010).

Our results indicate that the T ranges derived from chlorite thermometry in the mylonite and in veins cutting the mylonitic foliation overlap (Fig. 12d), with only a few analyses in the veins yielding T < 400°C. This overlap suggests that chlorite veining occurred early in the deformation history of BFZ045 (i.e. at T ≥ 450°C) and that it continued during decreasing T.

455   Constraining the T of formation of cataclasites is more difficult, because the chlorite grains might be fragments of the mylonitic chlorite. However, we only probed flake chlorite aggregate comparable to radiated chlorite in the cataclasite and we consider the radiate morphology as indicative of growth within the cataclasite (Fig. 10e). Thus, although we cannot rule out that a few of the probed grains were fragments, our results indicate that the cataclasite formed at T ≥ 320 °C and potentially as high as 450-500 °C. The lowest T estimate from chlorite thermometry (300-320 °C) is derived from a few grains in the cataclasite and

460   in the vein (Fig. 11d), and still locates the observed deformation activity in the middle crust at T ≥ 300°C.This is consistent with the results of Marchesini et al. (2019), who estimated a minimum T of 350°C for the early stages of deformation and emplacement of quartz veins along the dextral fault zone BFZ300 (conjugate to BFZ045). Considering an average P of 3.5 kbar during ductile-brittle deformation along BFZ045 and an average crustal density of 2.7 g/cm3, the depth of deformation corresponds to approximately 13 km, which is consistent with the depth typically considered as representative of the base of

465   the seismogenic crust at the BDTZ (e.g. Scholz, 1990, Kohlstedt et al., 1995). We note that our P estimate is valid only for the mylonitic creep stage of the deformation history of BFZ045, as no suitable geobarometer was found in the cataclasite.

5.2 Interpretation of quartz microstructures: stress history during mylonitic creep of BFZ045

Microstructural observations show that quartz in the BFZ045 mylonitic core accommodated deformation by dislocation creep. The most common recrystallization microstructures (bulges at the grain boundaries and within intracrystalline bands, and core

470   and mantle microstructures with subgrains of comparable size to that of the recrystallized grains: Figs. 4, 5) suggest that bulging and subgrain rotation were the dominant recrystallization mechanisms (Hirth and Tullis, 1992; Stipp and Kunze, 2008). The average recrystallized grain size in all our samples falls within the range where bulging, defined as slow grain boundary migration coupled to localised subgrain rotation at the mantle of the host grain, is expected to be the dominant recrystallization mechanism (Stipp et al., 2010). Our microstructural observations and EBSD maps are consistent with this.

475   The average recrystallized grain size of quartz decreases from the mylonitic shear zone boundary (16-18 µm) towards to shear zones centre (8-12 µm), which has been overprinted by the brittle fault zone core (Fig. 12). In all the areas investigated with EBSD, we regularly observed two populations of grains in which the coarser (relict) grain size contains subgrains of size comparable to the average grain size of the finer recrystallized grains (Figs. 7-10). The CPO of relict and recrystallized grains

is the same, and this is consistent with the host-controlled development of a CPO during subgrain rotation recrystallization

480 (e.g. Stünitz et al. 2003). Despite the slight differences in CPO patterns between the individual analysed sites (Figs. 8-10), the key observation is that the CPO of both the coarse (16-18 μm in samples PH16_1) and the fine (8-12 μm in samples PH16_3 and PH28_10) recrystallized grain size fraction is consistently inclined with the sinistral sense of shear of the samples. We interpret the consistent sinistral asymmetry of the quartz c-axis CPOs as strong evidence that the different recrystallized grain size fractions all developed during sinistral strike-slip ductile activity of BFZ045. Thus, the grain size variations, and in

485 particular the fine recrystallized grain size observed in samples PH16_3 and PH28_10, are interpreted to result from the stress history during mylonitic deformation of BFZ045, and not from discrete events of late reactivation and overprint of the fabric. We interpret the recrystallized grain size of 16-18 μm as representative of the long term 'steady state' mylonitic flow of BFZ045 at a differential stress of 73-80 MPa. Such grain size is the most representative of the partially- (Fig. 7) and of the nearly completely (Fig. 8) recrystallized quartz ribbons in the BFZ045 mylonite at distances ≥ 4 cm from the brittle fault core,

490 and occurs as relict grain size in quartz clasts embedded in the cataclasite, where it is overprinted by finer recrystallized grains (Fig. 10). It is worth noting that quartz in the mylonite in close proximity to the cataclasite, as well as in clasts within the cataclastite (samples PH28_7-10 and PH16_3 in Fig. 2), systematically exhibits a large number of recrystallized grains belonging to the finer population (8-12 μm, Figs. 9, 10). This overprint is interpreted as the evidence of a local increase in stress (up to 120 MPa) during mylonitic creep (Kidder et al. 2016). The average recrystallized grain size of 16-18 μm is

495 associated with relict grains of 25-28 μm (Figs. 7-8), and un-recrystallized portions of quartz contain subgrains of similar size (≥ 25 μm, Figs. 7b-d). We speculate that the 25-28 μm grain size population might represent an early, lower stress (i.e. around 50-60 MPa) dynamic recrystallization event within BFZ045, which was later overprinted by recrystallization occurring under progressively increasing differential stress.

Our discussion of the stress history of BFZ045 relies on the GOS method to separate between relict and recrystallized grains.

500 It is known that the GOS method has a slight grain size bias, which results in higher GOS values for larger grains (Cross et al., 2017). However, this bias has no impact on the ability to separate between relict and recrystallized grains where their size overlaps on the cumulative grain size distribution, and the GOS-based separation is considered robust (Cross et al., 2017). One key observation that supports our GOS-based separation is that relict grains systematically contain subgrains of the same size of the new, finer recrystallized grains. Thus, we are confident that our analysis has reliably identified different recrystallized

505 grain sizes.

In summary, the differential stresses estimated from the different populations of recrystallized quartz grains increase from 73-80 MPa to a peak value of 120 MPa towards the contact with the cataclasite. An earlier, lower stress (ca.54 MPa) deformation is possibly recorded in the (few) relict quartz grains of 25-28 μm that contain subgrains of around 17 μm of average size (Figs. 7, 8). We are aware of the uncertainties and limitations of the palaeopiezometric calibrations, and our estimated flow stresses

510 must be taken with care. However, we consider the systematic decrease in recrystallised grain size towards the cataclastic fault core to be meaningful and to reflect a change in the rheological conditions during mylonitic creep. Given the similar T

conditions across the studied profile, we conclude that this change reflects an increase in stress and strain rate. To explain this increase in stress and strain rate towards the shear zone centre, we discuss two possibilities:

(1) Increasing stress and strain rate towards the brittle shear zone centre may reflect the rheological evolution of a shear zone that is narrowing with progressive exhumation from the ductile to the brittle crust. In such a model, the peak stress conditions are reached at the brittle-ductile transition under progressively decreasing T (e.g. Kohlstedt et al., 1995; Behr and Platt, 2011). The results of our chlorite thermometry study support this model, as they are consistent with an overall T decrease from 450-500 °C to 320 °C during protracted mylonitic creep followed by a cataclastic overprint along the brittle fault core. In this scenario, BFZ045 would represent a case of narrowing shear zone that evolved from a distributed- to a progressively more localised ductile deformation and eventually brittle deformation during cooling and exhumation (type II shear zone of Fossen, 2017). During this evolution, dislocation creep and fluid-assisted veining occurred simultaneously, as expected in the 270-350° C temperature range considered typical of the frictional-viscous transition in quartz-rich rocks (Dunlap et al., 1997; Handy et al., 1999; Stöckhert et al., 1999; Stipp et al., 2002). Our work is unable to constrain the amount of exhumation associated with the cooling and progressive localization in the brittle fault core, as the strike-slip nature of BFZ045 cannot be responsible of significant exhumation. Considering a transpressional regional tectonic regime during the sinistral strike-slip activity of BFZ045 (stage 1 of deformation in Mattila and Viola, 2014), we speculate that the combination between thrusting and erosion was the main exhumation process of the Olkiluoto basement at around 1.75 Ga. In this scenario, BFZ045 was active within the Olkiluoto basement while it was being passively exhumed. However, we emphasize that a detailed appraisal of the mechanisms responsible of the passive exhumation of the Olkiluoto basement is beyond the scope of this study. Kärki and Paulamäki (2006) estimated a regional geothermal gradient of ca. 40 °C km^{-1} during retrogressive metamorphic conditions that culminated in the post-D$_4$ exhumation of the Olkiluoto basement. Assuming a regional geothermal gradient of ca. 40 °C km^{-1}, mylonitic deformation of BFZ045 at 440-500 °C would have occurred at ca. 11-12 km depth, whereas cataclastic deformation at 320-400 °C at 8-9 km depth.

(2) Alternatively, and assuming that the cataclasite formed at similar T (and depth) of the mylonite (T ≥ 400 °C), the increase in stress recorded by the finer recrystallized grain size might be attributed to external stress loading from seismic faulting in the overlying upper crust (i.e. seismic loading) (e.g. Küster and Stöckhert, 1998; Trepmann and Stöckhert, 2003; Trepmann et al., 2017; Trepmann and Seybold, 2019). The presence of pseudotachylytes along the BFZ045 fault core indicates that the fault was capable of generating earthquakes, and the seismogenic behaviour of other faults in the Olkiluoto basement has been previously discussed (Marchesini et al., 2019 and refs. therein). Thus, local high differential stresses in the BFZ045 mylonites could had been induced by seismic activity in the overlying upper crust. However, the fine-grained recrystallized fraction is exclusively localised in the immediate vicinity of the brittle fault core of BFZ045, whereas in case of earthquake-induced stress variations a more diffuse overprint within the entire width of the shear zone (and perhaps even outside of it) would be expected. Dislocation glide-controlled deformation microstructures of quartz typically interpreted as the evidence of seismic loading in the ductile crust, such as conjugate micro-shear zones, short wavelength undulatory extinction, and sub-basal deformation lamellae (Trepmann and Stöckert, 2013; Trepmann et al., 2017) have not been observed in the mylonite and in the damage

zone of BFZ045 (Figs. 3-5). Furthermore, cataclasites and pseudotachylytes are not mylonitised, and this is consistent with overall decreasing temperature conditions that inhibited the efficiency of thermally activated creep processes. Thus, we favour the model whereby the documented decrease in the recrystallized grain size of quartz towards the BFZ045 fault core reflects the rheological evolution of a narrowing shear zone, which reached peak stress conditions at the BDTZ.

550   **5.3 Conceptual model of the fault slip behaviour of BFZ045 at the base of the seismogenic zone**

In order to estimate the relative contributions of variations in fluid pressure and differential stress in facilitating different fault slip behaviours, we modelled a possible failure mode evolution of BFZ045 using the λ-σ failure mode diagram (Cox, 2010), with the following assumptions and using the following parameters:

-        We assumed a strike-slip Andersonian regime of faulting, according to the deformation history proposed by Mattila
555   and Viola (2014). This is consistent with the dominant strike-slip stretching lineations and slickenlines observed on the core samples. In a strike-slip regime, the vertical stress is σ2, which we assume to correspond to the lithostatic load during deformation. This was estimated at 300-350 MPa during mylonitic creep from the phengite barometer. The maximum differential stress during stage 1 and stage 2 was considered to be in the range between 55 and 60 MPa, whereas during stage 3 and stage 3 to stage 4 transition we consider a differential stress increasing progressively from 73 to 123 MPa. σ1 and σ3
560   values were calculated for a stress ratio R of 0.3 estimated by Mattila and Viola (2014) for the N-S sinistral faults in Olkiluoto. R is defined as R= σ2- σ3/ σ1- σ3

-        Strain rate during mylonitic creep was calculated using the dislocation creep flow law of quartzite Eq. (1):

$$\dot{\varepsilon} = A\sigma^n f_{H2O}^m \exp(-Q/RT)$$

565   (1)

where $\dot{\varepsilon}$ is the strain rate, A an empirical constant, σ the differential stress, n the stress exponent, f_{H2O} the water fugacity, m the water fugacity exponent, Q the activation energy, R the gas constant, and T the temperature. Using the flow law for wet quartzite of Hirth et al. (2001), we estimated the following strain rates during mylonitic creep: $\dot{\varepsilon}$ = 4.3 x 10^{-13} s^{-1} (for a differential stress of 50 MPa during stage 1), $\dot{\varepsilon}$ = 1.1 x 10^{-12} s^{-1} (for a differential stress of 73-80 MPa at the beginning of stage
570   3), and $\dot{\varepsilon}$ =6.9 x 10^{-12} s^{-1} (for the peak stress conditions during stage 3). Water fugacity was calculated with Wither's fugacity calculator based on Pitzer and Sterner (1994) equation of state for 450º and 3.5 Kbar (water fugacity exponent m = 1 in Hirth et al., 2001).

-        We assumed that viscous creep in the mylonite occurred at fluid pressure conditions higher than hydrostatic (λ=0.6),
575   based on the Pf > 210 MPa proposed by Marchesini et al. (2019) for brittle failure under overall ductile conditions of the conjugate fault BFZ300.

-      Failure envelope for λ -σ failure mode diagrams were calculated using a friction coefficient λ of 0.6 (common value for granitoids, e.g. Sibson 1985), a cohesive strength of 26 MPa and a tensile strength of 13 MPa, which were taken from
580 tensile strength measurements of granitic gneisses of Olkiluoto (Aaltonen et al., 2010).

Figure 13 shows the resulting model: stage 1 to stage 3 are representative of the deformation under ductile conditions, while stage 4 represents the final transition to brittle deformation. Failure envelopes were calculated for progressively shallower depths (Figs. 13c, d) in order to account for the progressive exhumation discussed in section 5.2. BFZ045 was initially undergoing ductile deformation at differential stress < 60 MPa and a strain rate of ca. 10^{-13} s^{-1} (Fig. 13a, stage 1), developing
585 a 25-28 µm recrystallized fraction. According to the failure envelope, low differential stresses (<80MPa) are necessary for extensional- and hybrid fractures to occur, therefore the emplacement of the foliation-parallel veins (Fig. 13b, stage 2) must predate the development of the finest recrystallized fractions developed under peak values (ca. 120MPa) of differential stress. While the foliation-parallel veins are consistent with mode I opening mode due to hydrofracturing, the overall geometric stress conditions during ductile deformation of BFZ045 are expected to generate en-echelon vein systems oblique to the foliation.
590 Thus, a transient reorientation of the stress field in the fault zone must be invoked to explain the foliation-parallel veins during stage 2. A regional rotation of the stress field appears unlikely, given the constant orientation of the stretching lineation and slickenlines in the core samples, and the consistent asymmetry of the pre- and post-vein quartz c-axis CPO (Figs. 7-9).

Transient high fluid pressure reaching lithostatic values (λ = 1) during low-differential stress mylonitic creep was necessary to trigger a change in the deformation behaviour, with a switch from viscous creep to mode I fracturing along the mylonite
595 foliation resulting in the emplacement of quartz veins (Fig. 13b, stage 2). The average subgrain size within the vein quartz is 24 µm (although the larger fraction is represented by subgrains smaller than 15 µm), which is similar to the population of the coarser recrystallized grains in the mylonite (Fig. 7). This might indicate that the quartz vein emplaced during an overall low differential stress creep event, which was later overprinted by progressively higher stress deformation as indicated by the subgrains < 15 µm in size and by the average recrystallized grain size of 12 µm both inside the vein and in the surrounding
600 quartz-rich mylonite.

Veining was then followed by a drop in fluid pressure (e.g. Sibson, 1989, 1993; Cox 1995) and a switch back to mylonitic creep (Fig. 13c, stage 3) under progressively higher stress conditions in a narrowing shear zone during slight cooling and exhumation (Fig. 13c, stage 3). Peak stress conditions recorded in the recrystallized grain size of quartz were reached in a highly localized shear zone at the fault core and corresponded to ca. 120 MPa (peak stress and strain rate during stage 3, Fig.
605 13c). Cataclasites and pseudotachylytes overprinted this localised shear zone and formed the brittle fault core of BFZ045 (Fig. 13d, stage 4). In order to meet the brittle shear failure criterion, high values of pore fluid pressure (λ> 0.75) is required at the peak stress of ca. 120MPa, but we cannot rule out that shear failure occurred by a combination of increase in fluid pressure and differential stress after mylonitic creep had ceased (Fig. 13d). Any potential increase of stress beyond the ca. 120 MPa estimated from the 8 µm recrystallized grain size cannot be captured by our microstructural analysis. We must note that the
610 actual path of variation of pore fluid pressure from stage 2 to stage 4 is not known, and we have no control on the extent of

drop of pore fluid pressure after stage 2 (i.e., we do not know the value of λ during stage 3 mylonitic creep and prior to cataclasite formation in stage 4).

In summary, we propose the following conceptual model for the deformation history and the fault slip behaviour of BFZ045 in the Olkiluoto metamorphic basement (Fig. 13):

615

1. Stage 1 is represented by long-term mylonitic creep along a N-S trending shear zone (Fig. 13a);

2. Mylonitic creep was punctuated by the emplacement of foliation-parallel quartz veins (formation of mode I fractures, stage 2; Fig.13b);

3. During stage 3, the mylonite and the veins were overprinted by viscous creep under increased differential stress towards
620 what is now the BFZ045 brittle fault core (Fig.13.c);

4. During stage 4, cataclastic deformation and local generation of pseudotachylytes along the mylonitic foliation overprinted all the pre-existing structures (Fig.13.d).

Conclusions

This study shows that deformation microstructures can be used to evaluate the stress history of a narrowing shear zone
625 deforming across the brittle-ductile transition in the continental crust, and to reconstruct the deformation history of fault zones that experienced cyclical brittle-ductile fault slips. The fault zone BFZ045 exploited a mylonitic precursor in the Paleoproterozoic basement in SW Finland, and records transient brittle deformation in the form of syn-kinematic quartz veins emplaced during ongoing mylonitic creep in response to transiently high fluid pressure. Mylonitic deformation continued after the vein emplacement, as evidenced by the dynamic recrystallization of the vein quartz. Mylonitic creep occurred under
630 progressively increasing differential stress localised towards the shear zone centre in an overall narrowing shear zone that was deforming under slightly decreasing T from 400-500° C to ≥ 320° C. Mylonitic deformation at the shear zone centre records peak stress conditions of around 120 MPa, and was followed by brittle deformation that generated cataclasites and minor pseudotachylytes in the fault core. The entire deformation history documented in this study occurred at the base of the seismogenic crust at an estimated depth range of 9-13 km.

635 The constraints derived from microstructural analysis shaped the proposed conceptual model of the evolution of BFZ045 slip behaviour, which highlights the important role of transiently sub-lithostatic fluid pressure in triggering vein emplacement during ongoing mylonitic deformation, as well as of the progressive increase in stress and strain rate during viscous creep towards peak conditions reached at the BDTZ in the Fennoscandian Shield. This study shows that microstructural study leading to the acquisition of independent constraints offers the potential to reconstruct in detail the evolutionary history of fault zones
640 that experienced a transition in deformation mode at the BDTZ. In addition to deriving a conceptual model of varying fault slip behaviours at the BDTZ, the methods and the results of this work complement and expand thorough site characterization studies of deep geological disposal facilities.

Solid Earth
Discussions

Open Access

EGU

References

Aaltonen, I., Lahti, M., Engström, J., Mattila, J., Paananen, M., Paulamäki, S., Gehör, S., Kärki, A., Ahokas, T., Torvela, T. and Front, K.: Geological Model of the Olkiluoto Site. Version 2.0., Posiva Working Report 2010-70, Posiva Oy, Eurajoki, 2010.

655 Aaltonen, I., Engström, J., Gehör, S., Kosunen, P. and Kärki, A.: Geology of Olkiluoto, Posiva Working Report 2016-16, Posiva Oy, Eurajoki, 2016.

Aoya, M., Kouketsu, Y., Endo, S., Shimizu, H., Mizukami, T., Nakamura, D. and Wallis, S.: Extending the applicability of the Raman carbonaceous-material geothermometer using data from contact metamorphic rocks, Journal of Metamorphic Geology, 28(9), 895–914, doi:10.1111/j.1525-1314.2010.00896.x, 2010.

660 Austrheim, H.: Fluid and deformation induced metamorphic processes around Moho beneath continent collision zones: Examples from the exposed root zone of the Caledonian mountain belt, W-Norway, Tectonophysics, 609, 620–635, doi:10.1016/j.tecto.2013.08.030, 2013.

Behr, W. M. and Platt, J. P.: A naturally constrained stress profile through the middle crust in an extensional terrane, Earth and Planetary Science Letters, 303(3), 181–192, doi:10.1016/j.epsl.2010.11.044, 2011.

665 Bestmann, M. and Prior, D. J.: Intragranular dynamic recrystallization in naturally deformed calcite marble: diffusion accommodated grain boundary sliding as a result of subgrain rotation recrystallization, Journal of Structural Geology, 25(10), 1597–1613, doi:10.1016/S0191-8141(03)00006-3, 2003.

Beyssac, O., Goffé, B., Chopin, C. and Rouzaud, J. N.: Raman spectra of carbonaceous material in metasediments: a new geothermometer, Journal of Metamorphic Geology, 20(9), 859–871, doi:10.1046/j.1525-1314.2002.00408.x, 2002.

670 Bons, P. D., Elburg, M. A. and Gomez-Rivas, E.: A review of the formation of tectonic veins and their microstructures, Journal of Structural Geology, 43, 33–62, doi:10.1016/j.jsg.2012.07.005, 2012.

Bos, B. and Spiers, C. J.: Frictional-viscous flow of phyllosilicate-bearing fault rock: Microphysical model and implications for crustal strength profiles, Journal of Geophysical Research: Solid Earth, 107(B2), ECV 1-1-ECV 1-13, doi:10.1029/2001JB000301, 2002.

675 Ceccato, A., Menegon, L., Pennacchioni, G. and Morales, L. F. G.: Myrmekite and strain weakening in granitoid mylonites, Solid Earth, 9(6), 1399–1419, doi:https://doi.org/10.5194/se-9-1399-2018, 2018.

Cox, S. F.: Faulting processes at high fluid pressures: An example of fault valve behavior from the Wattle Gully Fault, Victoria, Australia, Journal of Geophysical Research: Solid Earth, 100(B7), 12841–12859, doi:10.1029/95JB00915, 1995.

Cox, S. F.: Structural and isotopic constraints on fluid flow regimes and fluid pathways during upper crustal deformation: An 680 example from the Taemas area of the Lachlan Orogen, SE Australia, Journal of Geophysical Research: Solid Earth, 112(B8), doi:10.1029/2006JB004734, 2007.

Cox, S. F.: The application of failure mode diagrams for exploring the roles of fluid pressure and stress states in controlling styles of fracture-controlled permeability enhancement in faults and shear zones, Geofluids, doi:10.1111/j.1468-8123.2010.00281.x, 2010.

685 Cross, A. J., Prior, D. J., Stipp, M. and Kidder, S.: The recrystallized grain size piezometer for quartz: An EBSD-based calibration: EBSD-Based Quartz Grain Size Piezometer, Geophysical Research Letters, 44(13), 6667–6674, doi:10.1002/2017GL073836, 2017.

Derez, T., Pennock, G., Drury, M. and Sintubin, M.: Low-temperature intracrystalline deformation microstructures in quartz, Journal of Structural Geology, 71, 3–23, doi:10.1016/j.jsg.2014.07.015, 2015.

690 Dunlap, W. J., Hirth, G. and Teyssier, C.: Thermomechanical evolution of a ductile duplex, Tectonics, 16(6), 983–1000, doi:10.1029/97TC00614, 1997.

Fossen, H. and Cavalcante, G. C. G.: Shear zones – A review, Earth-Science Reviews, 171, 434–455, doi:10.1016/j.earscirev.2017.05.002, 2017.

Freeman, J. J., Wang, A., Kuebler, K. E., Jolliff, B. L. and Haskin, L. A.: Characterization of natural feldspars by Raman 695 spectroscopy for future planetary exploration, The Canadian Mineralogist, 46(6), 1477–1500, 2008.

Fusseis, F. and Handy, M. R.: Micromechanisms of shear zone propagation at the brittle–viscous transition, Journal of Structural Geology, 30(10), 1242–1253, doi:10.1016/j.jsg.2008.06.005, 2008.

Gueydan, F., Leroy, Y. M., Jolivet, L. and Agard, P.: Analysis of continental midcrustal strain localization induced by microfracturing and reaction-softening, Journal of Geophysical Research: Solid Earth, 108(B2), doi:10.1029/2001JB000611, 700 2003.

Handy, M. R. and Brun, J.-P.: Seismicity, structure and strength of the continental lithosphere, Earth and Planetary Science Letters, 223(3), 427–441, doi:10.1016/j.epsl.2004.04.021, 2004.

Handy, M. R., Franz, L., Heller, F., Janott, B. and Zurbriggen, R.: Multistage accretion and exhumation of the continental crust (Ivrea crustal section, Italy and Switzerland), Tectonics, 18(6), 1154–1177, doi:10.1029/1999TC900034, 1999.

705 Handy, M. R., Hirth, G. and Hovius, N.: Continental Fault Structure and Rheology from the Frictional-to-Viscous Transition Downward, in Tectonic Faults: Agents of Change on a Dynamic Earth, MITP. [online] Available from: https://ieeexplore.ieee.org/document/6285583 (Accessed 13 July 2019), 2007.

Hey, M. H.: A new review of the chlorites, Mineral. Mag. J. M. Soc., 224, 277–292, https://doi.org/10.1180/minmag.1954.030.224.01, 1954.

710 Hirth, G. and Beeler, N. M.: The role of fluid pressure on frictional behavior at the base of the seismogenic zone, Geology, 43(3), 223–226, doi:10.1130/G36361.1, 2015.

Hirth, G. and Tullis, J.: Dislocation creep regimes in quartz aggregates, Journal of Structural Geology, 14(2), 145–159, doi:10.1016/0191-8141(92)90053-Y, 1992.

Hirth, G. and Tullis, J.: The brittle-plastic transition in experimentally deformed quartz aggregates, Journal of Geophysical

715 Research: Solid Earth, 99(B6), 11731–11747, doi:10.1029/93JB02873, 1994.

Hirth, G., Teyssier, C. and Dunlap, J. W.: An evaluation of quartzite flow laws based on comparisons between experimentally and naturally deformed rocks, Int J Earth Sci, 90(1), 77–87, doi:10.1007/s005310000152, 2001.

Kärki, A. and Paulamäki, S.: Petrology of Olkiluoto, 2006.

Kidder, S., Hirth, G., Avouac, J.-P. and Behr, W.: The influence of stress history on the grain size and microstructure of

720 experimentally deformed quartzite, Journal of Structural Geology, 83, 194–206, doi:10.1016/j.jsg.2015.12.004, 2016.

Kirilova, M., Toy, V., Rooney, J. S., Giorgetti, C., Gordon, K. C., Collettini, C. and Takeshita, T.: Structural disorder of graphite and implications for graphite thermometry., Solid Earth, 9(1), 2018.

Kjøll, H. J., Viola, G., Menegon, L. and Sørensen, B. E.: Brittle–viscous deformation of vein quartz under fluid-rich lower greenschist facies conditions, Solid Earth, 6(2), 681–699, doi:https://doi.org/10.5194/se-6-681-2015, 2015.

725 Kohlstedt, D. L., Evans, B. and Mackwell, S. J.: Strength of the lithosphere: Constraints imposed by laboratory experiments, Journal of Geophysical Research: Solid Earth, 100(B9), 17587–17602, doi:10.1029/95JB01460, 1995.

Kouketsu, Y., Mizukami, T., Mori, H., Endo, S., Aoya, M., Hara, H., Nakamura, D. and Wallis, S.: A new approach to develop the Raman carbonaceous material geothermometer for low-grade metamorphism using peak width, Island Arc, 23(1), 33–50, doi:10.1111/iar.12057, 2014.

730 Kukkonen, I. T. and Lauri, L. S.: Modelling the thermal evolution of a collisional Precambrian orogen: High heat production migmatitic granites of southern Finland, Precambrian Research, 168(3), 233–246, doi:10.1016/j.precamres.2008.10.004, 2009.

Küster, M. and Stöckhert, B.: High differential stress and sublithostatic pore fluid pressure in the ductile regime — microstructural evidence for short-term post-seismic creep in the Sesia Zone, Western Alps, Tectonophysics, 303(1), 263–277, doi:10.1016/S0040-1951(98)00256-X, 1999.

735 Lafuente, B., Downs, R. T., Yang, H. and Stone, N.: The power of databases: the RRUFF project, in Highlights in mineralogical crystallography, pp. 1–29, Walter de Gruyter GmbH., 2016.

Lahtinen, R.: Crustal evolution of the Svecofennian and Karelian domains during 2.1 - 1.79 Ga: with special emphasis on the geochemistry and origin of 1.93 - 1.91 Ga gneissic tonalites and associated supracrustal rocks in the Rautalampi area, central Finland ; with 7 tables, Geologian Tutkimuskeskus, Espoo., 1994.

740 Lahtinen, R., Korja, A. and Nironen, M.: Chapter 11 Paleoproterozoic tectonic evolution, in Developments in Precambrian Geology, vol. 14, edited by M. Lehtinen, P. A. Nurmi, and O. T. Rämö, pp. 481–531, Elsevier., 2005.

Lanari, P., Wagner, T. and Vidal, O.: A thermodynamic model for di-trioctahedral chlorite from experimental and natural data in the system MgO–FeO–Al 2 O 3–SiO 2–H 2 O: applications to P–T sections and geothermometry, Contributions to Mineralogy and Petrology, 167(2), 968, 2014.

745 Mänttäri, I., Talikka, M., Paulamäki, S. and Mattila, J.: U-Pb ages for tonalitic gneiss, pegmatitic granite, and diabase dyke, Olkiluoto study site, Eurajoki, SW Finland, Posiva Oy., 2006.

Mänttäri, I., Engstroem, J., Lahaye, Y. and Pere, T.: U-Pb ages for PGR dykes, KFP, and adjacent older leucosomic PGRs from ONKALO underground research facility, Olkiluoto, Eurajoki, SW Finland, Posiva Oy., 2010.

Marchesini, B., Garofalo, P. S., Menegon, L., Mattila, J. and Viola, G.: Fluid-mediated, brittle–ductile deformation at 750 seismogenic depth – Part 1: Fluid record and deformation history of fault veins in a nuclear waste repository (Olkiluoto Island, Finland), Solid Earth, 10(3), 809–838, doi:https://doi.org/10.5194/se-10-809-2019, 2019.

Massonne, H.-J. and Schreyer, W.: Phengite geobarometry based on the limiting assemblage with K-feldspar, phlogopite, and quartz, Contributions to Mineralogy and Petrology, 96(2), 212–224, 1987.

Mattila, J. and Viola, G.: New constraints on 1.7 Gyr of brittle tectonic evolution in southwestern Finland derived from a 755 structural study at the site of a potential nuclear waste repository (Olkiluoto Island), Journal of Structural Geology, 67, 50–74, 2014.

Melosh, B. L., Rowe, C. D., Gerbi, C., Smit, L. and Macey, P.: Seismic cycle feedbacks in a mid-crustal shear zone, Journal of Structural Geology, 112, 95–111, doi:10.1016/j.jsg.2018.04.004, 2018.

Menegon, L., Pennacchioni, G., Malaspina, N., Harris, K. and Wood, E.: Earthquakes as Precursors of Ductile Shear Zones in 760 the Dry and Strong Lower Crust, Geochemistry, Geophysics, Geosystems, 18(12), 4356–4374, doi:10.1002/2017GC007189, 2017.

Nguyen, P. T., Harris, L. B., Powell, C. M. and Cox, S. F.: Fault-valve behaviour in optimally oriented shear zones: an example at the Revenge gold mine, Kambalda, Western Australia, Journal of Structural Geology, 20(12), 1625–1640, doi:10.1016/S0191-8141(98)00054-6, 1998.

765 Nironen, M.: The Svecofennian Orogen: a tectonic model, Precambrian Research, 86(1–2), 21–44, 1997.

Nordbäck, N. and Mattila, J.: Brittle Fault Systems of the ONKALO Underground Research Facility, 2018.

Pajunen, M., Airo, M., Elminen, T., Mänttäri, I., Niemelä, R., Vaarma, M., Wasenius, P. and Wennerström, M.: Tectonic evolution of the Svecofennian crust in southern Finland, Geological Survey of Finland, Special Paper, 47, 15–160, 2008.

Pennacchioni, G. and Mancktelow, N. S.: Nucleation and initial growth of a shear zone network within compositionally and

770 structurally heterogeneous granitoids under amphibolite facies conditions, Journal of Structural Geology, 29(11), 1757–1780, doi:10.1016/j.jsg.2007.06.002, 2007.

Pere, T.: Fault-related local phenomena in the bedrock of Olkiluoto with particular reference to fault zone OL-BFZ100, Posiva Oy., 2009.

Pfiffner, O. A.: Basement-involved thin-skinned and thick-skinned tectonics in the Alps, Geological Magazine, 153(5–6),

775 1085–1109, doi:10.1017/S0016756815001090, 2016.

Pitzer, K. S. and Sterner, S. M.: Equations of state valid continuously from zero to extreme pressures for H2O and CO2, J. Chem. Phys., 101(4), 3111–3116, doi:10.1063/1.467624, 1994.

Ranalli, G.: Rheology of the lithosphere in space and time, Geological Society, London, Special Publications, 121(1), 19–37, doi:10.1144/GSL.SP.1997.121.01.02, 1997.

780 Saintot, A., Stephens, M., Viola, G. and Nordgulen, Ø.: Brittle tectonic evolution and paleostress field reconstruction in the southwestern part of the Fennoscandian Shield, Forsmark, Sweden, Tectonics, 30(4), 2011.

Scholz, C.: The Mechanics of Earthquakes and Faulting, Cambridge University Press, Cambridge., 1990.

Scholz, C. H.: Earthquakes and friction laws, Nature, 391(6662), 37, doi:10.1038/34097, 1998.

Sibson, R. H.: Fault zone models, heat flow, and the depth distribution of earthquakes in the continental crust of the United

785 States, Bulletin of the Seismological Society of America, 72(1), 151–163, 1982.

Sibson, R. H.: A note on fault reactivation, Journal of Structural Geology, 7(6), 751–754, doi:10.1016/0191-8141(85)90150-6, 1985.

Sibson, R. H.: Earthquake faulting as a structural process, Journal of Structural Geology, 11(1), 1–14, doi:10.1016/0191-8141(89)90032-1, 1989.

790 Sibson, R. H.: Conditions for fault-valve behaviour, Geological Society, London, Special Publications, 54(1), 15–28, doi:10.1144/GSL.SP.1990.054.01.02, 1990.

Sibson, R. H.: Implications of fault-valve behaviour for rupture nucleation and recurrence, Tectonophysics, 211(1), 283–293, doi:10.1016/0040-1951(92)90065-E, 1992.

Sibson, R. H.: Load-strengthening versus load-weakening faulting, Journal of Structural Geology, 15(2), 123–128,

795 doi:10.1016/0191-8141(93)90090-W, 1993.

Sibson, R. H. and Rowland, J. V.: Stress, fluid pressure and structural permeability in seismogenic crust, North Island, New Zealand, Geophys J Int, 154(2), 584–594, doi:10.1046/j.1365-246X.2003.01965.x, 2003.

Skyttä, P. and Torvela, T.: Brittle reactivation of ductile precursor structures: The role of incomplete structural transposition at a nuclear waste disposal site, Olkiluoto, Finland, Journal of Structural Geology, 116, 253–259, 2018.

800 Stipp, M. and Kunze, K.: Dynamic recrystallization near the brittle-plastic transition in naturally and experimentally deformed quartz aggregates, Tectonophysics, 448(1), 77–97, doi:10.1016/j.tecto.2007.11.041, 2008.

Stipp, M. and Tullis, J.: The recrystallized grain size piezometer for quartz, Geophysical Research Letters, 30(21), doi:10.1029/2003GL018444, 2003.

805 Stipp, M., Stünitz, H., Heilbronner, R. and Schmid, S. M.: The eastern Tonale fault zone: a 'natural laboratory' for crystal plastic deformation of quartz over a temperature range from 250 to 700°C, Journal of Structural Geology, 24(12), 1861–1884, doi:10.1016/S0191-8141(02)00035-4, 2002.

Stipp, M., Tullis, J., Scherwath, M. and Behrmann, J. H.: A new perspective on paleopiezometry: Dynamically recrystallized grain size distributions indicate mechanism changes, Geology, 38(8), 759–762, doi:10.1130/G31162.1, 2010.

Stöckhert, B., Brix, M. R., Kleinschrodt, R., Hurford, A. J. and Wirth, R.: Thermochronometry and microstructures of quartz—

810 a comparison with experimental flow laws and predictions on the temperature of the brittle–plastic transition, Journal of Structural Geology, 21(3), 351–369, doi:10.1016/S0191-8141(98)00114-X, 1999.

Streit, J. E. and Cox, S. F.: Fluid pressures at hypocenters of moderate to large earthquakes, Journal of Geophysical Research: Solid Earth, 106(B2), 2235–2243, doi:10.1029/2000JB900359, 2001.

Stünitz, H., Fitz Gerald, J. D. and Tullis, J.: Dislocation generation, slip systems, and dynamic recrystallization in

815 experimentally deformed plagioclase single crystals, Tectonophysics, 372(3), 215–233, doi:10.1016/S0040-1951(03)00241-5, 2003.

Suominen, V.: The chronostratigraphy of southwestern Finland with special reference to Postjotnian and Subjotnian diabases, Espoo., 1991.

Torvela, T. and Ehlers, C.: From ductile to brittle deformation: structural development and strain distribution along a crustal-

820 scale shear zone in SW Finland, International Journal of Earth Sciences, 99(5), 1133–1152, 2010.

Trepmann, C. A. and Seybold, L.: Deformation at low and high stress-loading rates, Geoscience Frontiers, 10(1), 43–54, doi:10.1016/j.gsf.2018.05.002, 2019.

Trepmann, C. A. and Stöckhert, B.: Quartz microstructures developed during non-steady state plastic flow at rapidly decaying stress and strain rate, Journal of Structural Geology, 25(12), 2035–2051, doi:10.1016/S0191-8141(03)00073-7, 2003.

825 Trepmann, C. A. and Stöckhert, B.: Short-wavelength undulatory extinction in quartz recording coseismic deformation in the middle crust – an experimental study, Solid Earth, 4(2), 263–276, doi:https://doi.org/10.5194/se-4-263-2013, 2013.

Trepmann, C. A., Stöckhert, B., Dorner, D., Moghadam, R. H., Küster, M. and Röller, K.: Simulating coseismic deformation of quartz in the middle crust and fabric evolution during postseismic stress relaxation — An experimental study, Tectonophysics, 442(1), 83–104, doi:10.1016/j.tecto.2007.05.005, 2007.

830 Trepmann, C. A., Hsu, C., Hentschel, F., Döhler, K., Schneider, C. and Wichmann, V.: Recrystallization of quartz after low-temperature plasticity – The record of stress relaxation below the seismogenic zone, Journal of Structural Geology, 95, 77–92, doi:10.1016/j.jsg.2016.12.004, 2017.

Tuisku, P. and Kärki, A.: Metamorphic petrology of Olkiluoto, Posiva Oy., 2010.

Viola, G., Mancktelow, N. S. and Miller, J. A.: Cyclic frictional-viscous slip oscillations along the base of an advancing nappe

835   complex: Insights into brittle-ductile nappe emplacement mechanisms from the Naukluft Nappe Complex, central Namibia, Tectonics, 25(3), doi:10.1029/2005TC001939, 2006.

Viola, G., Venvik Ganerød, G. and Wahlgren, C.-H.: Unraveling 1.5 Ga of brittle deformation history in the Laxemar-Simpevarp area, southeast Sweden: A contribution to the Swedish site investigation study for the disposal of highly radioactive nuclear waste, Tectonics, 28(5), doi:10.1029/2009TC002461, 2009.

840   Wehrens, P., Berger, A., Peters, M., Spillmann, T. and Herwegh, M.: Deformation at the frictional-viscous transition: Evidence for cycles of fluid-assisted embrittlement and ductile deformation in the granitoid crust, Tectonophysics, 693, 66–84, doi:10.1016/j.tecto.2016.10.022, 2016.

White, J. C.: Transient discontinuities revisited: pseudotachylyte, plastic instability and the influence of low pore fluid pressure on deformation processes in the mid-crust, Journal of Structural Geology, 18(12), 1471–1486, doi:10.1016/S0191-

845   8141(96)00059-4, 1996.

White, J. C.: Paradoxical pseudotachylyte – Fault melt outside the seismogenic zone, Journal of Structural Geology, 38, 11–20, doi:10.1016/j.jsg.2011.11.016, 2012.

Yardley, B. and Baumgartner, L.: Fluid processes in deep crustal fault zones, Tectonic Faults–Agents of Change on a Dynamic Earth, 295–318, 2007.

850

Sample name	PH28_7a		PH28_7b		PH28_5a		PH28_5b		PH28_5c		PH28_5d		PH28_9		PH28_10	
N. measurement	n=5		n=5		n=15		n=18		n=12		n=16		n=8		n=10	
		s.d.		s.d.		s.d.		s.d.		s.d.		s.d.		s.d.		s.d.
SiO_2	47.74	0.36	47.90	0.16	47.95	0.25	48.02	0.37	47.81	0.39	48.17	0.39	47.70	0.57	47.40	0.51
TiO_2	0.08	0.01	0.08	0.03	0.09	0.03	0.07	0.04	0.06	0.04	0.10	0.03	0.16	0.14	0.11	0.05
Al_2O_3	34.09	0.32	34.20	0.42	34.24	0.54	34.17	0.52	34.31	0.35	34.05	0.70	34.86	0.82	34.92	0.47
Cr_2O_3	0.01	0.01	0.01	0.02	0.01	0.02	0.02	0.02	0.02	0.03	0.01	0.01	0.02	0.01	0.01	0.01
Fe_2O_3	0.00	0.00	0.00	0.00	0.00	0.00	0.00	0.00	0.00	0.00	0.00	0.00	0.00	0.00	0.00	0.00
FeO	2.38	0.24	2.37	0.14	2.21	0.29	2.25	0.18	2.21	0.14	2.24	0.46	2.89	0.21	2.63	0.00
MnO	0.03	0.03	0.03	0.02	0.02	0.02	0.02	0.02	0.03	0.02	0.01	0.02	0.03	0.03	0.02	0.02
MgO	1.49	0.07	1.38	0.05	1.38	0.15	1.47	0.12	1.41	0.04	1.45	0.21	0.99	0.47	1.35	0.11
CaO	0.01	0.01	0.02	0.01	0.07	0.19	0.02	0.02	0.03	0.03	0.02	0.01	0.01	0.01	0.03	0.02
Na_2O	0.12	0.02	0.14	0.03	0.13	0.02	0.13	0.03	0.14	0.01	0.15	0.03	0.13	0.02	0.16	0.02
K_2O	11.15	0.06	11.06	0.11	11.07	0.08	11.06	0.09	11.01	0.18	11.09	0.08	9.48	0.28	10.85	0.14
NiO	0.01	0.01	0.01	0.01	0.01	0.02	0.01	0.02	0.02	0.03	0.02	0.02	0.00	0.00	0.04	0.03
Structural formulae on the basis of 11 O																
		s.d.		s.d.		s.d.		s.d.		s.d.		s.d.		s.d.		s.d.
Si	3.14	0.02	3.14	0.02	3.14	0.01	3.15	0.02	3.16	0.02	3.15	0.02	3.13	0.02	3.10	0.03
Ti	0.00	0.00	0.00	0.00	0.00	0.00	0.00	0.00	0.00	0.00	0.00	0.00	0.01	0.01	0.01	0.00
Al	2.64	0.02	2.64	0.03	2.65	0.03	2.64	0.04	2.61	0.04	2.63	0.05	2.70	0.04	2.69	0.04
Cr	0.00	0.00	0.00	0.00	0.00	0.00	0.00	0.00	0.00	0.00	0.00	0.00	0.00	0.00	0.00	0.00
Fe^{3+}	0.00	0.00	0.00	0.00	0.00	0.00	0.00	0.00	0.00	0.00	0.00	0.00	0.00	0.00	0.00	0.00
Fe^{2+}	0.13	0.01	0.13	0.01	0.12	0.02	0.12	0.01	0.13	0.01	0.12	0.03	0.16	0.01	0.14	0.02
Mn	0.00	0.00	0.00	0.00	0.00	0.00	0.00	0.00	0.00	0.00	0.00	0.00	0.00	0.00	0.00	0.00
Mg	0.15	0.01	0.14	0.01	0.14	0.01	0.14	0.01	0.15	0.02	0.14	0.02	0.10	0.05	0.13	0.01
Ca	0.00	0.00	0.00	0.00	0.00	0.01	0.00	0.00	0.00	0.00	0.00	0.00	0.00	0.00	0.00	0.00
Na	0.01	0.00	0.02	0.00	0.02	0.00	0.02	0.00	0.01	0.00	0.02	0.00	0.02	0.00	0.02	0.00
K	0.94	0.01	0.93	0.01	0.93	0.01	0.92	0.01	0.93	0.00	0.93	0.01	0.79	0.03	0.91	0.01
Ni	0.00	0.00	0.00	0.00	0.00	0.00	0.00	0.00	0.00	0.00	0.00	0.00	0.00	0.00	0.00	0.00

Table 1. Average compositions EPMA of white mica along the foliation.

Fault rock	Mylonite		Cataclasite	Veins
Sample name	PH28_10	Ph16_2	Ph28_9	P28_6
N. measurament	14	8	23	15
Chemical composition (wt%)				
SiO2	25.830	25.240	23.520	24.430
TiO2	0.081	0.038	0.086	0.057
Al2O3	21.750	22.080	23.160	21.880
FeO	29.850	30.420	36.430	36.570
MnO	0.480	0.290	1.056	0.981
MgO	12.190	11.210	5.710	6.720
CaO	0.020	0.077	0.015	0.054
Na2O	0.049	0.056	0.017	0.023
K2O	0.025	0.062	0.101	0.012
Total	90.274	89.473	90.095	90.726
Structural formulae on the basis of 14 O				
Si	2.701	2.673	2.571	2.648
Ti	0.006	0.003	0.007	0.005
Al	2.680	2.756	2.984	2.795
Fe3+	0.000	0.000	0.000	0.000
Fe2+	2.610	2.695	3.330	3.315
Mn	0.043	0.026	0.098	0.090
Mg	1.900	1.770	0.930	1.086
Ca	0.002	0.009	0.002	0.006
Na	0.010	0.011	0.004	0.005
K	0.003	0.008	0.014	0.002
XFe= Fe/(Fe+Mg)	0.579	0.604	0.782	0.753

Table2. Representative chlorite EPMA for structural zones of fault core of BFZ045.

(a)

400 Km

N

1 Km

(b)

A

B

Repository level

-500 m

BFZ 045   BFZ 300

-1000 m

Migmatites   TTG-style granitoids   Granitic pegmatite   500 m

D4 deformation zone   —— Fault zone
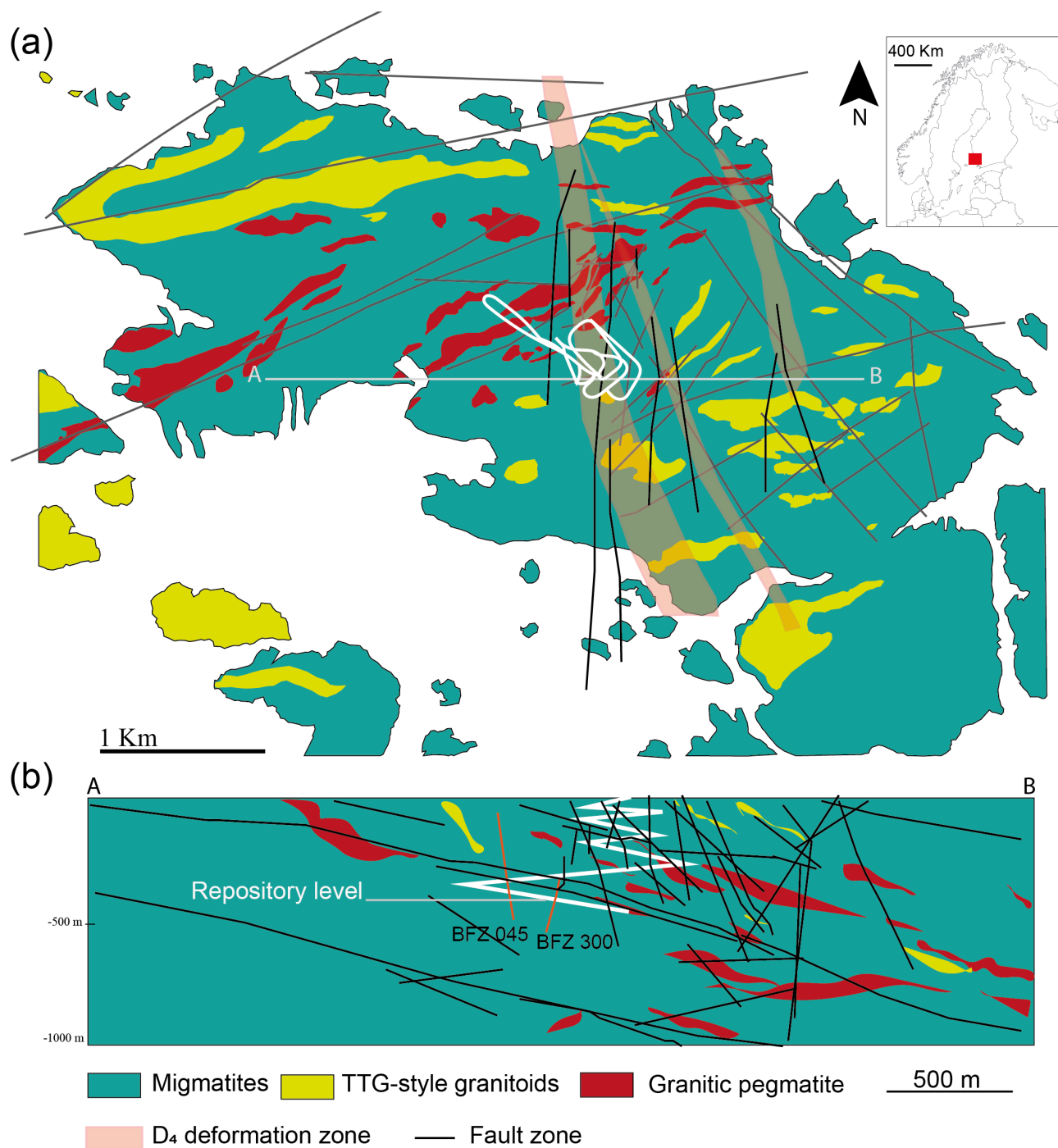
Figure 1. Geological setting of Olkiluoto, SW Finland (inset on top-right). (a) Schematic geological and structural map, showing surface intersection of modelled brittle fault zone (BFZ) and ductile deformation zone, modified from Aaltonen et al. (2016) and Skytta and Torvela (2018). The white line indicates the location of the underground Onkalo facility. A-B is the trace of the cross section shown in (b). (b) East-west cross section across the underground infrastructure, with the tunnel shown as white line. Sub vertical fault BFZ045 described in this study and its conjugate BFZ300 are shown as orange lines.

860
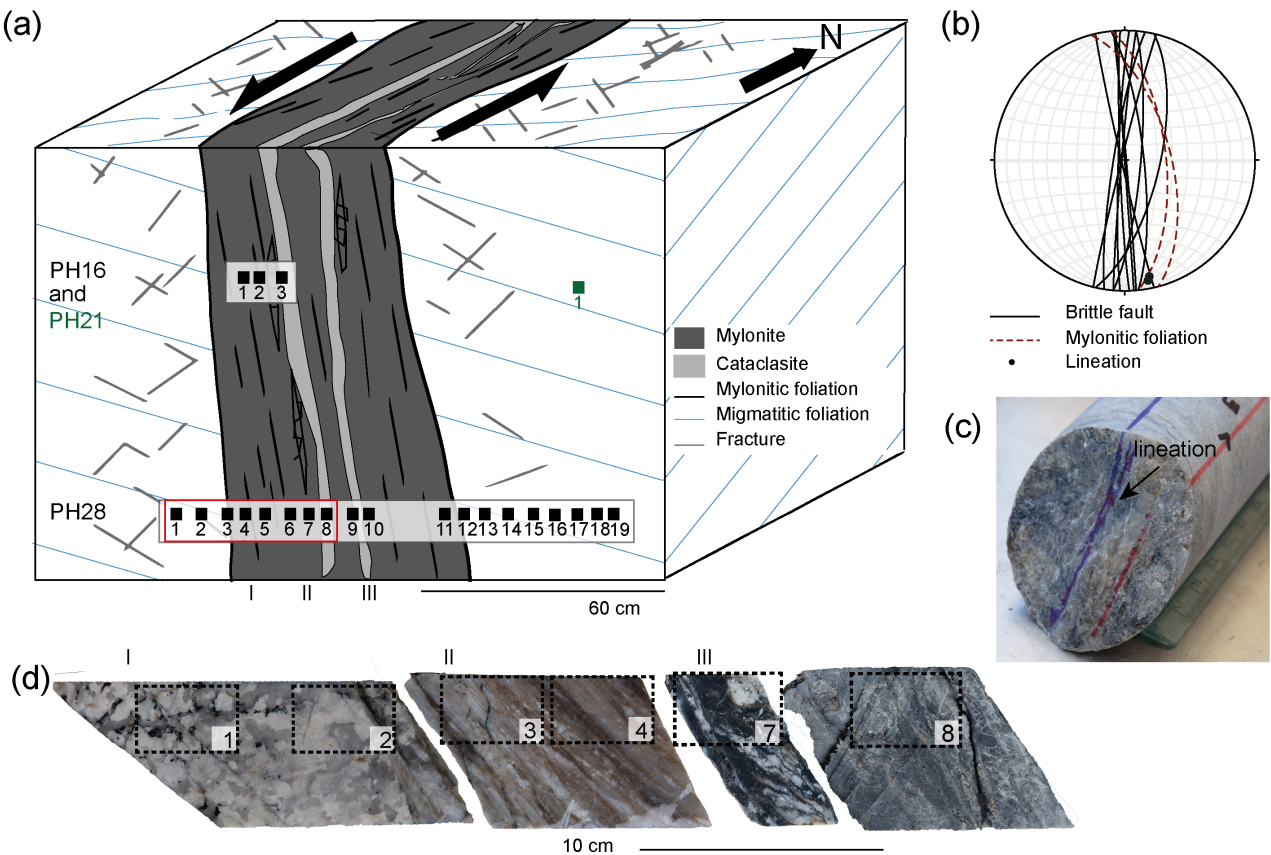
Figure 2. BFZ045 fault geometry. (a) Schematic representation of fault architecture from core logs, vertical axis not to scale. Grey rectangles locate the studied drill cores PH28 and PH16, black squares show sample location. The red rectangle indicates the samples shown in (d). (b) Stereoplot of BFZ045 fault core orientation and mylonitic foliation observed at different drill hole intersection along the Onkalo facility (Aaltonen et al., 2016). (c) Core sample along PH28 drill core within the fault core unit. The core sample exposes the mylonitic foliation, where the blue line indicates the stretching lineation, which is parallel to chlorite striae. The red line indicates the lower part of the core (d) Samples from PH28 drill core representative of the fault units: damaged coarse-grained host rock (I), and fault core with mylonites and chlorite rich cataclasites (II-III). Dashed lines outline the area of petrographic thin sections.

865

870
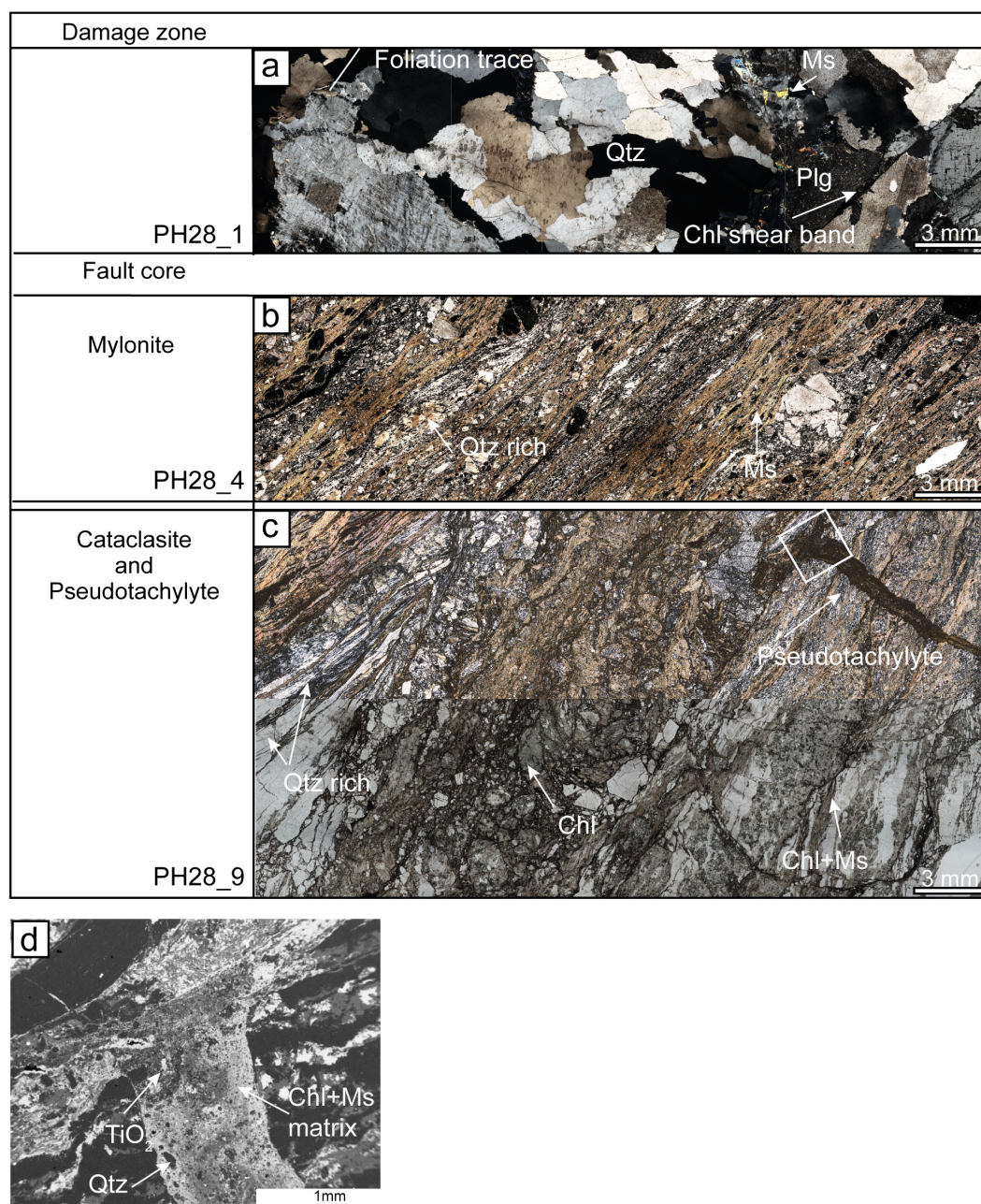
Figure 3. Polarized light microscope images of characteristic lithologies for the damage zone (a) and fault core (b-c). Stitched microphotographs in cross-polarized light and plane polarized light. (a) Damage zone shows the original magmatic textures and mineral assemblage of the host rock. White arrow shows a chlorite-rich shear band oriented at a low angle to the mylonitic foliation of the fault core. (b) Mylonite in the fault core. Foliation is defined by the alternation of quartz-rich and mica-rich domains. Porphyroclasts of feldspars are preferentially located in mica-rich domains. (c) Fault core cataclasite with characteristic pseudotachylyte injection veins (arrow). The cataclasite matrix is enriched in chlorite and Ti-oxides. (d) Scanning electron microscope (SEM) image of the pseudotachylyte injection vein. Rounded quartz clast (dark grey) and Ti-oxides (white) are surrounded by a chlorite and mica rich ultrafine grained matrix.

875

880

31

Solid Earth
Discussions
Open Access
EGU
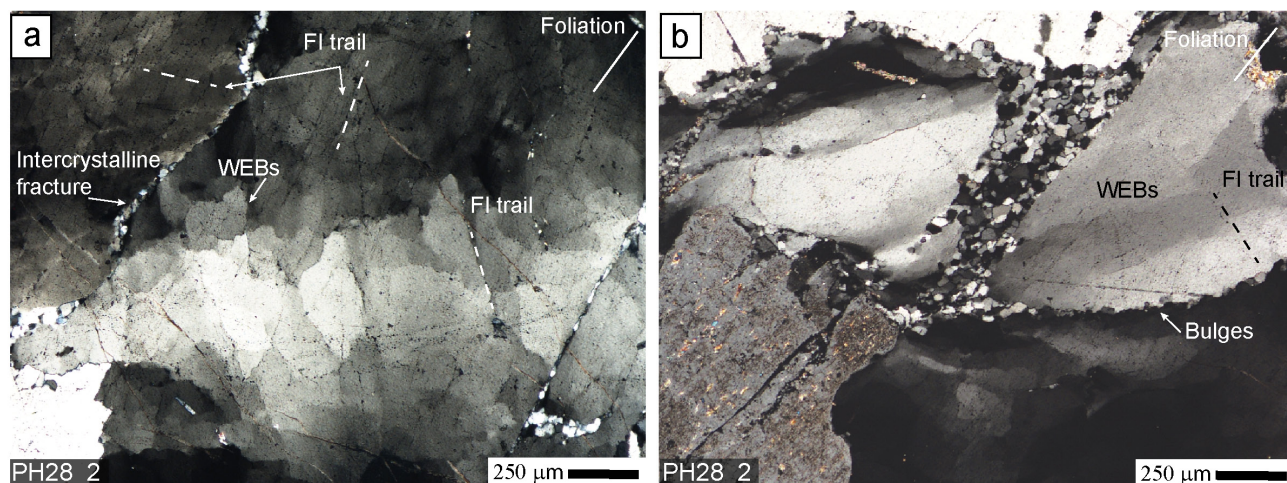
Figure 4. Quartz microstructures in the damage zone. Cross polarized light. (a) Quartz with wide extinction bands (WEBs) and undulatory extinction. WEBs are bounded by sets of fluid inclusions trails (FI trail, dashed lines). Intercrystalline deformation bands and well-developed FI trails developed sub-parallel to the foliation. (b) Polygonal recrystallized quartz grains, with small grain size (~20 µm), forming bands oriented sub-parallel to the foliation. The white arrow shows sutured grain boundaries between magmatic quartz grains, indicative of bulging.

885
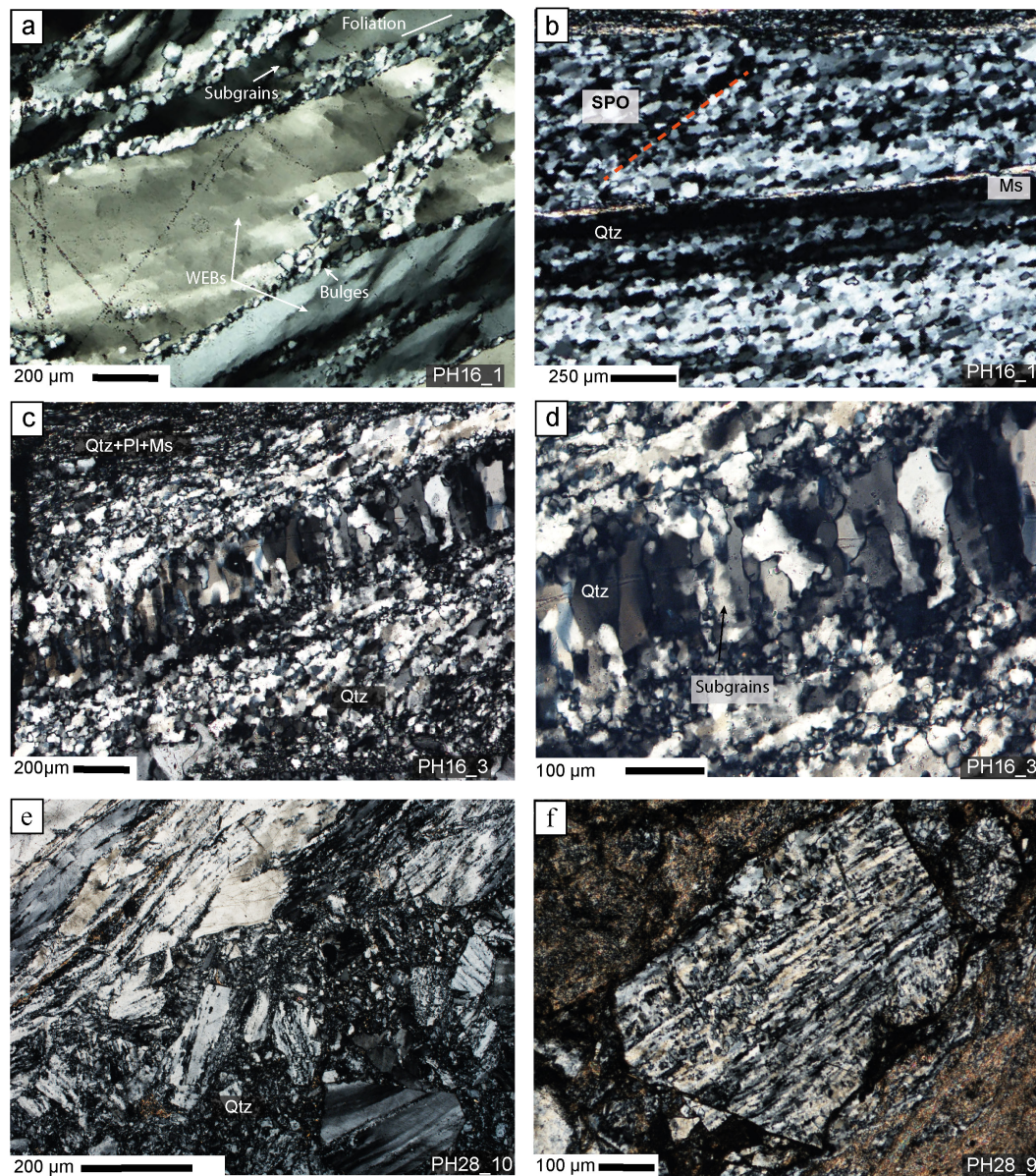
Figure 5. Quartz microstructures in the fault core. Microphotograph in cross polarized light. (a)Quartz ribbons in the shear zone boundary are stretched along the foliation and show typical core-and-mantle microstructure, with recrystallization localized at the grain boundaries. Ribbons contain also well-developed WEBs. (b) Completely recrystallized quartz ribbon. The recrystallized grains show a shape preferred orientation indicating a sinistral sense of shear. Thin muscovite (Ms) layers define the mylonitic foliation, together with the elongated and recrystallized quartz domains. (c) Quartz veins along the foliation, infilling of a mode I fracture at a distance of ~ 1cm from the cataclasite fault core. Quartz grains elongation in the veins is normal to the vein wall and to the foliation. (d) High magnification view of the quartz infilling the vein. Bulges along the grain boundaries, and subgrains within the grains are visible. (e) Contact between the mylonite and the cataclasite. Quartz form almost entirely recrystallized polycrystalline ribbons. (f) Detail of a sub-angular polycrystalline clast of quartz in the cataclasite.The trace of the mylonitic foliation is still visible in the clast, and is only slightly rotated with respect to the trace of the foliation in the mylonite. The surrounding matrix is a fine mixture of white mica and plagioclase.
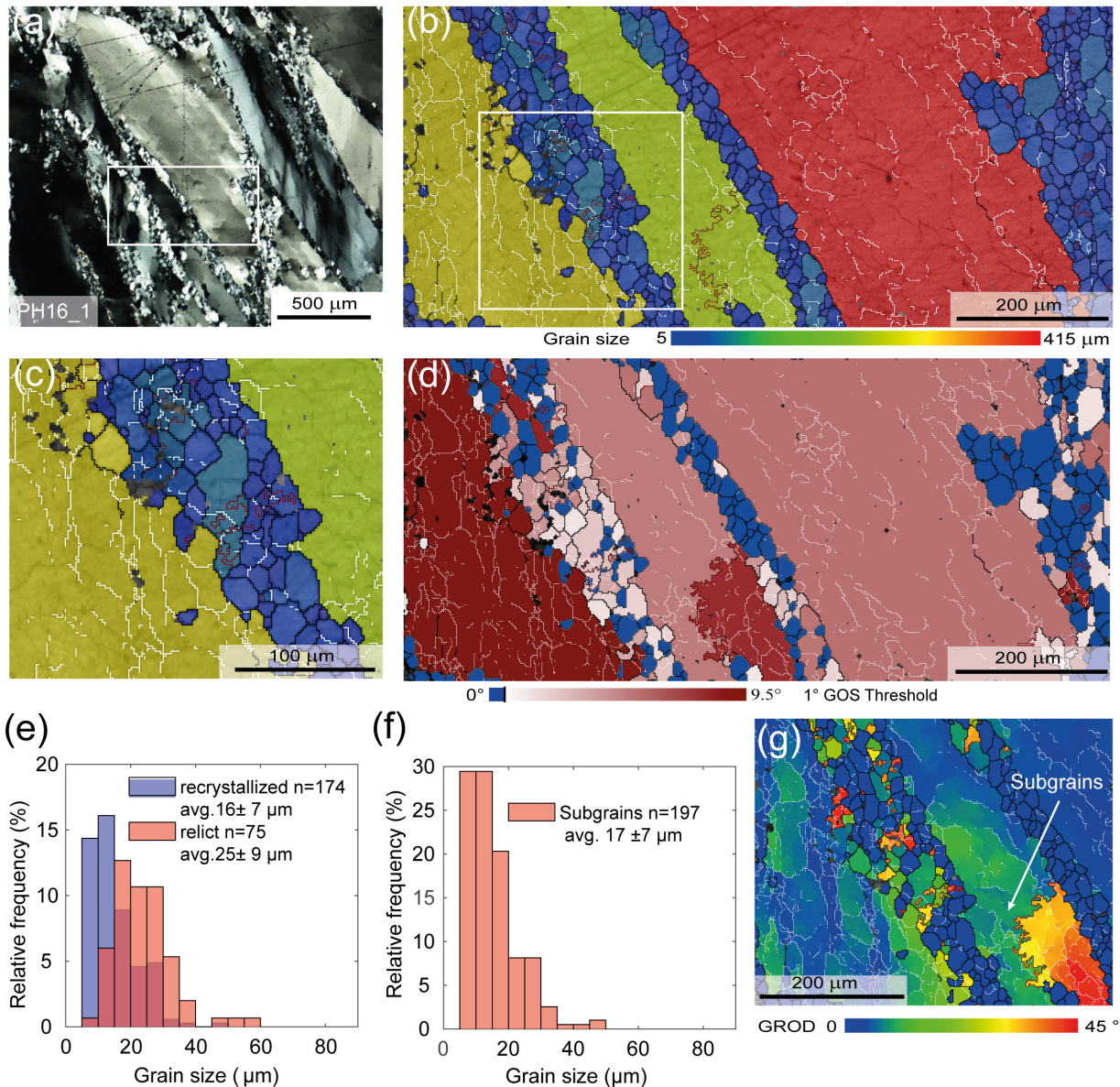
33

Figure 6. EBSD data of quartz from the mylonitic fault core. In all the EBSD maps, black lines correspond to high-angle boundaries (misorientation > 10°), white lines to low-angle boundaries (misorientation between 2° and 10°), and red lines to Dauphiné twin boundaries (misorientation of 60° around the c-axis). (a) Quartz ribbons and intracrystalline bands of recrystallized grains (Fig. 5a). Cross polarized light. The box locates the EBSD map shown in (b-d, g). (b-c) Grain size map (diameter of the equivalent circle, μm), the higher magnification in (c) highlights the presence of subgrains in the large relict quartz grains and in the recrystallized grains. (d) Grain orientation spread (GOS) for each grain, coloured relative to the GOS threshold (black line) between recrystallized (blue) and relict (red) grains. (e) Histogram of grains size distribution of grains in the intercrystalline bands. (f) Histogram of subgrains size distribution of subgrains in the relict quartz from the intercrystalline bands (light red in (d)). (g) Grain Orientation Distribution maps (GROD) was used to estimate visually the subgrains size in the quartz ribbon.

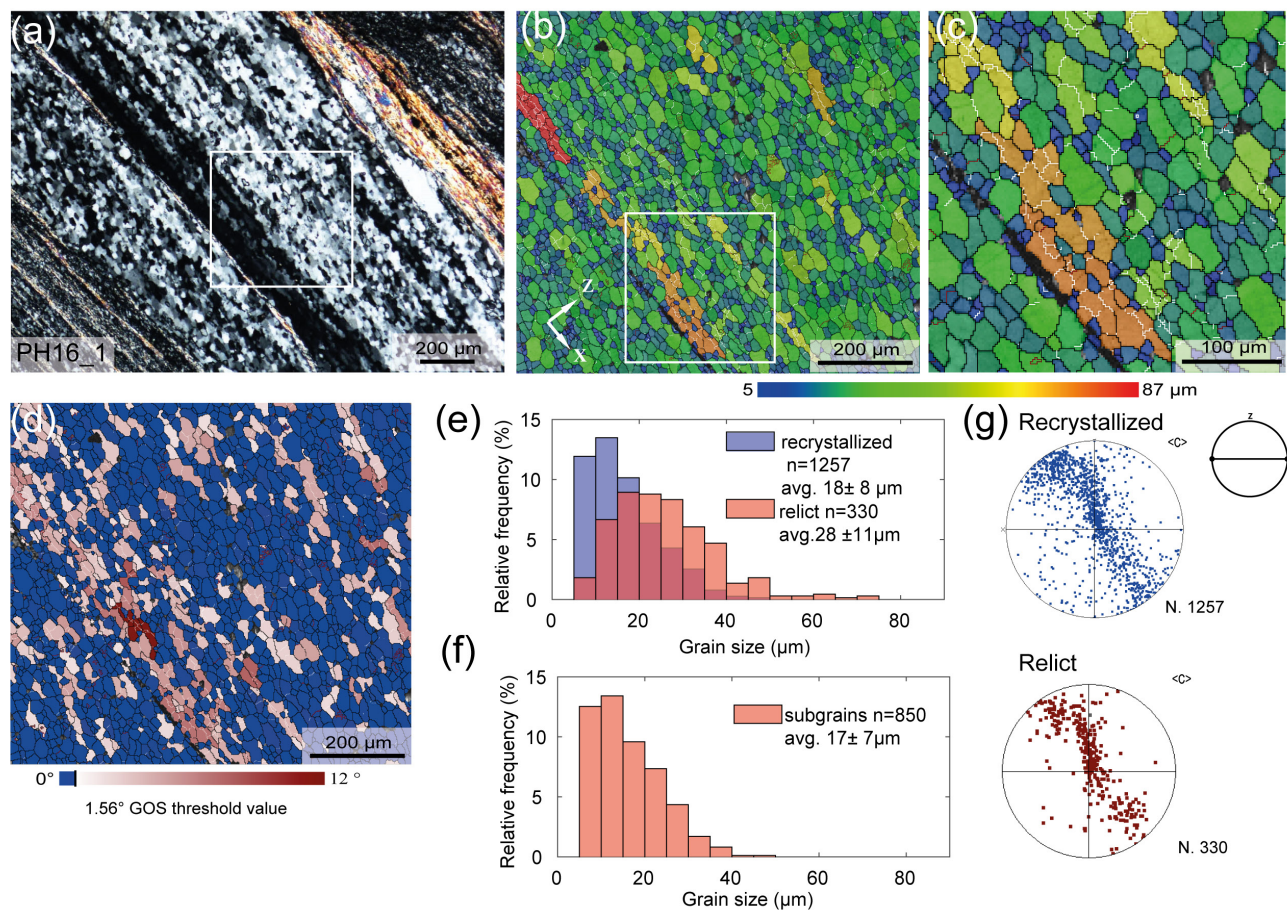Solid Earth
Discussions
Open Access
EGU

Figure 7. EBSD data of quartz from a recrystallized ribbon in the mylonite. (a) Polycrystalline ribbons of recrystallized quartz grains elongated parallel to the mylonitic foliation (Fig. 5b). Cross polarized light. The box indicates the EBSD maps shown in (b-d). Colour coding of the boundaries like in Figure 6. (b, c) Grain size map (diameter of the equivalent circle, μm) and detail (c) showing that the larger grains contain subgrains of the same size as the surrounding finer grains.(d) GOS map showing that the GOS values are mostly under the threshold, indicative of high degree of recrystallization. (e) Histogram of the grain size distribution for recrystallized and relict grains. (f) Histogram of the subgrain size distribution in the relict quartz grains identified in (d) and (e).(g) Pole figure of the c-axis orientation of recrystallized and relict grains, colour coded like the GOS map in (d). Equal area, lower hemisphere projection.
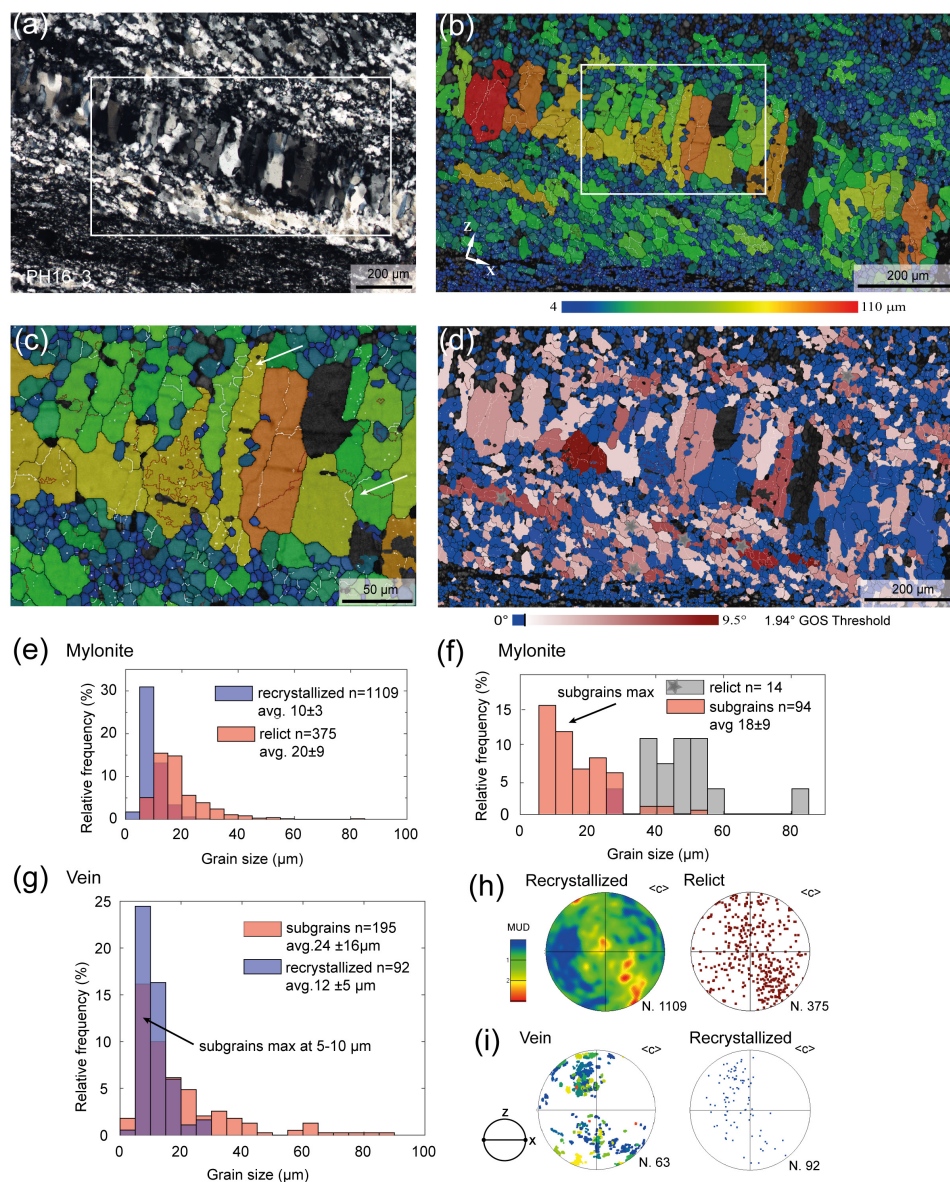
910

915

Figure 8. EBSD data of quartz from a foliation-parallel vein in the mylonite near the contact to the cataclasite. Colour coding of the boundaries like in Figure 6. (a) Quartz vein along the foliation. Quartz in the mylonite show a strong SPO consistent with the sinistral sense of shear of BFZ045. Cross polarized light. (b) Grain size map (diameter of the equivalent circle, µm. (c) Details of previous maps. Bulges and subgrains (white arrows) of similar size of the bulges are evident within the vein quartz. (d) GOS map of quartz in the vein and of the surrounding mylonite. The GOS threshold value of 1.94° separates relict grains (red) from recrystallized grains (blue).Grey stars indicate relict grains plotted in (f) for subgrain size estimates. (e) Histogram of the grain size distribution in the mylonite, with relict and recrystallized grains separated with the GOS method. (f) Histogram of the subgrain size distribution (red) in relict quartz of the mylonite (grey). (g) Histogram of the recrystallized grain size (red) and subgrains size (blue) distribution in the vein. (h-i) Pole figures of the c-axis orientation of the recrystallized and relic quartz in the mylonite (h) and in the veins (i). Equal area, lower hemisphere projection.
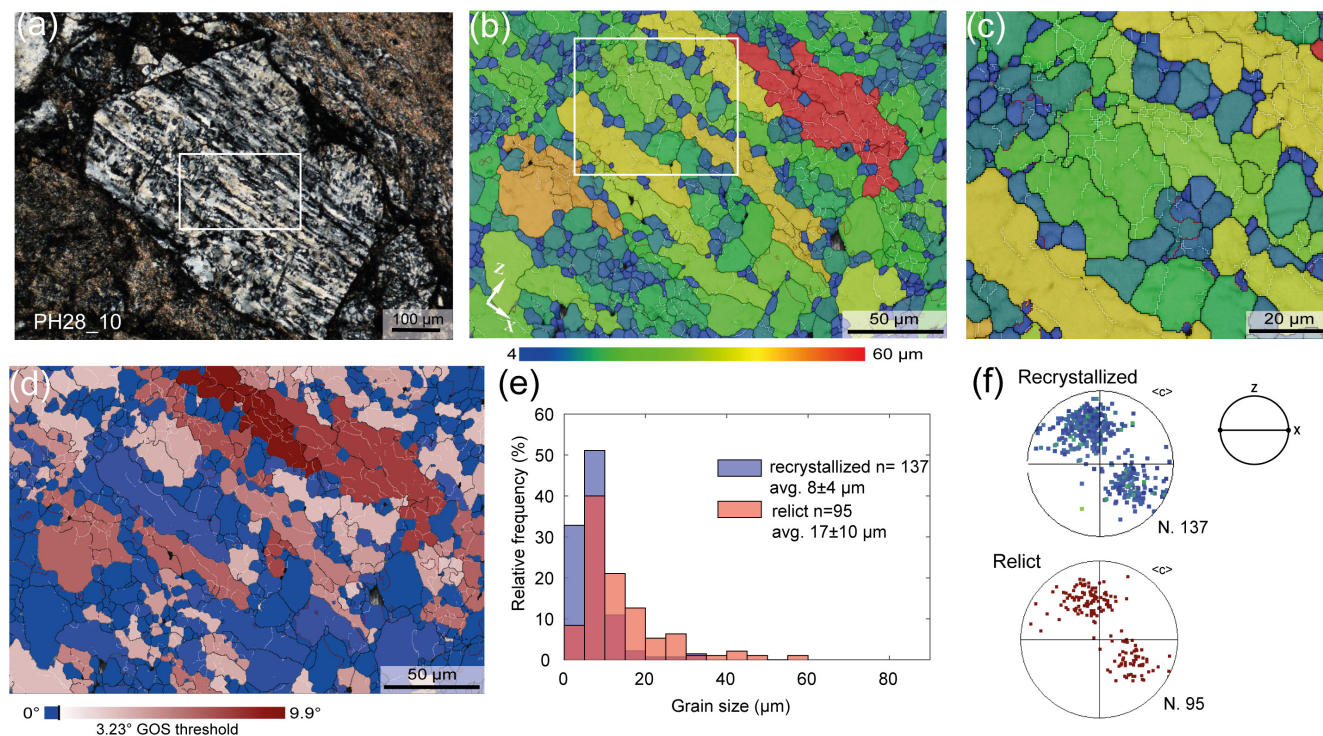
930

Figure 9. EBSD data of quartz from a clast in the cataclasite. Colour coding of the boundaries like in Figure 6. (a) The analysed quartz clast (Fig. 5f). The white rectangle locates the EBSD map shown in (b-d). (b-c) Grain size map (diameter of the equivalent circle, μm). The map highlights the presence of subgrains in the coarser elongated quartz grains with size comparable to the surrounding finer quartz. (d) GOS map. (e) Histogram of the grain size distribution of the recrystallized (blue) and relict (red)
935 **grains. (f) Pole figure of the c-axis orientation of recrystallized and relict grains. Equal area, lower hemisphere projection, color coded as GOS map.**
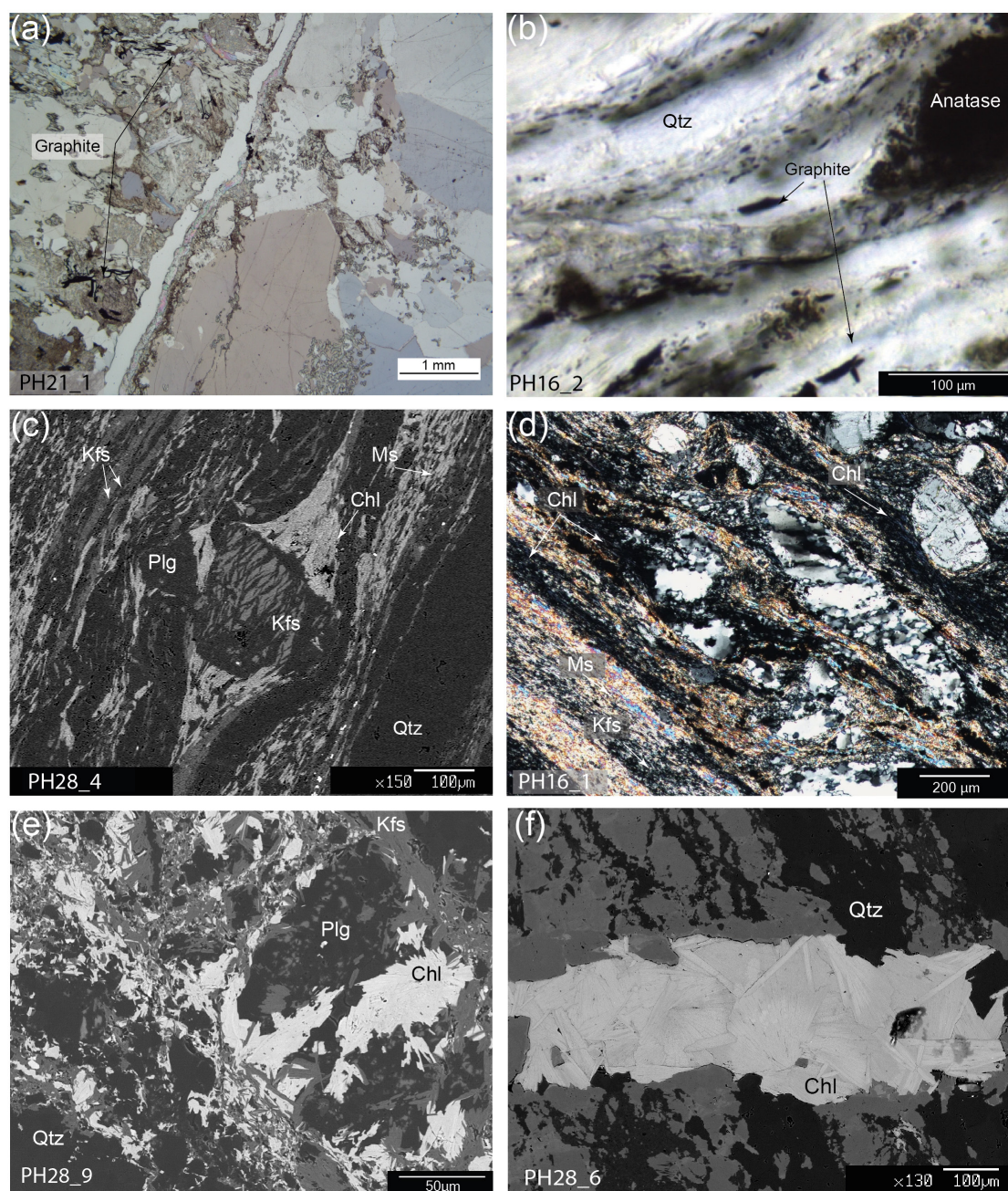
Figure 10. Light microscopy and SEM backscattered electron (BSE) images of characteristic microstructural domains and mineral assemblages used for geothermobarometry estimates. (a) Graphite flakes in association with radiate chlorite in the host rock. Plane polar light. (b) Detail of graphite grains along the mylonitic foliation of BFZ045. Plane polar light. (c) Chlorite in pressure shadows around a K-feldspar porphyroclast in the mylonite. White mica and a fine grained recrystallized K-feldspar assemblage is common along the foliation. (d) Light microscope image of a microstructure similar to (c), cross polar light. (e-f) SEM BSE images of radiate chlorite used for chlorite thermometry in the cataclasite matrix (e) and in a vein cutting the mylonitic foliation (f). The trace of the mylonitic foliation in (f) is oriented ca. NW-SE.
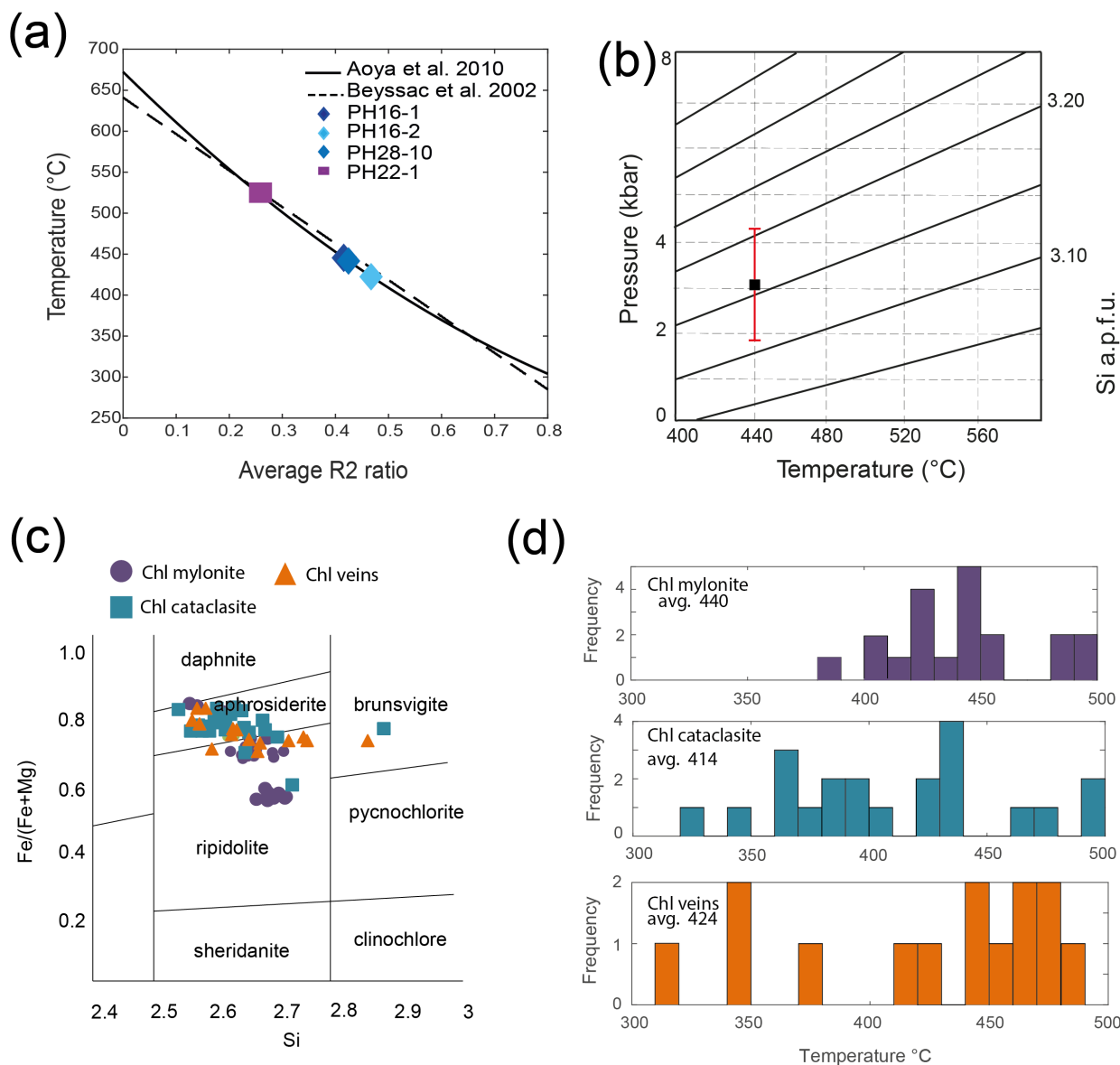
Figure 11. Results of P-T estimates. (a) Carbonaceous material Raman geothermometer. Average R2 ratio (refer to text for explanation) for graphite rich mylonitic and host rock samples was measured to derive a T estimate using the method of Beyssac et al. (2002) and Aoya et al. (2010). (b) Estimated P of mylonitization using the Si-in-phengite barometer (Massonne and Schreyer, 1987) for the average T of 440° C obtained with the carbonaceous material Raman thermometry.Red line show the total spread of the Si values obtained. Black square show the (c) Chlorite compositional diagram based on Hey (1954). (d) Chlorite formation temperature estimated for mylonitic foliation, veins and cataclasite using the method of Lanari et al. (2014).

945

950
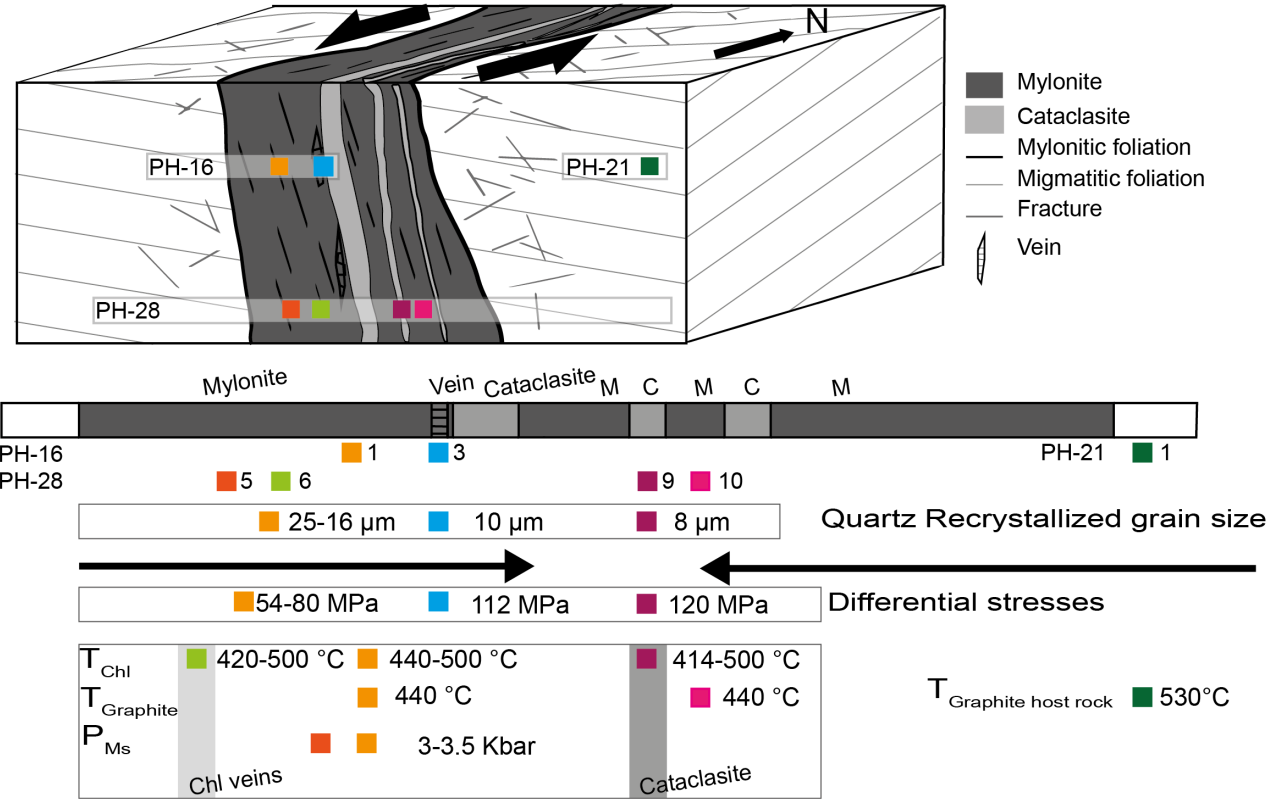
Figure 12. Schematic summary of the quartz recrystallized grain size, differential stresses, and P–T conditions of deformation for BFZ045 derived in the present study, in relationship to the fault core geometry. Each sample is coloured differently to indicate the spatial position of the results described in section 4 of this paper.
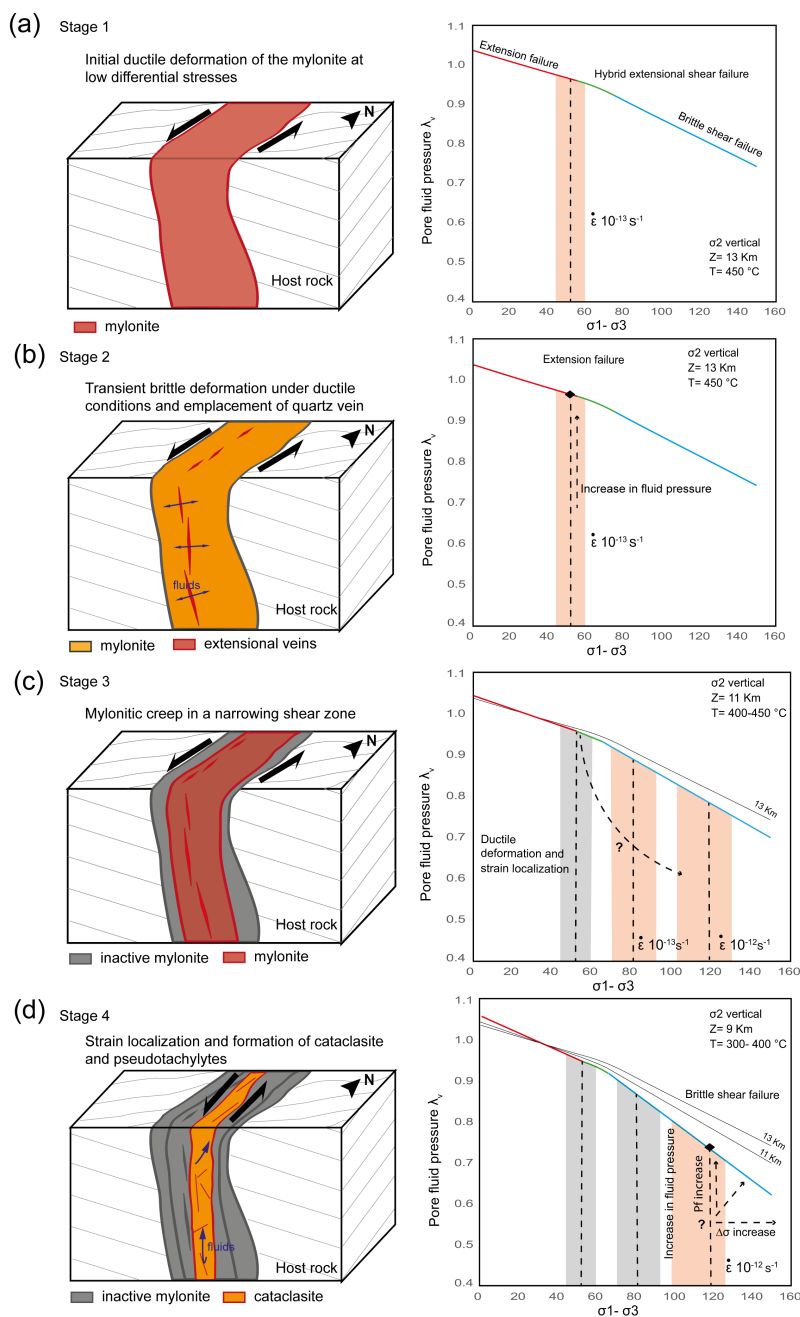
Figure 13. Conceptual model of the temporal and mechanical evolution of the BFZ045 fault zone (see text for more details). Grey lines: traces of metamorphic foliation in the host rock. In the schematic fault scheme evolution, red displays the active deformation process, grey represents the inactive deformation processes, and orange suggests a transition in the deformation. BFZ045 was characterized by (a) the development of mylonite under low differential stress followed by (b) a transient increase in fluid pressure responsible for the emplacement of quartz vein. (c) Progressive exhumation and cooling resulted in strain localization toward the centre of the mylonitic fault core in an overall narrowing shear zone, with subsequent deformation of the fault under brittle condition and associated formation of cataclasite and pseudotachylyte (d).